Development of Novel Two-Dimensional Floating Strip Micromegas Detectors with an In-depth Insight into the Strip Signal Formation

München, den 18.04.2019

Development of Novel Two-Dimensional Floating Strip Micromegas Detectors with an In-depth Insight into the Strip Signal Formation

Dissertation an der Fakultät für Physik
der
Ludwig-Maximilians-Universität München

vorgelegt von
Felix Fidelio Klitzner
geboren in Gräfelfing

München, den 18.04.2019

Erstgutachter: Prof. Dr. Otmar Biebel
Zweitgutachter: Prof. Dr. Wolfgang Dünnweber

Tag der mündlichen Prüfung: 29.05.2019

Kurzfassung

Floating Strip Micromegas Detektoren sind mikrostrukturierte Gasdetektoren (MPGDs). Aufgrund kurzer Ionendriftwege und hochsegmentierter Auslesestrukturen sind diese Detektoren hocheffiziente Einzelteilchendetektoren mit sehr guter räumlicher und zeitlicher Auflösung bis zu sehr hohen Teilchenflussdichten von mehreren MHz/cm^2.

In dieser Arbeit werden neuartige zweidimensionale Floating Strip Micromegas Detektoren mit drei Schichten Kupferstreifen entwickelt und umfassend untersucht. Unter den Floating Strips, die über hochohmige Widerstände mit Hochspannung verbunden sind, befinden sich zwei Auslesestreifenlagen, die parallel (x-Strips) und senkrecht (y-Strips) zu der Floating Strip-Schicht angeordnet sind.

Um die Signalentstehung im Detektor, dessen Kopplung auf die Auslesestreifen sowie die Antwort von ladungsempfindlicher Elektronik auf die im Detektor erzeugten Stromsignale zu verstehen, wird eine detaillierte Detektorsimulation entwickelt.

Die Simulationsergebnisse führen zur Einführung von y-Strips mit alternierender Streifenbreite um die Signale auf beiden Ausleselagen zu optimieren. Mit Hilfe dieser Resultate werden mehrere Anodenstrukturen entwickelt und zu Detektoren zusammengebaut. Charakterisierungsmessungen zeigen eine gleichzeitige Erhöhung der Signalamplitude auf beiden Ausleselagen: um einen Faktor von 2 auf der senkrechten und um einen Faktor von 4,8 auf der parallelen Ausleselage, bezogen auf Detektordesigns mit gleichmäßiger Streifenbreite.

Diese neuartigen Detektoren mit 0,5 mm und 0,3 mm Streifenperiodizität werden erfolgreich unter Bestrahlung mit 20 MeV Protonen getestet. Auf dem Detektor mit kleinerem Streifenabstand ist keine Verschlechterung der Pulshöhe auf den beiden Auslesestreifenlagen zu beobachten. Hocheffizienter Einzelteilchennachweis ist bis zur höchsten untersuchten Teilchenrate von 1 MHz möglich.

Die neuartigen Detektoren mit 0,5 mm Streifenperiodizität werden in hochenergetischen und Hochraten-Myonen- und Pionstrahlen untersucht. Die räumliche Auflösung wurde bei senkrechtem Einfall auf (79 ± 4) µm für die x-Strips und (54 ± 2) µm für die y-Strips bei einer Effizienz von $(98,0 \pm 0,2)$ % bestimmt. Die räumliche Auflösung bleibt unter (152 ± 8) µm für Einfallswinkel bis zu 40° mit einem 6 mm Driftbereich und einer Winkelauflösung von $\binom{+2.2^\circ}{-1.8^\circ}$ und $\binom{+2.1^\circ}{-1.7^\circ}$ für x- bzw. y-Lage mit einer Effizienz über 96%. Die räumliche Auflösung und Effizienz wird nur minimal beeinflusst durch eine 10%ige Pulshöhenreduzierung bei einer Teilchenflussdichte von 4,7 MHz/cm^2.

Es wurde ein zweidimensionaler Floating Strip Micromegas Detektor mit einer aktiven Fläche von $19,2 \times 19,2$ cm^2 und niedrigem Materialbudget (0,8% X_0) entwickelt und gebaut. In Messungen mit einer radioaktiven ^{55}Fe Quelle wurde eine homogene Pulshöhe über die gesamte aktive Detektorfläche beobachtet.

Floating Strip Micromegas Detektoren mit besonders geringem Materialbudget können als Einzelteilchendetektoren in ionenbasierten medizinischen Bildgebungsanwendungen eingesetzt werden, um die Bildqualität zu verbessern. Mit solchen Detektoren wird das Profil eines Protonen- und Kohlenstoffionenstrahls in einem therapeutischen Energiebereich im Heidelberger Ionentherapiezentrum gemessen. Die Strahlprofilmessung vor und nach dem Durchqueren von gewebeähnlichen Schichten eines Phantoms ermöglicht die Unterscheidung der Gewebeschichten anhand ihrer Dichte.

Abstract

Floating strip Micromegas detectors are one kind of micro-pattern gaseous detectors (MPGDs). Due to short ion drift paths and highly segmented readout structures, these detectors are highly efficient single particle tracking devices with very good spatial and temporal resolution up to very high particle flux densities of several MHz/cm^2.

In this thesis novel two-dimensional floating strip Micromegas detectors with three layers of copper strips are developed and extensively studied. Two of the three layers are readout strip layers which have strips parallel (x-strips) and perpendicular (y-strips) to the floating anode strips, placed below the floating strip layer, which is connected to high-voltage via high ohmic resistors.

A detailed detector simulation is developed to understand the signal formation in the detector, its coupling to the readout strips as well as the response of charge sensitive front-end electronics to the current signals generated in the detector.

The simulation results lead to the introduction of striplines with non-uniform width on the y-strips as a means of improving performance. Several anode structures are developed on this idea and assembled into detectors. Characterization measurements show simultaneous signal amplitude enhancements on both readout strip layers, a factor of 2 on the perpendicular and a factor of 4.8 on the parallel readout strip layer, with respect to designs with uniform readout strip width.

These novel detectors with 0.5 mm and 0.3 mm strip pitch performed perfectly under irradiation with 20 MeV protons. No pulse height degradation is observed on the smaller with respect to the larger pitch detector on either of the two readout strip layers. Highly efficient single particle tracking is possible up to the highest investigated particle rate of 1 MHz.

The novel 0.5 mm strip pitch detectors are investigated in high energy and high rate muon and pion beams. Spatial resolution at perpendicular incidence of (79 ± 4) µm for the x-layer and (54 ± 2) µm for the y-layer are observed at an efficiency of (98.0 ± 0.2) %. The spatial resolution stays below (152 ± 8) µm for incidence angles up to 40° from a 6 mm drift space with an angular resolution of $\binom{+2.2^\circ}{-1.8^\circ}$ and $\binom{+2.1^\circ}{-1.7^\circ}$ for x- and y-layer, respectively, while the efficiency remains above 96%. Spatial resolution and efficiency are only minimally affected by a 10% pulse height reduction observed at a particle flux density of 4.7 MHz/cm^2.

A low material budget two-dimensional floating strip Micromegas detector (0.8% X_0) is developed and built with an active area of 19.2×19.2 cm^2. In measurements with a radioactive ^{55}Fe source a homogeneous pulse height is observed over the full detector active surface.

Floating strip Micromegas detectors especially designed with a low material budget can be included as single particle tracking devices in ion transmission-based medical imaging applications to improve the image quality. Such detectors are used to measure the profile of a proton and carbon ion beam in a therapeutic energy range at the Heidelberg Ion Therapy center. The beam profile before and after the particles traverse tissue equivalent layers of a phantom allow to distinguish tissues according to their density.

Contents

Chapter 1

Introduction and Motivation

In this thesis novel floating strip Micromegas[1] detectors with a two-dimensional strip readout are developed and studied in detail. Floating strip Micromegas detectors are planar micro-pattern gaseous detectors (MPGDs) with a segmented strip anode. Due to their low material budget, high rate capability and good spatial and temporal resolution MPGDs are used in a broad field of science. In the following, a few applications of MPGDs are highlighted, focusing on Micromegas.

1.1 Applications of Micro-Pattern Gaseous Detectors

Micro-pattern gaseous detectors are a relatively new detector technology and show great potential due to their low material budget, high-rate capability and excellent spatial and temporal resolution. Consequently, they can be found in several high-energy physics and astrophysics experiments or even in industrial applications like medical imaging or homeland security. A detailed review of innovative applications of micro-pattern gaseous detectors can be found in [Francke and Peskov, 2014]. In the following, a few are highlighted.

The COMPASS[2]-experiment at CERN[3] was the first large scale experiment using a combination of 12 Micromegas detectors each with an active area of $40 \times 40\,\mathrm{cm}^2$ and 22 triple GEM[4] detectors of $31 \times 31\,\mathrm{cm}^2$ size. They were used in conjunction with other conventional gaseous detectors in high-intensity muon and hadron beams for the investigation of the nucleon spin structure and the spectroscopy of hadrons [Bravar, 1999].

An upcoming major upgrade featuring resistive strip Micromegas detectors as one of the two main detector technologies is the so-called 'New-Small-Wheel' - upgrade project of the ATLAS[5] experiment at the LHC[6] at CERN [Kawamoto et al., 2013]. Together with sTGC[7] detectors, the MPGDs will cover an active area of more than $150\,\mathrm{m}^2$ where they will reconstruct tracks of high energetic muons at estimated photon and neutron background hit rates on the order of several $10\,\mathrm{kHz/cm}^2$, as it is expected for the HL-LHC[8].

[1] MICRO-MEsh GAS
[2] Common Muon and Proton Apparatus for Structure and Spectroscopy
[3] Conseil Européen pour la Recherche Nucléaire, European Organization for Nuclear Research, Geneva, Switzerland
[4] Gaseous Electron Multiplier
[5] A Toroidal Lhc AparatuS
[6] Large Hadron Collider
[7] Small strip Thin Gap Chamber
[8] High Luminosity-LHC

The International Linear Collider (ILC) project plans precision measurements with e^+e^- - collisions to test the Standard Model of particle physics and potentially discover new physics. The inner tracker will be a high-performance TPC[9]. Due to the low material budget as well as high-rate capability, the signal amplification will be either managed by Micromegas or GEM anode structures [Diener, 2012].

The CAST[10] experiment is in operation since 2002, searching for hypothetical particles called "axions" which are among the most interesting candidates for dark matter in the universe [Arik et al., 2011]. Axions themselves are not directly detectable. They can however be converted into photons in a strong magnetic field. Thus the CAST experiment searches with the help of a 9.5 T magnet for hints of X-rays originating from the conversion process of an Axion, which are being detected by − among other technologies− Micromegas.

MPGDs also find use in applications regarding public concern like smoke detectors or sensors for dangerous gases. This can be achieved for instance by equipping the monitored area with pulsed UV sources which are being recorded by a GEM-based position sensitive UV detector [Bidault et al., 2006], [Bidault et al., 2007]. In the case of a fire producing smoke or dangerous gases, both absorbing UV light, the amplitude of the signal and the counting rate in the detector drops, raising an alarm.

MPGDs are also used e.g. for neutron time-of-flight measurements used at nTOF[11] [Pancin et al., 2004] at CERN or neutrino oscillation measurements at T2K[12] [Abgrall et al., 2011] in Japan. More recently a new MPGD-based technology has been developed at CERN, which is called µ-RWELL [Bencivenni et al., 2015] and is a combination of a Micromegas and GEM detector.

The use of Micromegas in medical applications like ion transmission imaging is explained in more detail in section 1.3 as it is also part of the research presented in this thesis.

The applications mentioned above demonstrate that MPGDs find use in a very broad field of science. The improvement of those detectors depends on deepening our understanding of the physics principles behind their operation. This motivates research and development on MPGDs as it is presented in this work.

1.2 Performance of One-Dimensional Floating Strip Micromegas Detectors

Micromegas detectors are micro-structured gaseous detectors that were invented by [Giomataris et al., 1996] and have been steadily improved over the past 20 years. Floating strip Micromegas detectors, an adaption of standard Micromegas, with one-dimensional strip readout have proven to be high-rate capable particle tracking detectors with good spatial and temporal resolution. Their development and performance has been discussed in detail in [Bortfeldt, 2014] and is only very briefly mentioned here. The working principle is explained in chapter 2. They allow highly efficient single particle tracking at fluxes up to $7\,\mathrm{MHz/cm^2}$ at a spatial resolution below 100 µm. A key element of this detector principle is the floating anode strip, which allows to reduce the consequences of discharges between micro-mesh and anode that can occur due to the high signal amplification needed in gaseous detectors. As a direct consequence the reconstructed pulse height in the detector is only reduced by around 20 % at particle rates up to 80 MHz, see Figure 1.1.

[9] Time Projection Chamber
[10] CERN Axion Solar Telescope
[11] neutron Time Of Flight
[12] Tokai to Kamioka

This makes the detector very attractive for applications where high spatial resolution with low material budget are needed in high particle rate environments. Thus, a specific application of these detectors is in medical applications as single particle tracking detectors, where high particle rates are usually required to keep the treatment time as short as possible. Measurements at the Heidelberg Ion Therapy Center (HIT) have been carried out by [Bortfeldt, 2014] and show that floating strip Micromegas detectors are well suited as a tracking chamber in medical imaging applications. As this is a very specific application, the idea is explained in the next section.

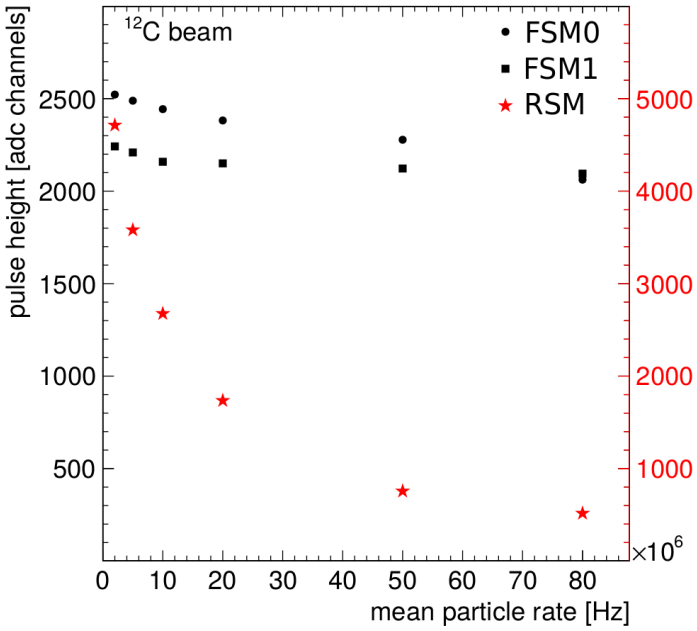

Figure 1.1: Reconstructed pulse height in two floating strip Micromegas (FSM0 and FSM1) and a resistive strip Micromegas (RSM, 90 MΩ/cm strip resistivity) as a function of the particle beam intensity. The almost constant pulse height of the floating strip Micromegas as a function of the particle rate is a key element to efficiently reconstruct single particle tracks up to the several MHz rate regime. Picture taken from [Bortfeldt, 2014].

1.3 Floating Strip Micromegas Detectors with Two-Dimensional Strip Readout for Medical Imaging Applications

Before detailing how floating strip Micromegas detectors with two-dimensional strip readout find use in medical imaging applications, the idea behind particle therapy is briefly explained.

Particle based therapy is a term used to distinguish it from conventional X-ray therapy, which is using photons. Both therapy forms are used in cancer treatment centers all over the world and aim at destroying the tumor's desoxyribonucleic acid (DNA) while sparing the surrounding healthy tissue as much as possible.

The difference between particle and photon-based therapy lies in the physics of how the respective radiation interacts with matter. The photon interaction is a combination of different purely statistical processes depending on the energy of the photon. Therefore no definite range of a single photon can be defined in matter. However, the energy-loss per unit path of a charged particle is well described by the Bethe-Bloch formula [Segrè et al., 1953], which results in a well defined range in matter. This leads to an inverse energy deposition profile in tissue, as can be seen in Figure 1.2 for a photon and proton beam. The relative dose i.e.

the deposited energy per unit mass is plotted against the beam penetration depth in water, which is comparable to the tissue density of a human body. More detailed information on particle interaction with matter can be found in chapter 2.

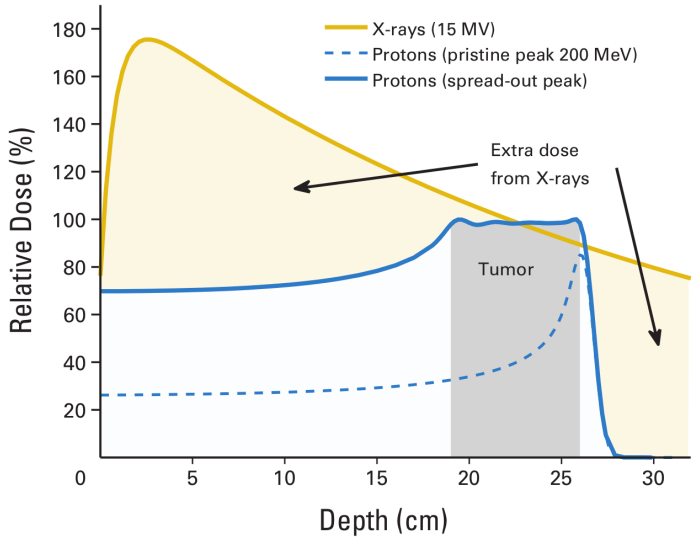

Figure 1.2: Depth-dose profiles for conventional X-ray (photon) therapy and proton therapy, aiming to deliver the lethal dose to a deep-seated tumor. As the Bragg-peak of the protons (dashed, blue line) can be adjusted by the beam energy, the dose (blue line) can be delivered precisely to the tumor location (darkgrey shaded) [Mitin and Zietman, 2014].

While the photon beam dose deposition has its maximum close to the surface (here around 3 cm), the maximum dose deposition of the proton beam, the so-called Bragg-peak, can be adjusted with the beam energy to lie precisely in the tumor's location. This leads to an approximately 60% reduction of the integral dose to healthy tissue [Goitein, 2007]. More recently, heavier particles like carbon ions are also used for radiation therapy due to their reduced amount of multiple scattering in the human body [Rinaldi, 2011]. However, fragmentation of the heavier particles needs to be taken into account.

Precise knowledge of the Bragg-Peak position in the patient during treatment, is the key to efficiently deliver the dose to the tumor's location. Misplacement due to e.g. motion of organs need to be known precisely. The use of ion based images of the patient prior or in between treatment could be an alternative to using X-ray images where range calibration curves introduce additional uncertainties [Rinaldi, 2011]. The dose is found to be reduced by a factor of 50-100 using ion transmitted based images instead of X-ray computer-based tomographies [Schneider et al., 2004]. However, ions undergo multiple coulomb scattering processes during the passage through matter, depending on the radiation length [13] X_0 of the medium. These small deviations from the assumed particle trajectory cause uncertainties in the aquired final radiography or tomography. To reduce these effects, the precise knowledge of each particle's trajectory in three-dimensional space is necessary, including its energy.

The principle of an ion transmission image based setup with multiple two-dimensional floating strip Micromegas detectors used as a single particle tracking system is sketched in Figure 1.3. After the tracking system, a multi-layer Residual Range Telescope (RRT) detector is used to measure the particle residual range after traversing the object.

[13] the radiation length X_0 is the mean distance describing the energy-loss of a high-energy electron to $1/e$ of its initial energy

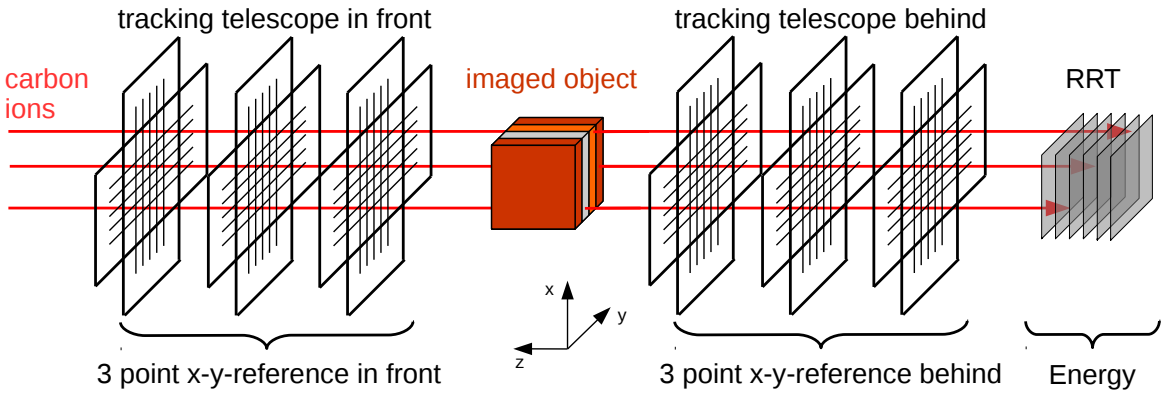

Figure 1.3: Schematic setup of a tracking system consisting of six two dimensional floating strip Micromegas detectors, three placed in front and three behind an object or patient. Single ion trajectories can thus be reconstructed with high precision in front and behind the test object. The particle energy i.e. range is determined after the tracking telescope with a Residual Range Telescope (RRT).

The advantage of using a two-dimensional hit position resolving Micromegas is obvious, as thus there is no need to use two one-dimensional detectors rotated 90° with respect to each other, to extract the particle hit information in both dimensions simultaneously. This reduces the material budget in the path of the particles and thus additional multiple scattering. The scenario illustrated here mirrors an ideal situation in which one has at least three measurement points in front and behind the imaged object, to reconstruct the ion tracks. This minimizes extrapolation errors originating from a fully constrained line fit with only two measurement points.

With the knowledge of each particle track direction in front and behind the imaged object, the most likely path (MLP) can be calculated. In combination with a RRT also capable of measuring single particles, this can help to increase the image's spatial resolution [Li et al., 2006]. By minimizing the material budget of the tracking Micromegas on the $0.005 \cdot X_0$ level, which corresponds to (200 ± 50)µm water equivalent thickness [Magallanes, 2017], these gaseous detectors are ideal for inclusion in applications where minimal multiple scattering is needed.

Simulations on the benefit of floating strip Micromegas as part of a single particle tracking system in a clinical environment is already well advanced, see [Meyer, 2019]. Proton based radiographies with small animals are planned. Due to the light particle nature, the material budget of the trackers needs to be extremely low to allow efficient high quality particle trajectory reconstruction.

1.4 On the Content of this Thesis

The first two-dimensional floating Micromegas anode was developed by J. Bortfeldt at LMU and first measurements with a detector equipped with the anode have been performed by König [2015]. Further measurements were carried out at the Heidelberg Ion Therapy Center (HIT) and the MLL Tandem accelerator in Garching, Munich. The results can be found in [Bortfeldt et al., 2017] and [Klitzner, 2016], respectively.

In this thesis, novel two-dimensional floating strip Micromegas detectors have been developed. Based on a detailed detector simulation to understand the signal formation in the detector

and the coupling process to the readout strips, several anode structures have been developed to improve the signal yield on both readout strip layers. The anode PCBs[14] have been assembled in detectors and extensively studied with a radioactive ^{55}Fe source and with ion beams in various test beam campaigns.

The main aspects covered are briefly described in the following:

- The theoretical background of particle interaction with matter is explained in chapter 2. It includes the creation of ionization charge by passage of a charged particle or photon in a gas volume, drift and diffusion of charge carriers in gases and the necessary amplification process taking place in MPGDs. The functional principle of Micromegas in general will be explained and three different Micromegas types will be described.
- Material and methods used in the context of a detector simulation, readout electronics interfacing the constructed detectors and analysis algorithms are described in chapter 3.
- A detailed detector simulation on the signal formation in two-dimensional floating strip Micromegas including the response of charge-sensitive readout electronics is presented in chapter 4.
- The developed and investigated two-dimensional floating strip Micromegas anode PCBs and constructed detectors are presented in chapter 5. An estimation about reflection or resonance effects of the signal in the detector when using strip lines with non-uniform width is described. The full material budget of the detectors is calculated and listed in units of radiation length.
- Signals measured on both readout strip layers of the investigated anodes are characterized in chapter 6.
- Particle reconstruction efficiency and spatial resolution on both readout strip layers are investigated in test beams with 20 MeV protons (chapter 7) and 20 to 150 GeV muons and pions (chapter 8) for perpendicularly incident and inclined particle tracks.
- Different floating strip Micromegas serving as low material budget single particle trackers for ion transmission imaging are investigated at the Heidelberg Ion Therapy Center (HIT) in chapter 9. The focus lies on beam shape reconstruction of proton and carbon ion beams before and after traversing tissue equivalent phantoms.

[14] Printed Circuit Board

Chapter 2

Theoretical Background and Functional Principle of Micromegas Detectors

In this chapter the underlying physics processes of particle interaction with matter are described. The focus will lie on interaction in thin gaseous detectors, such as Micromegas, thus the drift and amplification of charge carriers in gases is discussed. Consequently, the functional principle of Micromegas detectors will be explained and different types of Micromegas are presented.

2.1 Particle Interaction with Matter

In gaseous detectors particles can only be detected through their interaction with matter. The dominant interaction mechanisms for charged particles are ionization and excitation. For highly relativistic particles *bremsstrahlung* also needs to be taken into account. The mean energy loss of charged particles (with mass $m_0 \gg m_e$) per unit length can be described by the Bethe-Bloch formula [Segrè et al., 1953]

$$\left\langle \frac{dE}{dx} \right\rangle = -4\pi N_A r_e^2 m_e c^2 \rho \frac{Z z^2}{A\beta^2} \left(\frac{1}{2} \ln \frac{2 m_e c^2 \beta^2 \gamma^2 T_{max}}{I^2} - \beta^2 - \frac{\delta}{2} \right) \quad , \tag{2.1}$$

with r_e: classical electron radius; m_e: electron mass; c: speed of light; ρ: density, Z: charge in units of e and A atomic weight of the absorbing material; z: charge in units of e , $\beta = v/c$: velocity v of the incident particle and $\gamma = 1/\sqrt{1-\beta^2}$; $T_{max} \approx 2 m_e c^2 \beta^2 \gamma^2$: maximum energy transfer to an electron in a single collision [Grupen and Shwartz, 2008].

To be largely independent of the absorbing material properties, energy loss i.e. the stopping power is usually given in units $\mathrm{MeV\,cm^2/g}$ with $dE/dX = dE/(\rho \cdot dx)$, as can be seen in Figure 2.1 for the stopping power of a muon in Copper as a function of $\beta\gamma$. From the equation follows, that relativistic particles with an energy corresponding to $\beta\gamma \approx 4$ have an energy loss on the order of $2\,\mathrm{MeV\,cm^2/g}$ for almost all absorber materials, thus they are usually called *minimum-ionizing particles* (MIPs). Particle energies used for measurements presented in this thesis vary in a range between $\beta\gamma \approx 0.2$ (20 MeV protons, see chapter 7) and $\beta\gamma \approx 1000$ (20 to 150 GeV muons, see chapter 8), where the energy loss/deposition in a detector varies by roughly a factor of 10.

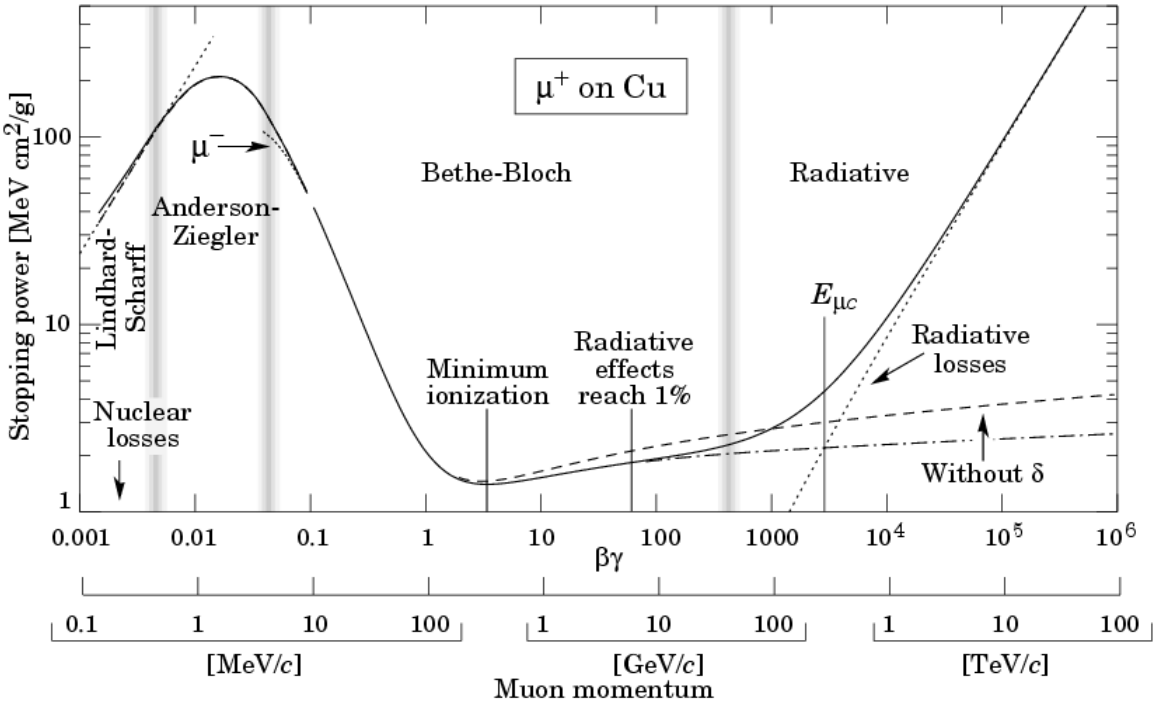

Figure 2.1: Mean stopping power (i.e. energy loss per density) loss for muons in copper. Figure taken from [Groom et al., 2001]

In the case of thin absorber materials e.g. micro-pattern gaseous detectors, strong fluctuations around the average energy loss described by Bethe-Bloch exist because of possible large energy transfers to target electrons (producing so-called 'delta-electrons'). The most probable energy-loss in a layer of thickness d can then be described by [Bichsel, 1988]

$$\left.\frac{\Delta E}{\Delta x}\right|_p = 2\pi N_A r_e^2 m_e c^2 z^2 \frac{Z}{A} \cdot \frac{\rho}{\beta^2}\left(\ln\frac{2m_e c^2\gamma^2\beta^2}{I} + \ln\frac{\xi\cdot d}{I} + 0.2 - \beta^2 - \delta\right) \quad , \tag{2.2}$$

with $\xi = 2\pi N_A r_e^2 m_e c^2 z^2 \frac{Z}{A} \cdot \frac{\rho}{\beta^2}$. The energy-loss distribution of charged particles in a gaseous detector is thus expected to be strongly asymmetric but can be well described by a Gaussian convoluted *Landau distribution*. Increasing the absorber thickness reduces this effect and for very thick absorbers the energy-loss can be approximated by a Gaussian distribution [Grupen and Shwartz, 2008]. It should be noted that the ionization produced by a charged particle can be divided into primary and secondary ionization. While primary ionization is caused by direct production of electron/ion-pairs through the ionizing particle, secondary ionization is due to the interaction of primary ionization charge carriers (e.g. delta-electrons) with the target material or by intermediate excited states of atoms. The latter, as stated by Penning [1927], actually can contribute the most to the total created ionization charge, depending on the used detector gas. Properties of commonly used noble and molecular detector gases at NTP[1] are shown in table 2.1

[1]Normal Temperature and Pressure: 20°C and 1013 mbar, respectively

gas	density [mg cm^{-3}]	W_i [eV]	$dE/dx\|_{\min}$ [keV cm^{-1}]	n_T [cm^{-1}]
He	0.179	41.3	0.32	8
Ne	0.839	37	1.45	40
Ar	1.66	26	2.53	97
Xe	5.495	22	6.87	312
CH_4	0.667	30	1.61	54
C_2H_6	1.26	26	2.91	112
iC_4H_{10}	2.49	26	5.67	220
CO_2	1.84	34	3.35	100
CF_4	3.78	54	6.38	120
Ar:CO_2 93:7 vol.%	1.67	26.6	2.59	97
Ne:CF_4 80:20 vol.%	1.43	40.4	2.44	56

Table 2.1: Properties of noble and molecular gases at NTP. W_i: average energy to create an electron-ion pair, n_T: total number of created electron-ion pairs per cm per MIP. Extracted from [Tanabashi et al., 2018]. The two gas mixtures used for measurements in this thesis are also stated, calculated from the volumetric mixing ratios of the constituent gases.

The interaction mechanism of photons, which neither carry electric charge nor have a mass, is completely different from charged particles. It can be subdivided into three main processes, depending on the energy of the photon and also on the target material properties.

At photon energies roughly below 100 keV, the dominant process is the photo-absorption, where the photon is fully absorbed by a target electron, transferring the total energy. For small binding energies of the electron to the nucleus compared to the photon energy, the electron is directly released and carries the residual energy as kinetic energy. If the binding energy is higher than the photon energy, the electron can be lifted to a higher energy level in the atom. Consequently, a different electron falls onto a lower energy level by emitting a secondary photon with a different energy or by emitting an electron on a different shell with smaller binding energy (so-called Auger-effect).

For photon energies between 100 keV and $2\,m_e \approx 1$ MeV, the Compton-scattering process is the dominant photon interaction mechanism. Parts of the photon energy are delivered to a target electron, while the photon is scattered with lower energy under an angle $\theta > 0$.

For photon energies larger than $2\,m_e \approx 1$ MeV, the pair-production cross-section rises and becomes the dominant interaction above 2 MeV, where the photon can create electron-positron pairs in the vicinity of a nucleus or electron coulomb field [Kleinknecht, 2005].

All three processes discussed are of purely statistical nature, thus, a definite range of a single photon in matter can not be defined. However, the number of photon interactions per unit volume is strongly dependent on the target material properties. Thus, a collimated photon beam with intensity I_0 diminishes exponentially in a target of thickness x, following

$$I(x) = I_0 \cdot \exp^{-\mu x} \quad , \tag{2.3}$$

where μ is the absorber dependent *attenuation* coefficient in units cm^{-1}, also often found as *mass-attenuation* coefficient in units cm$^2/g$. The mass-attenuation coefficient for copper as a function of the photon energy and the different interaction processes is shown in Figure 2.2.

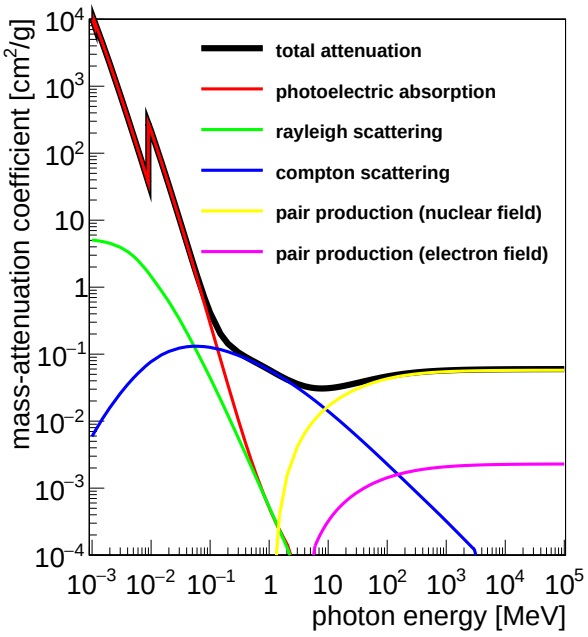

Figure 2.2: Mass-attenuation coefficient in Copper as a function of the photon energy. The contributions of the different interaction processes are shown. The mass-attenuation coefficient is dominated by the photoelectric effect, Compton scattering and pair production in the nuclear field for low, medium and high photon energies, respectively. Data extracted from [Linstrom and Mallard, 2019].

2.2 Drift and Diffusion of Charge Carrier in Gases

As the primary charge carrier in Micromegas detectors are the electrons created in the gas volume defined by the drift region, the drift and diffusion of electrons in different typical detector gas mixtures is described in this section. However, if it comes to the amplification process via Townsend avalanches in the amplification region (see section 2.3), the drift of the ions is the dominant process for the creation of the signal on the anode strips, see chapter 4.

Ions in a gas volume in the presence of an electric field E move on average with a velocity v^+ in direction of the electric field lines. The velocity is dependent on the ion mobility μ^+ and the pressure p of the gas, following [Kleinknecht, 2005]

$$v_d^+ = \mu^+ E \cdot \frac{p_0}{p} \quad , \tag{2.4}$$

with the normal pressure p_0=1013 mbar. Ion mobilities in different gases also used for simulations or measurements presented in the later chapters are listed in table 2.2.

The factor of two higher ion mobility for a Ne:CF_4 gas mixture compared to the commonly used Ar:CO_2 gas mixture can be used in applications where fast signal processing is desired, as the signal duration induced on the anode strips of a Micromegas is also reduced by 50%.

The drift of electrons in gases is a much more complex process. Due to their low mass and point-like interaction, their average mean free path is much larger than for ions. Thus, their mobility is increased by a factor of 10^2 to 10^3 [Kleinknecht, 2005]. Quantum-mechanical interference effects and elastic scattering with noble gas atoms lead to large variations of the interaction cross-section, depending on the energy of the electron (Ramsauer-effect). The effective electron drift velocity is defined as the time the electron needs averaged over all

mean free paths. By adding quencher gases such as CO_2 or CF_4 elastic scattering with the noble gas atoms can be reduced, increasing the effective electron drift velocity.

Figure 2.3 shows the electron drift velocity and transverse diffusion for different detector gases, simulated with MAGBOLTZ [Biagi, 2018]. The high drift velocity and low diffusion for CF_4 based gas mixtures is clearly visible and can, depending on the user specific application, be exploited.

gas	ion	mobility μ^+ [$cm^2V^{-1}s^{-1}$]
Ar	Ar^+	1.7
CO_2	CO_2^+	1.09
Ar	CO_2^+	1.72
Ne	Ne^+	4.7
CF_4	CF_3^+	1.12
Ne	CF_3^+	3.16
H_2O	H_2O^+	0.7

Table 2.2: Ion mobility in various gases at NTP taken from [Kleinknecht, 2005], [Santos et al., 2018], [Ellis et al., 1976],[Cortez et al., 2019].

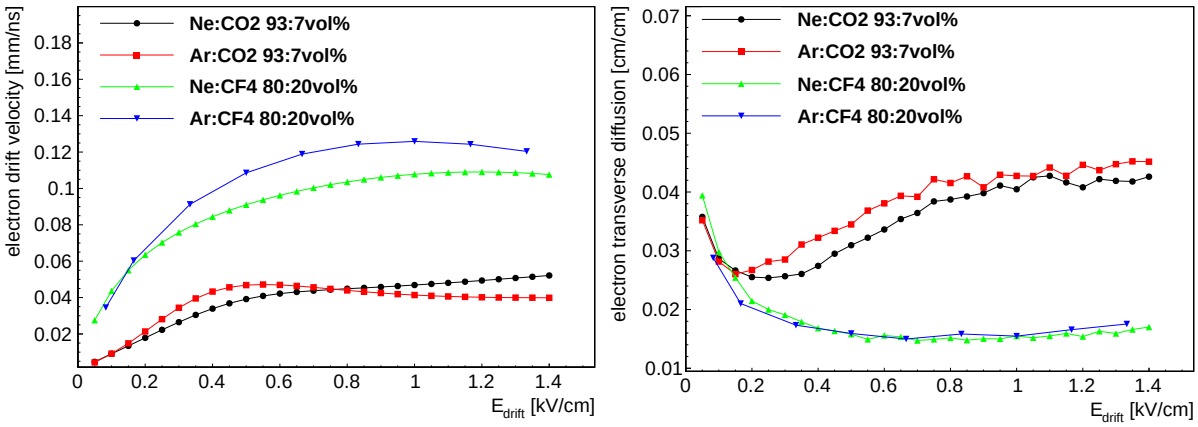

Figure 2.3: Electron drift velocity (left) and transverse diffusion (right) as a function of the drift field for gas mixtures Ne:CO_2 93:7 vol.% (black dots), Ar:CO_2 93:7 vol.% (red squares), Ne:CF_4 80:20 vol.% (green triangles pointing upwards) and Ar:CF_4 80:20 vol.% (blue triangles pointing downwards), simulated with MAGBOLTZ [Biagi, 2018] at 20°C and 1013 mbar.

2.3 Townsend Amplification in Gases

Due to the small amount of charge carriers created per unit length in a gaseous detector, an amplification process is usually needed to obtain a well measurable signal on the readout structure. Micromegas are proportional counters, as the measured signal on the anode is proportional to the initial number of charge carriers created e.g. by an ionizing particle. The underlying process is called Townsend amplification or avalanche multiplication.

Assume λ to be the mean free path of an electron, placed in a gas volume in the presence of an electric field E. If E is high enough, such that the electron reaches enough energy within λ to ionize a gas atom, an exponential amplification process takes place.

Assuming N_0 as the number of initial electrons, the number of resulting electrons after the avalanche process $N(d)$ can be calculated by

$$N(d) = N_0 \cdot e^{\alpha d} = N_0 \cdot G \quad , \tag{2.5}$$

with the first Townsend coefficient $\alpha = \lambda^{-1}$, the thickness of the amplification gap d and $G = \exp(\alpha d)$ describing the multiplication factor i.e. the *gas gain*. G is strongly dependent on the electric field, the parameters of the used gas such as the ionization cross-sections and density, and the amplification distance d [William, 1993]. Typical values of G for Micromegas detectors range from 10^2 to 10^4.

Figure 2.4 (left), shows the simulated number of electron/ion pairs created by a MIP traversing the 6 mm drift gap of a Micromegas, for two different gas mixtures [Veenhof, 2010]. The necessity of an amplification process is visible, as on average less than 40 electron/ion pairs are created. Figure. 2.4 (right), shows the first Townsend coefficient as a function of the amplification field strength E_{amp} for different gas mixtures, simulated with MAGBOLTZ [Biagi, 2018].

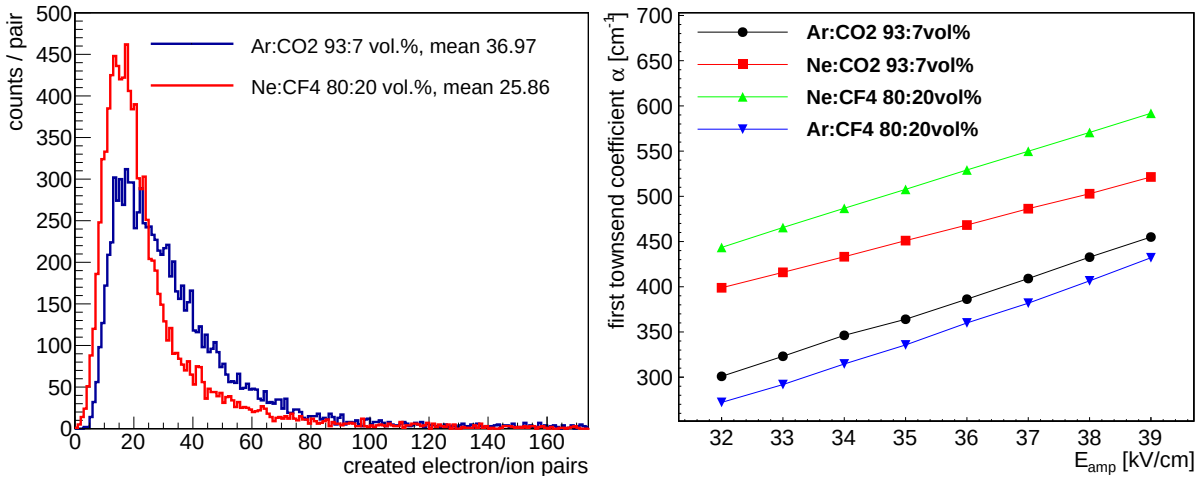

Figure 2.4: The left figure shows the number of created electron-ion pairs from a MIP perpendicularly traversing a 6 mm wide gas volume containing Ar:CO_2 93:7 vol.% (blue) and Ne:CF_4 80:20 vol.% (red), simulated with GARFIELD++ [Veenhof, 2010] at NTP. The right figure shows the first Townsend coefficient α as a function of the amplification field for gas mixtures Ar:CO_2 93:7 vol.% (black dots), Ne:CO_2 93:7 vol.% (red squares), Ne:CF_4 80:20 vol.% (green triangles pointing upwards) and Ar:CF_4 80:20 vol.% (blue triangles pointing downwards), simulated with MAGBOLTZ [Biagi, 2018] at 20°C and 1013 mbar. Note that Penning transfer [Penning, 1927] was not included in the simulations.

2.4 Functional Principle of Micromegas Detectors

Micromegas detectors are planar, high-rate capable, high resolution **micro-me**sh **gas**eous detectors with a micro-structured anode readout, proposed by Giomataris et al. [1996].

A typical Micromegas detector consists of a drift region and an amplification region. The two regions are separated by a thin conductive micro-mesh, typically made of stain-less steel. The micro-mesh, as the name suggests, is made from very thin wires with a typical diameter between 18 and 30 µm and mesh width smaller than 100 µm.

The drift region, formed by a planar cathode and the micro-mesh, has a typical width of 5-6 mm. A voltage of typically -1000 V applied to the cathode and -500 V applied to the micro-mesh creates a moderate electric field of $E_{drift} \approx 0.8$ kV/cm.

The amplification region is formed between the anode and the micro-mesh. The constant distance of around 0.1 mm is assured by a photolithographically produced pillar shaped spacer structure on the anode. As the anode strips are kept at ground potential via dedicated readout electronics, a considerably higher electric field of E_{amp}=39 kV/cm is created. The functional principle of a standard Micromegas is sketched in Figure 2.5.

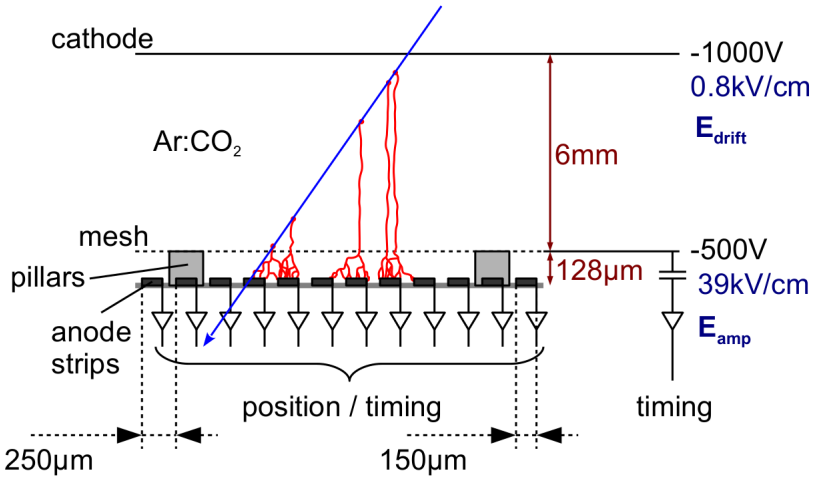

Figure 2.5: Schematic cut through a standard Micromegas detector. A charged particle (blue line) traverses the detector and creates electron/ion pairs along its path. Electrons drift through the micro-mesh into the amplification region, where they are multiplied in Townsend avalanches. The amplified signal is collected on anode strips where position and timing information can be recorded with dedicated readout electronics. Picture taken from [Bortfeldt, 2014].

If a charged particle (blue line) traverses the Micromegas, it usually creates around 20 to 70 electron/ion pairs in the gas along its path (for a MIP at NTP in a 6 mm drift region). Due to the applied electric field in the drift region, electrons drift towards the micro-mesh and ions towards the cathode. The maximum drift time of the electrons, which is defined by the drift region length and the electric field E_{drift}, is usually kept on the order of 100 ns, depending on the detector gas used (see section 2.2). When the electrons reach the micro-mesh, they are guided along the electric field lines through its holes into the amplification region. Depending on the applied amplification field E_{amp}, Townsend charge multiplication takes place with a gain between 10^2 and 10^4, as discussed in the last section. The amplification process is finished in less than 2 ns due to the high mobility of the electrons in the high electric fields. However, as most of the charge is created in the very last steps of the amplification process, the signal duration on the anode strips is dominated by the drift of the positive ions away from the anode strips to the micro-mesh, where they are neutralized. As the amplification region is very thin, this process takes around 50 to 300 ns at most, depending on the ion mobility. The resulting typically fC strong charge signals are then collected on the anode strips and processed by dedicated readout electronics (see chapter 3, section 3.2). The charge and timing information of each individual strip allows to reconstruct the position of the traversing particle with high precision. Due to the short signal duration of maximum 300 ns, this detector technology is very well suited for applications where high particle fluxes are expected.

2.5 Electron Transparency of the Micro-Mesh

The electrons created in the ionization process in the drift region move towards the micro-mesh. Ideally, all electrons enter the amplification region, to be collected on the anode strips after avalanche multiplication. However, the typical optical transparency of the micro-mesh is only on the order of 30% to 50%, depending on wire diameter and pitch. The electron mesh transparency depends on the ratio amplification and drift field and is thus much higher. It can reach almost 100% for optimum choice of drift and amplification fields, mesh geometry and detector gas mixture. This can be understood by the considerable ratio of E_{drift} and E_{amp}, as the drift field lines are bent through the holes of the mesh into the high field region. In the optimal scenario of 100% transparency, all drift field lines are bent through the holes and the electrons strictly follow the field lines, thus they are all guided into the amplification region. This can be achieved for very high ratios of $\xi = E_{amp}/E_{drift}$. Lowering the ratio leads to field lines ending on the micro-mesh, thus absorbing electrons and lowering the transparency. However, the electron mesh transparency is strongly dependent on the transverse diffusion of the electrons, as they can diffuse off the field lines and be absorbed on the mesh. Figure 2.6 (left), shows exactly this behavior for two different gas mixtures Ar:CO_2 and Ne:CF_4, which show a very different electron transverse diffusion behavior (see Figure 2.3). The transparency dependence on the chosen micro-mesh geometry is shown in Figure 2.6 (right), simulated with the GARFIELD package [Veenhof, 2010]. The notation "diameter/opening width", with diameter + opening width = pitch, was used to describe the geometric arrangement of the micro-mesh.

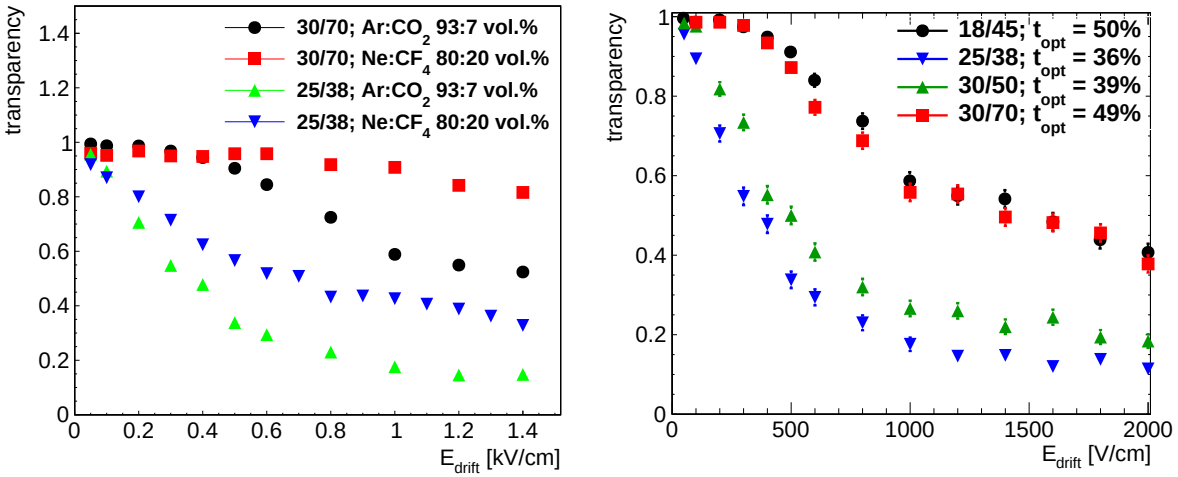

Figure 2.6: Left: Electron mesh transparency as a function of the drift field for gas mixtures Ar:CO_2 93:7 vol.% and Ne:CF_4 80:20 vol.%, with two different micro-mesh types, simulated with Garfield++ [Veenhof, 2010] at 20°C and 1013 mbar. Right: Transparency in a Ar:CO_2 93:7 vol.% gas mixture for different commercially available micro-mesh types, also the optical transparency is stated in the legend. Simulations and pictures taken from [Lösel, 2017].

2.6 Different Types of Micromegas

In this section different types of Micromegas detectors are introduced, mainly differing by the structure of their readout anode.

2.6.1 Standard Micromegas

The functional principle and setup of a standard Micromegas has already been explained in section 2.4, Figure 2.5. As charge multiplication i.e. signal amplification is needed in gaseous detectors like Micromegas, discharges between micro-mesh and anode strips can occur due to the high charge density in the avalanches. If the charge density in the avalanche exceeds a critical value[2], a conducting plasma develops between mesh and anode, equalizing the potentials until the discharge is stopped. This limit is usually refered to as Raether-limit [Raether, 1964]. Discharges are mostly created by heavy ionizing particles like α-particles or heavy nucleus fragments, originating from radioactive decays or showers in the atmosphere. Another source of discharges is created by increasing particle rates. Above a certain limit, avalanches of different particles are merged together in a similar point in space-time and thus locally exceed the Raether-limit.

Discharges in Micromegas are localized and non-destructive, but cause a dead-time to the whole detector, as no avalanche process can take place if the potential difference between mesh and anode drops below a certain point. In the next two sections, two possible solutions to mitigate the dead-time problem caused by discharges in the standard Micromegas are presented.

2.6.2 Resistive Strip Micromegas

A possible solution to reduce the consequences of discharges in Micromegas detectors is the resistive strip technology [Alexopoulos et al., 2011]. The principle of the detector design is shown in Figure 2.7, which illustrates two schematic cuts through the chamber. The detector is assembled in a so-called bulk-Micromegas structure, where the mesh is laminated directly on top of the pillars. The difference to a standard Micromegas is that a resistive protection layer covers the copper strips on the anode printed circuit board (PCB).

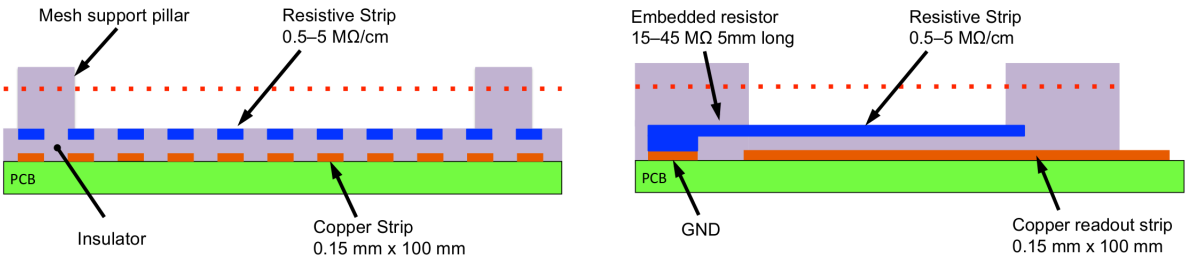

Figure 2.7: Schematic cut through the amplification region and anode PCB of a resistive strip Micromegas detector, for two orthogonal views. The strips typically have a resistivity of 0.5 MΩ/cm to 100 MΩ/cm. Picture taken from [Alexopoulos et al., 2011].

The resistive strips consist of graphite doped epoxy and are usually screen printed or sputtered onto a thin insulating layer of Kapton (around 50 µm thick). They match the pattern of the copper readout strips on the anode PCB and are connected either to the detector ground or an HV supply. Thus, depending on the detector geometry, either the mesh or the resistive strips can be supplied with high voltage.

Discharges induced by e.g. highly ionizing particles lead to a local voltage drop in a very confined region on a strip due to its high resistivity. The potential of this small region quickly

[2] A value of 1.77×10^6 e/0.01 mm^2 has been determined by Moll [2013] for a standard Micromegas with 128 µm amplification gap filled with a Ar:CO_2 93:7 vol.% gas mixture.

adapts to the mesh potential which interrupts the discharge. Due to the low capacitance of the affected region on the strip, the global voltage drop of the anode is negligibly small.

Due to the resistive strip layer serving as the anode strip in the amplification region, the moving charges during the amplification process induce current signals (via the Shockley-Ramo-Theorem) through the resistive strips directly on the readout copper strips, connected to the readout electronics. This allows the easy realization of a two-dimensional resistive strip anode with e.g. two perpendicular stacked layers of copper readout strips of adapted widths [Byszewski and Wotschack, 2012]. A detailed characterization of the signals induced on both readout strip layers of a two-dimensional resistive strip Micromegas can be found in [Lin et al., 2014]. To quickly summarize, the signal polarity on both readout strip layers is negative, as also observed for the one-dimensional resistive strip or the standard Micromegas. Due to the charge spreading along the resistive strips, multiple perpendicular readout strips respond to a single resistive strip signal, producing a V-shaped signal in a strip-time diagram of the perpendicular layer. This does not affect particles at perpendicular incidence relative to the readout plane. However, the angle reconstruction of an inclined particle track depends on the precise knowledge of the arrival time of each individual strip signal. As each resistive strip signal develops a V-shaped signal on the perpendicular readout strip layer that overlaps with signals from later arriving ionization charge, a µTPC-like track reconstruction (see section 3.5) is challenging on the perpendicular strips.

Resistive strip Micromegas yield excellent results in terms of spatial resolution and efficiency. However, due to their high strip resistivity and the necessity of charge drain from the full length of a resistive strip, a rate depended charge-up of the anode is observed. This results in a pulse height drop of the measured signal for very high particle rates in the MHz region (again depending on the absolute value of the strip resistivity), which leads to a drop in efficiency at a certain point.

2.6.3 Floating Strip Micromegas

The setup and working principle of a floating strip Micromegas with one-dimensional readout structure as it has been pioneered by Bortfeldt [2014] is shown in Figure 2.8.

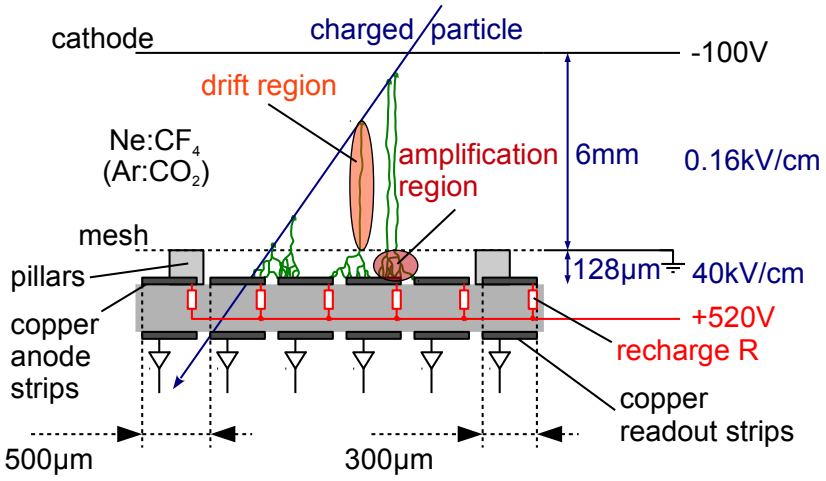

Figure 2.8: Sketch and functional principle of a floating strip Micromegas with one-dimensional segmented readout structure.

The anode strips of floating strip Micromegas are individually connected to high voltage via high ohmic resistors (typically above 20 MΩ), while the micro-mesh is at ground potential.

Signals collected on the anode strips are either decoupled via congruent readout strips below the anode strips (integrated setup) or via capacitors soldered directly to the anode strips (discrete setup). The strip capacitances are on the order of few pF/10 cm. In combination with the high ohmic recharge resistor, this scheme enables a powerful discharge protection.

Upon occurrence of a discharge, the floating potential of the affected strips quickly levels to the mesh potential, so that the discharge is quenched. As other strips remain unaffected by the discharge, the rest of the detector remains fully operational. Due to the small overall capacitance of a floating strip, the recharge time is on the order of 1 ms [Bortfeldt, 2014]. This reduces the dead time due to a discharge by about three orders of magnitude, compared to a standard Micromegas. Additionally, the copper strips are easy to clean and very robust in general, leading to negligible aging effects.

An additional advantage of floating strip Micromegas is the absence of resistive material in the active region, which may become charged by radiation leading to unwanted additional electrical fields on top of the amplification field in high rate environments of $\mathrm{MHz/cm^2}$ particle fluxes. Thus the floating strip principle with a typical strip pitch of 0.5 mm allows for highly efficient single particle reconstruction up to $7\,\mathrm{MHz/cm^2}$ [Bortfeldt, 2014]. For higher rates, multiple particle hits will get merged together on one strip. Solutions to regain single particle resolution are a smaller strip pitch, two-dimensional resolving strip readout structure or even implementing a pixel segmented anode structure.

A first two-dimensional floating strip Micromegas anode with two layers of perpendicular readout strips has already been tested in [Bortfeldt et al., 2017] and [Klitzner, 2016]. However, the signal amplitude on both readout strip layers was observed to be highly asymmetric. Furthermore, the signal formation process on the perpendicular layer turned out to be more complex than initially thought. This thesis presents the detailed understanding of the underlying physics processes that lead to the observed signals on both readout layers of a two-dimensional floating strip Micromegas detector. From the gathered experience, novel two-dimensional floating strip anode designs have been developed and extensively tested in different test beam campaigns.

Chapter 3

Material and Methods

In this chapter the software packages used to simulate and understand the physics processes in the detector are briefly introduced. Furthermore the used readout electronics interfacing the detectors investigated during this thesis are explained and an outlook is given to a new front-end chip which allows significantly faster data taking due to on-chip zero suppression. Last but not least, typical signals measured with a two-dimensional floating strip Micromegas detector are shown and algorithms used to analyze the data acquired within different measurement campaigns described in chapters 6 to 9 are presented.

3.1 Simulation Packages

As multiple simulation packages have been used to understand the signal formation process in a two-dimensional floating strip Micromegas detector, the different software frameworks are introduced briefly in the following. A detailed detector simulation is described in chapter 4.

The MAGBOLTZ package [Biagi, 2018] has been used to simulate electron mobilities in various gases, i.e. to understand the movement of the charge carriers in the drift region in Micromegas detectors. MAGBOLTZ computes drift gas properties by numerically integrating the Boltzmann transport equation, i.e. simulating the electron path including scattering inside a gas volume. Thus electron parameters like drift velocity, diffusion or even Townsend avalanche coefficients may be calculated. In order to simulate macroscopic parameters like the electron drift velocity, MAGBOLTZ uses a large database containing microscopic information about the studied gas, where parameters like scattering cross sections, energy loss, excitations levels of noble gas atoms or vibrational and translational modes of quencher gases like CO_2 are stored.

Within the ANSYS APDL[1] environment [ANSYS, Inc., 2013] a three-dimensional model of a floating strip Micromegas detector with two-dimensional anode readout structure was created, including drift and amplification region. ANSYS is a numerical simulation program, based on a finite-element method (FEM). Detailed information about the ANSYS working principle can be found in [Wang and Nelson, 2002]. As a valuable result from the ANSYS calculations, the electric field maps in drift and amplification regions of the Micromegas detector were extracted in all three space coordinates.

The Garfield++ package [Veenhof, 2010] is a toolkit used for detailed simulation of the physics processes in gaseous or semi-conductor based detectors. However, the main application is up to now for micro-pattern gaseous detectors. It is subdivided into three main categories, such

[1] ANSYS Parametric Design Language

as ionization, electric field incorporation and transport of charge carriers in gases. Ionization processes e.g. in the drift region of the Micromegas are handled by the so-called HEED program (High Energy ElectroDynamics) [Smirnov, 2005]. It generates ionization patterns for fast charged particles and provides atomic relaxation processes and dissipation of high-energy electrons. Electric field lines used for the drift of charge carriers in the detector can either be constructed in Garfield++ directly with solutions in the thin-wire limit made of wire or planes (which has not been used for the simulations in this thesis) or it can import electric field line configurations from a finite element solving program such as ANSYS. The drift and amplification of the charge carriers are computed by the MAGBOLTZ package described above.

3.2 Readout Electronics: The Scalable Readout System (SRS)

The readout of the detectors presented in this thesis was performed with the so-called Scalable Readout System (SRS), which is being developed by the RD51[2] collaboration since 2009. A schematic view of the main components is shown in Figure 3.1.

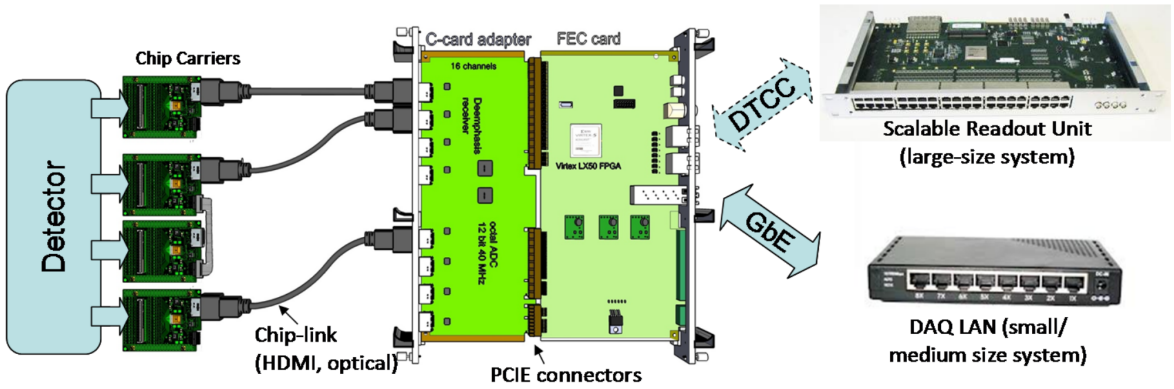

Figure 3.1: Schematic view of the different SRS components [Martoiu et al., 2013].

The principle idea is that the user can choose between different front-end electronics that fits the used detector technology best while the SRS provides a common readout back-end that can be scaled up to large systems.

The very first component in the readout chain is the front-end chip, which is usually an Application Specific Integrated Circuit (ASIC). Its main job is to amplify and shape the raw signals generated in the detector. In the SRS, these front-end ASICs are mounted on a hybrid board which carries among other things additional protection circuits against high input currents originating from e.g. discharges in the detector.

The front-end hybrid board transmits the data usually via HDMI cables to an adapter card. The data are in the case of an analogue front-end chip digitized by an Analog-to-Digital Converter card (ADC). The adapter card is connected to a Front-End Concentrator card (FEC) which provides communication with a computer using Gigabit Ethernet.

For the SRS, a maximum of 8 HDMI cables can be connected to the adapter card, which allows a total of 16 front-end boards in one stand-alone FEC system, assuming master-slave hybrid functionality[3]. For larger systems, a so-called Scalable Readout Unit (SRU) can be

[2] www.cern.ch/rd51-public

[3] The data from the slave hybrid board are transmitted to the adapter card via the master hybrid board

used that allows the synchronous use of multiple FEC cards.

In the following two different types of SRS compatible front-end hybrid boards will be explained, the analogue APV25 and the digital VMM-based hybrid board. While only the first has been used for the data acquisition of the Micromegas systems discussed in the later chapters, the latter one is an appropriate alternative if high data throughput at high trigger rates is needed.

3.2.1 The Analogue APV25 Front-end Hybrid Board

The core element of the hybrid board discussed in this section is the APV25 deep sub-micron CMOS ASIC [French et al., 2001]. It was originally designed for the readout of silicon microstrip detectors used in the inner tracker of the CMS[4] experiment at the LHC. The APV25 is a radiation tolerant, low noise and low power analogue pipeline chip, fabricated in a 0.25 µm CMOS process. It features 128 channels each equipped with a pre-amplifier and 50 ns CR-RC shaper, storing the data sampled at the LHC bunch crossing frequency of 40.08 MHz in a 192 cell deep analogue pipeline. Thus a maximum trigger latency of $192 \times 25\,\text{ns} = 4.8\,\mu\text{s}$ is possible.

Upon receiving a trigger signal, a user configurable number of time bins[5] are consecutively output to the DAQ[6] system. The core structure of the UDP[7] based frames is sketched in Figure 3.2, which is 140 clock cycles (c.c.) long. It consists of a digital header (three c.c.), a digital address (eight c.c.), an error bit and a data part (128 c.c.) containing the analogue charge information of all 128 channels for a specific time bin.

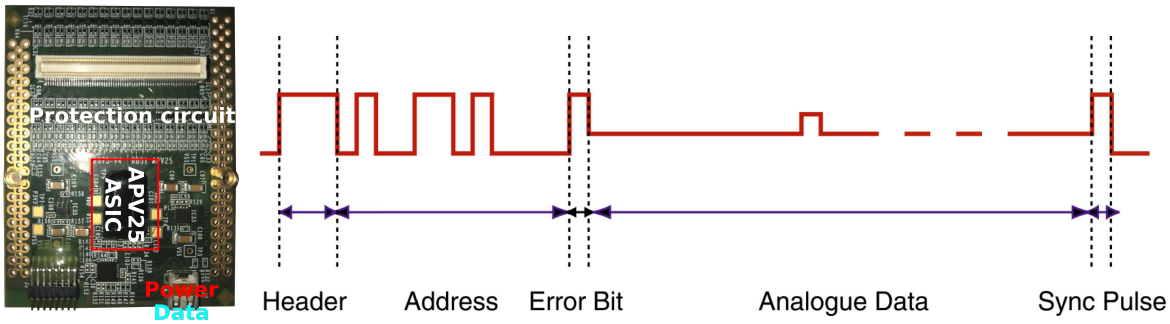

Figure 3.2: Photo of the APV25 front-end hybrid board (left) and the output format of a typical APV25 UDP-frame after received trigger signal [Jones, 2001].

The APV25 front-end hybrid boards are designed as either master or slave boards, where the HDMI power and data cable is always connected to the master, powering both hybrids. Data of the slave are transmitted to the master via a flat ribbon cable. The analogue data of both hybrids are transmitted parallelly on two lines via HDMI cable to the ADC card, digitizing the data with two eight-channel 12 bit ADC's operated at 40 MHz.

With a maximum number of eight HDMI cables connectable to the ADC card, a total of 2048 channels can be read out in one FEC + ADC card stand-alone system. Due to the minimal UDP frame size containing 140 clock cycles − which includes the data of all 128 channels − a maximum trigger frequency of 285 kHz per APV per time bin is theoretically possible. With two bytes necessary for data transmission and storage for each clock cycle [Zibell, 2014],

[4] Compact Muon Solenoid
[5] one time bin equals a 25 ns clock cycle
[6] data acquisition
[7] User Datagram Protocol

the data rate created from one APV per time bin is already 638 MBit/s at the maximum trigger frequency, assuming the FEC card transmits the data of all 128 channels to the DAQ computer. This is already close to the 1 GBit bandwidth limitation of the card itself.

In measurements with hybrid boards attached to multiple Micromegas detectors in the next chapters, usually around 18 to 27 time bins are read out to allow for pulse shape analysis, which reduces the trigger frequency to the lower kHz region. This motivates the use of a new front-end chip introduced in the next section, which allows for high data throughput at high trigger rates with a multiple Micromegas detector system, as it is the case for the measurements presented in chapter 9.

3.2.2 The Digital VMM Front-end Hybrid Board

The VMM front-end chip [De Geronimo et al., 2012] is an ASIC specifically designed for the readout of Micromegas and sTGC detectors in the ATLAS New Small Wheel (NSW) at CERN, which will replace the current small wheel after LS2 in 2021 [Kawamoto et al., 2013]. It needs to cope with the high trigger rates and particle fluxes that the detectors have to face with expected hit rates of $\mathcal{O}(10^5)$ hits per channel per second. Due to the limited bandwidth of the readout links, on-chip zero suppression and digitization is required.

The ASIC has undergone various versions, the first one was available in 2012 and extensively tested. The functional principle of the third version of the VMM, submitted in 2016, is sketched in Figure 3.3 (right). It features 64 channels each equipped with a linear amplifying and shaping network with adjustable peaking times of 25, 50, 100 and 200 ns and adjustable gains of 0.5, 1, 3, 4.5, 6, 9, 12 and 16 mV/fC [Iakovidis, 2018]. The chip is able to handle signals of opposite polarity in an input capacitance range up to 2 nF per channel.

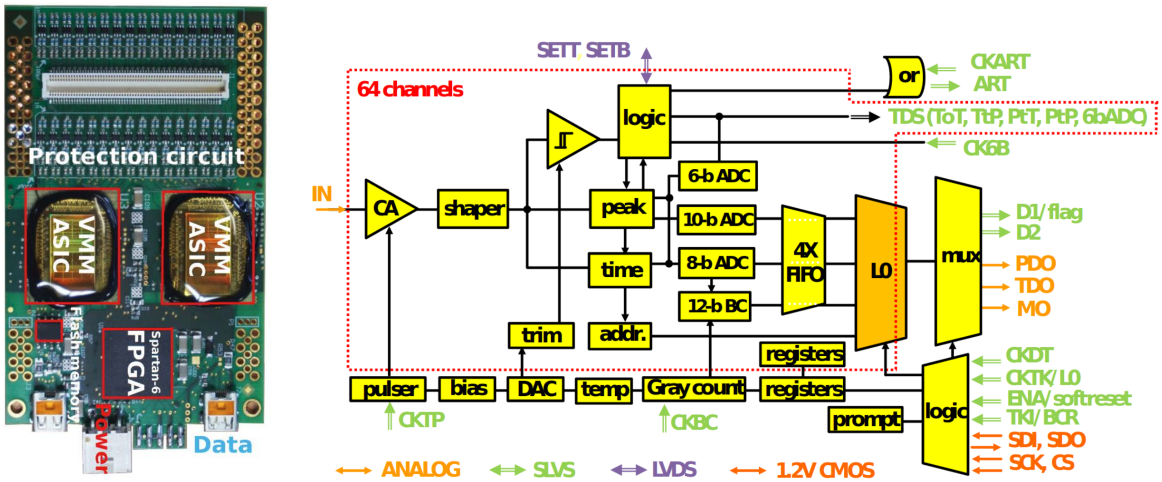

Figure 3.3: Photo of a VMM front-end hybrid board equipped with two VMM3 ASICs interfaced by a Spartan-6 FPGA [Lupberger et al., 2018](left) and the VMM3 architecture (right) [Iakovidis, 2018].

Once current signals arrive at the input of the chip, the signal is amplified, shaped and fed into a comparator circuit, where the amplitude of the signal is compared to a user adjustable threshold. If the signal exceeds the threshold, it is processed by peak and time detectors and the values are stored in analog memories, waiting for readout. The comparator circuit is connected to a neighboring logic which enables the possibility to also read out neighboring sub-threshold strips. Pulse height (PDO) and fine timing (TDO) informations are then digitized by a 10-bit and 8-bit ADC, respectively. A coarse timing information from the bunch

crossing clock counter, operated at the 40 MHz LHC clock, is latched into a 12-bit memory. Fine and coarse timing generate an effective 20 bit deep time stamp with ns resolution. After the conversion time, which takes typically 250 ns, the channel is reset and the complete data set of 38 bits per hit is stored in a four hit deep buffer in continuous mode. Depending on the chip mode of operation, a maximum of up to 4 MHz hit rate per channel is thus theoretically possible. However, the readout lines on the ASIC itself are clocked with a maximum frequency of 200 MHz with an option of double data rate, leading to a maximum readout rate of 21 Mhits/s per VMM, equivalent to 800 MBit/s of data flow [Lupberger et al., 2018].

The SRS-based VMM front-end hybrid boards carry two VMMs yielding a total of 128 channels − the same as the APV25 hybrid board. Additionally, a Spartan-6 FPGA is interfacing the two VMMs for distribution of clock, configuration, slow control and receiving the multiplexed output data. The digital data is sent via HDMI cables to the adapter card which houses eight HDMI type A plugs. As the VMM data is already digital, the card mainly holds LVDS drivers and provides the hybrid boards with appropriate power [Lupberger et al., 2018]. The adapter card is directly connected to the FEC card, which again is responsible for communication with the DAQ computer via Gigabit Ethernet. As the VMM hybrid will also come in a master and slave system, a total of 16 hybrid boards with 2048 channels can be operated with a single FEC + adapter card stand-alone system.

In the following an estimation on the maximum trigger rate with 16 VMM hybrids connected to the SRS, mounted on a detector telescope consisting of 16 Micromegas strip layers, is evaluated. Assuming a bottleneck of 1 Gbit/s bandwidth limit of the network, 38 bit data size per VMM hit, three channels hit per Micromegas per event, one VMM per detector and 16 VMM's in total in a one FEC + adapter card system, yields the maximum trigger frequency f_{max}

$$f_{max} = \frac{1\,\text{Gbit/s}}{38\,\text{bit/hit} \cdot\ 3\,\text{hits/VMM} \cdot\ 16\,\text{VMM}} \approx 550\,\text{kHz} \quad . \tag{3.1}$$

Note that in this calculation the frequency is only limited by the 1 Gbit/s Ethernet connection from the FEC to the DAQ computer. A possible upgrade of the FEC to a 10 or 100 Gigabit Ethernet seems feasible although data reduction needs to be taken into account as the Virtex-6 FPGA on the FEC is not capable of handling higher bandwidths. Doing the same calculation with an APV25 based hybrid board with three time bin read out, the maximum achievable trigger rate is around 9.3 kHz. This is a huge gain in trigger rate thanks to the online zero suppression and digitization of the chip.

The VMM-hybrids thus may provide a solution to the high data rates expected in the medical application of floating strip Micromegas used as a tracking system for ion radiography, presented in chapter 9.

The VMM-based SRS is currently being tested extensively and a first complete setup is expected to be tested in our labs in mid 2019. See Figure 3.4 for a VMM SRS setup at a laboratory at CERN with fully working readout chain, measured with VMM hybrid boards mounted on a GEM detector.

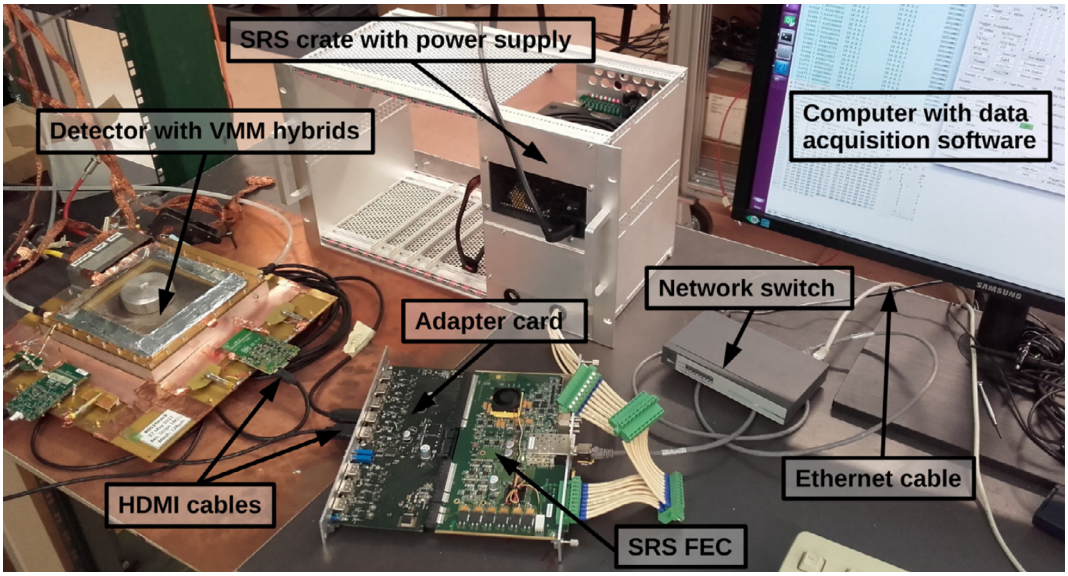

Figure 3.4: Full working readout chain of VMM hybrid boards mounted on a GEM detector, connected to the SRS [Lupberger et al., 2018].

3.3 Signal Cluster Reconstruction

In the following sections, methods and algorithms used to process the signals generated in Micromegas detectors are explained. The C++ core analysis framework was initially developed by Bortfeldt [2014] and has been further adapted and extended in this work.

A scenario of a particle traversing the detector nearly perpendicularly to the readout plane is sketched in Figure 3.5, creating signals on three adjacent strips.

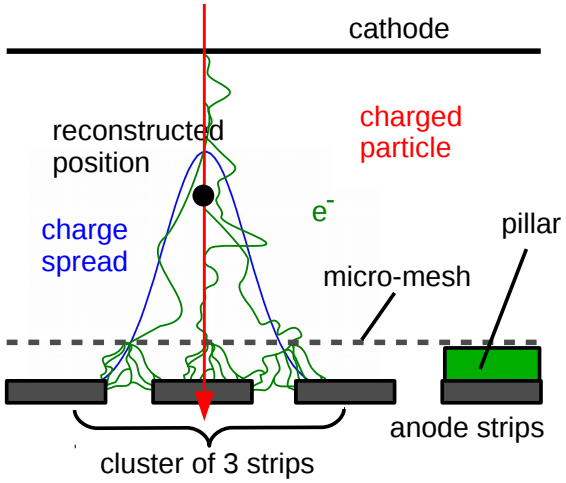

Figure 3.5: A charged particle (red) traverses the Micromegas detector and creates electron/ion-pairs along its path. The corresponding electrons (green) drift towards the amplification region where they are amplified in Townsend avalanches until they are collected by the anode strips. For a perpendicularly incident particle the charge is typically Gaussian distributed (blue line) over a cluster of around 2 to 4 strips at a pitch of 0.5 mm, depending on the transverse diffusion of the electrons in the drift gap.

Depending on the transverse diffusion of the electrons in the drift gap and anode strip pitch, typically around two to four strips collect signals from electron avalanches in the amplification region. For two-dimensional floating strip Micromegas detectors, two layers of readout strips are placed underneath the floating strips which are connected to high voltage. For all measurements presented in the later chapters, SRS-based APV25 hybrid boards have been mounted on both readout strip layers of the Micromegas via 130 pin Panasonic[8] connectors. Each strip signal is processed by the linear amplifying and shaping stages of the front-end chip, allowing extraction of the charge and timing information of each individual strip. A typical event display of a cosmic muon traversing a two-dimensional floating strip Micromegas detector perpendicularly to the anode plane measured on both readout strip layers is shown in Figure 3.6 (left).

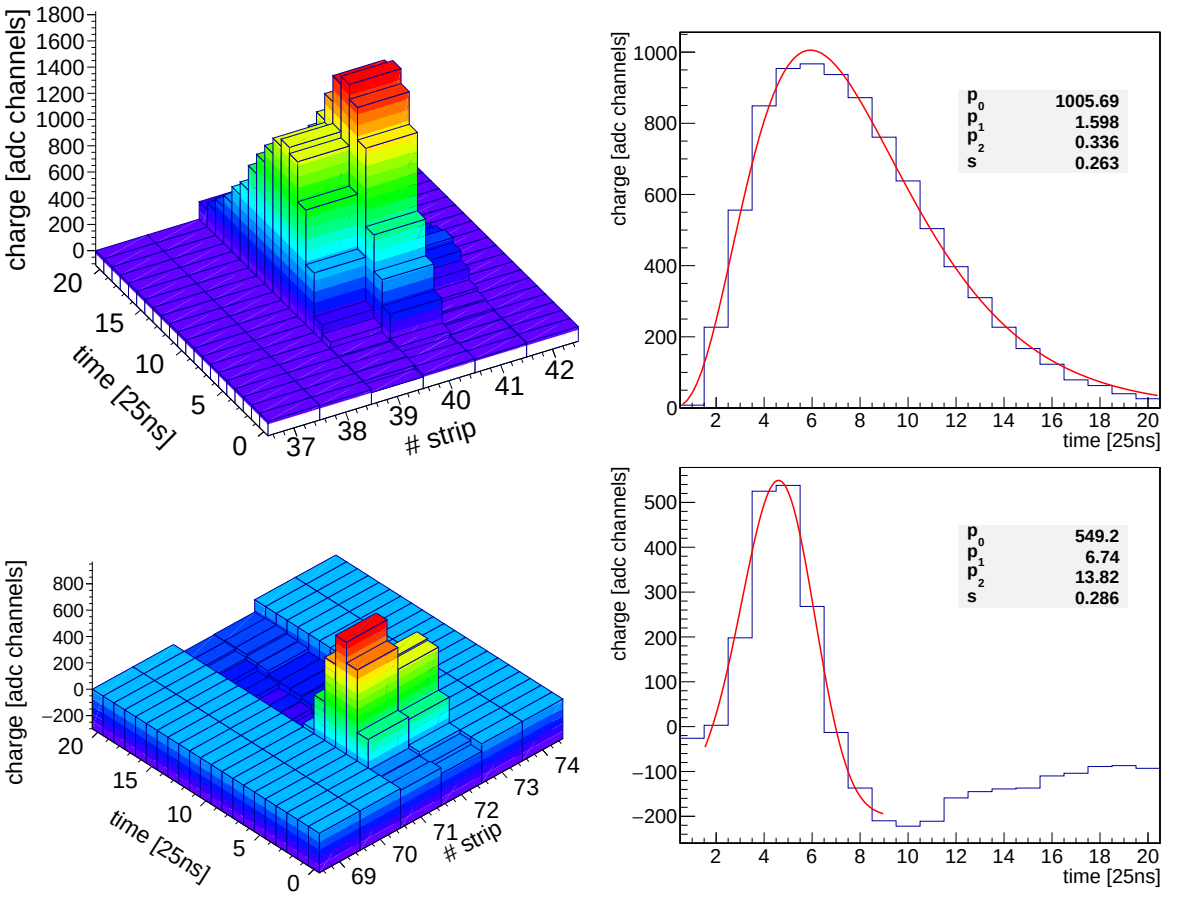

Figure 3.6: Left: Typical offset- and common-mode noise corrected signals recorded with APV25 chips on the parallel readout strip layer (top) and the perpendicular readout strip layer (bottom) of a two-dimensional floating strip Micromegas detector for a perpendicularly incident cosmic muon. The polarity of the APV25 recording the signals on the perpendicular layer has been inverted. Right: Parameters like pulse height, width and timing are extracted with a fit to a single strip signal with the skewed Gaussian function defined in eq. 3.2.

The front-end chip channel specific baseline has been subtracted and common-mode noise has been corrected. To extract the charge and timing information of strip signals, sampled at 40 MHz by the APV25 front-end chip, the strip pulse can be fit with a skewed Gaussian function

[8] part number AXK5SA3277YG

$$q(t) = p_0 \cdot \exp\left(- \left(\frac{t^s - p_1}{p_2} \right)^2 \right) \quad , \tag{3.2}$$

where t is the time in multiples of 25 ns bins, p_0 is the pulse height, p_1 is a parameter describing the timing of the maximum, p_2 is describing the width and $s \in]0, 1]$ defines the skewness of the Gaussian. An example of a fit to a strip of the parallel and perpendicular readout layer is shown in Figure 3.6 (right). A different approach to fit an inverse Fermi-function to the rising edge of the strip pulse was also studied but ultimately showed worse results than the skewed Gaussian. However a fit to the strip pulse is only necessary if precise timing information is needed e.g. for the application of the so-called µTPC method described in section 3.5, used for inclined particle tracks. No degradation of the spatial resolution has been observed for perpendicular particle tracks when no fit has been performed to the strip pulses.

Knowing the charge and timing information of each individual strip, a group of adjacent strips can be merged together into a so-called cluster of strips. Usually a strip is considered hit if its associated charge exceeds $3\sigma_{\text{strip}}$, where σ_{strip} is the standard deviation of the strip amplitude due to uncorrelated background effects such as electronics noise. This allows e.g. for the reconstruction of the cluster charge q_{cluster} defined as

$$q_{\text{cluster}} = \sum_{\text{strip}}^{\text{cluster}} q_{\text{strip}} \quad , \tag{3.3}$$

the sum of all charges q_{strip} of the strips in the cluster. The cluster charge is thus proportional to the total deposited energy of the traversing particle in the detector.

3.4 Position Reconstruction: Centroid Method

The centroid or center of gravity method is a common way to determine the position in segmented anode chambers like Micromegas. The position x_{mean} can be calculated by the following equation:

$$x_{\text{mean}} = \frac{\sum_{\text{strip}}^{\text{cluster}} x_{\text{strip}} \cdot q_{\text{strip}}}{q_{\text{cluster}}} \quad , \tag{3.4}$$

where x_{strip} is the position of the center of the strip and q_{strip} the charge associated to it. The centroid method is a reliable method to reconstruct the position of particles perpendicularly traversing the detector, as the charge distribution typically has a Gaussian profile over the strips in the cluster, see Figure 3.5. The centroid method thus reconstructs the position of the particle in a plane in the middle of the drift region. For inclined tracks, non-homogeneous ionization along the particle track leads to a degradation of the position information derived from the centroid method. However to improve the signal reconstruction a different method using the strip time information instead of the charge can be applied, which will be introduced in the next section.

3.5 TPC-like Single Plane Track Reconstruction

For inclined particle tracks with an inclination angle $\Theta \geq 8°$ [Iakovidis, 2014] [Ntekas, 2016] a TPC-like method can be used to reconstruct either the angle or the position of the traversing particle. It is inspired by the reconstruction technique used in Time Projection Chambers (TPC) [Nygren, 1974] and adapted to micro-structured detectors. Thus in this context it is often refered to as the µTPC method. The idea is sketched in Figure 3.7.

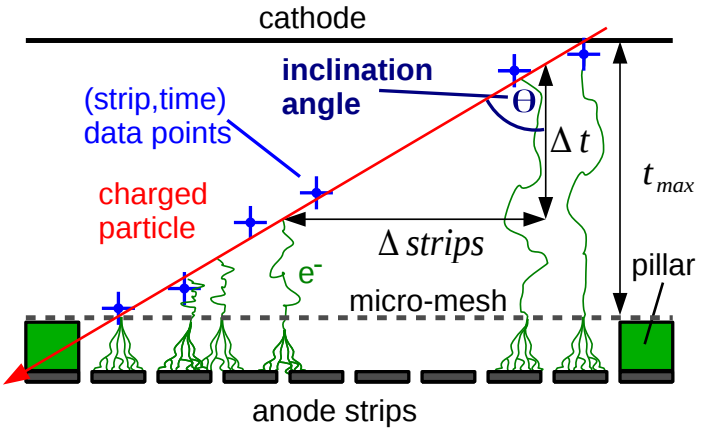

Figure 3.7: For a particle traversing the detector under an angle of $\Theta > 15°$, typically more than three anode strips collect charge signals, assuming a strip pitch of 0.5 mm. Ionization electrons created in the drift region close to the cathode will travel longer to reach the amplification region than electrons created close to the micro-mesh. The strip-timing information can be used to reconstruct the angle or position of the particle by a linear fit to the strip-time data points (light blue).

If a particle traverses the detector under an angle $\Theta > 15°$ typically more than three strips collect signals on the anode. Electrons created in close proximity to the cathode will travel longer than electrons created close to the mesh, which nearly instantaneously reach the amplification region. As the drift velocity v_d of the electrons can either be simulated or measured, the timing information t_e can be directly translated into a drift distance $z = v_d \cdot t_e$. The angle or position of the traversing particle can then be reconstructed from the slope and intercept of a line fit to the drift distance-strip points, as will be described in the next sections.

The µTPC method used for the analysis of the data presented in the later chapters is subdivided into several steps, which will be explained in the following. First of all, due to the non-homogeneous ionization nature of particles in thin absorbers like Micromegas, empty strips i.e. strips which do not receive charge inside a cluster will be allowed in the cluster building algorithm. A maximum of up to four adjacent empty strips are allowed for the highest considered angle $\Theta = 40°$. The strip charge-time distributions are then fit with the skewed-Gaussian function defined in eq.3.2, see Figure 3.6 (right). The most important parameters of the fit to all strip signals measured with 20 GeV to 150 GeV muons traversing the detector under an angle of 40° are shown in Figure 3.8. The soft (green dashed lines) and hard limits (red dashed lines) used for the µTPC line fit error assignment are superimposed. It will be explained in the following paragraphs.

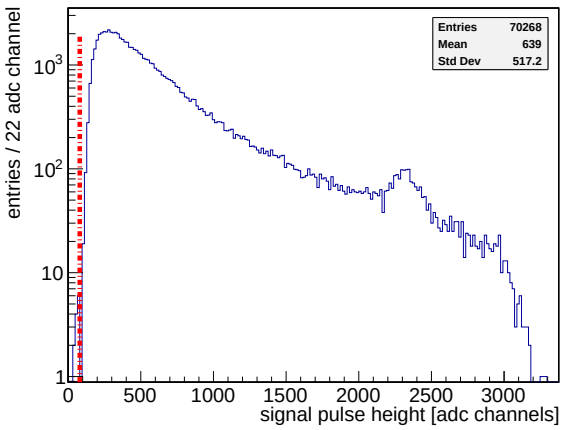

(a) signal pulse height

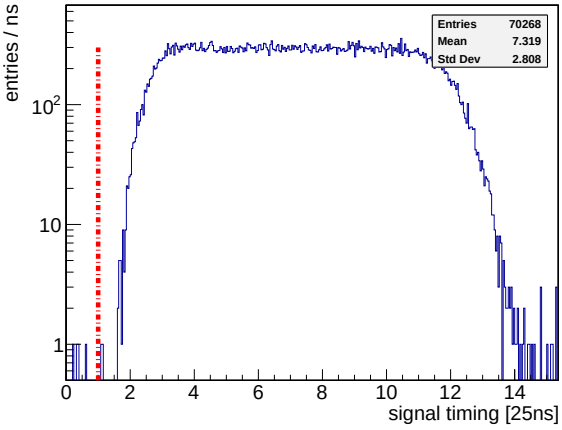

(b) signal timing

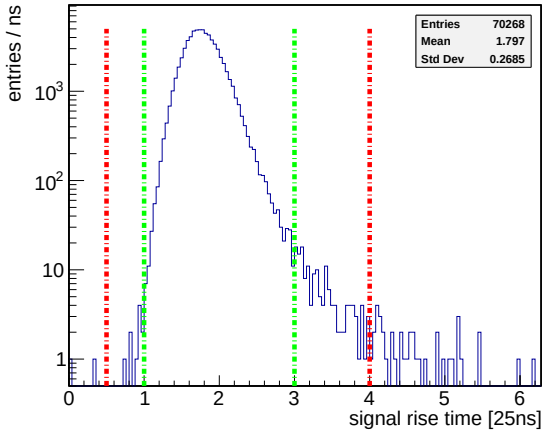

(c) signal rise time

Figure 3.8: Measured most important signal parameters from the skewed Gaussian fit described in eq. 3.2 to around 70000 strip signals (here the perpendicular readout layer is shown) for 20 to 150 GeV muons traversing the detector under an angle of $\Theta = 40\,°$, measured at $E_{amp} = 50\,kV/cm$ and $E_{drift} = 0.08\,kV/cm$.

Note that the reconstructed signal pulse height exceeds the typically 1800 adc channels dynamic range of the digitized APV25 raw data due to a different base-line subtraction algorithm used for these measurements, which takes the minimum rather than the mean of the adc values. The peak at around 2400 adc channels corresponds to electronics channel saturation.

Due to the on average homogeneous position distribution of ionization electrons in the drift gap, a box-like shape for the electron drift times is expected, which can be seen in the signal timing distribution. The slightly asymmetric rising and falling edge is primarily due to the well defined timing on the anode strips for electrons created very close to the mesh (rising edge) and the disturbed timing for signals of electrons that need to travel through the complete length of the drift region (falling edge), consequently suffering more from diffusion.

In the next step, the point errors of the strip-time data points used for the µTPC line fit are assigned, following mainly Bortfeldt [2014]. Errors in the strip-dimension are set to 0.5 strips. Errors in the time-dimension are set depending on the signal pulse height, absolute timing and rise time, defined by:

- errors are initialized with 1 time bin i.e. 25 ns

- errors are increased by factor of 3 if the rise time exceeds the region between the soft limits (green dashed line in Figure 3.8)

- completely exclude the data point (i.e. set the error to 1000) if the rise time exceeds the hard limits (region between the red dashed line in Figure 3.8), the absolute timing is smaller than 1 time bin, the pulse height is smaller than 80 adc channels or the first/last strip in the cluster has a 25% smaller pulse height than the neighboring strip.

While the requirement on the signal rise time is to identify failed signal fits, the hard exclusion aims mainly at identifying strip signals originating from capacitive coupling of the neighboring strip signal (see strip 54 in Figure 3.9, left). After the error assignment, a first µTPC line fit is performed. Depending on the quality of the fit i.e. $\chi^2/\mathrm{ndf} > 3$, a Hough-based algorithm [Hough, 1959] is used to identify points that are not compatible to a straight line (see Figure 3.9, right), increasing their y-error by a factor of 10.

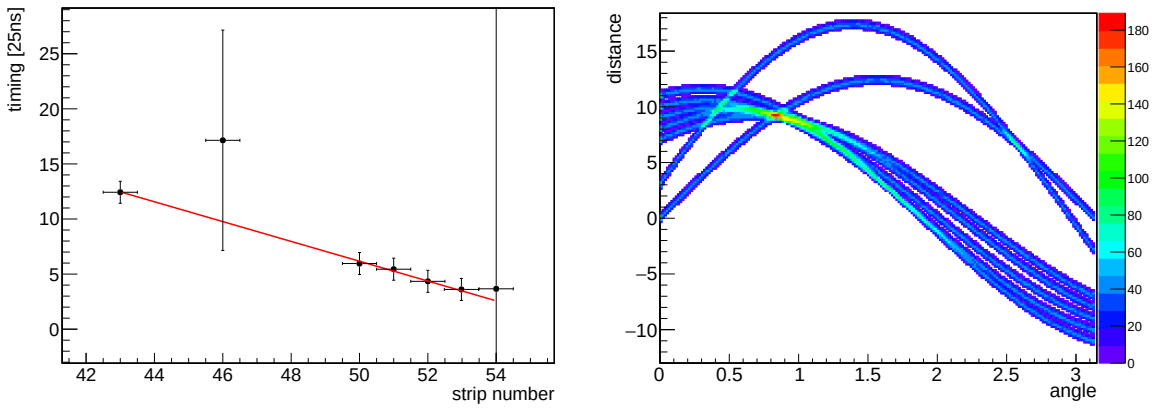

(a) final line fit (b) intermediate Hough transformation

Figure 3.9: Line fit to the strip-time data points created by a muon traversing the detector under an angle of $\Theta = 40\,^\circ$ (left). The errors of the points in y-direction have been chosen according to the method described in this section. Outlier points are found with a Hough-transformation (right) and then excluded in the line fit by changing the y-error accordingly, see e.g. strip 46 for this particular event.

After the transformation, a final line-fit is performed (Figure 3.9, left), which is then being used for angle or position reconstruction of the traversing particle, described in the next two sections.

3.5.1 µTPC Angle Reconstruction

The slope p_1 of the µTPC line fit defines the reconstruction of the particle track angle by:

$$\Theta = \arctan\left(\frac{p_s}{p_1 \cdot v_d \cdot 25\,\mathrm{ns}}\right) \quad , \tag{3.5}$$

where p_s, the strip pitch and v_d, the electron drift velocity, are known parameters. A typical distribution of the µTPC reconstructed angle is shown in Figure 3.10 for 20 MeV protons traversing the detector under an angle of 30°.

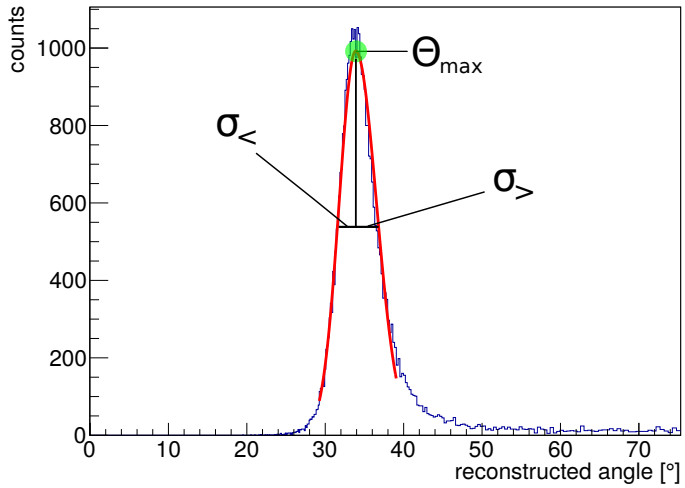

Figure 3.10: Typical distribution of the reconstructed angle via the µTPC method for 20 MeV protons traversing the detector under an angle of $\Theta = 30°$. The distribution is fit with a piece-wise defined Gaussian function to extract the most probable reconstructed angle and the angular resolution.

As can be seen from the Landau-like shaped angle distribution, the µTPC angle reconstruction tends to reconstruct higher values. It can be attributed to random electronic noise, falsely interpreted as a signal, and capacitive coupling between neighboring strips, which can not be completely suppressed by the µTPC algorithm described in the previous section. While the latter is not much of a problem for small chambers, a time dependent charge correction of each cluster strip signal might be considered for micro-pattern gaseous detectors with strip lengths in the order of 1 m [Lösel, 2017] i.e. with much larger strip-to-strip coupling.

To extract the most probable reconstructed angle and the angular resolution of the detector, the distribution is fit with a piece-wise defined Gaussian function. Note that a histogram of a transformed variable (e.g. the arctan of the slope p_1 in this case) needs to have a variable bin width as a shift of the mean distribution value occurs depending on the shape of the initial variable. For more details see [Bortfeldt, 2014].

A detailed analysis of the µTPC angle reconstruction as a function of different amplification and drift fields can be found in section 7.4 with 20 MeV protons and in appendix C for 20 GeV to 150 GeV muons and pions.

3.5.2 µTPC Position Reconstruction

Due to non-homogeneous ionization of high energy charged particles in the drift region of the Micromegas, the spatial information derived from the centroid method degrades steadily when increasing the track inclination. Figure 3.11 (left), shows a Garfield++ based simulation of a muon traversing the 6 mm wide drift gap of the detector under an angle of $\Theta = 40°$. The difference between the centroid position x_{mean}, which is by definition reconstructing the particle position in a plane in the middle of the drift gap, and the true particle position x_{true} is clearly visible. The right figure shows the residual defined as the difference between x_{mean} and x_{true} as a function of the angle for 0, 10°, 20°, 30° and 40°.

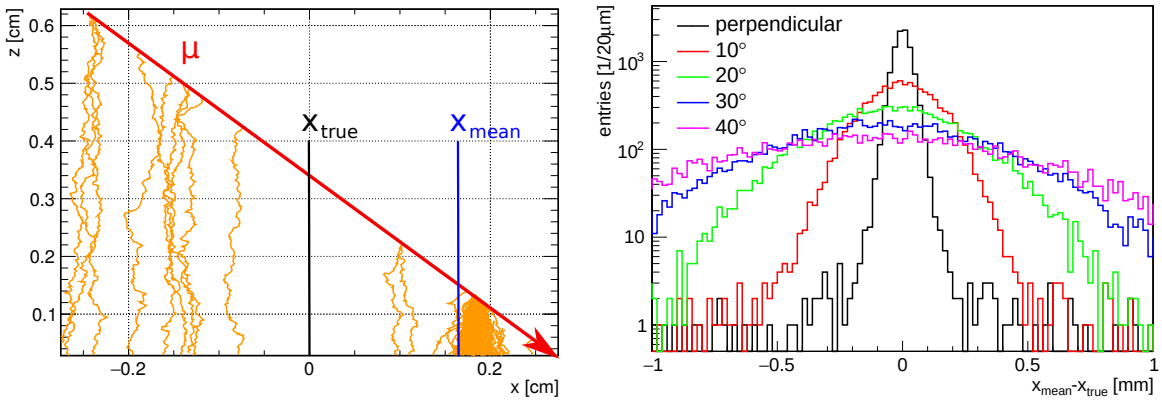

Figure 3.11: Garfield++ simulation of a 2 GeV muon passing through the 6 mm drift gap of the detector filled with Ar:CO_2 93:7 vol.% under an angle of $\Theta = 40°$ (left) and a drift field strength of 0.5 kV/cm. The inhomogeneous ionization of the MIP along the path is clearly visible. Simulated residuals between charge weighted mean position and true position for 10k muons (as indicated in the left figure) are shown as a function of the inclination angle Θ (right).

However, by knowledge of the strip-time correlation due to the µTPC line-fit, the true particle hit position can be reconstructed, if the timing t_{mid} in the middle of the drift gap is known. It can be determined e.g. from the strip timing distribution shown in Figure 3.8 b.) or by the mean value of the timing of fastest and slowest strip responding in a cluster, corresponding to a signal originating from ionization electrons created close to the mesh or close to the cathode, respectively. The latter showed better results compared to the expected drift time, see [Klitzner, 2016].

A different approach to determine t_{mid} has been shown in [Flierl, 2018], which has also been used in this thesis and thus will be explained briefly in the following.

Generally, the µTPC hit position in the middle of the drift gap can be calculated by

$$x_{\mu TPC} = \frac{t_{mid} - p_0}{p_1} \quad , \tag{3.6}$$

where p_0 is the intercept and p_1 the slope of the µTPC line-fit. To determine t_{mid}, the position is initially reconstructed by explicitly assuming $t_{mid} = 0$. The correlation of the residual, between µTPC and centroid position, and the inverse µTPC slope p_1, then directly allows for the determination of t_{mid}, see Figure 3.12 (left). By fitting the correlation with a straight line, the slope of the fit can be directly interpreted as a correction to the used t_{mid}, which was assumed to be zero in this particular example. Usually this procedure needs to be iterated two or three times until the correlation between residual and inverse slope becomes horizontal, as the µTPC position resolution gets better the closer t_{mid} approaches the true value.

The timing can then be used to determine the position for inclined tracks with the µTPC line fit evaluated at t_{mid}, as it is illustrated in Figure 3.12 (right), which shows a measured signal of a muon traversing the detector under an angle $\Theta = 40°$. The difference of the µTPC position compared to the centroid position x_{mean} is visible.

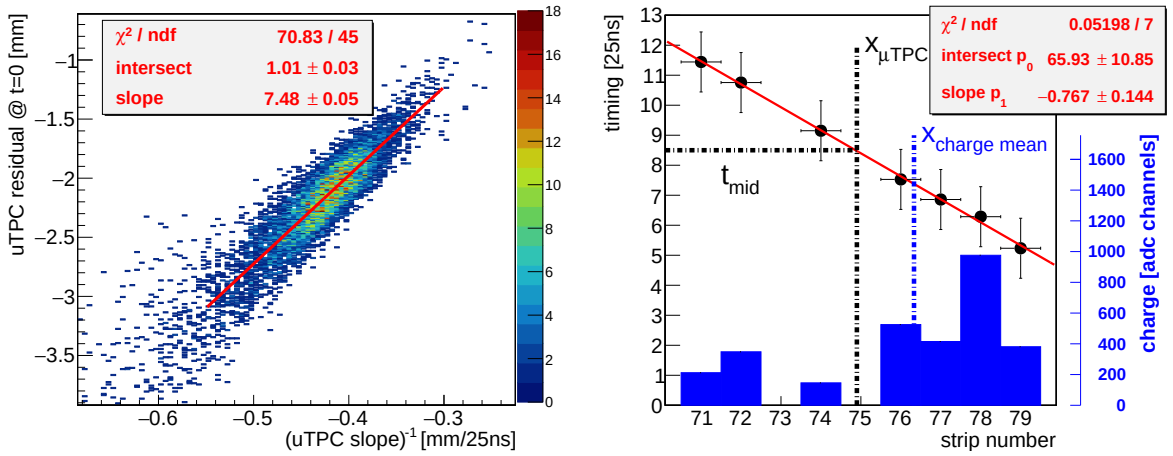

(a) t_{mid}-determination (b) $x_{\mu TPC}$-determination

Figure 3.12: Left: Determination of the timing t_{mid} (first iteration) from a linear fit to the correlation between µTPC residual and inverse µTPC slope, measured with 20 to 150 GeV muons traversing the detector at an angle $\Theta = 40°$. Right: Event display of the determination of the µTPC hit position $x_{\mu TPC}$ using t_{mid} found after the second iteration of a line fit to the correlation shown in the left figure.

Measurements at particle inclination angles between 0° and 40° with 20 to 150 GeV muons have been carried out at the CERN SPS H8 beam line, where µTPC and centroid position reconstruction are compared in detail, see chapter 8.

3.6 Tracking with Multiple Micromegas Detectors

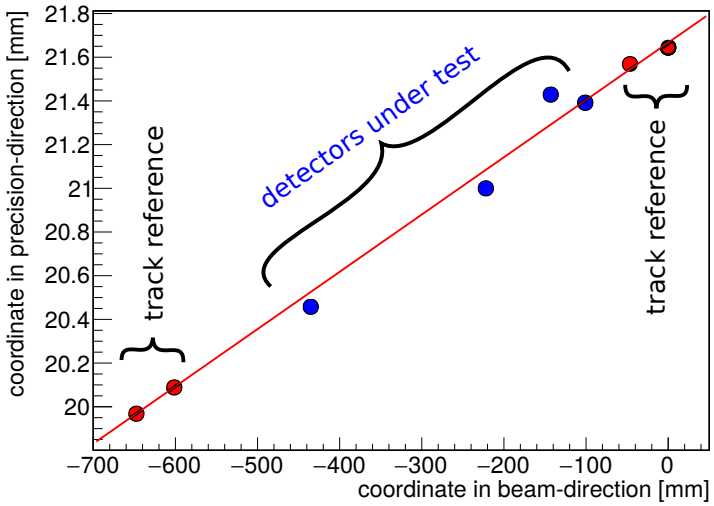

Figure 3.13: Typical event for a particle traversing a multiple detector system. Hits are registered in each detector and the track (red line) is defined through a set of reference detectors (red dots). Detectors under study can then be investigated when comparing the registered hit (blue dots) with the track prediction.

In the previous sections, the reconstruction of the signals generated in Micromegas detectors and thus the precise determination of a particle hit position in a single layer was discussed. In the following, methods and techniques are introduced which show how the track of a

particle traversing a multiple Micromegas detector system can be reconstructed with high precision, allowing for e.g. systematic studies on the performance of individual detectors. A typical event display of a high energy muon track measured by an eight detector system can be seen in Figure 3.13. While the red dots are position measurements from the so-called tracking system that defines the track, which are usually detectors with a well known excellent performance, the blue dots are measurements by detectors which are under test. The comparison of measured hit and track prediction can be used to study the detectors under test in detail.

3.6.1 Track Fitting

If a set of hit positions x_i (y_i) and z_i is known and a linear correlation is expected, a fit with a straight line can be performed in the two-dimensional parameter space. Two different methods will be described in the following: A method based on analytic χ^2-minimization and an iterative Kalman-filter based algorithm.

Analytic χ^2-Minimization

Assume a set of data points (z_i, x_i), $i = 0, .., n$, measured from n detector layers, a two parameter function fit such as a straight line $x(z) = az + b$ can be performed analytically by minimizing the weighted sum of the squared track residuals [Horvat, 2005]. This considerably accelerates the track finding procedure as no iterative fitting algorithms need to be used. A detailed explanation can be found in appendix A.1. The method has been applied for the previously described µTPC line fit and also for the track fits in the later chapters with multiple Micromegas serving as a tracking telescope.

Kalman-Filter-based Track Reconstruction

If multiple hits are registered per detector layer per event, i.e. multiple particles are traversing the detector simultaneously, it is important to match the correct hits in the detectors. Consequently from a set of multiple track candidates the true tracks have to be determined. One possibility is to use a Kalman-filter based track reconstruction to iteratively search through all possible track combinations in the detector telescope. The method is based on matrix multiplications in four dimensions. A detailed description of the algorithm can be found in appendix A.2. The working principle is sketched in Figure 3.14.

3.6.2 Detector Alignment

Proper detector alignment is crucial to allow high precision tracking with micro-structured chambers like Micromegas, as the internal spatial resolution is usually below 100 µm. However, measuring the absolute detector position externally (e.g. with a ruler or similar) is usually only possible on the mm level. Thus, the routines to adjust the detector position in three dimensional space on the µm level with the help of particle tracks are discussed in the following.

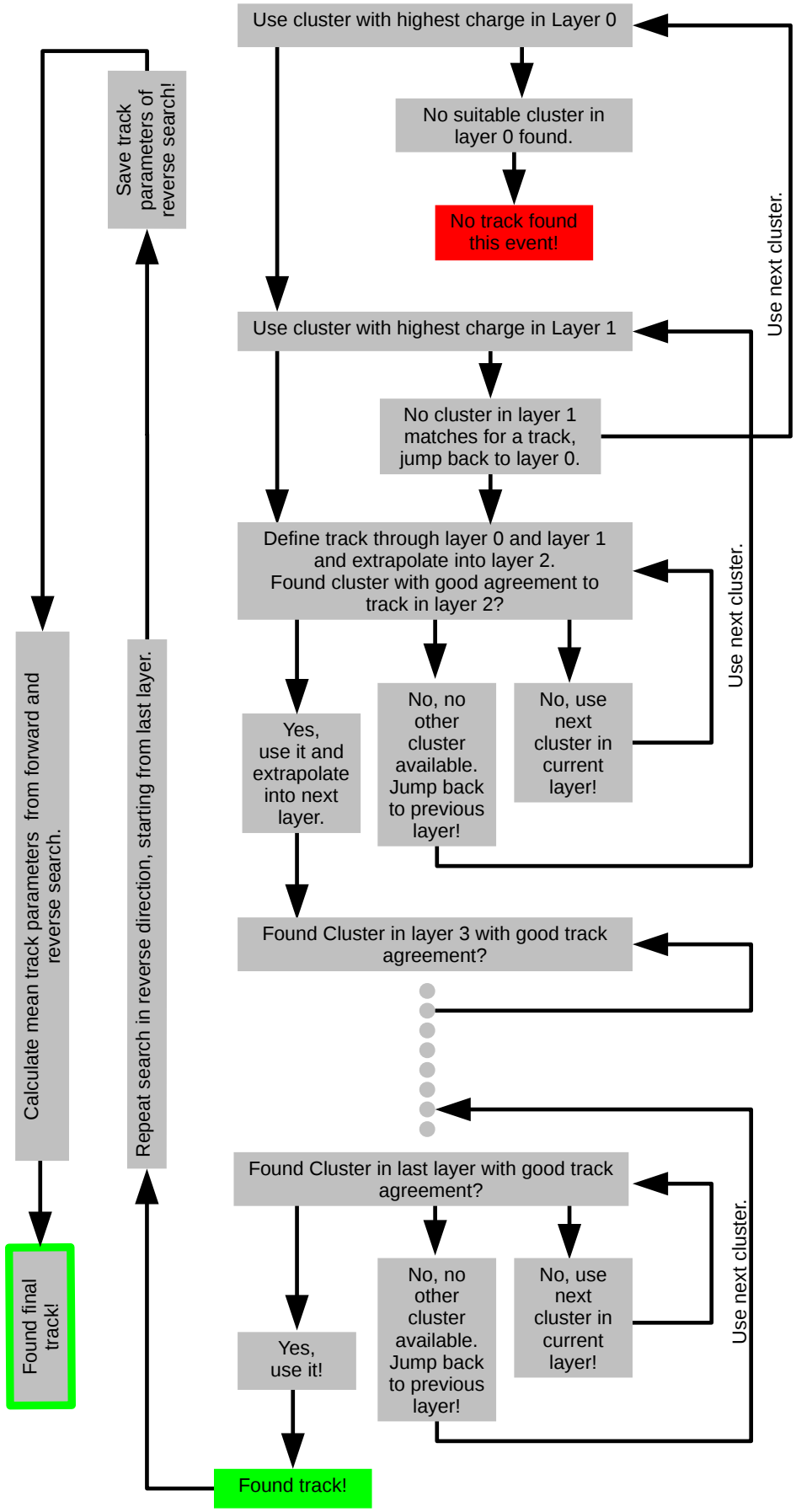

Figure 3.14: Principle of the iterative Kalman-filter based tracking algorithm usable if more than one cluster per detector e.g. more than one track is present in the tracking system. Picture taken from [Klitzner, 2016].

Assume a detector system consisting of n detectors with $n > 2$ and the coordinate system chosen such that the z-axis is orientated along the particle beam direction. The anode plane i.e. readout plane of detector i thus allows for the reconstruction of a particle hit position in x and y-direction, assuming a two-dimensional hit resolving anode PCB. The first and last detectors in the setup are aligned with respect to each other in x- and y-direction by simply calculating the difference between the measured hit positions in both dimensions. In the next step a track is defined through the first and last detector and interpolated into the detector layers $i = 2, ..., n-1$. The residual Δx_i (Δy_i) at layer i in i.e. x-direction (y-direction) is defined as

$$\Delta x_i = x_{\text{track,i}} - x_i \quad , \tag{3.7}$$

where $x_{\text{track,i}}$ is the track prediction at the detector position z_i and x_i the actually measured hit. Calculating the residual for many particle tracks yields a Gaussian distribution as shown in Figure 3.15. For a well aligned detector, the mean value of the distribution $\overline{\Delta x}$ ($\overline{\Delta y}$) is centered around zero. Deviations from zero in either x or y-direction directly allow to correct for a shift of the detector in the respective direction.

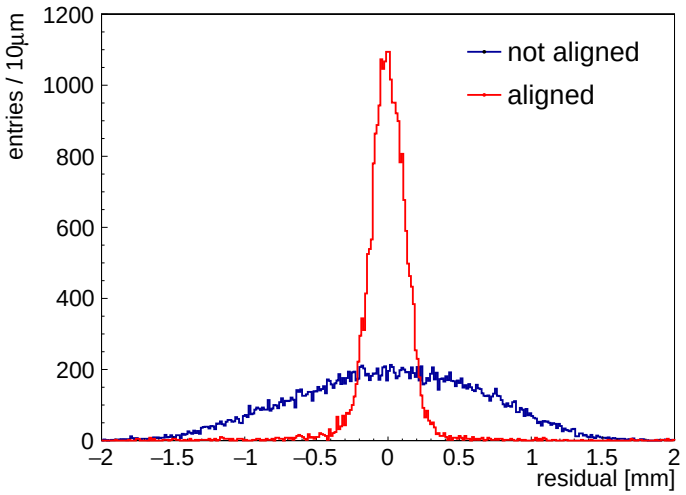

Figure 3.15: Residual distribution for a not aligned (blue) and aligned (red) detector shows a significant improvement of the residual width. Deviations of the assumed detector position in x, y and z direction as well as relative rotations need to be corrected.

The linear dependence of the residual distribution Δx_i (Δy_i) on the track slope m_x (m_y)

$$\Delta x_i = p_1 \cdot m_x + p_0 \tag{3.8}$$

allows a correction Δz_i of the detector position z_i along the beam axis by

$$\Delta z_i = -p_1 \quad , \tag{3.9}$$

where p_1 is the slope and p_0 the intersect of the linear fit to the correlation between Δx_i (Δy_i) and m_x (m_y).

A rotation Θ_i of the detector i around the y-axis (x-axis) can be corrected by the linear correlation of the residual Δx_i (Δy_i) on the hit position x_i (y_i)

$$\Delta x_i = p_1 \cdot x_i + p_0 \tag{3.10}$$

following

$$\Theta_i = \arctan(p_1) \quad . \tag{3.11}$$

Finally, a rotation Φ_i of the detector i around the z-axis i.e. around the beam axis can be corrected by the linear correlation of the residual Δx_i (Δy_i) on the hit position y_i (x_i)

$$\Delta x_i = p_1 \cdot y_i + p_0 \tag{3.12}$$

following

$$\Phi_i = \arctan(p_1) \quad . \tag{3.13}$$

A typical residual distribution measured in the x-coordinate of a not aligned detector as a function of the x-position and y-position is shown in Figure 3.16 in a particle beam with 20 to 150 GeV muons. The obvious correlations allow for a correction of relative rotations Θ (left) and Φ (right).

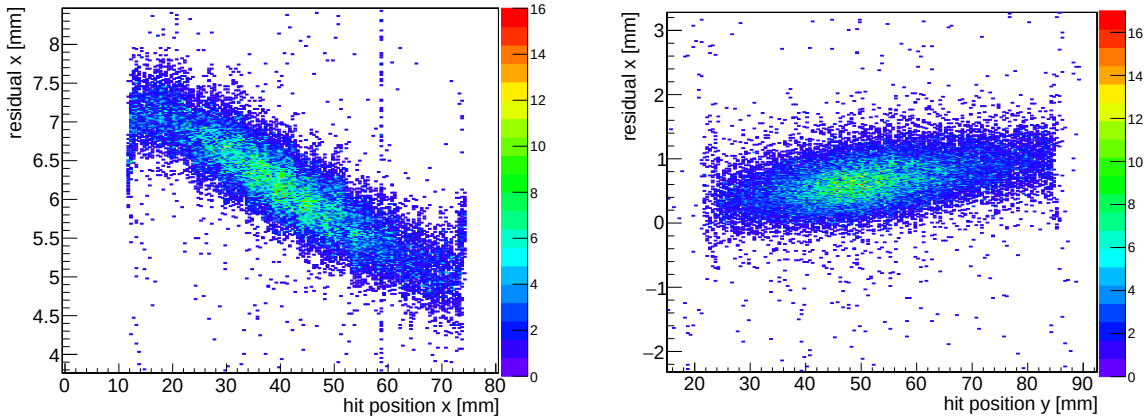

(a) rotation around y-axis

(b) rotation around z-axis

Figure 3.16: Residuals in x-direction plotted against the x-position (left). The obvious correlation allows for a correction of a rotation $\Theta = 20°$ of the detector with respect to the beam axis. The residual in x-direction plotted against the hit position in the other direction, in this case the y-direction, allows for a correction of the rotation $\Phi = 0.57°$ of the detector around the z-axis i.e. the beam axis (right).

3.6.3 Spatial Resolution

Various techniques exist to determine the spatial resolution of a detector in a tracking system based on measured tracks. Two are being explained in the following, as they have been used in the analysis presented in the later chapters.

Geometric Mean Method

The so-called geometric mean method [R. K. Carnegie, 2005] can be used to determine the spatial resolution of a detector in a set of at least three detectors, assuming they have the same characteristics and thus equal spatial resolution. A track defined by the measured hit positions of the detectors can be extrapolated into the detector under study. The spatial

resolution σ_{SR} is then defined by the geometric mean of inclusive (σ_{in}) and exclusive (σ_{ex}) residual distribution

$$\sigma_{\mathrm{SR}} = \sqrt{\sigma_{\mathrm{in}} \cdot \sigma_{\mathrm{ex}}} \quad . \tag{3.14}$$

σ_{in} and σ_{ex} are the widths of a Gaussian fit to the residual distribution of the detector under study if the detector is included and excluded in the track fit, respectively.

Track Extrapolation Method

If the spatial resolution of a detector needs to be determined while the operational parameters are varied, a set of reference detectors can be used to extrapolate the track into the detector under study. The spatial resolution of the reference detectors however needs to be previously determined with the geometric mean method. The exclusive residual distribution of the studied detector – featuring a width σ_{ex} – is consequently a convolution of the detector's intrinsic spatial resolution σ_{SR} with the uncertainty of the track predicted position with σ_{track}. σ_{track} can be analytically determined similar to the χ^2-minimization of the track fit, see appendix A.1.

The calculated tracking accuracy i.e. uncertainty as a function of the track position along the beam axis of a four reference detector system (TMMs), assuming an intrinsic spatial resolution of 43 µm each, is shown in Figure 3.17. A minimum of the track accuracy of around 20 µm can be reached in the center of the reference system.

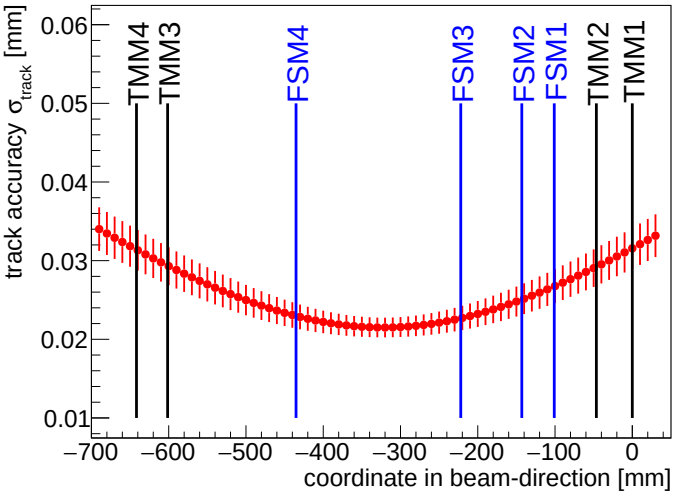

Figure 3.17: Calculated track accuracy according to [Horvat, 2005] of a detector system consisting of four reference detectors (TMMs, black lines) as a function of the position in beam direction. The track accuracy at the positions of the detectors under test (FSMs, blue lines) can be used for the determination of the spatial resolution.

The spatial resolution σ_{SR} of the detector under study thus can be determined via deconvolution of the track uncertainty σ_{track} at the detector position z_i in beam-direction from the exclusive residual width σ_{ex}, following

$$\sigma_{\mathrm{SR}} = \sqrt{\sigma_{\mathrm{ex}}^2 - \sigma_{\mathrm{track}}^2} \quad . \tag{3.15}$$

Chapter 4

Signal Formation in Two-Dimensional Floating Strip Micromegas Detectors

First measurements with a two-dimensional floating strip Micromegas have shown different signals on parallel and perpendicular readout strips with respect to signal amplitude, shape, polarity and duration. In this chapter, the detailed simulation of the signal formation in the detector is presented to understand the observed signals. The used simulation packages have already been introduced in section 3.1. A three-dimensional model of the anode PCB with two layers of readout strips below the floating strips is created. Electron avalanches are simulated in the amplification region formed by the anode strips and the micro-mesh, approximated as a uniform plane. The latter assumption was necessary as the fine structure of the micro-mesh wires lead to a huge amount of finite elements required in ANSYS, which was not supported in the used version. Directly induced currents on electrodes by the movement of charges towards the anode strips are simulated. Furthermore, all significant capacitances on the PCB have been simulated and a model to predict capacitive coupling between the anode strip layers was developed. From the combination of induced and capacitively coupled signals, the response of charge sensitive front-end electronics connected to the readout strips is calculated. Finally, the ionization process of a charged particle in the drift region and the electron transfer to the amplification region is simulated. The front-end electronics response in the example of the APV25 chip is calculated, taking finite front-end board input impedance and strip capacitance into account.

4.1 Three-Dimensional Model of the Amplification Region Simulated with ANSYS

A two-dimensional floating strip Micromegas has been modeled within the ANSYS environment [ANSYS, Inc., 2013] including amplification and drift region. In this and the following sections, the focus lies on the amplification region between floating strips and micro-mesh. The typical unit cell size of the simulated volume covers either three or five strips with a pitch of 0.5 mm. Due to the fine structure of the micro-mesh with a wire pitch below 100 µm, the amount of finite elements needed to approximate a unit cell of at least a size of 1.5 mm × 1.5 mm was not supported in the used ANSYS version. Thus, the micro-mesh is assumed to be a homogeneous plane. An amplification gap width i.e. a distance between floating strip upper surface and micro-mesh lower surface of either 128 µm or 150 µm has been

used. We chose the coordinate system such that the direction perpendicular to the anode plane defines the z-direction. A copper strip thickness of 35 µm has been assumed for all strip layers if not stated elsewhere. Floating strips are oriented in y-direction, thus resolving particle positions in x-direction. They are separated from the perpendicular readout strips by 25 µm insulating material with an assumed relative permittivity of 4. Perpendicular readout strips are oriented in x-direction, allowing to reconstruct a particle position in y-direction. Thus they will be referred to as y-strips. A third layer of readout strips, parallel to the floating strips, is placed below the y-strips, separated by a 25 µm insulating layer. Thus they are referred to as x-strips. Figure 4.1 (left), shows the unit cell geometry, covering three strips in each layer with a floating strip width of 0.3 mm, y-strip width of 0.4 mm and x-strip width of 0.3 mm.

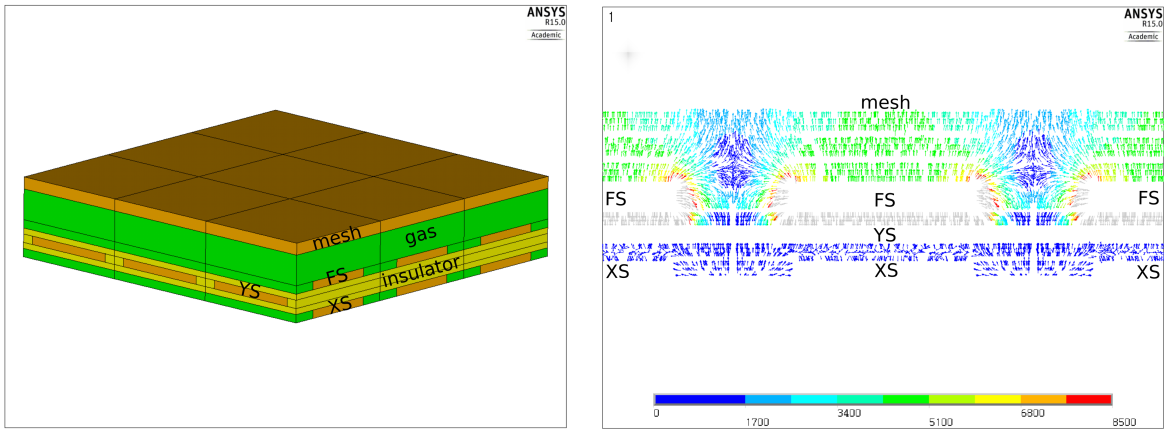

Figure 4.1: The left figure shows a possible two-dimensional floating strip anode PCB including the amplification region of a 3x3 strip unit cell, modeled in ANSYS [ANSYS, Inc., 2013]. Electrodes e.g. strips and mesh are orange (copper), gas volumes green and the PCB material yellow (Kapton). The right figure shows the electric field line configuration in the $x-z$-plane calculated by ANSYS when applying 580V to the floating strips. The field strength is encoded in the colors, ranging from 0 to 85 kV/cm. FS: floating strip, XS: x-strip, YS: y-strip.

Materials with different electrical properties are colored individually, such as conductor (orange), insulator (yellow) and gas (green). The reason for placing the y-strips between floating strips and the x-strips is discussed in the following sections, when details about signals generation and capacitive coupling are explained.

In a next step, potentials are assigned to the electrodes such as floating strips and ANSYS solves the field equations in three dimensional space. Figure 4.1 (right), shows the electric field solution when applying 580 V to the floating strip, while grounding all other electrodes. The field strength is encoded in the colors, ranging from 0 to 85 kV/cm. The non-uniformity of the electric field is clearly visible, originating from the segmented anode strip structure. While the electric field centrally above the floating strip is similar to the expected parallel plane field of 580 V/0.150 µm $\approx$ 40 kV/cm, maximum fields of 85 kV/cm are observed at the edges of the strips. This is mainly originating from the strip structure of the anode, but also, as you will see in the next section, due to the perpendicular readout strips placed very close below the floating strips.

4.2 Charge Carrier Drift and Amplification Simulated with Garfield++

The geometry created in ANSYS including potential and field maps are imported in Garfield++ [Veenhof, 2010], where charge carrier drift and amplification are simulated. Figure 4.2 shows the charge carrier drift lines projected onto the $x-z$-plane after completed gas amplification. Electrons are marked in orange, ions in grey. The electrodes such as the strips on the anode and the uniform plane micro-mesh are colored in brown.

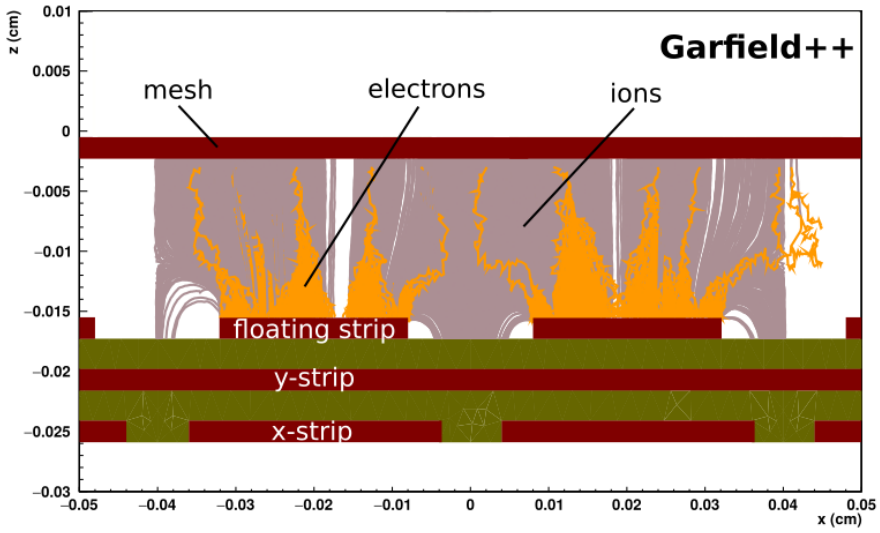

Figure 4.2: Geometric visualization of the Garfield++ simulation for the charge carrier drift and amplification between mesh and anode in a two-dimensional floating strip Micromegas detector, projected onto the $x-z$-plane. The electric field line configuration has been imported from the ANSYS unit cell shown in Figure 4.1.

For the simulations presented in the following sections, always Ar:CO_2 93:7 vol.% has been used as detector gas, unless explicitly stated differently. Penning transfer for Argon has been included, using a transfer probability of $r = 0.42$ [Şahin et al., 2010]. By variation of different floating strip parameters, the gain variation in a two-dimensional floating strip Micromegas was simulated.

Figure 4.3 shows the mean gas gain as a function of the amplification voltage for two different amplification gap scenarios. It is given by the ratio of the total number of produced avalanche electrons and the number of initial electrons, homogeneously distributed in a plane with $0.5 \times 0.5\,\mathrm{mm}^2$ directly underneath the micro-mesh. No significant dependence of the gain on the initial electron position within the plane i.e. the avalanche position in the amplification gap has been observed. Errors of the mean gain have been determined by conducting 10 identical simulations for the lowest simulated amplification voltage. For each of those, 500 initial electrons have been simulated and the average gain as well as fluctuations have been determined. The relative uncertainties from statistical fluctuations around the mean value of the 10 identical simulations is furthermore used as the uncertainty on the simulated gain.

From the empirical parametrization of the first Townsend coefficient [Townsend, 1910]

$$\alpha = \frac{A \cdot p}{T} \exp\left(-\frac{B \cdot p}{E_{\mathrm{amp}} \cdot T}\right) \tag{4.1}$$

and equation 2.5, the gain G can be re-written as

$$G = \exp\left(A \cdot \frac{p}{T} \cdot \exp\left(-B\,\frac{p \cdot d}{T \cdot U}\right) d\right) \quad , \tag{4.2}$$

assuming that $E_{\text{amp}} = U/d$ with an applied voltage U over an amplification gap d, T the temperature and p the pressure. A and B are gas dependent parameters which have been measured by Lippert [2012] with a standard Micromegas filled with Ar:CO_2 93:7 vol.% featuring a 128 µm amplification gap and are found to be $(98.4 \pm 0.9)\,\text{K}/(\text{bar}\,\mu\text{m})$ and $(2033 \pm 11)\,\text{K V}/(\text{bar}\,\mu\text{m})$. Equation 4.2 has been fit to the gain-voltage data points. The values for A and B resulting from the fit are stated in the legend. Within the fit errors both simulations show similar results. Averaging over both yields a mean value of $\bar{A} = (90 \pm 7)\,\text{K}/(\text{bar}\,\mu\text{m})$ and $\bar{B} = (1900 \pm 100)\,\text{K V}/(\text{bar}\,\mu\text{m})$, which is almost in agreement with the measurement. However, as for the measurements presented by Lippert [2012] a Micromegas with a strip width-to-pitch ratio of $150/250 = 0.6$ was used, a comparison with the 0.3 mm floating strips seems more feasible. We see, that the simulation yields around 10% to 15% smaller results than the measurements, which may be caused by the simplification of the micro-mesh being a homogeneous plane during the simulations, as the mean gain tends to increase for finer micro-mesh geometries as observed by Kuger [2017]. As the gain increases if the floating strip width is reduced while keeping the pitch constant (see Figure 4.4), the results from the 150 µm wide floating strip simulation fit better to the measurements.

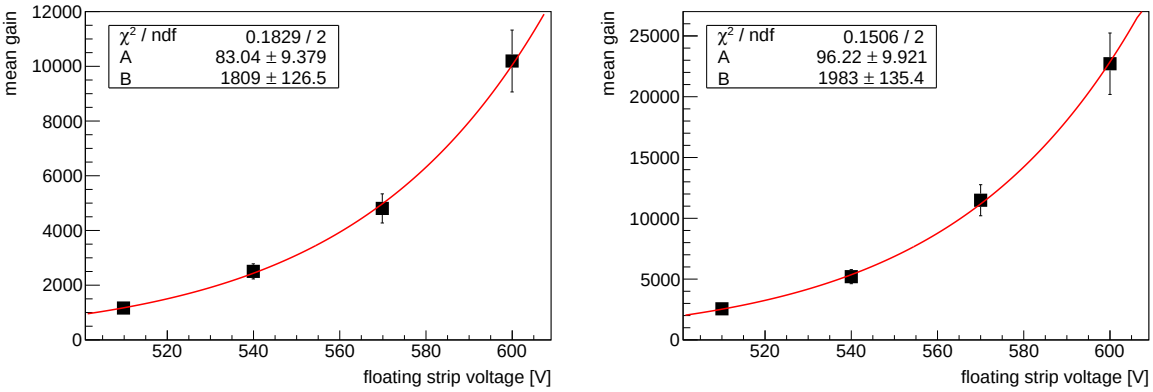

Figure 4.3: Mean gas gain of electrons homogeneously distributed in a plane directly underneath the micro-mesh in a size of the unit cell geometry with 0.5 mm floating strip pitch, as a function of the amplification voltage. The gas volume is filled with Ar:CO_2 93:7 vol.% at a pressure and temperature of 973 mbar and 20 °C, respectively. A Penning transfer rate of $r = 0.42$ has been used. Left: 0.3 mm floating strip width at an amplification gap of 0.150 mm. Right: 0.15 mm floating strip width at an amplification gap of 0.128 mm. Equation 4.2 has been fit to both gain curves. The resulting gas dependent parameters A and B are stated in the legend.

Good agreement is found when comparing the absolute gain of the simulation at a gap of 0.15 mm and a floating strip width of 0.3 mm with a gain measurement performed by Bortfeldt [2014] with 20 MeV protons and a floating strip Micromegas with one-dimensional strip readout. Consequently, the gain in a floating strip Micromegas with two-dimensional readout structure is expected to be not much different compared to a one-dimensional detector.

The mean gain as a function on the floating strip width is shown in Figure 4.4. With decreasing floating strip width a clear increase of the mean gain is observed. It can be understood similarly to the radial electric field lines in an anode wire chamber: The field strength increases close to the electrode which is in this case the floating strip, if the strip width is small

compared to the strip pitch. This additionally increases the effective electron amplification distance.

No substantial gain difference has been observed when the floating strip pitch has been varied while the ratio width/pitch was held constant or the strip thickness has been varied.

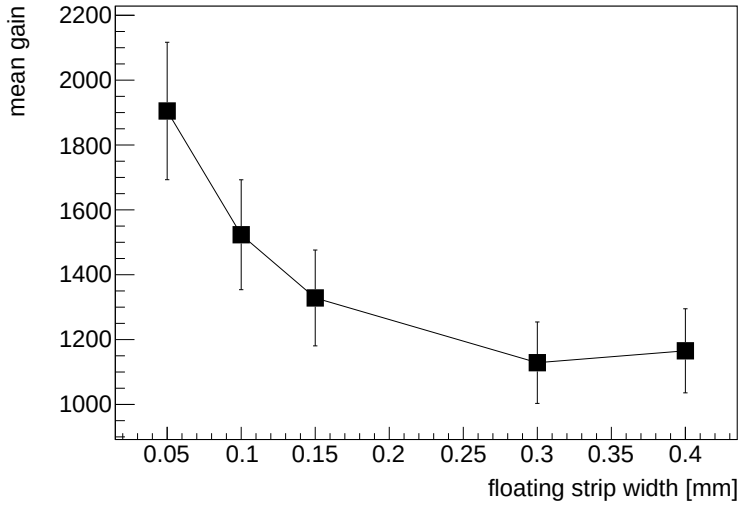

Figure 4.4: Mean gas gain of electrons homogeneously distributed in a plane directly underneath the micro-mesh in a size of the unit cell geometry at 510 V and an amplification gap of 0.150 mm. The floating strip width has been varied, while the pitch of 0.5 mm was held constant.

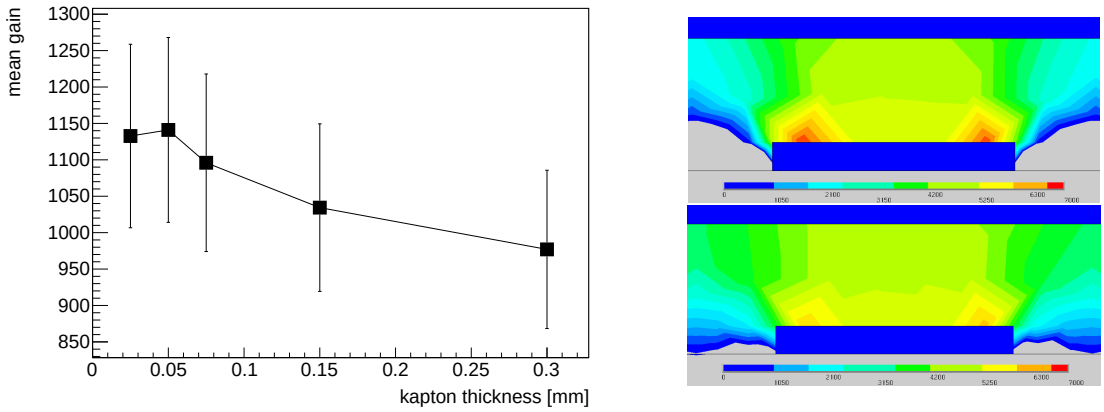

Figure 4.5: The left figure shows the mean gas gain as a function of the Kapton thickness between the floating strips and the y-strips at an amplification voltage of 510 V and an amplification gap of 0.150 mm, simulated with Garfield++ [Veenhof, 2010]. The floating strip pitch and width is 0.5 mm and 0.3 mm, respectively. The right figure shows the calculated local electric field of the floating strips for 0.025 mm (top) and 0.2 mm (bottom) Kapton thickness. The field strength is encoded in the colors ranging from 0 to 7kV/mm [ANSYS, Inc., 2013].

A small but not significant decrease of the gas gain is observed with increasing the insulation material thickness between the floating strips and the y-strips, as can be seen in Figure 4.5 (left). From the lowest simulated value of 0.025 mm up to the maximum value of 0.3 mm, a gain reduction of (14 ± 12) % is found. This can be understood by the higher amplification field on the edge of the floating strips depending on the distance of the grounded readout strip

directly beneath it, as can be seen in Figure 4.5 (right). However, it does not significantly influence the gain and as the uncertainty on the gain is on the same order as the trend, no definite statement can be made at this point.

The dependence of the mean gas gain on the temperature and pressure inside the gas volume is shown in Figure 4.6, for a 0.5 mm unit cell with 0.3 mm wide floating strips. Both gain curves have been fit with equation 4.2 to extract the gas dependent parameters A and B. The fit results for both curves are stated in the legend and are compatible within their errors. Comparing it again to the measurements performed by Lippert [2012] shows also that the simulated values are consistently smaller, caused by an around 10% underestimated absolute gain due to the simplified assumption of the micro-mesh being a homogeneous plane, as it was discussed already above.

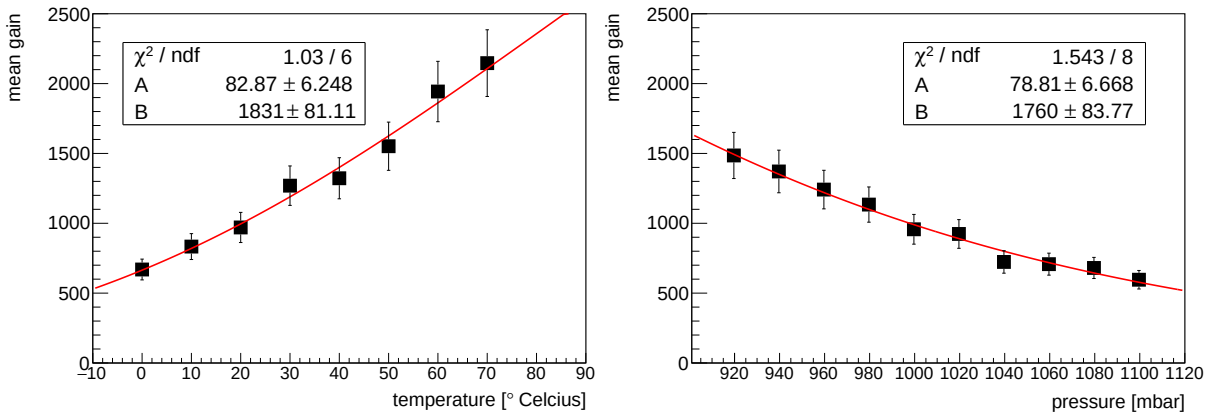

Figure 4.6: Mean gas gain for 500 electrons homogeneously distributed directly beneath the mesh in a 0.5 mm unit cell at an amplification voltage of 510 V, an amplification gap of 0.15 mm, a floating strip width of 0.3 mm and a pitch of 0.5 mm, simulated with Garfield++ [Veenhof, 2010]. The left and right figure show the dependence of the gain as a function of the temperature at a pressure of around 973 mbar and as a function of the pressure at 20° C, respectively. Both curves have been fit with equation 4.2 to extract the gas dependent parameters A and B.

4.3 Signal Generation on the Anode Strips

The coupling of the signal created in the amplification gap of the detector to the readout strips is a combination of two processes: Direct induced current and capacitively coupled current. The direct induced current on an electrode due to moving charges in the amplification region can be calculated by the theory proposed by Shockley [1938] and Ramo [1939], which is often referred to as *weighting field* theory. The capacitive coupling of the induced currents between the strip layers can be calculated if the capacitances of the electrodes in the detector are known, simulated or measured. In this section, we focus on the direct induced signal on the electrodes via weighting fields. The capacitive coupling will be covered in the next section.

Following the Shockley-Ramo theorem, the induced current $I_i^{\text{ind}}(t)$ on an electrode i by a moving charge q is given by

$$\begin{aligned} I_i^{\text{ind}}(t) &= -q/V_w \cdot \mathbf{E}_i[\mathbf{x}(t)] \cdot \dot{\mathbf{x}}(t) \\ &= -q/V_w \cdot |\mathbf{E_i}[\mathbf{x}(t)]| \cdot |\dot{\mathbf{x}}(t)| \cdot \cos(\Theta) \end{aligned} \tag{4.3}$$

where $\mathbf{E}_i/V_w$ is called the weighting field of electrode i, $\dot{\mathbf{x}}(t) = \mathbf{v}(t)$ the velocity of the moving

charge and Θ the angle between the two vectors. Both depend on the time t where the charge q is located at the position $\mathbf{x}(t)$ with a velocity $\dot{\mathbf{x}}(t)$. The weighting field of an electrode is defined as the electric field in case the charge q is removed and the electrode is set to voltage V_w, while all other electrodes are grounded. The result of the scalar product $\mathbf{E}_i[\mathbf{x}(t)] \cdot \dot{\mathbf{x}}(t)$ normalized by V_w is thus a measure describing the fraction of the charge q between $[-1, ..., 1] \cdot q$ that is actually induced on the electrode at a time t. Hence, the sign of the induced current is not only depending on the sign of the charge −of the moving particle− but also on the orientation of the particle velocity vector with respect to the direction of the weighting field.

Figure 4.7 shows the weighting field lines as calculated by ANSYS of the x-strips (left) and the y-strips (right). Note that for the weighting field calculation of a single strip, also the neighboring strips in the same readout strip layer need to be grounded, which is not the case for the shown figures.

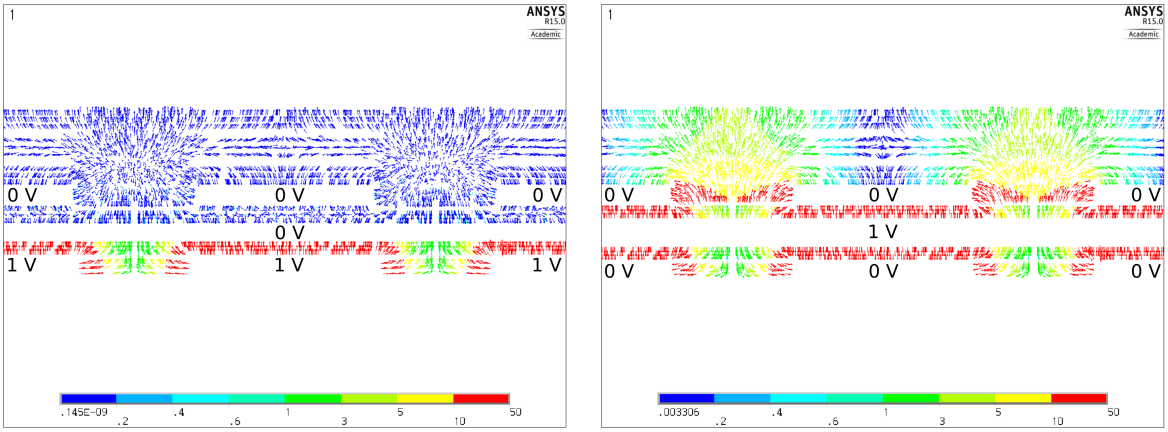

Figure 4.7: Weighting fields in the $x - z$-plane of parallel readout strips (left) and perpendicular readout strips (right) calculated by ANSYS [ANSYS, Inc., 2013] when applying 1V to the respective strips and grounding all others. The field strength is encoded in the colors, ranging from 0 to 500 V/cm. Note the non-linear scaling of the contours.

4.3.1 Induced Signals From Avalanches Centered Above a Floating Strip

Assume two electrons placed in the ANSYS unit cell geometry below the micro-mesh, centered above two floating strips. The electron avalanche towards the floating strips and the ion drift towards the micro-mesh is simulated by Garfield++ [Veenhof, 2010]. In the following, the directly induced signal on the perpendicular readout strips will be discussed in detail. Figure 4.8 shows the snapshot of the finished amplification process after all electrodes have received their charges. The most important weighting field lines of the right floating strip and a perpendicular readout strip are sketched.

Consider an electron-ion-pair which is created in the amplification process. The electron with charge $q = -e$ moves towards the floating strip, while the ion with charge $q' = -q = e$ moves towards the micro-mesh. From charge conservation follows that the total induced charge Q on the floating strip must be equal to the charge that arrived on the strip i.e. $Q = -e$. As the perpendicular readout strip does not receive any charge, the total induced charge Q on the strip must be zero. Consequently, the directly induced current by the electron and ion movement has to be strictly bipolar.

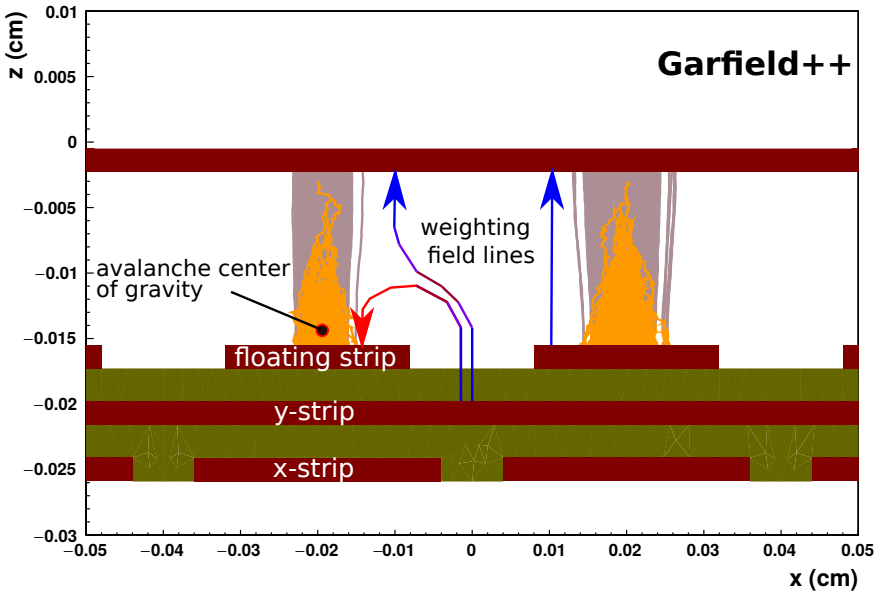

Figure 4.8: Two electron avalanches simulated with Garfield++ are shown [Veenhof, 2010]. To understand the created signals on the anode strip layers, the most important weighting field lines calculated by ANSYS in Figure 4.7 of the right floating strip and the perpendicular readout strip are sketched.

Now lets apply Shockley-Ramo's theorem Shockley [1938] Ramo [1939] to calculate the sign of induced currents by the charge created in the avalanche, starting with the electron component. From equation 4.3 follows, that the total induced current $I_y^{\text{ele}}(t)$ on the perpendicular readout strip is given by the sum over all created avalanche electrons N_0, following

$$I_y^{\text{ele}}(t) = \sum_{i=1}^{N_0} e/V_w \cdot |\mathbf{E}_{\text{y}}[\mathbf{x}_i(t)]| \cdot |\dot{\mathbf{x}}_i(t)| \cdot \cos(\Theta_i) \quad , \tag{4.4}$$

which is depending on the angle Θ_i of electron i between the weighting field of the perpendicular readout strip $\mathbf{E}_{\text{y}}/V_w$ evaluated at $\mathbf{x}_i(t)$ and the velocity $\dot{\mathbf{x}}_i(t)$. From Figure 4.7 (right), we find that the inflection point of the weighting field vectors is approximately at half of the amplification distance $d = 150\,\mu\text{m}$. Hence, for an electron i created at a distance x from the floating strip with $x < d/2$ directly follows that $\Theta_i < 90°$. For electrons created at $x > d/2$ from the floating strip thus follows that $\Theta_i > 90°$. We know that the electron mean free path λ in the amplification process can be calculated by $\lambda = 1/\alpha$, where α is the first Townsend coefficient. For typical amplification fields in Ar:CO_2 93:7 vol.% above 30 kV/cm this corresponds to $\lambda < 20\,\mu\text{m}$ at normal temperature and pressure. Thus more than 95% of the total charge is created within the last three steps of the amplification process, which is a maximum distance of $x = 3\lambda = 60\,\mu\text{m}$ away from the floating strip surface. As this is explicitly smaller than $d/2 = 75\,\mu\text{m}$, we can conclude that the total induced current of the electrons defined in equation 4.4 is positive i.e.

$$I_y^{\text{ele}}(t) = \sum_{i=1}^{N_0} e/V_w \cdot |\mathbf{E}_{\text{y}}[\mathbf{x}_i(t)]| \cdot |\dot{\mathbf{x}}_i(t)| \cdot \underbrace{\cos(\Theta_i)}_{>0} > 0 \quad , \tag{4.5}$$

as almost all electrons are created at $x < d/2$ which implies $\Theta < 90°$.

Now lets consider the signal induced by the ion movement towards the micro-mesh. The electron avalanche is finished in less than 2 ns to 3 ns. Due to the factor of 10^2 to 10^3 smaller mobility of the ions, without loss of generality, we can assume that the ions are all created at the same point in time t_0 corresponding to the time when the avalanche is finished. At the time t_0 all ions begin to drift towards the micro-mesh. As we know from the discussion above, more than 95% of the total charge is created at a distance $x < d/2$. Thus, the vast majority of the ions begin their movement with an angle $\Theta_i > 90°$, as the ion velocity vector is inverted compared to the electron velocity vector. For all times $t > t_1$, where t_1 corresponds to the time where the majority of the ion crosses the distance $x = d/2$ at the inflection point of the weighting field lines, follows $\Theta_i < 90°$. Thus the total induced current by the movement of the ions is first positive and then negative, depending on the time t:

$$I_y^{\text{ion}}(t) = \begin{cases} \sum_{i=1}^{N_0} -e/V_w \cdot |\mathbf{E}_\text{y}[\mathbf{x}_i(t)]| \cdot |\dot{\mathbf{x}}_i(t)| \cdot \underbrace{\cos(\Theta_i)}_{<0} > 0 \quad \forall\, t_0 < t < t_1 \\ \sum_{i=1}^{N_0} -e/V_w \cdot |\mathbf{E}_\text{y}[\mathbf{x}_i(t)]| \cdot |\dot{\mathbf{x}}_i(t)| \cdot \underbrace{\cos(\Theta_i)}_{>0} < 0 \quad \forall\, t > t_1 \end{cases} \tag{4.6}$$

Hence, the current signal on the perpendicular readout strip after all charges have arrived at the electrodes is expected to have an initial fast, positive signal from the electron movement to the floating strip and a much slower bipolar signal from the ion movement towards the micro-mesh, being positive for $x < d/2$ and negative after $x = d/2$. The total induced charge however is zero. The same argumentation holds also for the parallel readout strip. The floating strip however, will by definition receive the full charge $Q = -N_0 e < 0$ created in the avalanche, which is the combination of the electrons drifting towards the floating strips and the ions towards the micro-mesh.

Figure 4.9 shows the induced currents as a function of time calculated by Garfield++ for one floating strip, parallel and perpendicular readout strip. The negative current on the floating strip and the bipolar current on the perpendicular readout strip is visible. On the parallel readout strip also a bipolar current is induced, however, suppressed compared to the perpendicular signal by two orders of magnitude, as the weighting field lines are almost completely blocked by the perpendicular readout strip, as can be seen in Figure 4.7 (left).

The time evolution of the current can be subdivided into the two main signal components: the fast electron signal and the much slower ion signal. Note that the histogram has been re-binned to a 10 ns bin width to smooth the curve. In reality, the fast electron component is below 3 ns, which can be found in all three induced strip current histograms in the very first bin. The much slower ion component of the current signal is strongly depending on the mobility of the ions in the gas. In this simulation Ar:CO_2 has been used as detector gas which results in a maximum ion drift time of around 300 ns. In section 4.6 the strip signals have been simulated for a Ne:CF_4 based gas mixture, which reduces the signal duration on all electrodes to around 150 ns due to a factor of two higher ion mobility.

The zero-crossing point of the bipolar currents induced on the readout strips which is a measure for the turning point of the weighting field lines bending either to the floating strip or the micro-mesh strongly depends on the avalanche position in the amplification region.

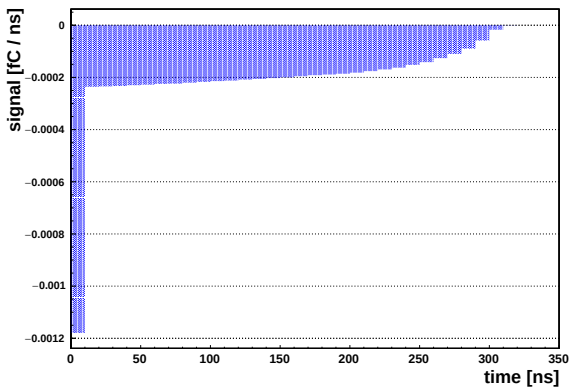

(a) floating strip

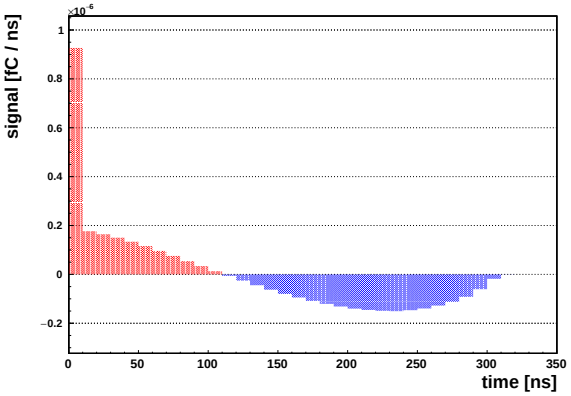

(b) parallel readout strip

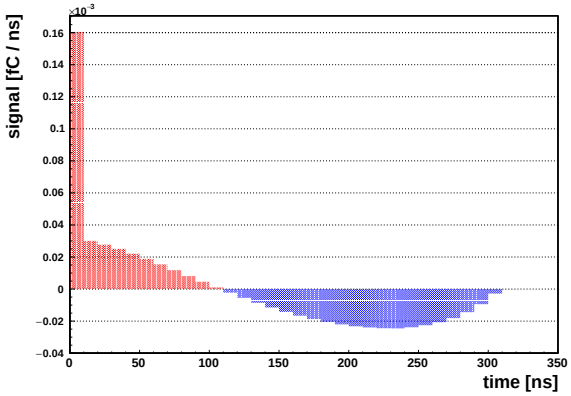

(c) perpendicular readout strip

Figure 4.9: Induced currents as a function of time from two electrons placed centrally above two floating strips on all strip layers on the anode, neglecting the capacitive coupling between floating and readout strips. The sign of the induced current is marked in blue (negative) and red (positive), resulting from different weighting field line configurations of the individual strip layers. Note the different scales on the y-axes for the perpendicular and parallel readout strip.

Furthermore the absolute value of the weighting field strength depends on the position in the amplification region, as can be seen in Figure 4.7. Hence, the induced signals on the perpendicular readout strip will be investigated in the following as a function of the initial electron position in the amplification gap. For the moment, the induced currents on the other electrodes are ignored, as they are in the case of the floating strip always delivering the total charge created in the amplification region, or in the case of the parallel readout strip, are negligibly small.

4.3.2 Induced Signal on the Perpendicular Readout Strip as a Function of the Avalanche Position

Figure 4.10 shows the ratio of positive and negative induced charge on the middle perpendicular readout strip as a function of the initial electron position. The position of the floating strips and the perpendicular readout strip is overlayed. For the simulation, 10k electrons have been placed directly underneath the mesh randomly distributed in a circular plane with a radius of 0.75 mm, centered above the perpendicular strip.

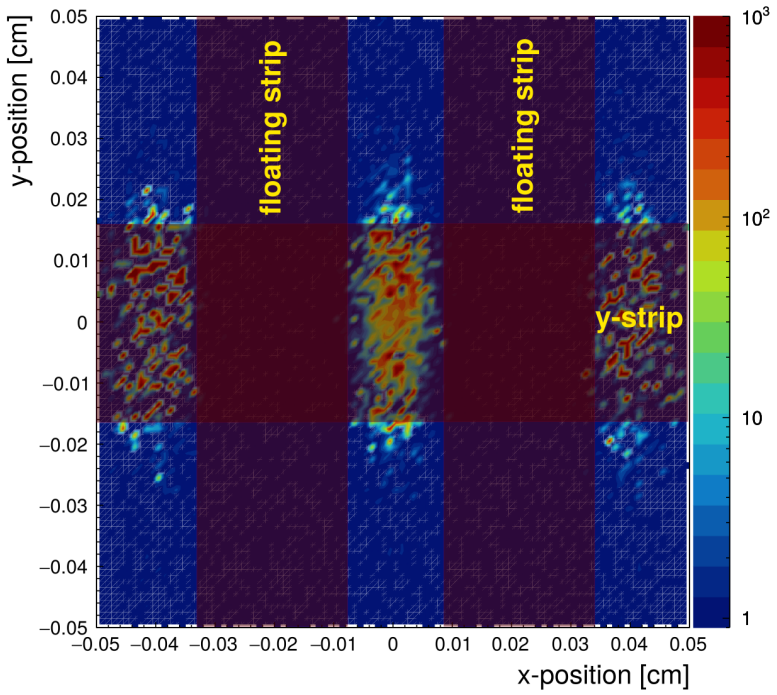

Figure 4.10: Ratio between positive and negative induced charge on the perpendicular strip (y-strip) as a function of the initial electron position i.e. the beginning of the avalanche. The position and orientation of the strips are overlayed.

Note that the ratio which is encoded in the colors of the contours has been manually set to a maximum value of 1000 for visibility reasons. The maximum ratio is even higher, as the negative component of the induced bipolar signal, generated by the ions, almost vanishes for avalanches created in the middle between two floating strips. This phenomena is discussed in the following.

It is clearly visible, that the ratio between positive and negative induced charge depends on the initial electron position. It can be understood by the fact that avalanches that are created between two floating strips will arrive at the edges of the floating strips. Consequently also most of the ions are created at the edges of the floating strips. As the electric field lines of the amplification field are also bending towards the grounded perpendicular strip (see Figure 4.1), the positive ions may follow the field lines in direction of the grounded perpendicular strip. As the weighting field lines of the perpendicular strip are oriented in the same way as these particular amplification field lines and the orientation between the weighting field line and velocity vector of the ions is anti-parallel, the induced current on the perpendicular strip will only be positive according to equation 4.3. Thus the total induced charge on the perpendicular strip will be >0. For avalanches created not between two floating strips, the probability that ions will follow field lines ending on the PCB is very small. Thus, the ratio of positive and negative induced charge is 1, as the total induced charge must be zero due to no ions moving towards the perpendicular readout strip, which is clearly visible in the Figure 4.10.

As a first result we find that the dominant induced current component on the perpendicular readout strip is positive. To determine which fraction of the total created charge in the amplification process is directly induced as positive charge to the perpendicular strip, the ratio between both is investigated as a function of the initial electron position, see Figure 4.11. It is from now on referred to as *signal strength*.

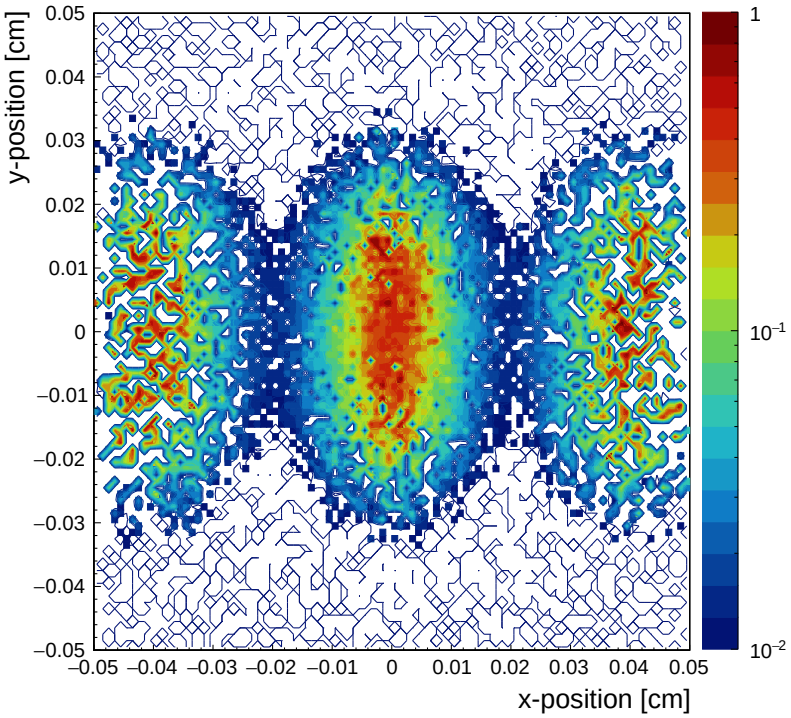

Figure 4.11: Signal strength on the y-strip i.e ratio between positive induced charge on the central perpendicular strip and total number of created avalanche electrons as a function of the initial electron position. The position and orientation of the strips are the same as in Figure 4.10

If the avalanche is located between the floating strips and above the perpendicular readout strip, on average around 30% to 50% of the total avalanche charge is found to be induced to the perpendicular readout strip. If the avalanche is located centered above a floating strip and also above the perpendicular readout strip a signal strength around 1% to 5% is found. In order to understand these percentages, the signal strength on the perpendicular strip is investigated as a function of the fraction of avalanche ions drifting to the PCB. This is shown in Figure 4.12. As the electron avalanches are located in a circular area with radius 0.75 mm around the central perpendicular strip, a significant fraction of the charge is not created above the central perpendicular strip and thus not interesting for the discussion in the following. The events where the avalanches are located above the perpendicular readout strip is marked in the figure. An almost linear dependence of the signal strength on the fraction of ions drifting on the PCB is observed. These are events where the avalanche takes place above but distributed along the perpendicular strip. For avalanches located over the floating strip, smaller signals are observed, whereas for avalanches located above the perpendicular strip, higher signals are induced, which is also visible in Figure 4.11. A maximum of up to almost 90% of the avalanche charge can be coupled to the perpendicular readout strip if the avalanche is created centrally between two floating strips above the perpendicular strip, assuming all of the avalanche ions are drifting towards the PCB. A y-strip signal strength of 100% is not possible, as the ions are not drifting to the readout strip itself but being absorbed by the PCB. Hence around 10% of the signal is lost in this PCB configuration, depending on the PCB thickness.

However, the fraction of ions drifting towards the PCB for an avalanche created centrally above the perpendicular strip is strongly depending on the avalanche electron end positions on the floating strips which in turn is subject to statistical fluctuations.

To conclude: even if an avalanche is created between two floating strips centered above the perpendicular strip, the induced positive charge depends on the end position of the avalanche. If the avalanche end position is located on the surface of the floating strip facing the micro-mesh, more ions will drift to the micro-mesh than to the PCB, which reduces the signal strength. If the avalanche end position is located on the edge of the floating strip, it is possible that almost all ions will end up on the PCB, thus inducing the maximum possible charge of up to 90%. Due to statistical fluctuations the signals in reality will lie somewhere between these two extreme scenarios, which is in agreement with the average signal strength of around 30% to 50% between the floating strips, visible in Figure 4.11.

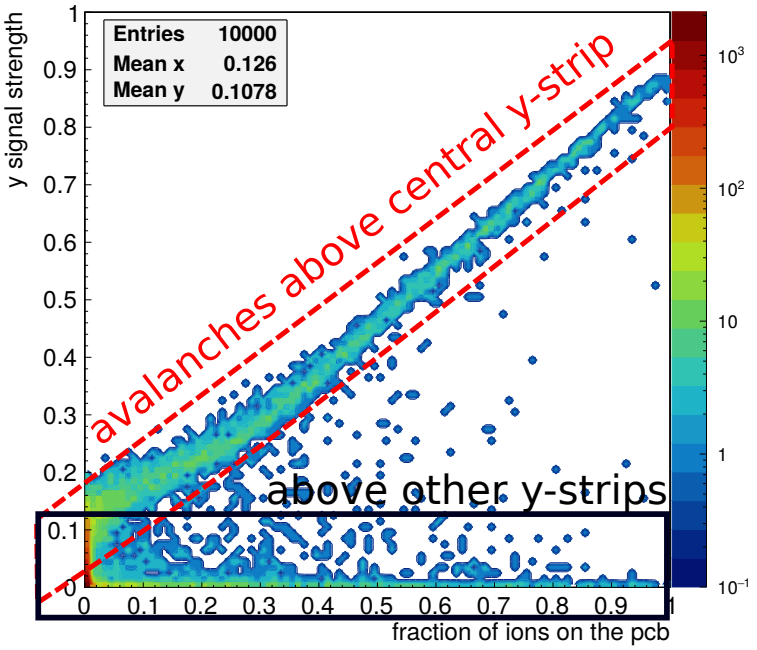

Figure 4.12: Signal strength on the central perpendicular readout strip as a function of the fraction of avalanche ions drifting towards the PCB. For the simulation 10k electrons have been randomly distributed in a circle with a radius of 0.75 mm, centered above the perpendicular strip. As only the signal strength of the central y-strip was calculated, the relevant avalanche events are those between the red dashed lines.

It should be stressed at this point that the signal strength on the perpendicular readout strip measured with a real detector will be the average signal from multiple avalanches located at different points on the floating strips. Thus the measured pulse height will effectively be the average of those. The fact that signals with higher positive charge and thus amplitude are created if avalanche ions drift towards the PCB may lead to a charge-up of the anode PCB between two floating strips. This should not influence the total charge created in the detector, but only the charge transferred to the perpendicular readout strip, as the ions may at some point not drift towards the PCB if the charge-up is on the same order as the floating strip voltage. However, measurements presented in chapter 8 show that the pulse height on the perpendicular readout strip is not influenced by such effects up to almost 5 MHz/cm^2 particle flux densities. An explanation may be a net effect of ions on the PCB recombining with electrons from future avalanches, leading to the net pulse height measured.

4.3.3 Characterization of the Signal Strength on the Perpendicular Readout Strip

In the following, the average signal strength on the perpendicular readout strip between two floating strips is investigated as a function of the anode PCB parameters, in order to maximize the signal. Figure 4.13 shows the signal strength as a function of the floating strip width, height (i.e. thickness) and the insulator thickness. In the simulation 500 electrons have been placed in the middle between two floating strips at 500 V with an amplification gap of 0.15 mm, centered above the perpendicular readout strip.

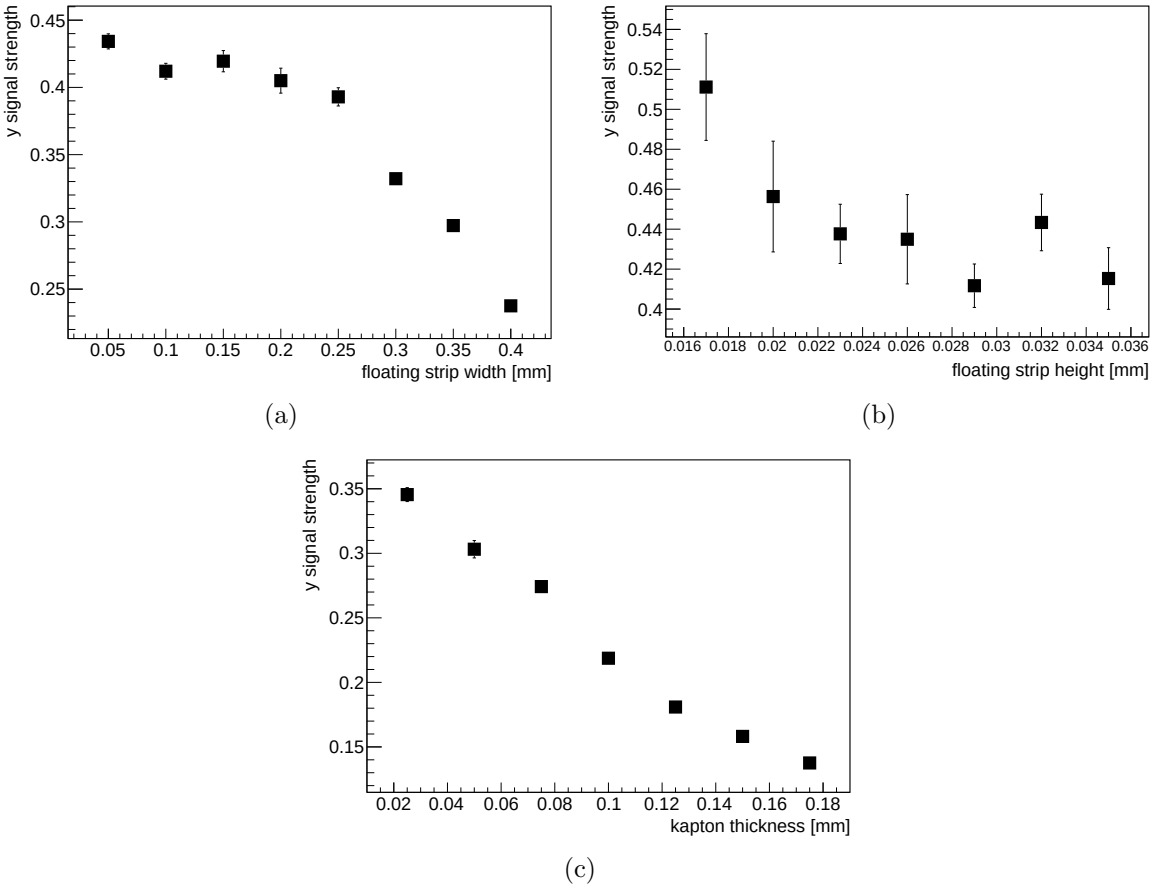

Figure 4.13: Average signal strength on the perpendicular strip between two floating strips a.) as a function on the floating strip width at a floating strip height of 0.035 mm and a 0.025 mm thick Kapton layer, b.) as a function of the floating strip height at a width of 0.2 mm and a 0.025 mm thick Kapton layer and c.) as a function of the Kapton layer thickness at a floating strip height of 0.035 mm and a width of 0.3 mm. The floating strip pitch is 0.5 mm and for each data point 500 electrons have been placed between two floating strips at 500 V centered above the perpendicular strip directly underneath the mesh at a distance of 0.15 mm from the anode strips.

The highest signals can be reached by reducing the floating strip width at constant strip pitch, as the fraction of ions drifting towards the PCB and the weighting field line density on the floating strip surface is increased. A small increase is also observed when reducing the floating strip height from 35 µm to 17 µm, although within the errors of the simulation the values are very similar. A clear increase is observed for the signal strength if the Kapton insulation layer thickness between floating strip and perpendicular readout strip is reduced. Simulations on the signal strength as a function of the perpendicular strip width showed

additionally that wider strips are favored due to more weighting field lines bending into the amplification region.

Summarizing the results of the signal strength on the perpendicular readout strip of a two-dimensional floating strip Micromegas anode motivates to place the perpendicular readout strip layer directly underneath the floating strip layer instead of the parallel readout strip layer, as a significant fraction of the total charge created in the amplification process is directly induced on the perpendicular strip. Additionally, the directly induced signal on the parallel strip is negligibly small. However, as will be explained in detail in the next section, the signal on the parallel strip is dominantly created by the capacitively coupled floating strip signal.

4.4 Capacitive Coupling between the Anode Strip Layers

To determine the transfer of charge by capacitive coupling between floating strips and readout strips, the capacitance of the floating strip to all surrounding electrodes needs to be known. The ANSYS geometry of the two-dimensional floating strip anode has been used to determine the capacitance between two strips, one on top of the PCB i.e. representing a floating strip and one embedded in the PCB i.e. representing a readout strip. To determine the capacitance between both strips, a charge Q has been placed on the one strip, while a charge $-Q$ has been placed on the other strip. The capacitance can thus be calculated by

$$C = \frac{Q}{\Delta U} \tag{4.7}$$

where ΔU is the resulting voltage difference between the two strips calculated by ANSYS. The simulated capacitance has been compared to the capacitance calculated with the formula for a parallel plate capacitor, following

$$C = \epsilon_0 \cdot \epsilon_r \cdot \frac{A}{d} \quad , \tag{4.8}$$

where ϵ_0 is the vacuum permittivity, ϵ_r the relative permittivity of the dielectric, A the surface and d the distance between the two plates. The ratio of simulated and calculated strip capacitance as a function of the strip width and distance is shown in Figure 4.14, assuming $\epsilon_r = 4$ for the PCB material[1].

Good agreement between simulation and direct calculation are observed for small strip distances and large strip widths. This is expected as the capacitance calculated from the parallel plate capacitor formula assumes two infinitely sized planes of zero thickness. With the simulation results from ANSYS the capacitances of all electrodes in a two-dimensional floating strip anode plus micro-mesh and ground planes has been determined. The relative capacitances between all electrodes are listed in Table 4.1 for a floating strip anode PCB consisting of 128 floating strips at a pitch of 0.5 mm, 0.4 mm wide perpendicular strips and 0.3 mm wide parallel strips both also with a pitch of 0.5 mm, with each layer separated by a 25 µm insulation layer. The coupling between the neighboring strips within one layer has been approximated with a PCB strip line formula from [Paul, 2007]. The coupling between a floating strip and its neighboring parallel readout strip has been neglected as it is considerably smaller than the other strip capacitances.

[1] the relative permittivity of typical PCB materials can vary between 3.4 (Polymid) and 4.7 (FR4), see `https://www.farnell.com/`

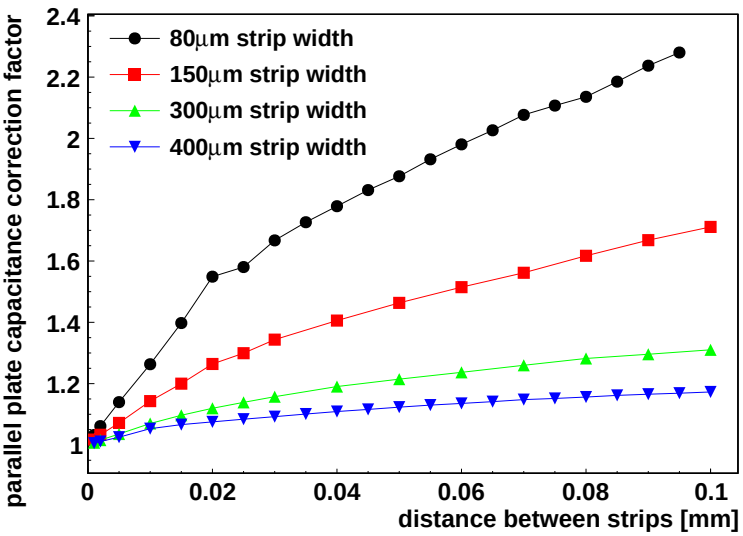

Figure 4.14: Ratio between simulated and calculated capacitance for two parallel strips with a thickness of 0.035 mm for different values of the strip width and distance.

capacitance between	symbol	capacitance [pF]
floating strip and x strip	C_x^f	2.13
floating strip and y strip	C_y^f	0.16
floating strip and mesh	C_m^f	3.07
floating strip and ground	C_g^f	2.22
floating strip and next neighbors*	C_{nf}^f	3.45
floating strip and all y-strips	C_{ay}^f	20.60
x strip and all y strips	C_{ay}^x	20.60
x strip and mesh incl. ground	C_{gm}^x	1.81
x strip and next neighbors*	C_{nx}^x	3.45
y strip and mesh incl. ground	C_{gm}^y	3.44
y strip and next neighbors*	C_{ny}^y	4.34

Table 4.1: Simulated capacitances in a two-dimensional floating strip Micromegas detector, using the correction factors from Figure 4.14. It has been assumed that the detector has 128 strips at a pitch of 0.5 mm, 0.3 mm wide floating strips, separated by 25 µm Kapton from the 0.4 mm wide perpendicular y-strips, separated by 25 µm Kapton from the 0.3 mm wide parallel x-strips. Thus the detector covers an active area of $6.4 \times 6.4\,\mathrm{cm}^2$ with a strip length inside the active area of 6.4 cm. The distance between mesh and anode strips is 0.128 mm, the mesh has been assumed to be a homogeneous plate. All strips have a thickness of 35 µm. The * denotes that the capacitance has been calculated using a formula to approximate neighboring PCB stripline capacitances, taken from [Paul, 2007]. The capacitance to ground has been calculated by assuming a 25 mm Aluminum frame around the active area which also carries the micro-mesh.

To determine the total capacitance of an electrode i.e. a strip, the relative capacitance to all other electrodes including ground needs to be summed. It has been calculated for the three strip layers of the anode and is shown in Figure 4.15 as a function of the perpendicular strip width for four different widths of the floating and parallel strip. The dependence of the total capacitance for each strip on the perpendicular strip width is visible. The strongest dependence is observed for the perpendicular strip itself, as it collects the capacitance of all

floating and parallel readout strips simultaneously and is only separated by a 25 µm thick insulator from both strip layers. This in particular would motivate to make the perpendicular readout strip as thin as possible as e.g. electronic noise is proportional to the strip capacitance and high capacitances lead to a signal loss when pulse amplifying/shaping electronics are connected to the strip, which will be explained in section 4.6. However, as we have seen in the last section, to increase the directly induced charge on the perpendicular readout strip, wider strips are preferred which need to be as close as possible to the amplification region. At this point there is already a motivation to reduce the width of the perpendicular readout strips directly below the floating strips and to increase their width between the floating strips. This avoids creating big capacitances in the detector while at the same time increasing the signal yield by the induced currents due to moving charges in the amplification gap.

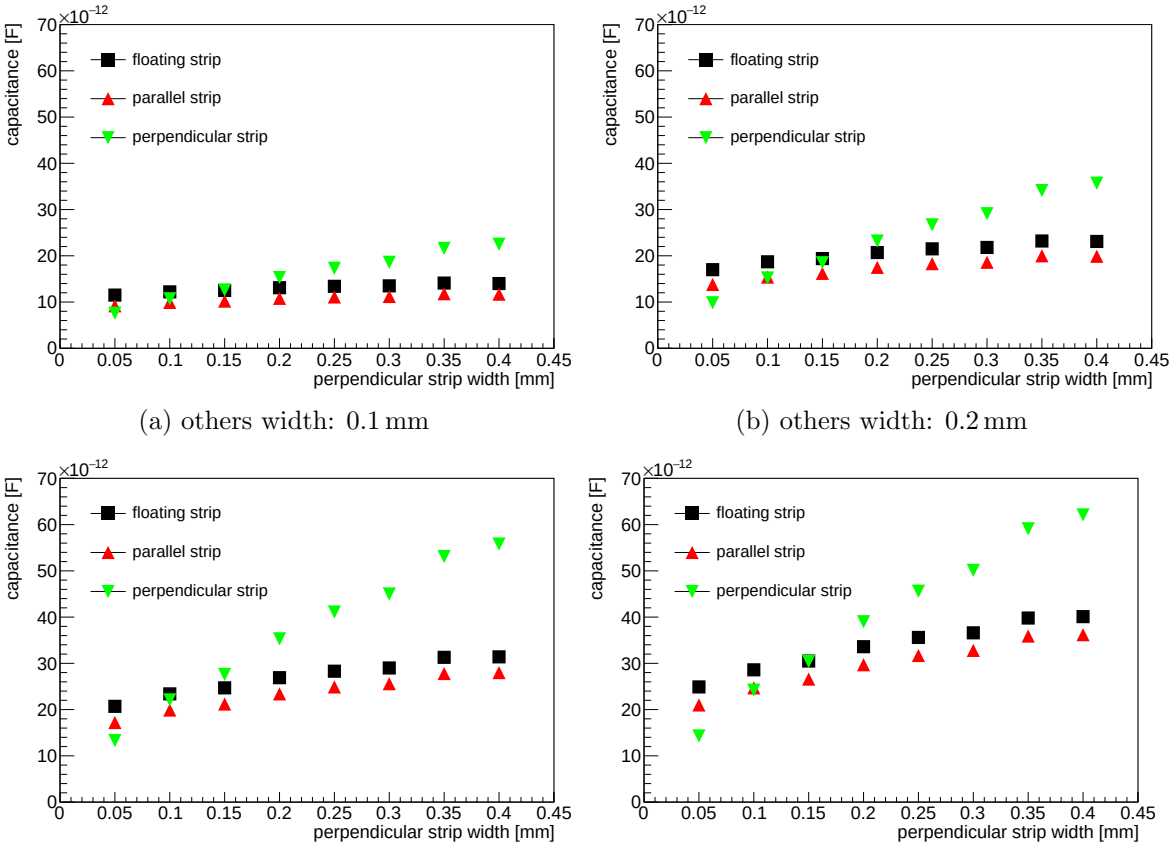

(a) others width: 0.1 mm

(b) others width: 0.2 mm

(c) others width: 0.3 mm

(d) others width: 0.4 mm

Figure 4.15: Total strip capacitances as a function of the perpendicular strip width in a two-dimensional floating strip Micromegas detector with 128 strips at a pitch of 0.5 mm and a floating and parallel strip width of a.) 0.1 mm, b.) 0.2 mm, c.) 0.3 mm and d.) 0.4 mm. The values are determined with the ANSYS based method, described in the main text.

From the capacitances of electrodes in the two-dimensional floating strip anode the capacitive coupling between the floating and readout strips can be calculated. Assume a floating strip receives the charge $q(t)$ from an electron avalanche in the amplification region. Then, the charge fraction $q_i^{\text{float}}(t)$ capacitively coupled from the floating strip to a readout strip i can be calculated by

$$q_i^{\text{float}}(t) = q(t)\frac{C_i^{\text{float}}}{C_i^{\text{float}} + C_{\text{other}}^{\text{float}}} = q(t)\frac{C_i^{\text{float}}}{C_{\text{float}}} \quad , \tag{4.9}$$

where C_i^{float} is the capacitance between the floating strip and readout strip i, C_{float} is the total floating strip capacitance and $C_i^{\text{float}}/C_{\text{float}}$ is in the following defined as the *coupling strength* between floating strip and readout strip i. Consequently optimum coupling strength between the floating strip and readout strip i is reached if the capacitances between the floating strip and all other electrodes $C_{\text{other}}^{\text{float}}$ are minimized. Finally, the capacitive coupling strength between the floating strip and a specific parallel or perpendicular readout strip can be calculated via equation 4.9, as we know the capacitances in the detector at this point. Figure 4.16 shows the coupling strength to the parallel strip (left) and the perpendicular strip (right) as a function of the perpendicular strip width for various floating and parallel readout strip widths. As it was already visible in Table 4.1 from the small capacitance between the floating strip and one perpendicular readout strip, the maximum coupled signal fraction to the perpendicular strip is about two orders of magnitude smaller than to the parallel strip. Contrary, for very small perpendicular strip widths over 40% of the floating strip charge can be coupled to the parallel readout strip.

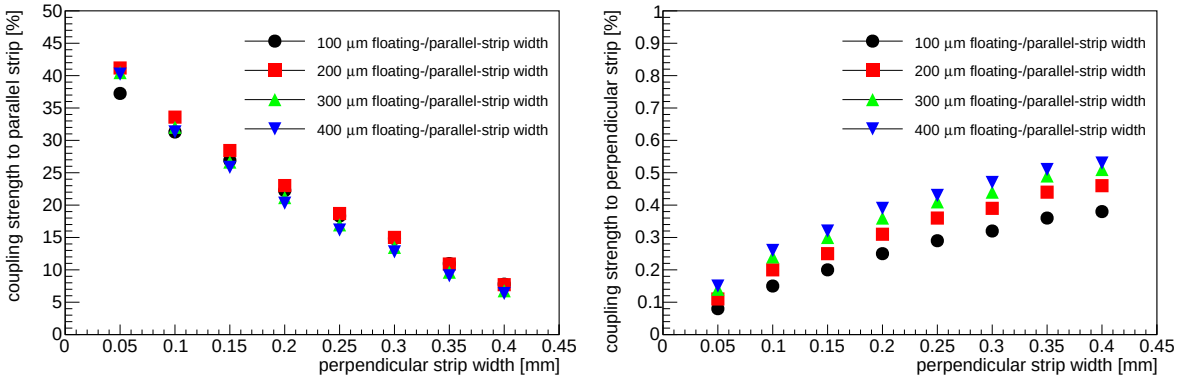

Figure 4.16: Calculated capacitive coupling strength between the floating strip and the parallel strip (left) and the floating strip and one perpendicular strip (right) as a function of the perpendicular strip width for different floating- and parallel-strip widths. Note that the maximum coupling to the perpendicular strip is about two orders of magnitude suppressed compared to the maximum coupling to the parallel strip.

4.5 Total Charge Coupled to the Readout Strip Layers

To estimate how much of the total created charge in the amplification process is coupled to the readout strips, 2.5 k electrons have been placed in a 5×5 strip Garfield++ unit cell with a radius of 0.5 mm beneath the mesh. At $t = 0$ the avalanches begin to develop towards the anode and are collected on the floating strips. In a first step, the current induced on the floating strips by the electron and ion movement is integrated and the total charge received on each floating strip is divided by the total number of electrons created in the amplification process. The results are shown in Figure 4.17. However it can be seen that only around 95% of the avalanche charge is detected. It can be attributed to electron attachment and recombination during the amplification process, as a relatively low floating strip voltage of 400 V was used during the simulation.

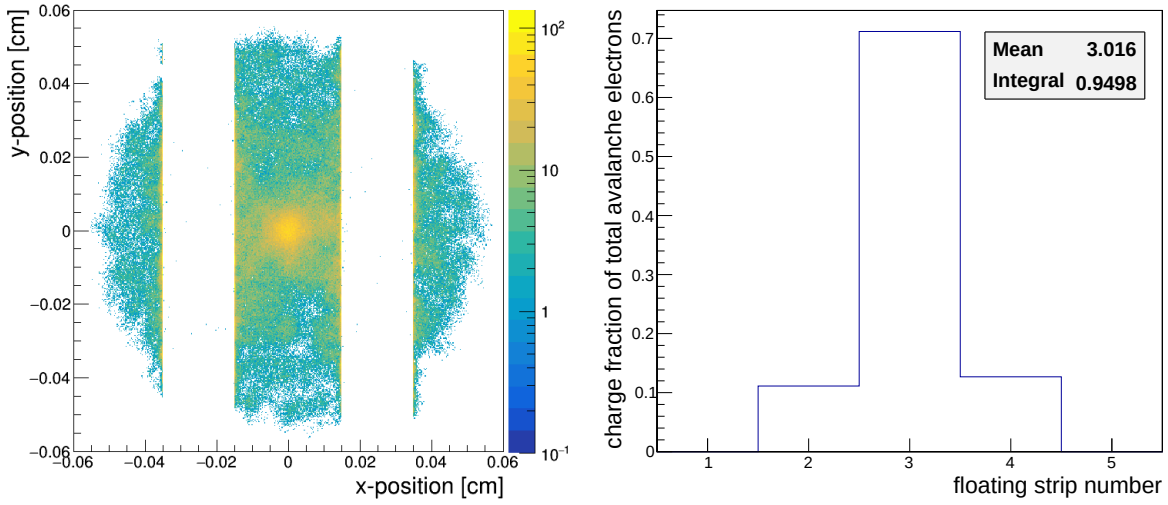

Figure 4.17: Simulated end positions of all avalanche electrons for roughly 2.5k electrons initially homogeneously distributed directly below the mesh within a circle with a radius of 0.5 mm, centered above the central floating and central perpendicular strip (left). The anode structure is clearly visible. Integrated current on each floating strip normalized by the total number of created avalanche electrons (right). The Garfield++ unit cell covered a range of five strips in both dimensions. The amplification voltage has been set to 400V over the 0.128 mm gap to speed up the simulation.

To calculate the total coupled charge to the readout strips, the directly induced currents are combined with the capacitively coupled floating strip signal. The capacitance of all strips has been calculated in the previous section. Recalling the values, the calculated capacitance between the floating strip and one perpendicular strip is $C_y^f = 0.16\,\text{pF}$ with a total floating strip capacitance of $C_f = 31.4\,\text{pF}$. This corresponds to a charge sharing of 0.51% between the floating strip and a specific perpendicular strip. Additionally it has been taken into account that each floating strip couples to all perpendicular readout strips. The charge sharing between a floating strip and the corresponding parallel readout strip was found to be 6.8%, calculated from the capacitance between floating and parallel strip of $C_x^f = 2.1\,\text{pF}$. Note that the coupling between a floating strip and its neighboring parallel readout strips has been neglected as the capacitance is much smaller compared to the congruent readout strip. Furthermore the charge sharing between the floating strips as well as the readout strips within the same layer has also been neglected as it only shifts the charge distribution on the respective strip layer but does not affect the total coupled signal fraction to the parallel readout strip layer.

The results of the currents on perpendicular and parallel readout strips, split into the different components of directly induced and capacitively coupled signals, is shown in Figure 4.18 (left) and Figure 4.19 (left). The total coupled charge is found to be around 6.4% and 8.7% of the total created charge in the amplification region, respectively, visible in the statistics box of the right figures. The shape of the curves is briefly explained. Note that total charge is defined as the integral over all 2.5k current signals from the avalanches. Due to the directly induced unipolar negative currents on the floating strips, the total charge converges to the maximum in around 300 ns, which corresponds to the maximum ion drift time in the amplification region. Thus the charge on the parallel readout strips follows the charge on the floating strips as the signal is dominantly capacitively coupled from the floating strips. For the perpendicular readout strip, however, the capacitively coupled signal is negligibly small and thus the induced bipolar current leads to a maximum total charge peaking at around

115 ns. The total charge does not converge to zero due avalanches located at the edges of floating strips, leading to ions also drifting towards the PCB, as discussed in the previous section.

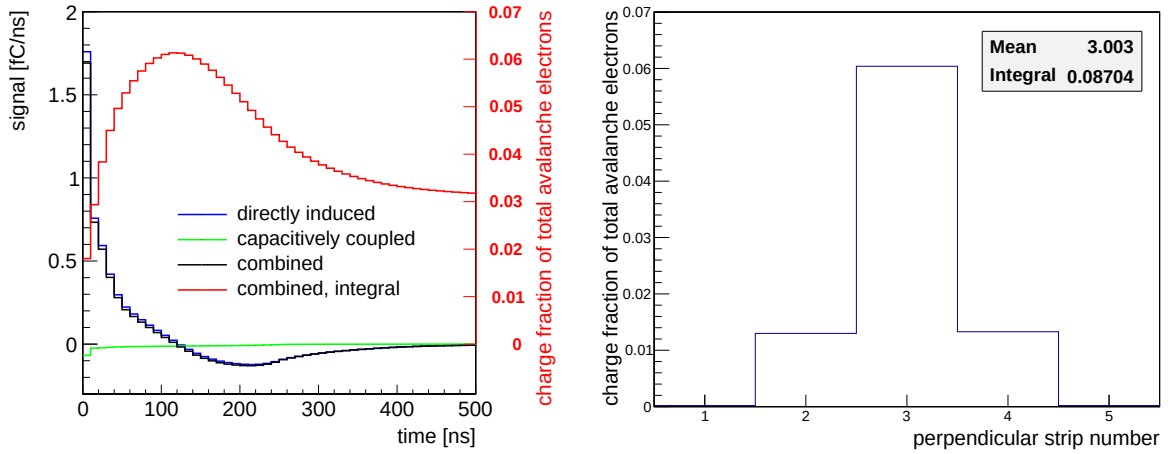

Figure 4.18: Left: Current on the central perpendicular strip as a function of time. The contributions from directly induced signal and capacitively coupled floating strip signal are shown. The integral current normalized by the total number of created electrons has been superimposed with a different scale. Right: Maximum of total coupled charge fraction as a function of the strip number.

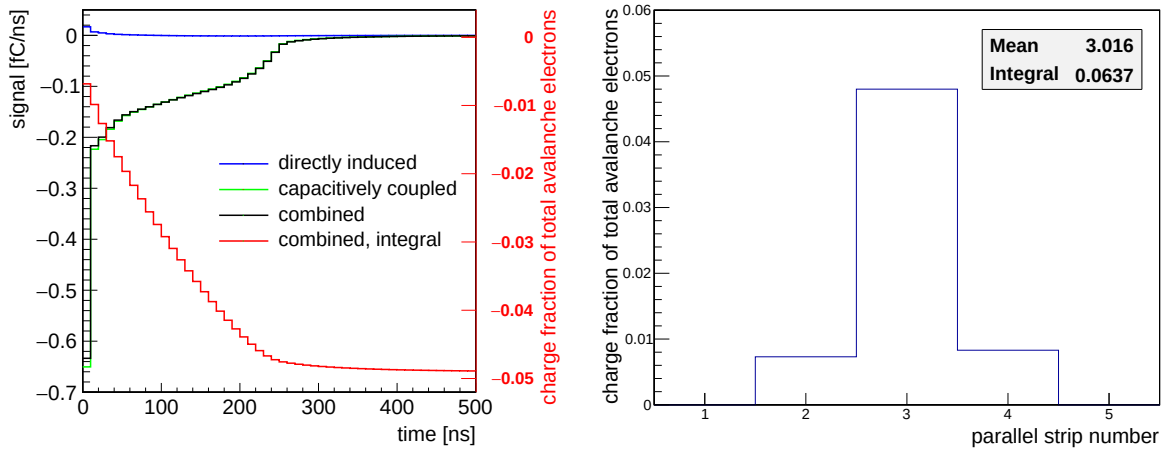

Figure 4.19: Left: Current on the central parallel strip as a function of time. The contributions from directly induced signal and capacitively coupled floating strip signal are shown. The integral current normalized by the total number of created electrons has been superimposed with a different scale. Right: Maximum of total coupled charge fraction as a function of the strip number .

However, a coupling strength to the readout strips below 10% of the total charge created in the amplification process is rather small. Thus, one aims in the ideal case to improve the charge coupling to both readout strip layers. The small signal on the parallel readout strip layer can be understood, as it is a result of the small capacitive coupling strength to the floating strips. The coupling strength is small due to the large capacitance created between the floating strip and all perpendicular readout strips. As already mentioned in the

previous section, the total capacitance of the floating strip can be reduced by adjusting the perpendicular strip width. Consequently, the capacitance between floating and parallel strips will be increased at the same time, which considerably increases the coupling strength to the parallel strip, as can be seen in Figure 4.16. However, by reducing the perpendicular strip width, the directly induced signal on it will be smaller as we have discussed in section 4.3. Thus, to increase the signal on both readout strip layers at the same time, a non-uniform perpendicular strip width has to be used to minimize the capacitance to the floating strips and parallel strips on the one hand while maximizing the directly induced currents due to charge carrier movement in the amplification region on the other hand. Based on these ideas, novel two-dimensional floating strip Micromegas anode designs have been developed with different perpendicular strip patterns to increase the signal amplitude on both readout strip layers. Their layouts are described in detail in chapter 5.

4.6 Response of Charge Sensitive Readout Electronics

In the last sections we have discussed the signal formation in the detector by induction of currents due to moving charges in the amplification region and by the capacitive coupling of currents on the floating strips onto the readout strips. In this section, we are focusing on the response of charge sensitive readout electronics to these signals, for the particular example of the APV25 ASIC (see section 3.2). Each channel of the APV25 features a charge sensitive pre-amplifier followed by a CR-RC type shaping amplifier [French et al., 2001]. Figure 4.20 shows the simplified electronic circuit including transfer function of such a linear amplifying and shaping network.

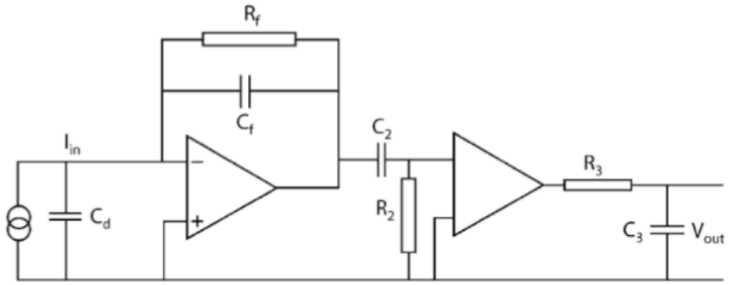

Charge-integrating amplifier with *CR–RC* shaping

$$\begin{cases} \hat{h}(t) = -\dfrac{1}{\tau(\tau_f - \tau)^2}\left[(\tau^2 + t(\tau_f - \tau))\, e^{-t/\tau} - \tau^2 e^{-t/t_f}\right] & t \geq 0 \\ \hat{h}(t) = 0 & t < 0 \end{cases}$$

$$\tau = C_2 R_2 = C_3 R_3 \text{ and } \tau << \tau_f = C_f R_f \qquad \hat{h}(t) \approx \frac{t}{\tau\,\tau_f} e^{-t/\tau}$$

Figure 4.20: Circuit of a typical charge sensitive amplifier with pre-amplifier and CR-RC shaping network including transfer function of the system. Figure courtesy of Gatti [2018].

The first stage is a charge pre-amplifier with a feedback capacitor C_f and resistor R_f, which integrates the current pulse I_{in} from the detector and converts it into a voltage signal. The falling edge of the voltage signal is characterized by the time constant $\tau_f = C_f \cdot R_f$ which is typically large compared to the duration of the detector current pulse to collect all charge created in the detector. The pre-amplifier is followed by a CR-RC linear amplifying and shaping stage, which transforms the voltage step into a voltage pulse with well defined amplitude and timing. The pulse is mainly characterized by the time constant of the CR-RC

network given by $\tau_p = C_2 \cdot R_2 = C_3 \cdot R_3$, which is much smaller than the integration time constant τ_f of the pre-amplifier feedback loop. In the example of the APV25 front-end chip, a time constant i.e. a peaking time of $\tau_p = 50\,\text{ns}$ has been chosen. As $\tau_f \gg \tau_p$, the transfer function of the linear amplifying and shaping stages can be approximated as

$$h(t) \approx \frac{t}{\tau_f \tau_p} \mathrm{e}^{-t/\tau_p} \quad . \tag{4.10}$$

The response $O(t)$ of this simplified circuit to a current signal $I_{\text{in}}(t)$ can be calculated by convoluting $I_{\text{in}}(t)$ with the transfer function, following [Blum et al., 2008]

$$O(t) = \int_{-\infty}^{+\infty} h(t-t') I_{\text{in}}(t') dt' \quad . \tag{4.11}$$

Assume the injected current signal to be a delta function like signal i.e. $I_{\text{in}}(t) = I_0 \delta(t)$ for $t \geq 0$ and $I_{\text{in}}(t) = 0$ for $t < 0$, the response simplifies to

$$O(t) = \int_{0}^{t} h(t-t') I_0 \delta(t') dt' \tag{4.12}$$

which reflects the shape of the transfer function and is called the delta response of the system, which is shown in Figure 4.21. It is compared to a direct measurement with an APV25 hybrid board, when internally injecting a delta like test pulse into a specific channel of the APV25 chip. The good agreement with the simplified transfer function defined in equation 4.10 and the measured digitized delta response of the APV25 chip is visible.

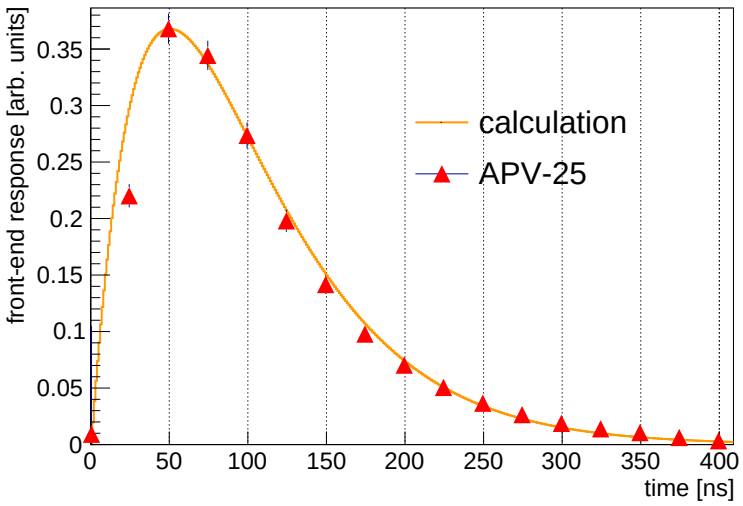

Figure 4.21: Calculated response of the charge-integrating amplifier followed by the CR-RC shaper shown in Figure 4.20 (orange) when assuming a shaping time constant of τ=50 ns and injecting a 1 ns delta pulse into the network. Measured response after digitization of the APV25 front-end chip (red data points, see section 3.2) when applying an internal generated test pulse to a specific channel. The two curves have been scaled to the same maximum.

To calculate the electronics response to the detector signals, the induced currents on the strips of the two-dimensional floating strip anode found with the Garfield++ simulation in Figure 4.9 can be convoluted with the transfer function defined in equation 4.10. The response

for the signals on one floating and perpendicular readout strip is shown in Figure 4.22. Note that the directly induced signal (i.e. neglecting capacitive coupling) on the parallel readout strips is suppressed by two orders of magnitude compared to the perpendicular readout strips, thus, its electronics response is not shown here.

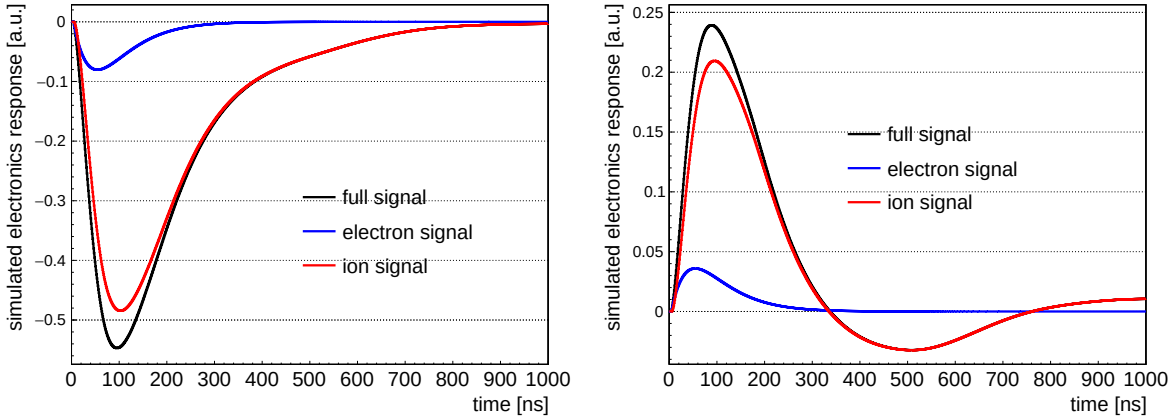

(a) floating strip

(b) perpendicular strip

Figure 4.22: Simulated response of the linear amplifying and shaping network from Figure 4.20 when feeding the induced currents (see Figure 4.9) on the floating strip (left) and perpendicular strip (right) into the network.

The electron (blue) and ion (red) component of the signals are also shown. As the much faster electron signal is finished in a few nano seconds, the output is basically the delta response transfer function of the system peaking at around 50 ns after the avalanche has finished. The much slower ion component, being responsible for most of the signal amplitude, takes around 300 ns and prolongates the peaking time to around 100 ns. The bipolar shape of the induced current on the perpendicular strip, as discussed above, is also visible in the electronics response. On the floating strip however, the completely negative induced current by the ions only generates a longer tail to the unipolar negative pulse. Note that this is the electronics response for only one avalanche centered above one floating strip. In reality, 20 to 70 electrons will be created by a MIP traversing the drift region of the Micromegas resulting in avalanches arriving at different points in time on the anode strips. Thus the final shape of the electronics response will look differently, as also finite front-end input impedance and strip capacitance has to be taken into account, which will be explained in detail in the following.

Assume a cosmic muon with a momentum of 2 GeV traverses a two-dimensional floating strip Micromegas with an active area of 6.4 x 6.4 cm^2 and a strip pitch of 0.5 mm on the anode, resulting in a total of 128 strips on each layer. The drift gap, defined by the cathode and a planar micro-mesh, has a width of 6 mm and is filled with a Ne:CF_4 80:20 vol.% gas. The amplification gap between micro-mesh and anode strips has a width of 0.128 mm. Cathode, mesh and anode strips have been set to -200V, 0V and 580 V, respectively. An event display of drift electrons released from a 2 GeV muon perpendicularly traversing the 6 mm drift gap of the detector can be seen in Figure 4.23 (left), simulated with Garfield++. For this particular event, the muon creates a total of 14 electron/ion-pairs along its path in the drift region. Note that for this simulation with the Neon based detector gas Penning transfer was not included. This on the one hand means that the total charge created either in the drift region by the ionization process of the muon or the avalanches taking place in the amplification region are underestimated. But on the other hand, both processes are of pure statistical nature. Thus, as we are explicitly only looking at one particular particle event in the detector, the

consequences of the Penning transfer play a minor role. Due to the applied electric field of 200 V/6 mm≈0.33 kV/cm, the electron/ion-pairs are separated and the electrons drift towards the micro-mesh plane (orange lines in Figure 4.23, left). Due to transverse diffusion of the electrons in the gas, the electron cloud spreads up to about ±0.3 mm at the end of the drift region. All electrons are transferred into to the amplification region, where the avalanches are simulated, i.e. a mesh-transparency of 100% is assumed in this case. The electron end points on the floating strips after finished gas amplification are visible in Figure 4.23 (right).

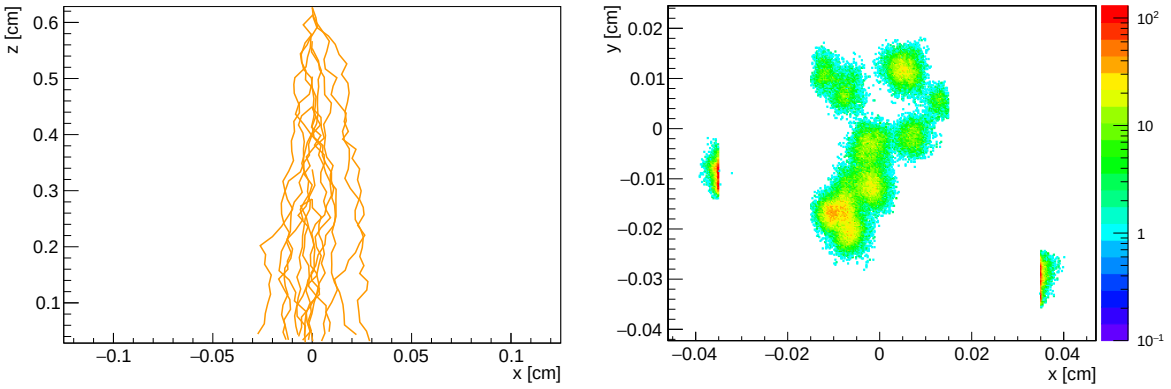

Figure 4.23: Left: Simulated electron drift lines of the ionization electrons (orange) created by a perpendicularly incident 2 GeV muon traversing the 6 mm width drift gap of the Micromegas detector filled with a Ne:CF_4 80:20 vol.% gas mixture. Right: Resulting avalanche electron end points on the anode. Drift and amplification voltage have been set to a typical working point for MIPs at -200V and 580 V, respectively.

The macroscopic circular structures of each electron avalanche with a diameter of around 100 µm on the surface of the floating strips are visible. In the complete amplification process, a total of 72000 electrons has been created, which corresponds to a mean gas gain of 5200. The currents created on the readout strips, defined by the sum of capacitively coupled signal from the floating strips and directly induced currents by the movement of the charges in the amplification region, are shown in Figure 4.24. Note that the time $t = 0$ corresponds to the first electron reaching the amplification region i.e. the beginning of the first avalanche.

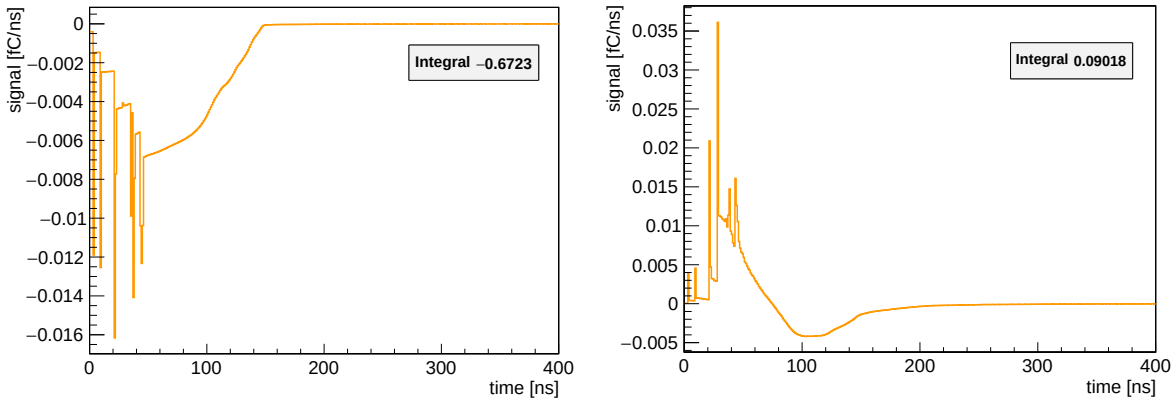

(a) parallel strip (b) perpendicular strip

Figure 4.24: Induced current as a function of time on both central readout strips for the signal created by the muon shown in Figure 4.23. The signal from capacitive coupling between the electrodes is incorporated.

The spikes in the current signals are due to the arrival of individual ionization electrons in the amplification region creating avalanches. The slower drifting ions create a constant negative current background on the parallel strip and the expected bipolar current on the perpendicular strip. As a Ne:CF_4 80:20 vol.% gas mixture has been used in this simulation, the ion mobility is around a factor of two higher than in Argon based gas mixtures. This reduces the current signal duration to around 150 ns. Integrating the current gives the total charge on the two strips of -0.67 fC on the parallel strip and 0.09 fC for the perpendicular strip. However, we need to disentangle the positive and negative part of the current signal on the perpendicular readout strip, as the used charge sensitive front-end electronics typically have small pulse shaping peaking times, like $\tau_p = 50$ ns of the APV25 readout chip. Thus by integrating only over the positive current on the perpendicular strip up to $t \approx 75$ ns, we find a total positive charge of 0.374 fC and -0.42 fC for the parallel strip. Both charges are comparable. We consequently conclude that the used readout electronics may significantly diminish the signal pulse height on the perpendicular strip layer if peaking times are chosen too long.

Now lets assume that each readout strip is connected to a linear amplifying and shaping network as was introduced before in the example of the APV25 front-end chip and is shown in Figure 4.20. Typically, charge sensitive pre-amplifiers feature low impedance inputs to the network, to allow almost the complete charge to flow into the front-end electronics. Thus in the ideal case of zero impedance electronics and detector strip capacitance, the total created charge on the strip can completely flow off the readout strip and be detected. However, in reality, the detector strip capacitance and the finite front-end electronics impedance lead to an unavoidable loss of the signal. In the following, we will estimate the ratio between the signal on the readout strip and the signal detected by the electronics, if we have a detector strip capacitance $C_{\mathrm{det}} \neq 0$ and front-end electronics input impedance $Z_{\mathrm{in}} \neq 0$. Consider the simplified electronic circuit as illustrated in Figure 4.25.

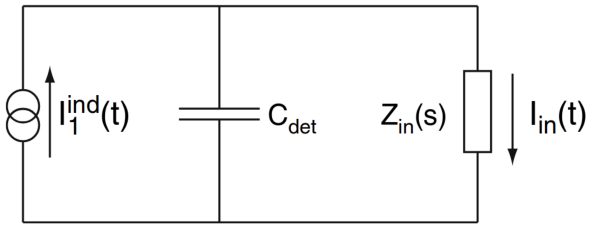

Figure 4.25: Input circuit and equivalent block diagram for a readout strip with capacitance C_{det} connected to an amplification network with impedance Z_{in}. The current signal $I_1^{\mathrm{ind}}(t)$ coupled to the readout strip is divided between the strip capacitance and the input impedance of the electronics. Figure taken from [Blum et al., 2008].

A strip is typically directly connected to the amplifier input and the induced current is thus divided between the input impedance and the detector strip capacitance [Blum et al., 2008]. To simplify the following calculations, we switch from the time domain into the Laplace domain, relieving us of solving a set of coupled differential equations in the time domain but only a set of linear algebraic equations in the Laplace domain. The induced current on a detector strip $I_{\mathrm{ind}}(t)$ is transformed into $I_{\mathrm{ind}}(s)$, following the bilateral Laplace transform

$$\mathcal{L}(I_{\mathrm{ind}}(t)) = I_{\mathrm{ind}}(s) = \int_{-\infty}^{+\infty} I_{\mathrm{ind}}(t) e^{-st} dt \quad , \tag{4.13}$$

where $s = \sigma + i\omega$ is in general a complex number with real and imaginary part σ and ω,

respectively [Blum et al., 2008]. As $I_{\mathrm{ind}}(s)$ has no direct physical meaning, we set $\sigma = 0$ and find that $s = i\omega$ represents the Fourier transform of the current signal with $\omega = 2\pi f$. In the Laplace domain, i.e. the frequency domain, it follows from the block diagram in Figure 4.25, that the amplifier input current $I_{\mathrm{in}}(s)$ into the front-end electronics is given by

$$I_{\mathrm{in}}(s) = \frac{1}{1 + s\tau_1} I_{\mathrm{ind}}(s) \qquad \tau_1 = R_{\mathrm{in}} C_{\mathrm{det}} \quad , \tag{4.14}$$

which is equivalent to a transfer function of an RC integration stage [Blum et al., 2008]. The current $\mathrm{I_{in}(s)}$ is then processed by the readout electronics chain shown in Figure 4.20. The voltage output signal $\mathrm{V_{out}}$ is given by the multiplication of the transfer function found in Equation 4.14 with the transfer function in Equation 4.10 from the pre-amplifier and shaping network Laplace transformed into the frequency domain, following

$$V_{\mathrm{out}}(s) = \frac{1}{1 + s\tau_1} \frac{A}{\tau_f \tau_p (s + 1/\tau_p)^2} I_{\mathrm{ind}}(s) = \tilde{h}_{\mathrm{tot}}(s)\, I_{\mathrm{ind}}(s) \tag{4.15}$$

where

$$\mathcal{L}[\tilde{h}(t)] = \tilde{h}(s) = \frac{A}{\tau_f \tau_p (s + 1/\tau_p)^2} \quad \text{with} \quad \tilde{h}(t) = \frac{A\, t}{\tau_f \tau_p} e^{(-t/\tau_p)} \tag{4.16}$$

and A is the total gain of the analogue chain, τ_f is the integration time constant of the pre-amplifier and τ_p the time constant of the CR-RC shaping network. Note that $\tilde{h}(t) = 0$ for $t < 0$, which reduces the bilateral to an unilateral Laplace transform with the lower integration bound $t = 0$.

Inverting the Laplace-transformation on the transfer function found in Equation 4.15 yields the delta response transfer function in the time domain $\tilde{h}_{\mathrm{tot}}(t)$ with

$$\begin{aligned} \tilde{h}_{\mathrm{tot}}(t) &= \mathcal{L}^{-1}[\tilde{h}_{\mathrm{tot}}(s)] \\ &= \mathcal{L}^{-1}\Big[\frac{1}{1 + s\tau_1} \frac{A}{\tau_f \tau_p (s + 1/\tau_p)^2}\Big] \\ &= \frac{A\,\tau_1}{\tau_f \tau_p} \frac{e^{-t/\tau_1} - e^{-t/\tau_p}}{(\tau_1/\tau_p - 1)^2} + \frac{A\, t}{\tau_f \tau_p} \frac{e^{-t/\tau_p}}{1 - \tau_1/\tau_p} \\ &= \frac{A}{\tau_f \tau_p} \Big(\tau_1 \frac{e^{-t/\tau_1} - e^{-t/\tau_p}}{(\tau_1/\tau_p - 1)^2} + t \frac{e^{-t/\tau_p}}{1 - \tau_1/\tau_p}\Big) \quad , \end{aligned} \tag{4.17}$$

which in turn can be used to calculate the electronics readout chain response via convolution of the induced current found with the Garfield++ simulation in Figure 4.24. Remember that the input impedance and strip capacitance enter the equation by $\tau_1 = R \cdot C$ where $R = \mathrm{Re}(Z_{\mathrm{in}})$ and $C = C_{\mathrm{det}} = C_{\mathrm{strip}}$, respectively. The maximum of the front-end response as a function of the front-end input impedance i.e. resistance and the detector strip capacitance is shown in Figure 4.26, normalized to the maximum expected pulse height at $C_{\mathrm{det}} = 0$ and $Z_{\mathrm{in}} = 0$.

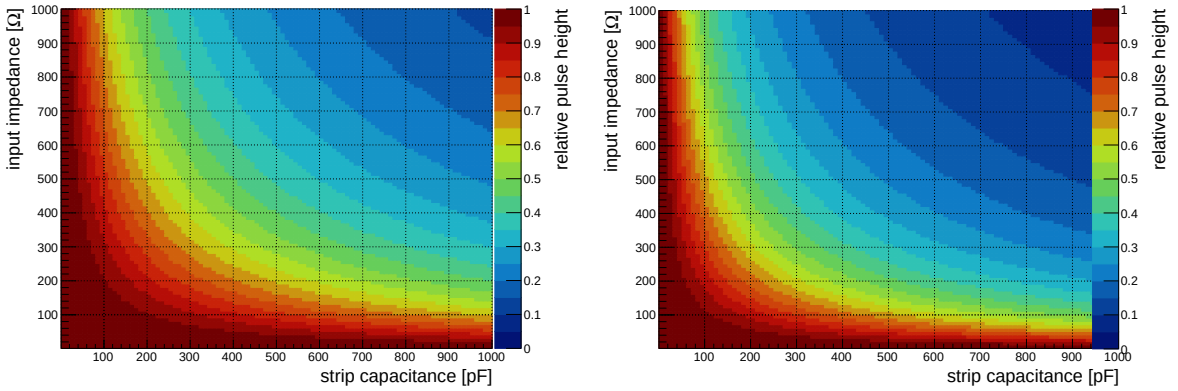

(a) parallel strip (b) perpendicular strip

Figure 4.26: Calculated relative strip pulse height of the current shown in Figure 4.24 after the analogue signal processing chain as a function of the input impedance of the front-end electronics and detector strip capacitance.

We find that the initially induced signal pulse height is mostly maintained if either the input impedance of the electronics or the strip capacitance is kept small. Specifically this means that the signal pulse height is independent of the strip capacitance up to 1 nF if a front-end input impedance is chosen with a resistance smaller than 50 Ω. On the other hand, small strip capacitances below 50 pF do not influence the signal pulse height with input impedances up to 1 kΩ. At the particular example of the APV25 front-end hybrid board, which was used for all measurements presented in the later chapters, the input impedance has been measured with a precision LCR meter from GW INSTEK [2018]. The hybrid has been configured through a DAQ computer in the same way as it has been used for measurements when mounted on a detector. The LCR meter has been connected to one strip of the hybrid input channels on the Panasonic 130 pin connector and a frequency sweep between 0.1 and 10 MHz with a sinusoidal pulse of 100 mV has been performed. The measured impedance Z with the resistance $R = \mathrm{Re}(Z)$ as a function of the input frequency is shown in Figure 4.27.

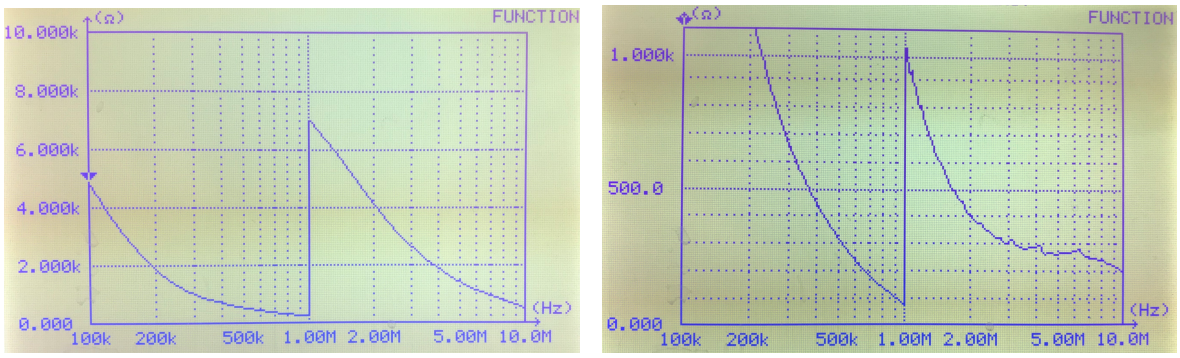

(a) impedance (b) resistance

Figure 4.27: Measured input impedance (left) and input resistance (right) as a function of the input pulse frequency [GW INSTEK, 2018] for a typical charge integrating front-end chip, here: a powered and configured APV25 hybrid board (see section 3.2).

The dependence of the impedance on the input frequency of the pulse is clearly visible. For frequencies below 1 MHz the effective resistance increases considerably. Consequently, the circuit is working like a high pass filter, which is desirable to suppress low frequent electronic noise. No satisfying explanation was found for the resonance effect observed at

1 MHz. However, the input signals created on both readout strips have a duration of around 150 ns (see Figure 4.24) i.e. a frequency around 5-6 MHz. Thus the effective input resistance to the APV25 amplifying and shaping network is around 300 Ω. The relative pulse height of the parallel and perpendicular strip as a function of the strip capacitance after convolution with the transfer function evaluated at $R = 300\,\Omega$ is shown in Figure 4.28.

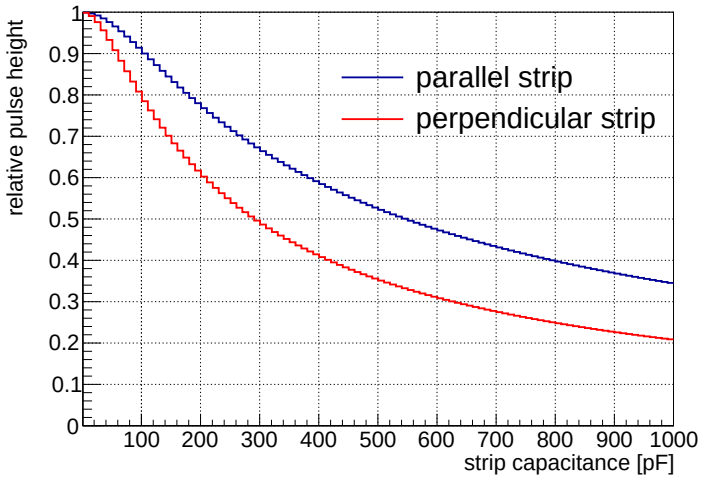

Figure 4.28: Relative pulse height for both strip layers as a function of the strip capacitance assuming R = 300 Ω input resistance to the amplifier network.

As we clearly see the measured pulse height on the APV is strongly depending on the strip capacitance and can lead to a reduction of about 80% on the perpendicular strips if the strip capacitance is increased to 1 nF. However, the strip capacitances for the 6.4 cm long readout strips are well below 100 pF, which would lead to a maximum pulse height reduction of about 20% on the perpendicular strip. However, a stronger capacitance dependence is observed for the perpendicular strip than for the parallel strip. It can be explained by an increase of the rise-time of the signal and as a consequence an increase of the effective peaking time of the front-end circuit if the strip capacitance is increased. This leads to a stronger signal loss on the perpendicular strips due to the bipolar shape of the current.

The values for the strip capacitances found in section 4.4 and the measured input impedance of the APV25 allow to calculate the response of the front-end chip to the signal created by the 2 GeV muon transversing the two-dimensional floating strip Micromegas detector. The results are shown in Figure 4.29 for the central parallel and perpendicular readout strip currents. Capacitances of 28 pF for the parallel and 49 pF for the perpendicular readout strips have been used, leading to a pulse height reduction of 1% and 8%, respectively.

The simulated response of the APV25 very well matches the measured signals on both readout strip layers in terms of signal shape and duration, as can be seen in Figure 3.6 for typical signals measured from a cosmic muon on both strip layers of a two-dimensional floating strip Micromegas detector. It confirms the validity of the detector simulation described in this chapter. However, the absolute signal pulse height strongly depends on the chosen anode PCB strip geometry and thus the capacitive coupling between the strip layers, which is the dominant effect for the signal generation on the parallel strips. For the optimization of the perpendicular strip pulse height, variations of the floating strip width need to be taken into account.

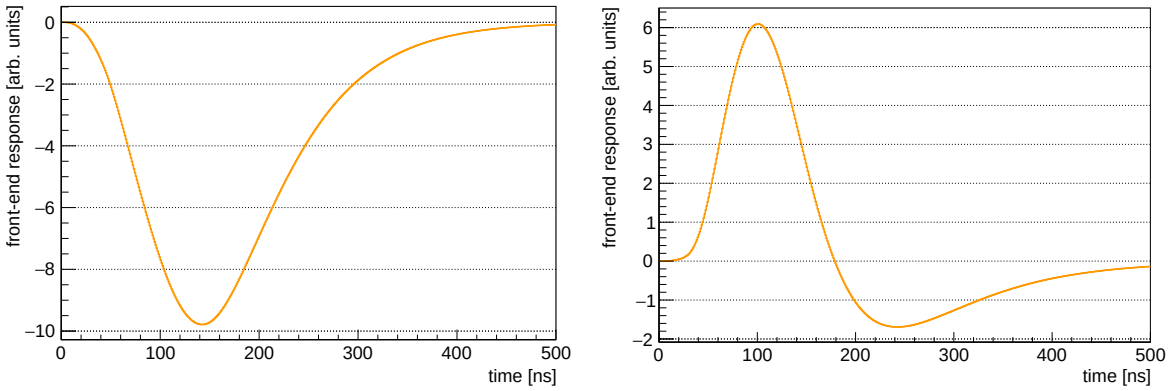

(a) parallel strip

(b) perpendicular strip

Figure 4.29: Simulated front-end response on the central parallel and central perpendicular readout strip when convoluting the current signals shown in Figure 4.24 with the delta response transfer function found in equation 4.17. An input impedance of 300 Ohm for the front-end electronics and a capacitance of 28 pF for the parallel and 49 pF for the perpendicular strip has been assumed, respectively.

Chapter 5

Newly Developed and Optimized Two-Dimensional Floating Strip Anode Structures

In this chapter, the newly developed and investigated two-dimensional floating strip Micromegas anode PCBs are introduced. The strip layer setup of each anode PCB and the ideas behind the chosen geometries are described, mostly based on the simulation results presented in the previous chapter. As for pulse height optimization reasons on both layers, a non-uniform perpendicular readout strip width is necessary, an estimation how the stripline geometry might influence the signal transmission on the strip is presented. Two different detector sizes have been developed during this thesis: A 6.4 x 6.4 cm^2 active area detector with 128 strips and a 19.2 x 19.2 cm^2 active area detector with 384 strips. The difference between the two geometries is not only the size of the active area but mainly the material budget of the full detector. The smaller detector with a stiff base plate of standard FR4 material with 1.6 mm thickness was used for R&D studies. The larger detector is a proof of principle to show that a detector with almost $20 \times 20\,cm^2$ active area can also be built with a very low material budget to minimize the impact due to multiple Coulomb scattering. Due to the larger active area and an anode PCB thickness of only around 0.1 mm, the PCB needed stabilization with a Nomex honeycomb structure glued to the bottom side of the PCB. An estimation of the full material budget and the influence of the support structure on the total material budget of the detector is shown in the last section. Additionally, possible improvements of the already thin anode are given to reduce multiple Coulomb scattering in the heavy Z materials of the detector.

5.1 Anode PCB Strip Line Configurations

Seven different two-dimensional floating strip Micromegas anode structures have been investigated. The first prototype[1] was investigated in proton and carbon ion beams and showed clearly that the position information of the particles could be reconstructed in both dimensions [Bortfeldt et al., 2017]. It features three layers of 128 strips at a pitch of 0.5 mm with 0.3 mm wide floating strips. The strip geometry of this anode structure, from now on refered to as 'design 1', is shown in Figure 5.1, (a). Note that the three 35 µm high copper strip layers are separated by two 25 µm thin insulation layers, made from Kapton flex material. Due to the manufacturing process, a single layer of 40 µm adhesive is necessary for the three

[1] designed by Jonathan Bortfeldt

flex PCB layer stack. It has been placed between the floating strip layer and the readout strip layer below the floating strips for this and for all anode structures described in the following. The total thickness of the PCBs was measured at different points which showed that the layer of glue has a negligible contribution to the total thickness of the PCB. Thus, the total thickness is given by the sum of the three copper layers plus the two insulating Kapton layers, 3 x 35 µm + 2 x 25 µm = 155 µm. However characterization measurements in [Klitzner, 2016] showed that the pulse height on both readout strip layers of anode design 1 was highly asymmetric, which left room for optimization.

Two new anode structures have been developed, similar to design 1, which are sketched in Figure 5.1, (b) and (c). The main difference is that the active area has been increased from 6.4 x 6.4 cm^2 to 19.2 x 19.2 cm^2, with a total of 384 strips per layer at the same pitch of 0.5 mm. While the floating strip geometry was untouched, the parallel strip width beneath the floating strip was increased from 0.08 mm to 0.3 mm in design 2. In design 3, the two readout strip layers have been interchanged and the width of the parallel strip was increased to 0.4 mm. Characterization measurements with an ^{55}Fe source and 20 MeV protons showed that similar pulse heights can be reached on both readout strip layers if the perpendicular readout strip is placed between the floating and parallel readout strip. This shields the strong capacitive coupling between the two congruent striplines [Klitzner et al., 2017]. However, by only shielding parts of the floating strip signal from the parallel strip with the perpendicular strip layer, huge capacitances were created in the detector and in general small pulse heights were observed on both readout strip layers, even if the pulse height ratio between perpendicular and parallel strips was close to 1.

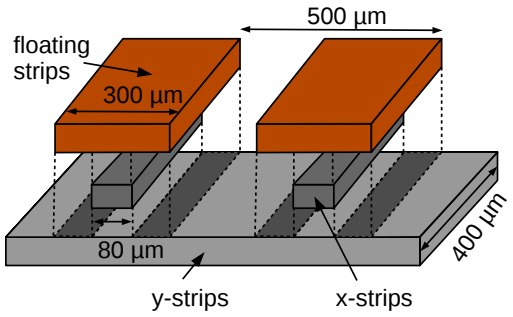

(a) design 1

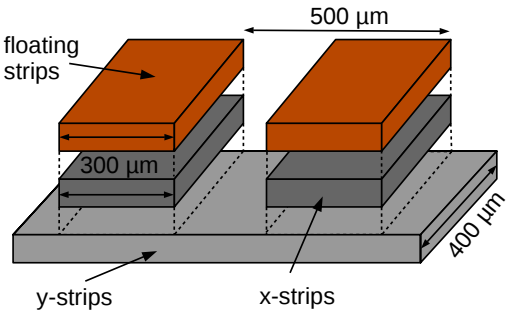

(b) design 2

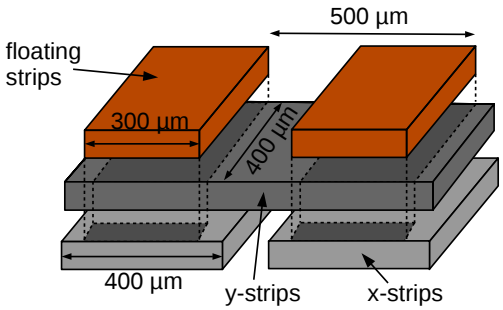

(c) design 3

Figure 5.1: Figures a.) to c.) show the strip line configurations of the first investigated two-dimensional floating strip anode layouts. Design 1 has already been investigated in [Bortfeldt et al., 2017] and [Klitzner, 2016] .

Consequently due to the needs of pulse height improvement based on the knowledge gained from the measurement results with anode design 1 - 3, a detailed detector simulation described

in the previous chapter was set up. It allowed to understand the signal generation in the detector and the coupling of the signals to both readout strip layers. Thus, new optimized anode structures have been developed to increase the pulse height on both readout strip layers simultaneously. To be independent of pulse height fluctuations during the measurements caused by deformations of the very thin anode PCB, the 0.155 mm three strip layer geometry of the new designs has been produced on a standard FR4 PCB, resulting in a total thickness of around 1.6 mm.

The simulation described in the previous chapter shows that the perpendicular strip pulse height depends on the distance to the amplification region, as the signal is directly induced from the movement of the charges in the amplification process. Thus, for all new designs, the perpendicular strip has been placed directly below the floating strips to maximize the signal yield. Furthermore, reducing the floating strip width while leaving the pitch constant, increases the yield as well. Thus, designs 4 - 6 feature a floating strip width of 0.15 mm at a pitch of 0.5 mm. To reduce the coupling between the floating strips and the perpendicular readout strips as the induced signals are of opposite polarity, the perpendicular strip width below the floating strip is reduced for all following designs. This reduces the capacitances of all strips in the detector considerably, which also increases the pulse height on both readout strip layers, due to the finite front-end electronics input impedance, as shown in section 4.6. As the signal on the perpendicular y-strip is dominantly induced by charge carrier movement between two floating strips, the y-strip width needs to be as large as possible between the floating strips. Due to a minimum required copper line distance of 0.1 mm as stated by the PCB manufacturer[2], the perpendicular strips have a width of 0.4 mm between the floating strips for design 4 - 6. As can be seen in the geometry of the strip layers in fig.5.2, the shape of the perpendicular strips differ between design 4 - 6.

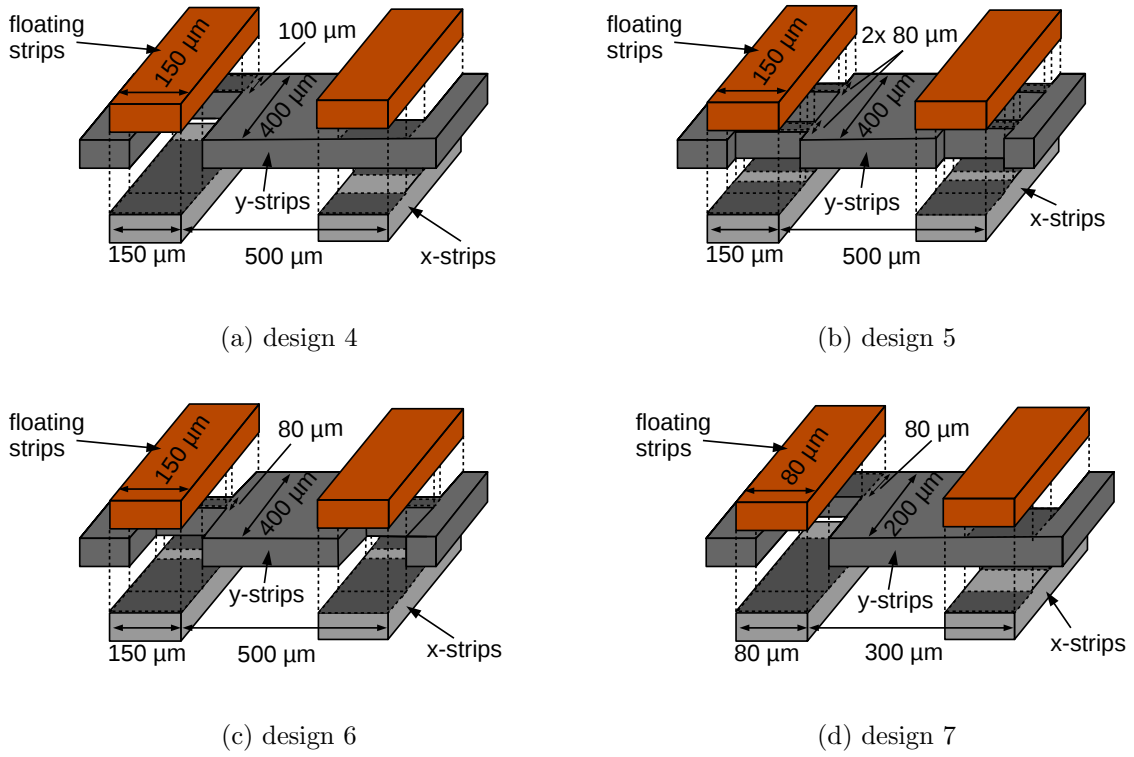

(a) design 4

(b) design 5

(c) design 6

(d) design 7

Figure 5.2: Figures a.) to d.) show the strip line configurations of optimized two-dimensional floating strip anodes, based on characterization measurements (see chapter 6) with the designs shown in Figure 5.1 and simulations shown in chapter 4 and the following section 5.2.

[2]Multi Circuit Boards Ltd., 2018, `https://www.multi-circuit-boards.eu`

The different patterns on the perpendicular y-strips are motivated by signal transmission in fast signal circuits, where a change of impedance on a stripline may cause signal loss due to reflection or resonance effects. An estimation on the impact of such effects is given in the next section. Additionally, the width of the perpendicular strip below the floating strips was set to three different values, to modulate the capacitive coupling strength between the floating strip and the congruent readout strip. This allowed to compare the measured pulse height with the simulation and thus to improve the detector simulation described in the previous chapter. The different perpendicular strip widths below the floating strip are 100 µm, 2 x 80 µm and 80 µm for design 4, 5 and 6, respectively.

To investigate, whether it is possible to decrease the strip pitch of the floating anode strips without decreasing the pulse height on either of the two readout strip layers, anode design 7 has been developed. The strip pitch in all layers has been reduced from 0.5 mm to 0.3 mm. As this allows a maximum perpendicular strip width of only 0.2 mm between the floating strips, the pulse height on the perpendicular strip will be significantly reduced, as predicted by simulation. To compensate this undesired effect, the floating strip width has also been reduced from 0.15 mm to 0.08 mm, which was the smallest manufacturable copper line width. Thus, the ratio between floating strip width and pitch of $0.08/0.3 \approx 0.27$ is even smaller than for the other designs 4 - 6 with $0.15/0.5 = 0.3$, which is favorable for the pulse height on the perpendicular strip. The pattern of the perpendicular strip was chosen to be similar to the meander-like pattern of design 4, as it was found to be the best working anode from measurements with high energy particles at CERN (see chapter 8). The width of the perpendicular strip below the floating strip was reduced from 0.1 mm to 0.08 mm to account for the smaller floating strip width and thus maintain the capacitive coupling strength between floating and parallel readout strip . However calculating the most important capacitances in a detector equipped with design 7 showed that the capacitive coupling between floating and parallel strip was still smaller than for design 4 - 6. To further increase it, the parallel readout strips were extended out of the active area of the detector, following the floating strips.

Comparison between the signals measured with APV25 front-end boards attached to both readout strip layers of the previously discussed anode structures is presented in the next chapter.

5.2 Discussion of Resonance Effects and Signal Reflection on Striplines with Alternating Patterns

Due to different signal coupling to the two readout strip layers (see simulation chapter 4) the shape of the perpendicular strip line needs to be adjusted for maximum pulse height on both readout layers. The different investigated strip shapes are shown in Figure 5.2. Changing the shape of a strip directly influences its capacitance and inductance. Thus, to assure that the current signals induced on the readout strip layers − when a particle traverses the detector − are able to flow off the readout strip into the front-end electronics, the change in capacitance or inductance and therefore impedance is worth investigating. However, measurements presented in the later chapters show that the signal generated in the detector on the perpendicular readout strip is not dependent on the shape of the pattern itself. Thus impedance difference related effects such as resonance and signal reflection on a stripline with an alternating pattern do not play a significant role for the signals generated in the detectors investigated in this thesis.

Nevertheless, assume the stripline configuration of the perpendicular strip to be like anode design 4. Then the different strip parts can be interpreted as an inductive (1) and capacitive (2) part, see Figure 5.3.

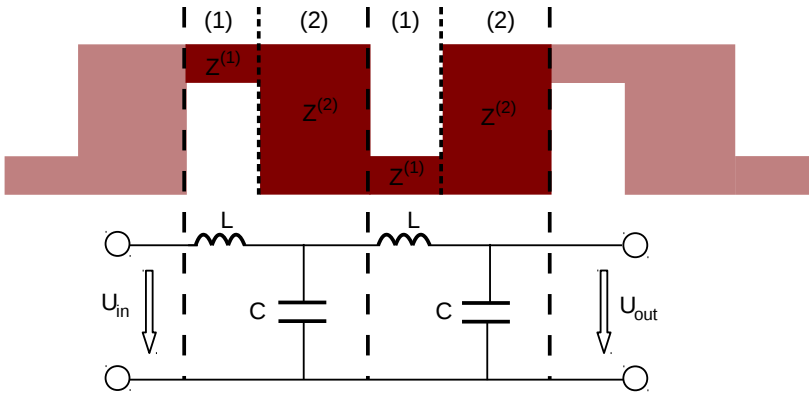

Figure 5.3: Sketch of the perpendicular strip pattern of anode design 4 and the equivalent electric circuit.

For this particular example, the thin strip part (1) below the floating strip will be approximated as the more inductive component. The strip part (2) between two floating strips will be approximated as the dominant capacitive component. For calculating the inductance of strip component (1), the wave impedance on the stripline has to be determined first:

$$L = Z_0^2 \cdot C \tag{5.1}$$

where L is the inductance, Z_0 the wave impedance and C the capacitance of the stripline. The wave impedance on asymmetric micro striplines can be approximated using [Nührmann, 2002]

$$Z_0 = \frac{75}{\sqrt{\epsilon_r}} \quad \ln\left(\frac{6 \cdot D}{0.75 \cdot b + d} + \frac{0.075 \cdot b}{D}\right) \tag{5.2}$$

where ϵ_r is the relative permittivity of the insulation material between the striplines, D the distance between two strip layers, d the strip thickness and b the strip width. Inserting the strip parameters for strip component (1) as defined in Figure 5.2 and Figure 5.3, the wave impedance is found to be

$$Z_0^{(1)} = \frac{75}{\sqrt{3.5}} \quad \ln\left(\frac{6 \cdot 25\mu\text{m}}{0.75 \cdot 100\mu\text{m} + 35\mu\text{m}} + \frac{0.075 \cdot 100\mu\text{m}}{25\mu\text{m}}\right) \approx 20\,\Omega \quad . \tag{5.3}$$

From the capacitances simulated in chapter 4 and shown in Figure 4.14, the strip capacitance with respect to the surrounding electrodes of the two stripline components are in the order of

$$C^{(1)} = 0.02\,\text{pF} \quad \text{and} \quad C^{(2)} = 0.04\,\text{pF} \quad , \tag{5.4}$$

using the approximation that the capacitance of (2) is mainly formed by the overlap with the micro-mesh, as it is always located between two floating strips. Following equation 5.1 the inductance of (1) is found to be

$$L^{(1)} = \left(Z_0^{(1)}\right)^2 \cdot C^{(1)} = (20\,\Omega)^2 \cdot 0.02\,\text{pF} = 8\,\text{pH} \quad . \tag{5.5}$$

Assuming the series connection of the inductance and capacitance as shown in Figure 5.3, the circuit can be seen as a series resonant circuit. Thus the resonance frequency f_0 can be calculated using

$$f_0 = \frac{1}{2\pi\sqrt{L\,C}} \tag{5.6}$$

with $L = L^{(1)}$ and $C = C^{(2)}$. Inserting the values yields a resonance frequency of

$$f_0 \approx \frac{1}{2\pi\sqrt{L^{(1)}\,C^{(2)}}} = 0.28\,\text{THz} \quad . \tag{5.7}$$

As the number of patterns on the perpendicular strips depends on the number of strips n_{strips} in the active area of the detector, this LC-circuit repeats n_{strips} times. To check what effect the series connection of two resonant circuit has on the resonance frequency of the combined system, assume the connection of two identical circuits as shown in fig.5.4.

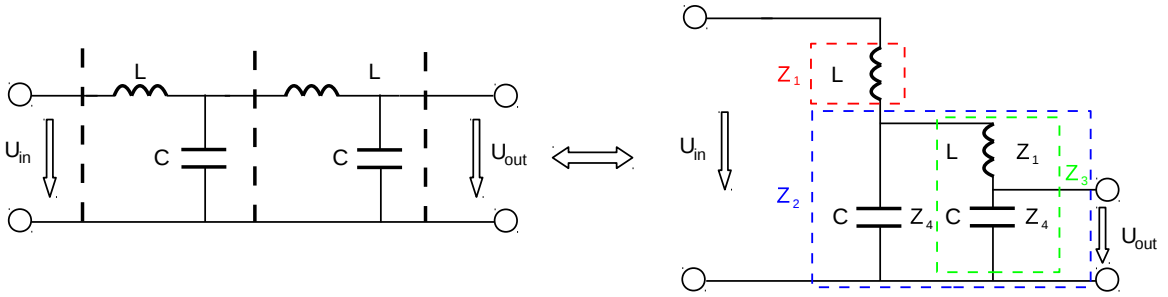

Figure 5.4: Electric circuit of anode design 4 for two consecutive strip patterns (left, see also Figure 5.3) re-arranged to visualize the similarity to a two-folded voltage divider (right).

The series connection of both resonant circuits can be treated like a two-folded voltage divider. Thus, the output voltage U_{out} is given by

$$\begin{aligned} U_{\text{out}} &= \frac{Z_2}{Z_1+Z_2}\,U_{\text{in}} \quad \text{with } Z_2 = \frac{Z_4 Z_3}{Z_4+Z_3} \text{ and } Z_3 = \frac{Z_4}{Z_1+Z_4} \\ &= \frac{1-\mathrm{i}\omega L}{(1+\omega^2L^2)(1-\omega^2LC)}\,U_{\text{in}} \quad \text{inserting } Z_1 = \mathrm{i}\omega L \text{ and } Z_4 = \frac{1}{\mathrm{i}\omega C} \quad , \end{aligned} \tag{5.8}$$

finding the same resonance frequency $\omega_0 = 1/\sqrt{LC} = 2\pi f_0$ as for the single pattern resonance frequency defined in eq. 5.6. From this directly follows that the number of patterns does not change the resonance frequency f_0 defined by $L = L^{(1)}$ and $C = C^{(2)}$ with $f_0 \approx 0.28\,\text{THz}$. As this frequency is almost five orders of magnitude different from a typical signal induced on the readout strip − which is in the order of 300 ns ⇔ 3.3 MHz − resonance related effects can be neglected. This has also been verified with measurements presented in the next chapters, as none of such effects have been observed.

However, if a signal propagates along a stripline and the impedance of the strip changes from $Z^{(1)}$ to $Z^{(2)}$, as indicated in Figure 5.3, signal reflections might occur. Following [Paul, 2007], the reflection ρ of an electro-magnetic wave on a transmission line can be calculated from

$$\rho = \frac{Z^{(1)} - Z^{(2)}}{Z^{(1)} + Z^{(2)}} = \frac{\Delta Z}{Z_{\text{total}}} \quad . \tag{5.9}$$

As reflection can occur on every impedance variation on the stripline i.e. at least 128 times in a detector consisting of 128 strips with the alternating pattern used in this particular example, one may try to minimize the signal reflection originating from the impedance differences. This has been realized in anode design 5. The pattern was adjusted with a very similar approach to minimize signal reflection on striplines used in fast signal circuits. The idea is sketched in Figure 5.5

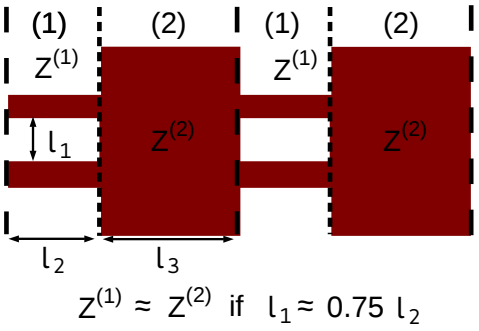

Figure 5.5: Sketch of the perpendicular strip pattern of anode design 5. The layout has been designed following [Nührmann, 2002] trying to equalize the impedance between strip part (1) and (2).

To achieve similar impedances for the strip parts (1) and (2) the stripline below the floating strip has been split into two lines adjusting the distance between both such that

$$l_1 \approx 0.75\, l_2 \quad , \tag{5.10}$$

where l_1 is the length under the floating strip and l_2 the distance between two floating strips. From [Nührmann, 2002] follows that then

$$Z^{(1)} \approx Z^{(2)} \quad . \tag{5.11}$$

5.3 6.4 cm x 6.4 cm Active Area Two-Dimensional Floating Strip Micromegas Detector with a Stiff Baseplate

Mainly for research and development purposes on the reconstructed pulse height on both readout strip layers of anode designs 4 - 7, a 6.4 x 6.4 cm^2 active area detector has been built. The detector components, including the anode PCB is sketched in Figure 5.6.

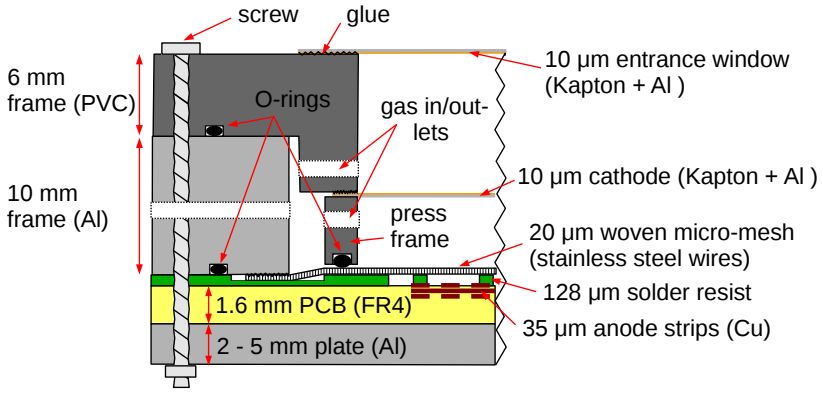

Figure 5.6: Sketch of the structure of the $64 \times 64\,mm^2$ active area two-dimensional floating strip Micromegas detector with 128 strips per layer.

The detector consists of three main components: a 6 mm thick PVC[3] cathode frame, a 10 mm thick Aluminum mesh frame and the 1.6 mm thick anode PCB. The cathode frame carries the cathode of the detector on the one side and the entrance window on the other side, both

[3] PolyVinyl Chloride i.e. plastic material

made of 10 µm thin Aluminum coated Kapton foil. As the detector is flushed with gas during operation, typically an overpressure of a few mbar is present inside the active volume. The combination of the two Kapton foils thus prevents the bulging of the cathode due to a pressure gradient with respect to both foil surfaces, which would introduce variations of the electric field in the drift region of the detector, see chapter 3.4.2 in [Bortfeldt, 2014]. The micro-mesh, which separates drift from amplification region, is glued with a two-component epoxy adhesive at a surface tension of about 10 N/cm to the 10 mm thick Aluminum mesh frame, thus assuring explicitly connection to ground potential. The spacer structure consisting of cylindrical pillars on the anode is made out of Pyralux PC 1025 solder resist [DuPont, 2011] and assures a constant distance between anode and micro-mesh. It has been produced on the PCB at LMU in a three-step process by conventional lithography of a photoresistive film described several times in literature, e.g. [Levinson, 2011]. Initially, the solder resist is laminated [Bungard, 2010] at 100°C with a relatively high laminator pressure (device specific scale) onto the full PCB. In a second step, the pillar pattern is transferred to the resist by exposing it with ultra-violet light and a negative photomask. In the final step, the exposed resist is developed in a sodium hydroxide solution, leaving only the desired geometry pattern of the resist on the anode. Due to the small floating strip width compared to the pitch, the pillars are elongated in the perpendicular direction of the floating strips with a size of 0.4 mm x 2 mm at a height of 0.128 mm, following an idea described in [Sidiropoulou et al., 2017]. They are arranged in a hexagonal pattern with a pitch of 4.8 mm over the anode, thus covering around 3% of the active area of the detector.

To prevent deformations of the 1.6 mm PCB in the active area of the detector, a relatively rigid Aluminum plate of 2 - 5 mm thickness has been screwed to the back-side of the PCB. Additionally, to assure that the micro-mesh does not follow deformations from the Aluminum frame onto which it is glued, a PVC frame of the thickness of the drift region inside the detector, outside of the active area, presses the mesh with an O-ring to a solder resist frame featuring the same height as the pillars. An expanded view of the detector components and a photograph of a half assembled detector is shown in Figure 5.7.

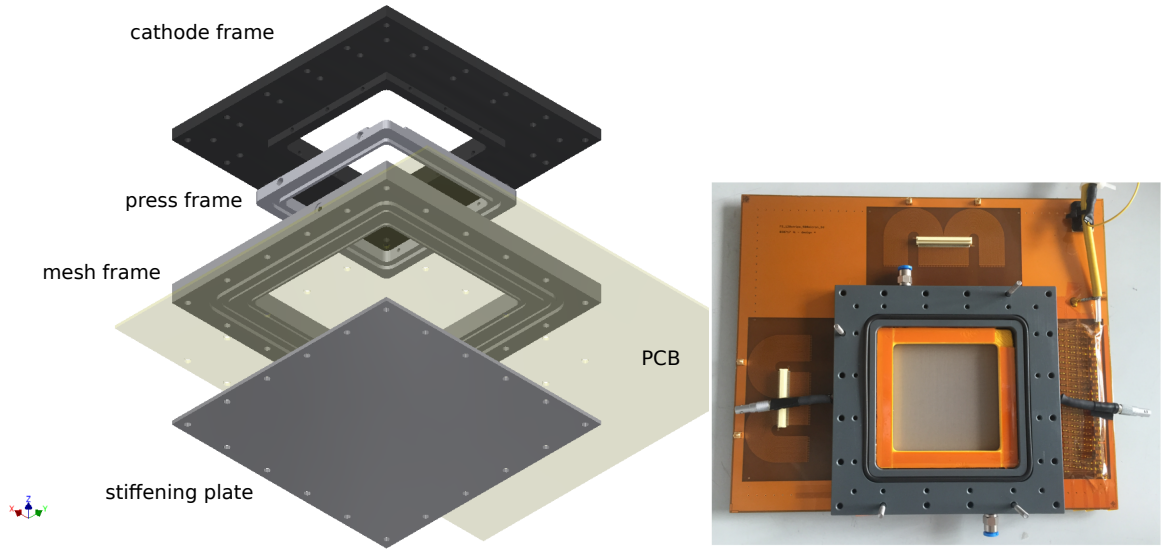

Figure 5.7: Left: Three dimensional expanded view of parts of the detector described in Figure 5.6, modeled with Inventor [Autodesk, 2018]. The PCB has been set to a 75% opacity for visibility reasons. Right: Half assembled detector with the active area in the middle of the photograph. The pressure frame to assure constant distance between anode and mesh is visible. Photograph taken from [Barfüsser, 2018]

The detector is sealed with two O-rings (Viton) surrounding the active area in the cathode and mesh-frame. Gas in- and outlets for either 4 or 6 mm PVC tubes are included in the mesh-frame. A second PVC mesh frame has been developed, which allowed to extract the signal induced on the micro-mesh via two Lemo cables. It can be used for triggering the readout electronics plugged to the strips of the detector. This is very useful for characterization measurements using e.g. 5.9 keV photons from a radioactive ^{55}Fe source presented in the later chapters, as it is the only possibility to trigger the APV25 based readout connected to both strip layers of the detector.

5.4 19.2 cm x 19.2 cm Active Area Two-Dimensional Floating Strip Micromegas Detector with Low Material Budget

Upon the idea of using two-dimensional floating strip Micromegas detectors as particle trackers in medical imaging applications, a significantly larger detector with low material budget was developed. The PCB designs 2 and 3 used as the anode for this detector geometry have already been described in section 5.1. The anode features in total 384 floating strips at a pitch of 0.5 mm, which yields a total active area of the detector of nearly 20 x 20 cm^2. This is a typical size of the field of view usually needed for tumor treatment in the human body with particle based radiation therapy [Combs et al., 2010]. The setup of the detector is sketched in Figure 5.8.

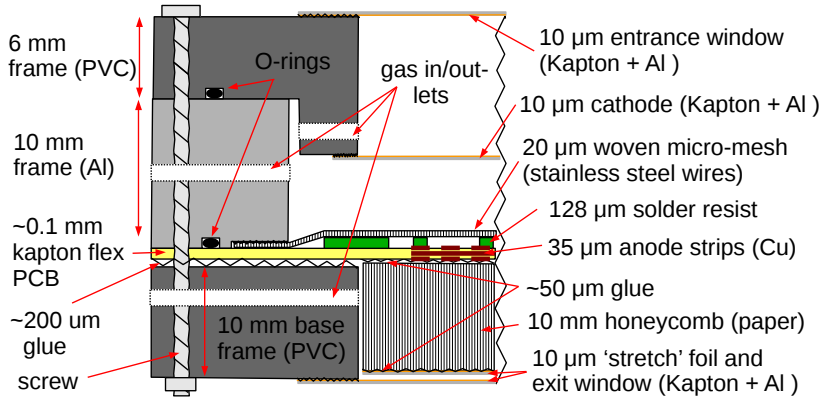

Figure 5.8: Sketch of the internal structure of the 192 × 192 mm^2 active area low material budget two-dimensional floating strip Micromegas detector with a total of 384 floating strips.

The main components, such as cathode-frame and mesh-frame, feature almost the same design as the small detector described in the previous section. Pillars have been photolithographically produced on the anode PCB similar as described in the previous section, however, with a circular shape at a diameter of 0.8 mm and a pitch of 5 mm, i.e. covering about 3% of the active area. Due to the very thin anode PCB of only 0.155 mm it is glued onto a 10 mm thick PVC frame ('anode frame') with a cutout of 19.3 x 19.3 cm^2 at the location of the active area, which carries the holes for fixation screws and also additional gas in- and outlets. To assure planarity of the anode PCB during the gluing process, it is sucked to a so-called 'stiff-back' [Müller, 2017]. The stiff-back is a lightweight Aluminum sandwich structure with a surface planarity $< 50\,\mu m/m^2$. The inner volume is formed by an Aluminum honeycomb structure, which can be evacuated with valves located at the sides. By holes in the planar surface, the anode PCB can be sucked to the stiff-back and consequently its planarity transferred to the anode. An approximately 200 µm thick layer of adhesive glue has been used to glue the anode on the PVC frame, outside the active area. The initial idea was to counteract

the gravitational sag and any intrinsic deformations of the thin anode in the active area by dynamically increasing the pressure below the anode with respect to the pressure in the drift region, such that the anode is pressed against the relatively rigid micro-mesh. However in the development process it turned out, that the anode PCB showed enormous deformations in the active area due to expansion effects caused by environmental temperature or humidity changes. Deviations from the initially flat anode surface with planarity values originally below 50 µm up to around 1 mm amplitude wavy structures were observed. Consequently, the anode had to be stabilized with a supportive structure also in the active area region of the detector. To minimize the material budget in the active area, Nomex honeycomb [Core Composites, 2017] was used, fixed with a minimal amount of glue at the bottom of the anode PCB during the gluing process with the stiff-back. The honeycomb, made out of Aramid-fiber, features a high strength to weight ratio with an average density of only 0.027 g/cm^3, depending on the unit cell size and wall thickness. The influence of the honeycomb to the total material budget of the detector is discussed in the next section. Trying to minimize the gravitational sag of the anode-honeycomb structure, the honeycomb has been glued to a stretched 10 µm thin Kapton foil, before gluing it to the anode. The expanded view of the main detector components and the first gluing step of the honeycomb is shown in Figure 5.9.

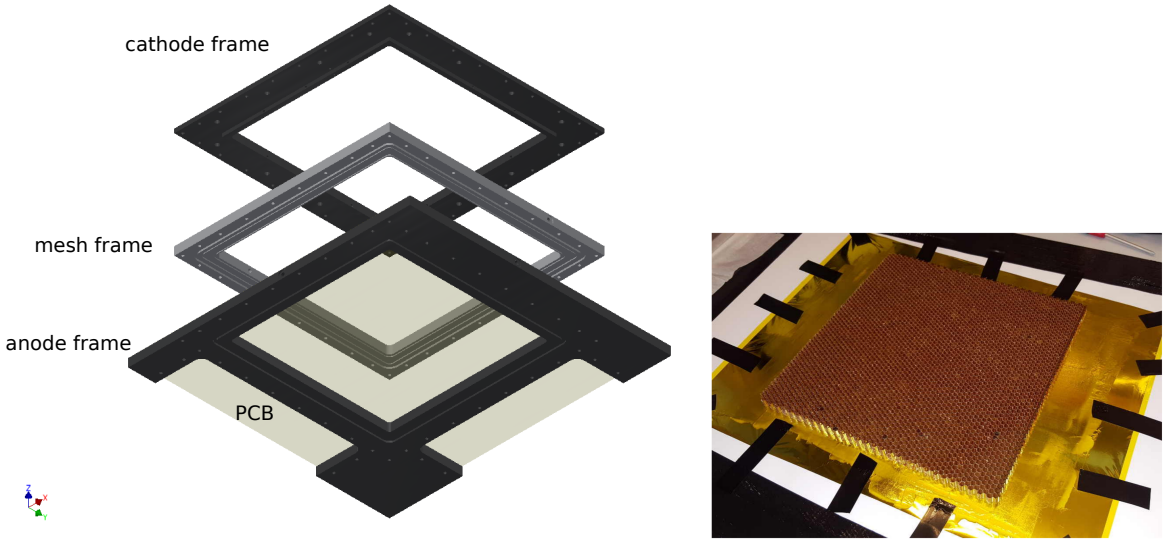

Figure 5.9: Left: Three dimensional expanded view of the detector parts described in Figure 5.8, modeled with Inventor [Autodesk, 2018]. The PCB has been set to a 75% opacity for visibility reasons. The honeycomb structure below the anode PCB is not shown. Right: Nomex honeycomb glued onto a stretched Kapton foil used to stabilize the thin anode PCB in the active area part of the detector. Picture taken from [Li, 2017].

The honeycomb structure together with an overpressure of a few mbars with respect to the active gas volume above the anode improved the planarity of the anode considerably. A measurement of the amplification gap homogeneity and thus the anode planarity – assuming a flat micro-mesh and a homogeneous pillar height – is possible during the detector operation, if the anode allows to reconstruct the position of a particle in both dimensions. As the measured pulse height of the particle is strongly dependent on the amplification gap width, the homogeneity of the pulse height can be translated into the planarity of the anode PCB. Figure 5.10 shows the reconstructed pulse height of 5.9 keV photons emitted from the radioactive decay of an ^{55}Fe source, measured on the full active area of the detector equipped with anode design 3.

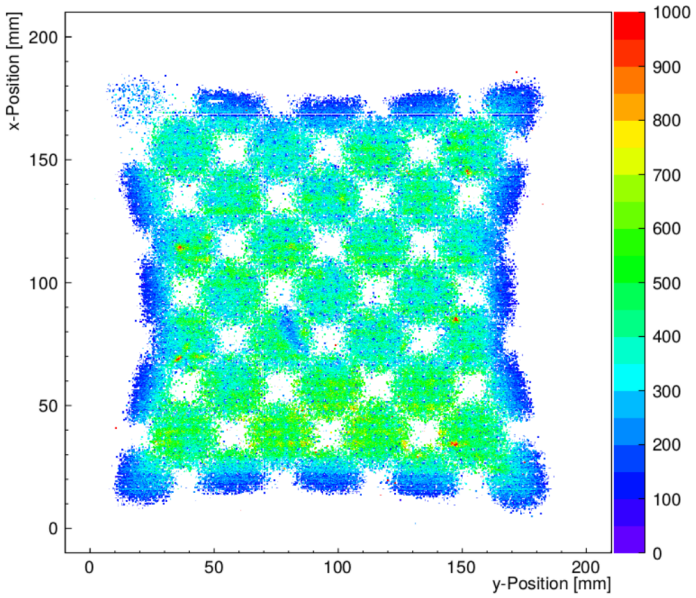

Figure 5.10: Reconstructed pulse height of 5.9 keV photons emitted from an ^{55}Fe-source placed at different positions on the detector at an amplification field of $E_{amp} = 37.5\,kV/cm$, a drift field of $E_{drift} = 0.167\,kV/cm$ and with a Ne:CF_4 93:7 vol.% gas mixture [Wieland, 2017]. Except effects at the border of the active area, a quite homogeneous pulse height is observed over the full detector surface.

The pulse height, in this example measured by the parallel strip layer, is encoded in the colors in arbitrary units. A homogeneous pulse height is observed over a large fraction of the active surface of the detector. The white spots in the active area are a consequence of the discrete source positions placed on a 10 mm thick Aluminum hole mask, creating beam-like profiles of the photons at a 38.6 mm hole spacing. The pillow-shaped structure i.e. the reduction of the pulse height at the borders of the active area is caused by a bulged anode induced by a slightly to high pressure difference between top and bottom side of the PCB, which was applied to compensate the gravitational sag of the anode supported by the honeycomb. This led to a not properly attached micro-mesh at the edges of the active area. To be independent of pressure induced deformations, a possible solution is to create a sandwich like structure consisting of two back-to-back glued anode PCBs, stabilized by the honeycomb in between, as it is done in a similar fashion for the construction of large scale Micromegas within the New Small Wheel upgrade project of the ATLAS detector at CERN [Kawamoto et al., 2013].

As the floating strips need to be individually connected to high voltage via high ohmic resistors, a screen printing like approach with a mixture of highly resistive polymer pastes between 1 kΩ/□ and 1 MΩ/□ [ESL ElectroScience, 2017] was used to create the resistors for each of the 384 strips. The initial idea was to avoid the time consuming process of soldering SMD resistors to each floating strip. Additionally, the use of SMD components limits the pitch of the strips and may cause complicated routing of the copper lines on the PCB. The method is briefly explained in the following and the different steps of the process are shown in Figure 5.11. In the first step, a solder resist support structure made from the same material as the pillars is photolithographically produced around the location of the resistors. Its purpose is to prevent the paste spreading over the small pitch of 0.5 mm. In the next step, the paste is pressed in the rectangular shaped holes of the support structure with the help of a stainless steel stencil, precisely aligned above the floating strips and the support structure. After distributing the paste over the solder resist structure, excess paste is removed and the PCB is cured in an oven for two hours at 150°C, according to specifications. Measuring a fraction of

234/384 from the resistances after curing showed a Gaussian distribution of about 3 MΩ width around the mean value of about 12 MΩ, with only a few outliers [Frank, 2017]. However, the target resistance of 22 MΩ was not reached within two trys with different PCBs, caused by not accurately mixed pastes and deviations in the solder resist support frame. While no evidence was found that the signal amplitude or timing generated in the detector depends on the floating strip resistance, one may try to minimize fluctuations of the resistance as it directly influences the current flowing during a discharge. Consequently too low resistances lead to non-efficient discharge quenching, destroying the floating strip principle.

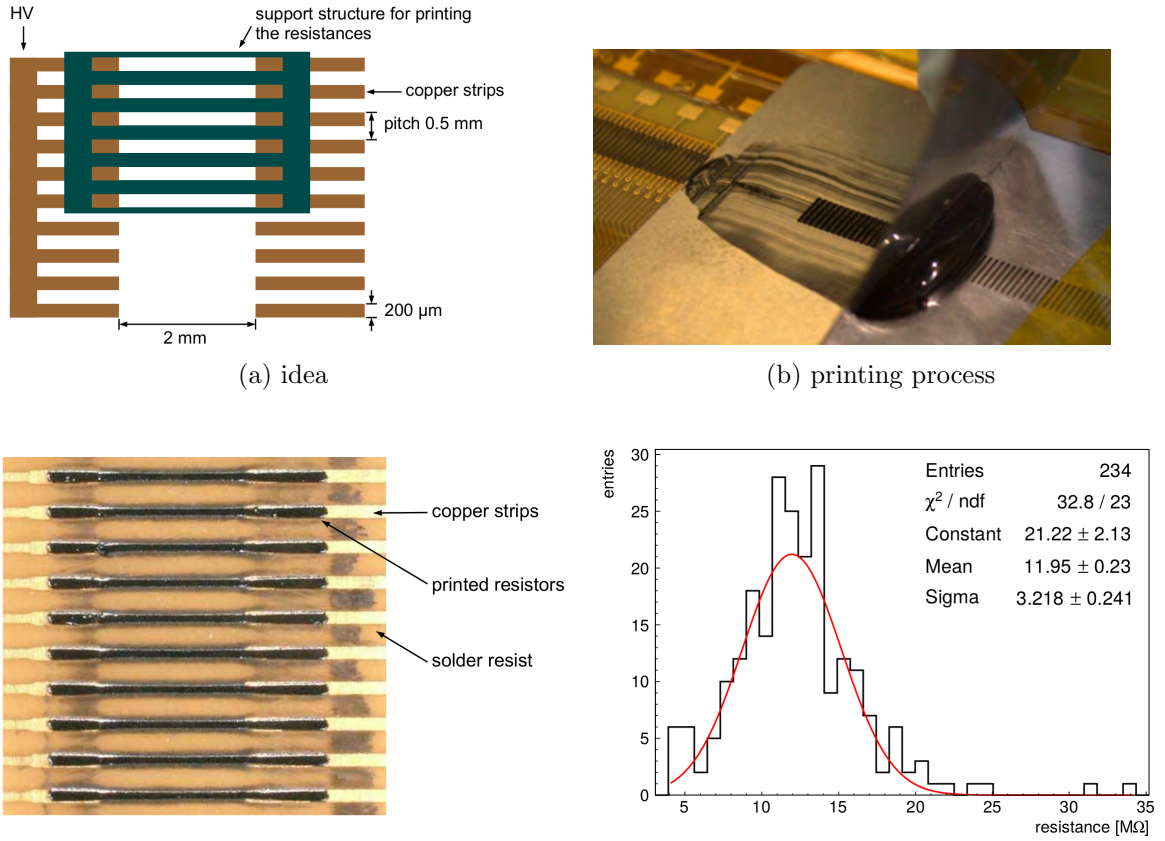

(a) idea

(b) printing process

(c) resistors after baking

(d) resistance results

Figure 5.11: Screen printing process of the resistors that individually connect the floating strips to high voltage. Pictures and photographs taken from [Frank, 2017].

Summarizing the results of the screen printing method yields two different findings: First, the production of the solder resist support structure was very time consuming and thus still needs improvement, as due to the small pitch the structure was very thin and unstable. During the development process with the sodium hydroxide solution problems often occurred that either the holes did not open properly or the fine structure was damaged, which resulted in completely removing the resist and restarting the full production chain. The second, more positive finding was, that if the support structure was well defined, the printing process of the resistors was uncomplicated and often worked within the first try. However, one must say, that the correct paste mixture to achieve the desired resistance values probably needs to be determined iteratively and a fluctuation of the resistance of at least 25% has to be considered.

To conclude, if one wants to avoid resistance fluctuations and the time consuming photolithographic process to produce the support structure, the use of SMD resistors can be a viable

alternative.

5.5 Influence of a Nomex Honeycomb Supported Anode PCB on the Material Budget of the Detector

The material budget of a detector can be expressed in units of radiation length X_0, which describes the thickness of a material after which an electron loses energy through *Bremsstrahlung* up to a value of $1/e \approx 36.8\,\%$ of its initial energy. X_0 is usually described in units cm or g/cm^2, which can be converted via the material density. The radiation length of many materials and composites have been measured experimentally and can be found on the Particle Data Group website[4] or in [Tanabashi et al., 2018]. However, if a composite is not listed, it can be calculated by the following formula

$$1/X_0 = \sum w_i/X_i \quad , \tag{5.12}$$

where X_i is the radiation length of the individual component and w_i the atomic mass fraction of the component inside the composite. A list of all material layers inside the 19.2 x 19.2 cm^2 active area of the two-dimensional floating strip Micromegas described in the previous section, including layer thickness and radiation length, is shown in Table 5.1. To account for e.g. the strip pattern of the anode or the woven structure of the micro-mesh, two different total radiation lengths of the detector have been calculated, a maximum and an effective one. The maximum radiation length $x_{\max}/X_0$ is defined as the maximum material budget a traversing particle sees i.e. assuming the worst case scenario that it hits a wire crossing in the micro-mesh with a total of 50 µm stainless-steel, a 128 µm solder resist pillar, each strip of the three 35 µm copper strip layers on the anode and a full cell wall length of the 10 mm thick honeycomb. A total thickness in terms of radiation length of $x_{\max} = 0.0296 X_0$ is found. As this is an unlikely event, additionally the effective radiation length x_{eff}/X_0 has been calculated, which takes into account the percentage of the detector area covered by each material. A thickness of $x_{\text{eff}} = 0.0079 X_0$ is determined.

The usage of the honeycomb glued on the back-side of the anode increases the maximum radiation length by about a factor of 2.7. For the effective radiation length however, which is the more realistic one, the difference is only around 14%, as around 97% of the honeycomb volume is void. The absolute values of the maximum radiation length without honeycomb is $x/X_0 = 0.0109$ and with honeycomb $x/X_0 = 0.0296$. The effective radiation length is without honeycomb $x/X_0 = 0.0069$ and $x/X_0 = 0.0079$ with honeycomb.

As we see in the calculated effective radiation length, the main contribution to the material budget of the detector are the very dense materials like the anode copper strips and the stainless steel micro-mesh. Possible improvements for future anode PCBs to additionally reduce the material budget are on the one hand to reduce the diameter of the micro-mesh wires to 18 µm with the same pitch of 63 µm, which additionally increases the gain and the micro-mesh transparency, as shown by [Kuger, 2017]. On the other hand, the anode PCB can be adjusted, such that the copper strip line thickness is reduced from 35 µm to 17 µm. Additionally, the parallel readout strip layer can be removed completely, which also makes the use of an additional insulation layer unnecessary, and coupling capacitors directly connecting to the anode floating strips can be used instead. Thus, the total thickness of the anode PCB could be reduced from 0.155 mm to 0.059 mm, which reduces not only the radiation length considerably, but also multiple Coulomb scattering of the traversing particles within the anode PCB.

[4] `http://pdg.lbl.gov/2018/AtomicNuclearProperties/`

component	material	thickness [mm]	ρ [$\frac{g}{cm^3}$]	X_0 [cm]	x_{max*}/X_0	x_{eff*}/X_0
Gas Window	Kapton	0.01	1.42	28.58	3.50e-5	3.50e-5
Gas	Ne:CF_4 (80:20)	10	0.00143	21933.89	4.56e-5	4.56e-5
Cathode	Kapton	0.01	1.42	28.58	3.50e-5	3.50e-5
Drift Gas	Ne:CF_4 (80:20)	6	0.00143	21933.89	2.74e-5	2.74e-5
Micro-Mesh	Stainless Steel	0.025	7.89	1.76	2.84e-3	1.13e-3
Pillar	Epoxy	0.128	1.08	38.79	3.30e-4	1.09e-5
Anode Strips	Copper	0.035	8.92	1.44	2.43e-3	1.46e-3
Insulation	Kapton	0.025	1.42	28.58	8.75e-5	8.75e-5
Readout Strips	Copper	0.035	8.92	1.44	2.43e-3	1.94e-3
Glue	Epoxy	0.01	1.08	38.79	2.58e-4	2.58e-4
Insulation	Kapton	0.025	1.42	28.58	8.75e-5	8.75e-5
Readout Strips	Copper	0.035	8.92	1.44	2.43e-3	1.94e-3
Glue	Epoxy	0.05	1.08	38.79	3.30e-4	1.29e-4
Honeycomb	Aramid Fiber	10	0.8	54.47	1.84e-2	6.65e-4
Glue	Epoxy	0.05	1.08	38.79	3.30e-4	1.29e-4
Stretch Foil	Kapton	0.01	1.42	28.58	3.50e-5	3.50e-5
Gas	Ne:CF_4 (80:20)	2	0.00143	21933.89	9.12e-6	9.12e-6
Gas Window	Kapton	0.01	1.42	28.58	3.50e-5	3.50e-5
Full Detector		28.51			2.96e-2	7.90e-3

Table 5.1: List of all components in the low material budget two-dimensional floating strip Micromegas detector. Values for the radiation length have either been extracted directly from [Tanabashi et al., 2018] or calculated via eq. 5.12 for composites. The * at max* denotes that the radiation length has been calculated for the full thickness of the layer i.e. the maximum possible energy loss of a particle in the detector. eff* accounts for the geometry of e.g. the woven structure of the micro-mesh wires.

In medical transmission imaging applications e.g. with protons at a therapeutic energy of $E_0 = 75\,\text{MeV}$ with $\beta\gamma \approx 0.3$, the energy loss is dominated by direct ionization and not by *Bremsstrahlung*. Thus the radiation length cannot be used for describing the energy loss in the detector. As the knowledge of the proton energy spectrum is important after traversing the detector, to keep the energy resolution on the accelerator level which is usually on the order of $\Delta E/E_0 \approx 1\%$, the maximum and minimum energy loss of the protons traversing the detector is estimated in the following. The energy loss of the protons is calculated with a SRIM based TRIM simulation [Ziegler et al., 2010], using the materials and densities listed in Table 5.1. Compounds were used as they can be found in the TRIM compound dictionary. Pillars and glue have been approximated with casted Epoxy and Aramid Fiber with Propylamine, using the densities stated in the table above. The gas volumes have not been considered in the simulation as they show a negligible contribution to the total energy loss in the detector. A minimum energy loss of $\delta E_{\text{min}} = 0.5\,\text{MeV}$ is found for the case if the 75 MeV proton traverses only one copper strip, the Kapton layers and the glue. A maximum energy loss of $\delta E_{\text{max}} = 1.2\,\text{MeV}$ is found with the same assumption as for the calculation of x_{max*}/X_0 described above, however, neglecting the contribution of the honeycomb wall of 10 mm thickness. This corresponds to an energy uncertainty of the protons after traversing the detector of $(\delta E_{\text{max}} - \delta E_{\text{min}})/E_0 \approx 0.9\%$, which is comparable to the assumed energy resolution of the accelerator. However, if the protons traverse multiple detectors, the energy spread may reach several percent, at which point the above mentioned reduction of the anode PCB material budget will be necessary to preserve the energy resolution of the accelerator. Including the honeycomb in the calculation yields a maximum energy loss of $\delta E_{\text{max}} = 9.2\,\text{MeV}$, with

$dE/dx \approx 0.8\,\mathrm{MeV/mm}$ inside the honeycomb wall. We see that the maximum energy loss of the protons will be dominated by the energy loss in the support structure if they traverse the complete length of a 10 mm honeycomb wall. Thus it needs to be considered to replace the honeycomb with a homogeneous layer of FR4 below the three-layer PCB, used for stabilization of the thin anode structure. Additionally, an over pressure below the PCB with respect to the active area of the detector needs to be applied to press the PCB against the micro-mesh. Though this increases the total material budget of the detector, it also leads to a more homogeneous energy loss of the protons in the detector.

Chapter 6

Signal Characterization Measurements

In this chapter, the signals on both readout strip layers of the different two-dimensional floating strip anode structures introduced in the previous chapter are investigated, measured with APV25 front-end hybrid boards, interfaced by the SRS. The measurements have been performed with either 5.9 keV photons emitted from a ^{55}Fe source or 20 MeV protons during a test beam campaign at the Tandem accelerator in Garching. All measurements have been performed with a Ne:CF_4 80:20 vol.% gas mixture. In the first section, signals of *classical* two-dimensional floating strip anodes are investigated, where classical refers to strips featuring a uniform width. The second section compares *novel* anode designs, where the main difference is the geometry of the perpendicular readout stripline below and between the floating strips. In the last part of the chapter, signals from a classical anode design are compared to a novel one, focusing on the gain in pulse height on both readout strip layers.

6.1 Signals from Classical Anode Designs

The signals measured with APV25 hybrid boards connected to both readout strip layers of anode designs 1, 2 and 3 (see Figure 5.1) are discussed in the following. Note that measurements with anode design 2 were only performed using 5.9 keV photons from a ^{55}Fe source at LMU, whereas anode design 1 and 3 have been tested with 20 MeV protons in two different test beam campaigns at the Tandem accelerator in Garching. Furthermore, anode design 1 features 128 anode strips, while the detector equipped with design 2 and 3 has a 9 times bigger active area with a total of 384 strips. This makes the direct comparison of the absolute pulse height between the anode designs difficult, as also ambient temperature, pressure as well as exact composition of the used detector gas play an important role for the gas gain. However, the behavior of the strip signals and cluster properties between both readout strip layers within the same anode structure can still be investigated.

The measurement setup with the ^{55}Fe source is similar to the setup explained in section 6.3, where the triggers for the APV25 boards are derived from the induced signal on the micromesh. For measurements with protons, traversing particles are triggered using a plastic scintillator equipped with a photo-multiplier tube [Hamamatsu, 2007] placed behind the detectors. The APV25 front-end chips were configured for negative signals on the parallel readout strips, which will be called x-strips from now on, and positive signals on the perpendicular readout strips, which will be called y-strips.

6.1.1 Raw Strip Signals

Typical signals of the strip with maximum charge on both readout strip layers in the detector equipped with anodes 1, 2 and 3 are shown Figure 6.1, recorded with APV25 front-end boards. Note that the signal on the x-strips has been multiplied by -1 to emphasize the negative polarity.

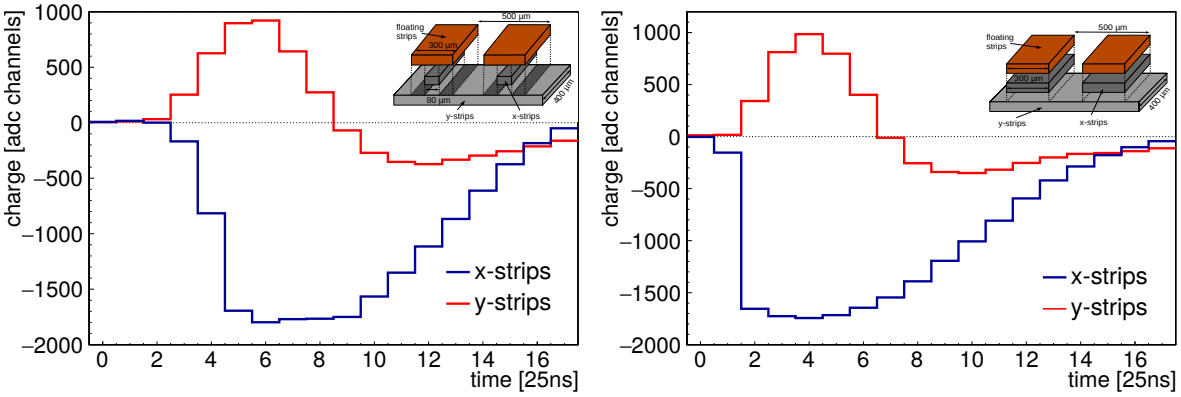

(a) design 1

(b) design 2

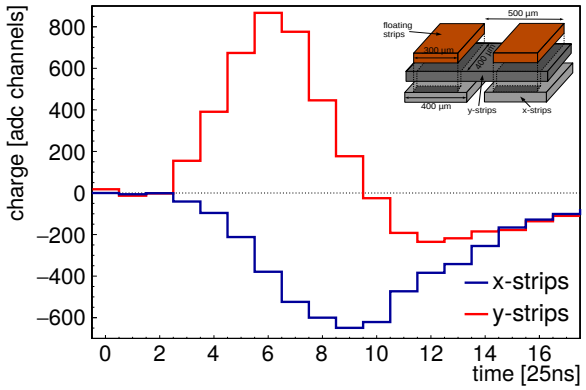

(c) design 3

Figure 6.1: Typical signals on the strip with maximum charge in the detector, created by a 20 MeV proton (a,c) and a 5.9 keV photon (b) acquired with anode design 1 to 3, recorded with APV25 front-end boards. The bin content of the x-strips has been multiplied by -1 to emphasize the negative polarity of the signals.

The signals on both readout strip layers follow the shape as expected from the simulations in chapter 4. The unipolar negative signal on the x-strips is dominantly created by capacitive coupling of the floating strip signal and the initially positive bipolar signal on the y-strips is created by the directly induced signal from the movement of the electrons and ions in the amplification region.

For the moment, we do not consider that the signals are measured at different amplification fields, as the idea was to pick signals with similar pulse height on the y-strip. The dependence on the amplification field will be investigated later. The difference of the anode structures in design 1 and 2 is mainly the width of the x-strip, which is increased from 0.08 mm in design 1 to 0.3 mm in design 2. This increases the capacitance between floating strip and x-strip considerably. As consequently the floating strip capacitance is dominated by the capacitance generated by the congruent x-strip, a huge fraction of the floating strip signal is capacitively coupled to the parallel strip. This is visible in the strip pulse on the x-strips, which is cut off by the maximum dynamic range of the digitized APV25 response for the anode designs

1 and 2. The stronger saturation effect with design 2 is visible at the much faster pulse rise. Note that saturation of the front-end electronics should in general be avoided as it distorts the charge measurement on the anode strips which is e.g. used to reconstruct the position of the traversing particle. Using the capacitance model developed in section 4.4, we can estimate how much of the floating strip signal is actually transferred to the parallel strip. For anode design 1, a total floating strip capacitance of $C^{float} = 21.9\,pF$ is calculated, of which $C^{float}_{x\text{-strip}} = 8.2\,pF$ is shared with the parallel x readout strip. Due to the much longer strips in anode design 2, a total floating strip capacitance of $C^{float} = 107\,pF$ is found with a x-strip capacitance of $C^{float}_{x\text{-strip}} = 85.3\,pF$. We see, that the capacitive coupling strength in design 2, where around 85/107 ≈80% of the floating strip signal is shared with the x-strip, is about a factor of two higher than in design 1 with around 37%. From the simulation results in chapter 4 we know, that the total induced positive charge on the y-strips is smaller than 10% for all three anode designs investigated in this section. Thus it is understandable that the APV25 connected to the x-strips saturates compared to the y-strips for the anode designs 1 and 2. Figure 6.2 shows the distribution of the maximum strip charge on x and y-strips for 50k proton signals measured with anode design 1. The asymmetric charge distribution as well as the electronics saturation of the x-strips above 1600 adc channels is clearly visible.

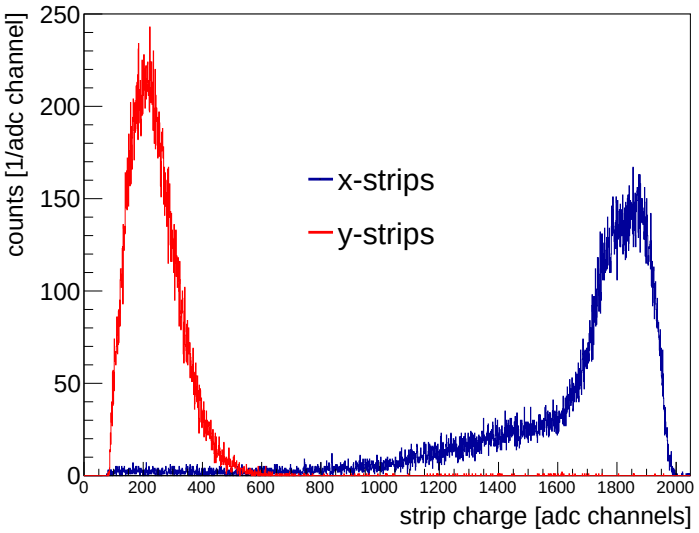

Figure 6.2: Charge on the strip with maximum charge for the x-strips (blue) and y-strips (red) of anode design 1, measured with 20 MeV protons at 32 kV/cm amplification field and 0.33 kV/cm drift field. The saturation of the amplifiers connected to the x-strips above 1600 adc channels is clearly visible.

Considering anode design 3, where both readout strip layers have been interchanged, we find that the y-strip signal is higher than the x-strip signal. The total floating strip capacitance is $C^{float} = 85.7\,pF$. However, only $C^{float}_{x\text{-strip}} = 5.2\,pF$ is shared with the x-strip, as the dominant capacitance is created by the perpendicular readout strips, which are in between the floating strips and the parallel readout strips. Thus, a coupling strength to the x-strip of $5/85 \approx 6\%$ is found, which is in the same region as the directly induced positive charge on the y-strips of around 9%, found with the Garfield++ simulation of the stripline geometry of anode design 3. Additionally, increasing the strip capacitance reduces the current signal flowing into the input of the APV25, leading to a non-negligible pulse height reduction as the strip capacitances reach into the 100 pF regime, as we see in Figure 4.28.

In the following, the pulse height as well as the fraction of saturated APV25 events are investigated as a function of the amplification field. Other signal characteristics like the

pulse width, maximum timing difference or strip charge ratio between x and y-strips can be found in the appendix B. If no error bars are visible in the following pictures, the markers are larger than the respective errors. In Figure 6.3 the mean value of the maximum strip charge distributions of x and y-strips is shown as a function of the amplification field. Remember that design 2 has been measured with 5.9 keV photons, while design 1 and 3 with 20 MeV protons. The mean energy loss of 20 MeV protons in the 6 mm wide drift region of the detector, filled with Ne:CF_4 80:20 vol.% gas, is about 15.5 keV, which is a factor of 2.6 higher than the energy deposited by the 5.9 keV photo-electron, which is being stopped within a few 100 µm in the drift region[1]. Thus higher amplification fields are necessary with ^{55}Fe measurements to reach similar pulse heights as with 20 MeV protons.

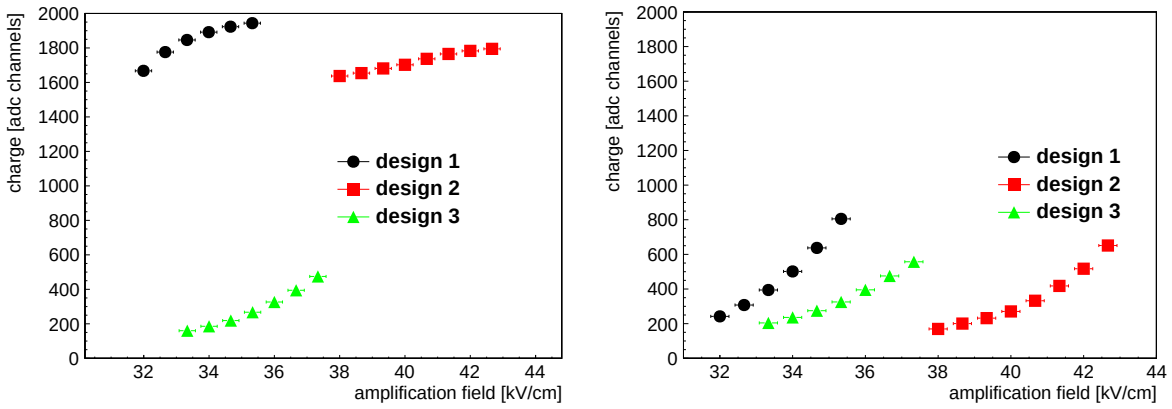

(a) x-layer (b) y-layer

Figure 6.3: Mean of the maximum strip charge distribution shown in Figure 6.2 on the x-strip (left) and y-strips (right) as a function of the amplification field strength for different anode structures at $E_{\text{drift}} = 0.33\,\text{kV/cm}$.

The mean x-strip pulse height on design 1 and 2 is for every amplification field above 1600 adc channels, which corresponds to the onset of saturation effects of the APV25 chip. Note that the dynamic range of the APV25 used for the measurement with design 2 had a different configuration compared to the measurements with design 1, which lead to a smaller dynamic range and thus to in general a smaller reconstructed mean strip charge. The expected exponential increase of the charge with increasing amplification field is only visible for the x-layer of anode design 3 and the y-layer signals, as the pulse heights are well below the electronics channel saturation.

Trying to compare the absolute pulse height of the y-strips in design 1 and 3, we see that design 1 shows a higher signal than design 3. Note that both measurements have been performed within one year time difference. Nevertheless, we would expect, that the pulse height in design 3 is bigger than in design 1, as the perpendicular strip is closer to the amplification region which increases the directly induced signal according to the simulation results. However up to now, we did not consider the total strip capacitance. If we calculate the capacitances of the y-strips in both designs, we find a capacitance of $C^{y\text{-strip}} = 16.1\,\text{pF}$ for design 1 and $C^{y\text{-strip}} = 139\,\text{pF}$ for design 3, which is almost a factor of 10 different. While a strip capacitance below 20 pF has a negligible effect on the fraction of the current signal flowing in the APV25, a strip capacitance of 140 pF leads to a considerable pulse height reduction of about 30% for the bipolar current signal, as we see in Figure 4.28. Additionally, the measurement results shown for anode of design 3 were performed with a prototype detector which

[1] proton energy loss determined with a Geant4 based simulation done by Bernhard Flierl, private communication

showed considerable anode PCB deformations in the active area of the detector, leading to a smaller average pulse height. Both mentioned reasons are an indication that the directly induced signal on the y-strips of design 3 is larger than observed by the measurements. However, as mentioned above, a direct comparison of both designs is not feasible due to the one year time difference between both measurements resulting in too many unknown parameters which influence the absolute pulse height measured by the detectors.

An estimation on the fraction of saturated events is shown in Figure 6.4. It has been calculated from the number of events where the strip charge exceeded the APV25 internal saturation threshold, which is typically around 1600 adc channels but can vary from APV25 to APV25 depending on the used configuration. The threshold has thus been adjusted for each APV25 individually in the analysis. It is clearly visible, that even for the lowest measured amplification field of 32 kV/cm in design 1, already around 40% of the total events drive the APV25 channels connected to the x-strips into saturation. As the coupling to the x-strips in design 2 is about a factor of 2 higher than in design 1, about 90% of the strip signals are already saturated at the lowest measured amplification field with design 2. Due to their small signal amplitudes, no saturation effects are observed on the y-strips of the anode designs, which leaves room for optimization.

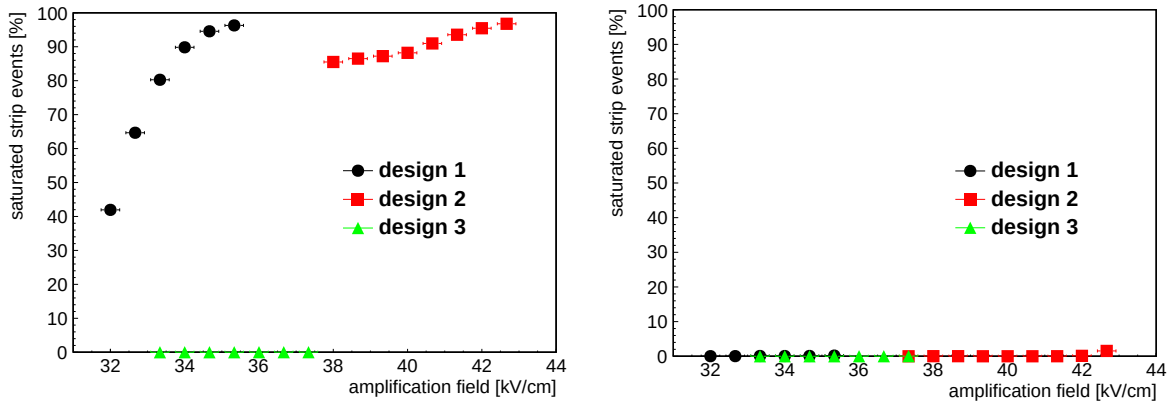

(a) x-layer (b) y-layer

Figure 6.4: Fraction of saturated events, determined from the strip charge distribution shown in Figure 6.2 on the x-strips (left) and y-strips (right) as a function of the amplification field strength for different anode structures.

6.1.2 Hit Cluster Properties

In the previous section, the signals in the detector have been compared according to the maximum detected charge on a strip. In the following, a group of adjacent strips is merged into a cluster of strips, as described in section 3.3. The cluster multiplicity i.e. the number of hit strips within a cluster and the total cluster charge is investigated in the following.

Figure 6.5 shows the average cluster multiplicity and cluster charge as a function of the amplification field for the three designs. We see, that the number of strips in the cluster is directly correlated to the cluster charge. This is understandable, as very small signals vanish in the noise. On the other hand, very large signals tend to pull neighboring strips over threshold via capacitive coupling, which thus seemingly increases the cluster size. This is best visible on the cluster charges measured with anode design 1 and 2 on the x-strips, as the strip signals are much higher than all the others. Up to 7 strips are found on average for one photon cluster in the detector. A quick estimation on the expected number of strips responding to one photon event is given in the following. The 5.9 keV photo-electron produces an almost

point like ionization charge cloud on the size of about 50-250 µm at a random position in the 6 mm long drift gap [2]. Assuming the photon gets absorbed in the proximity of the cathode, the produced electrons drift the full 6 mm until they reach the micro-mesh. On their way to the mesh, the electrons spread up to a charge cloud on the order of 400 - 800 µm width, strongly depending on the transverse diffusion of the electrons in the gas. See Figure 2.3 for the transverse diffusion of the electrons as a function of the gas mixture and the drift field. As all three anode structures feature an anode strip pitch of 0.5 mm, only between one and three strips effectively receive signals after the amplification process. We can conclude, that the high cluster multiplicity is only caused by capacitive coupling of the extremely high signals on the x-strips to neighboring strips.

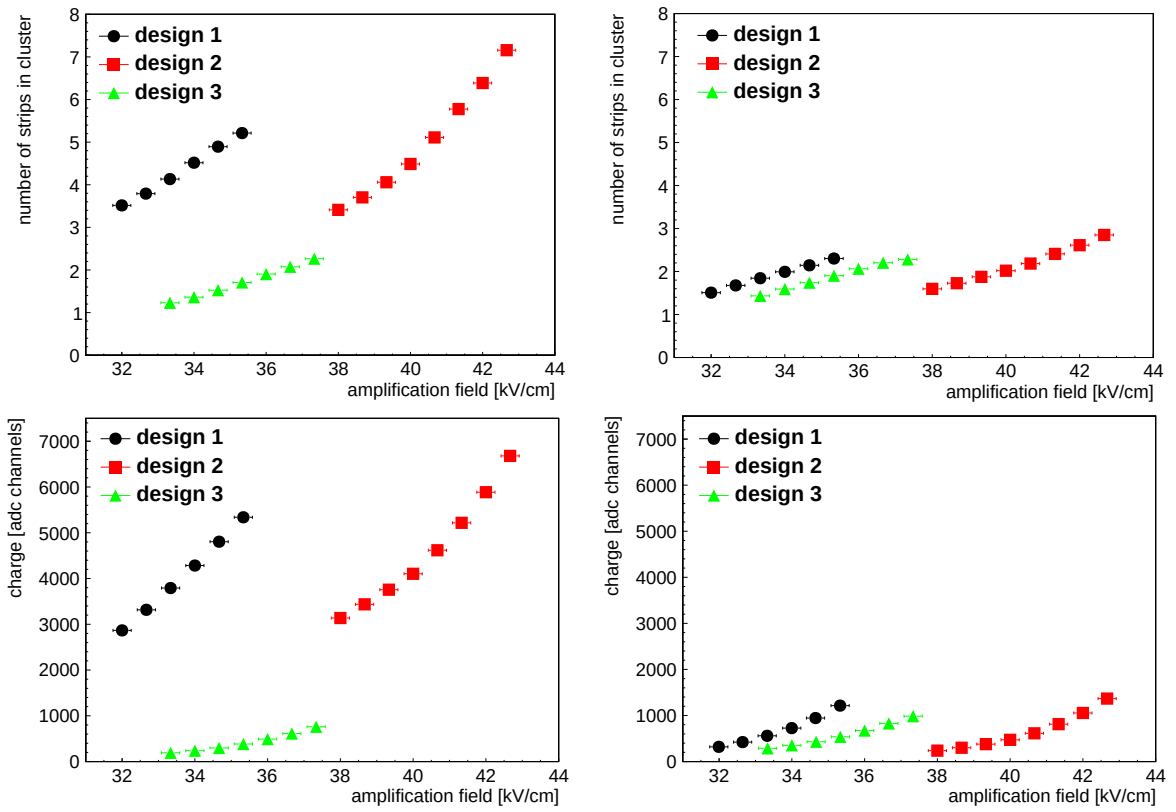

(a) x-layer (b) y-layer

Figure 6.5: Mean number of hit strips per cluster (top) and total cluster charge (bottom) on the x-strips (left) and y-strips (right) as a function of the amplification field for different anode structures at $E_{\text{drift}} = 0.33\,\text{kV/cm}$.

The cluster multiplicity for the x-strips of design 3 and all other y-strips show significantly smaller values, closer to the expectation. However one must say that too small pulse heights can also lead to a loss of strips on the cluster boarders if the charge does not exceed the three sigma charge requirement in the analysis.

To compare the absolute signal pulse heights on both readout strip layers within one anode design, the cluster charge ratio defined as the cluster charge of the y-strips divided by the cluster charge of the x-strips is investigated. It is shown as a function of the amplification field in Figure 6.6 for all three anode designs.

[2] Garfield++ heed based simulation for the transport of a 5.9 keV photon in a 6 mm gas volume filled with Ne:CF_4 gas at a 80:20 vol.% mixture with a drift field of 0.33 kV/cm at 960 mbar and 20° C

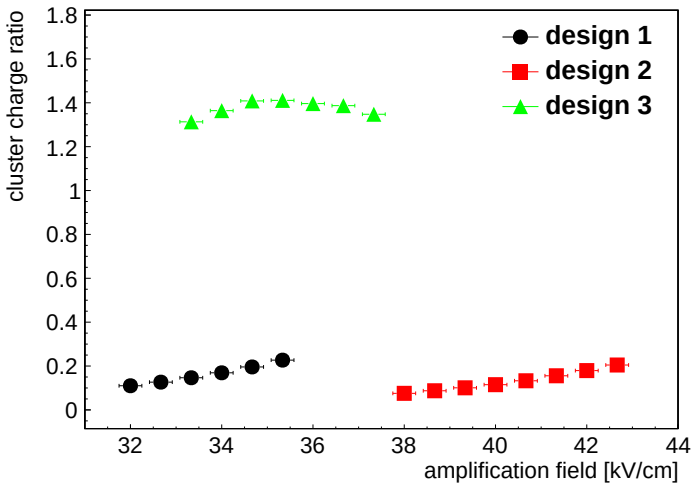

Figure 6.6: Ratio between y-strip and x-strip cluster charge as a function of the amplification field for different anode structures at $E_{\text{drift}} = 0.33\,\text{kV/cm}$.

Usually a similar pulse height on both readout strip layers is desired. Thus we find that anode design 3 shows the best simultaneous signal reconstruction on both layers with a ratio of about 1.3, being almost independent of the amplification field. Anode designs 1 and 2 show a ratio well below 0.3, i.e. a much smaller signal on the y-strips compared to the x-strips. It is in reality even smaller than visible here, as the x-strip signals recorded with the APV25s were saturated for all amplification fields. This also explains why the ratio increases with increasing amplification field for the two designs.

If we recall the values from the Garfield++ simulation, we find that the highest induced charge on the perpendicular layer is expected for design 3, as the strips are closest to the amplification region. The fraction of charge coupled to the y-strip is expected to be around 8-9% of the total created charge in the amplification region (see section 4.5). For interchanged readout strip layers, as for design 1 and 2, the induced charge on the y-strips is consequently reduced. We can conclude from the simulations, that the induced signals on the y-strips must be smaller than 9% of the charge created. From the capacitive coupling estimation between floating and parallel strip we expect about 37% charge sharing for design 1 and 80% for design 2. The measured cluster charge ratio shows that for both designs the ratio is smaller than 1/10 th (smallest ratio measured at the smallest amplification field where the x-layer is still saturated). It is even a lot smaller in design 2 as visible in the figure, due to much more saturated x-strip signals. For design 1 this leads to an estimated signal strength on the y-strips of below $37\%/10 \approx 3.7\%$, which is in the same order as the signal measured on design 2 as the strip capacitance of the y-strip of the two designs are similar and the coupling between floating and perpendicular strip is negligibly small.

To conclude, the best simultaneous signal reconstruction on both readout strip layers is achieved with anode design 3, which shows similar pulse height on both layers. However, the signals measured with this design are very small in general, which is on the one hand the result of shielding the strong capacitive coupling to the parallel strips by the perpendicular strips, which effectively only reduces the pulse height on the parallel strips. And on the other hand, it is due to creating big capacitances in the detector when placing the 0.4 mm wide perpendicular readout strip layer at a 0.5 mm strip pitch directly below the floating strips at a distance of only 25 µm. We saw, that the highest capacitance is found on the perpendicular readout strip with 140 pF for 20 cm long strips, as it combines both the capacitances from the floating and parallel readout strip layer. This leads to a reduction of the pulse height measured with the APV25 front-end electronics of around 30%. We clearly see, that the geometry of

the anode PCB needs to be improved to increase the signal yield on the perpendicular strip layer, without creating big capacitances in the detector. Additionally the capacitive coupling strength from the floating strip to the parallel strip needs to be carefully adjusted to create signals of the same order as the perpendicular strip.

6.2 Signals from Novel Anode Designs

Upon the need to increase the signal yield on the perpendicular readout strip without creating big capacitances in the detector, novel two-dimensional floating strip Micromegas anode designs have been developed. The stripline geometry of the three copper strip layers has already been introduced in the previous chapter. The key element of the novel anode designs are the perpendicular readout strips with a periodically alternating stripline width to reduce the capacitance to the floating/parallel strips while at the same time maximizing the directly induced signal. This also requires, that the floating strip width needs to be small compared to the pitch.

Detectors with anode designs 4, 5 and 6 (see Figure 5.2) have been investigated at the same test beam campaign, thus with similar temperature, pressure and detector gas. The detector equipped with anode design 7 was investigated one year later, however, trying to have similar conditions as with the other designs. The measurement setup regarding readout and triggering was identical for all designs and is explained in more detail in the next chapter, as we here only focus on the signal characteristics on both readout strip layers of the new anode designs. All detectors discussed in this section feature 128 strips with a pitch of 0.5 mm for anode design 4 - 6 and a pitch of 0.3 mm for design 7, at an amplification gap of 128 µm.

Signals from 20 MeV protons on both readout strip layers are recorded with APV25 front-end boards. The trigger for the APV25 based readout was derived from a low material budget triple GEM detector placed in front of the floating strip Micromegas, with the possibility to also compare particle position reconstruction and reconstruction efficiency in both dimensions.

Note that the detectors equipped with anode design 4 and 6 contain a woven 30/70 µm micro-mesh, design 5 and 7 a woven 25/38 µm micro-mesh. This leads to a different electron mesh transparency for the different detectors, which influences the absolute pulse height measured in the detector. The impact is estimated in the following. All measurements in this section have been performed with a Ne:CF_4 80:20 vol.% gas mixture with a drift field of 0.33 kV/cm, while the amplification field has been varied. From the simulation results of the transparency (see Figure 2.6) we find a mesh transparency for the 30/70 µm micro-mesh of (95 ± 1) % and for the 25/38 µm micro-mesh of (67 ± 3) % at $E_{drift} = 0.33$ kV/cm. Thus the reconstructed pulse height is about a factor of (1.42 ± 0.08) higher with the 30/70 µm micro-mesh than with the 25/38 µm micro-mesh.

6.2.1 Raw Strip Signals

Signals on the strip with maximum charge on both readout strip layers of the novel anode structures are shown in Figure 6.7, averaged over 40k events from 20 MeV protons at $E_{amp} = 37.5$ kV/cm and $E_{drift} = 0.33$ kV/cm.

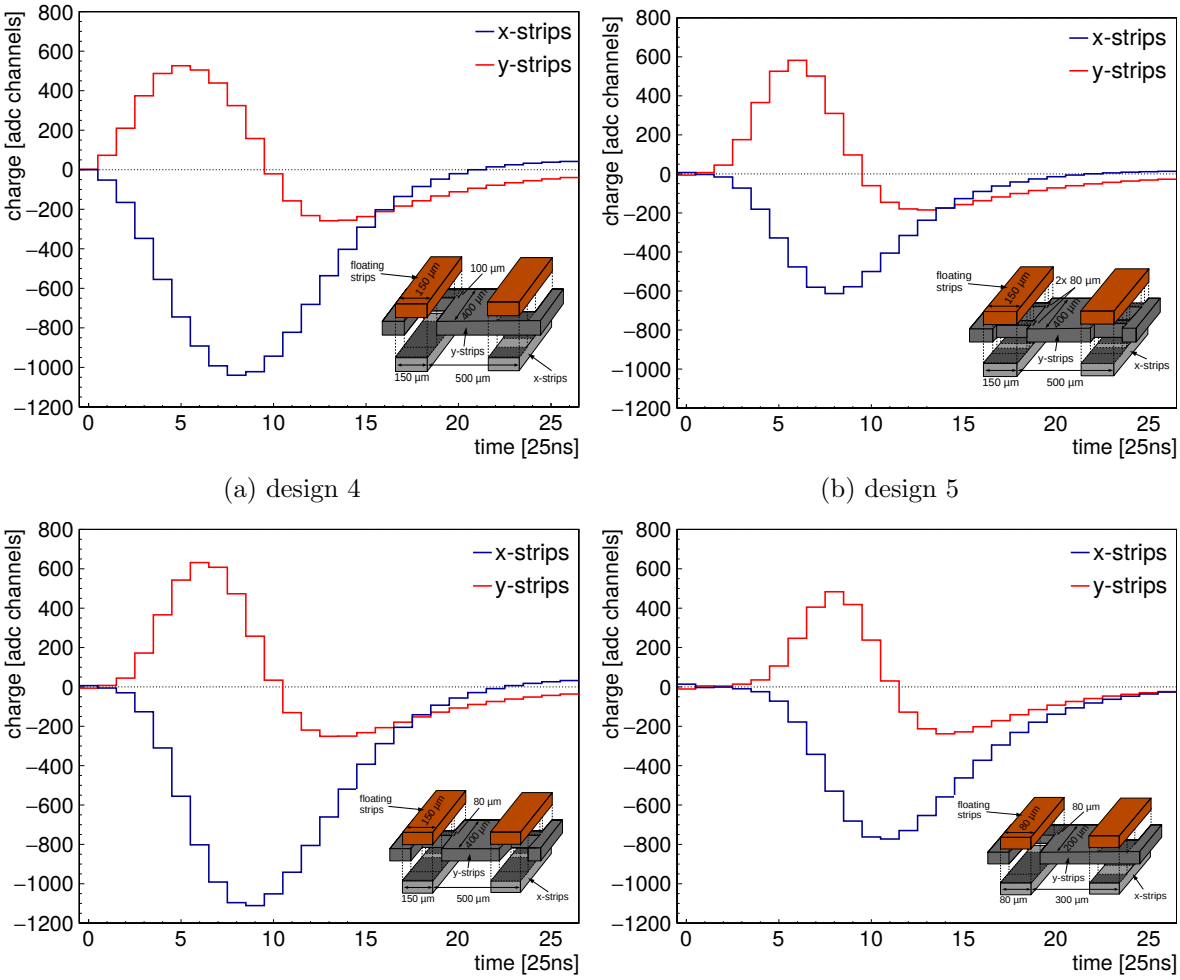

(a) design 4

(b) design 5

(c) design 6

(d) design 7

Figure 6.7: Average signal on the strip with maximum charge created from 40k 20 MeV protons measured with all novel anode designs at $E_{amp} = 37.5\,kV/cm$ and $E_{drift} = 0.33\,kV/cm$, recorded with APV25 front-end boards. The bin content of the x-strips has been multiplied by -1 to emphasize the negative polarity of the signals.

As we see immediately compared to the signals from the classical anode designs in Figure 6.1, the signals measured with the APV25s on the x-layer are not saturated and thus all in a similar range as the signals on the y-layer. The timing difference of the point with maximum charge between x and y-layer is caused by the different ion drift signal components. For the x-layer, the negative signal is created by the ion drift from the floating strips to the micromesh. For the y-layer, the positive signal by the ion movement is induced up to around half of the amplification gap, as discussed in section 4.3, thus the maximum is reached earlier.

The absolute pulse height increase of the y-strips on the novel anode designs compared to the classical designs is presented in section 6.3 with measurements using a ^{55}Fe source in a climate chamber under identical measurement conditions.

The maximum charge on a strip of both readout strip layers for all novel designs is shown in Figure 6.8 as a function of the amplification field at a drift field of 0.33 kV/cm with a Ne:CF_4 80:20 vol.% gas mixture.

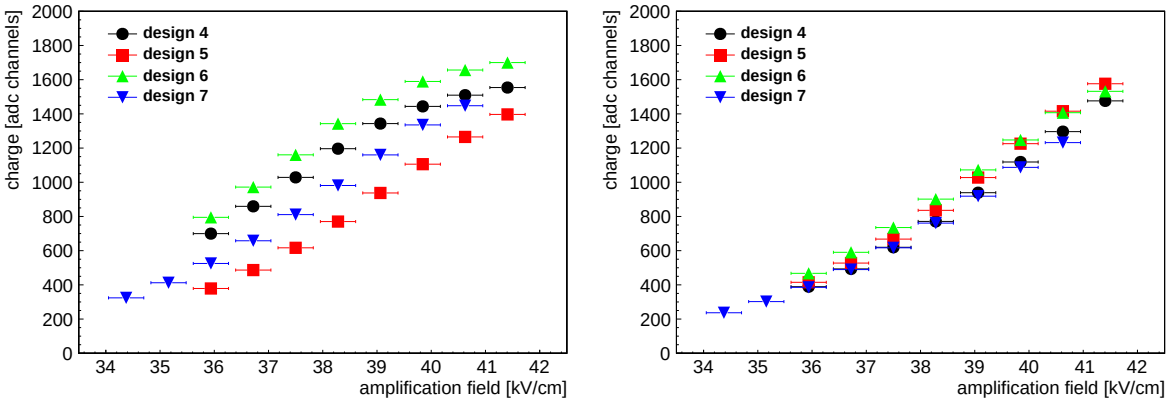

(a) x-layer (b) y-layer

Figure 6.8: Maximum strip charge on the x-strips (left) and y-strips (right) as a function of the amplification field strength and the anode design.

The first thing that comes to mind is the spread of the strip charge on the x-strips, while the y-strips show a quite similar pulse height over the investigated amplification field range. As anode designs 4 - 6 only show a variation of the perpendicular strip width beneath a floating strip, which according to the simulations should only influence the capacitive coupled signal on the parallel strips, this agrees very well with the expectations. Additionally, we find that the perpendicular strip pattern seems to have no distinct influence on the y-strip pulse height. As the strip pitch of design 7 has been reduced from 0.5 mm to 0.3 mm, the reduction of the floating strip width from 0.15 mm to 0.08 mm, which increases the direct induced signal on the y-strips according to simulations, seems to compensate the reduction of the perpendicular strip width between the floating strip from 0.4 mm to 0.2 mm, which leads to a reduction of the y-strip signal. We hereby can conclude that it is possible to build two-dimensional floating strip Micromegas detectors at a strip pitch of only 0.3 mm with maintaining the pulse height on both readout strip layers compared to a 0.5 mm pitch.

To cross-check the expected signal yields on the parallel strip layer, which is dominantly capacitively coupled from the floating strip, Table 6.1 summarizes the capacitances of floating strip and parallel readout strip for all novel anode designs. They are compared with the measured absolute pulse heights at $E_{\text{amp}} = 36.7\,\text{kV/cm}$, where almost no electronics channel saturation of the APV25s was observed according to Figure 6.9.

anode	C_{float} [pF]	$C_{\text{float}}^{x\text{-strip}}$ [pF]	$C_{\text{float}}^{x\text{-strip}}/C_{\text{float}}$ [%]	pulse height [adc channels]
design 4	14.6	4.85	33.3	860
design 5	16.6	4.21	25.4	487
design 6	14.3	5.06	35.3	971
design 7	9.0	3.04	33.8	658

Table 6.1

When comparing the pulse height of the two detectors with same micro-meshs i.e. design 4 with design 6 we find good agreement between the expected capacitive coupling strength and the measured pulse height. As the capacitances stated are a combination of ANSYS simulation and calculations taking into account the different anode PCB geometries, it is difficult to address a certain statistical or systematic error. However an absolute error of about 1 pF seems to be in a reasonable dimension. If we compare design 6 with design 5 we find that the expected coupling ratio of $35.3/25.4 \approx (1.4 \pm 0.2)$ is smaller than the ratio of

the measured pulse heights which is $971/487 \approx (2.0 \pm 0.2)$[3], which can be attributed to a smaller pulse height measured in design 5 caused by the smaller electron mesh transparency. Rescaling the pulse height of design 6 with the above determined factor of (1.42 ± 0.08) for the two different meshes, yields a ratio of $971/1.42/487 \approx (1.4 \pm 0.2)$, which is again in very good agreement with the capacitive coupling predictions. A comparison of the strip pulse height measured on design 7 with design 5 is not feasible, as the amount of charge created in the amplification process is distributed on a different number of strips due to the pitch difference.

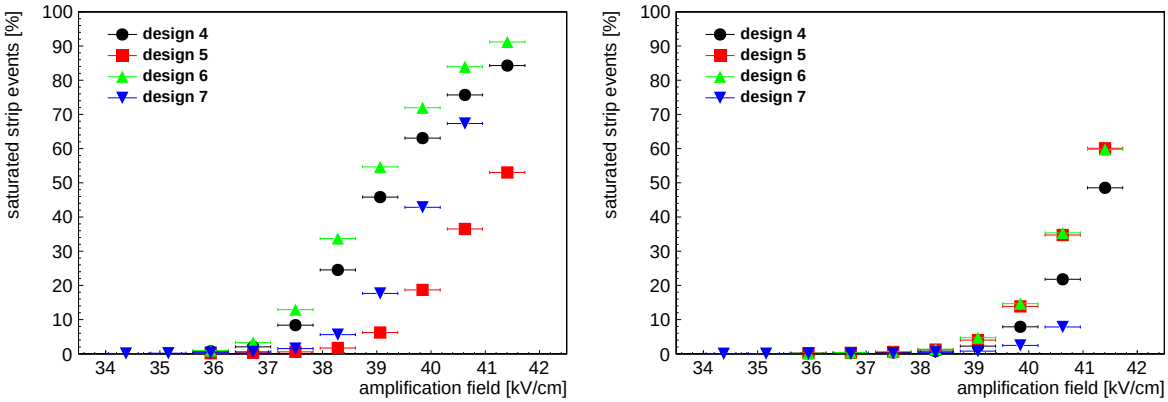

(a) x-layer (b) y-layer

Figure 6.9: Electronics channel saturation on the x-strips (left) and y-strips (right) as a function of the amplification field strength and the anode design.

6.2.2 Hit Cluster Properties

The cluster multiplicity and charge of both readout strip layers for all novel anode designs is shown in Figure 6.10 and Figure 6.11, respectively.

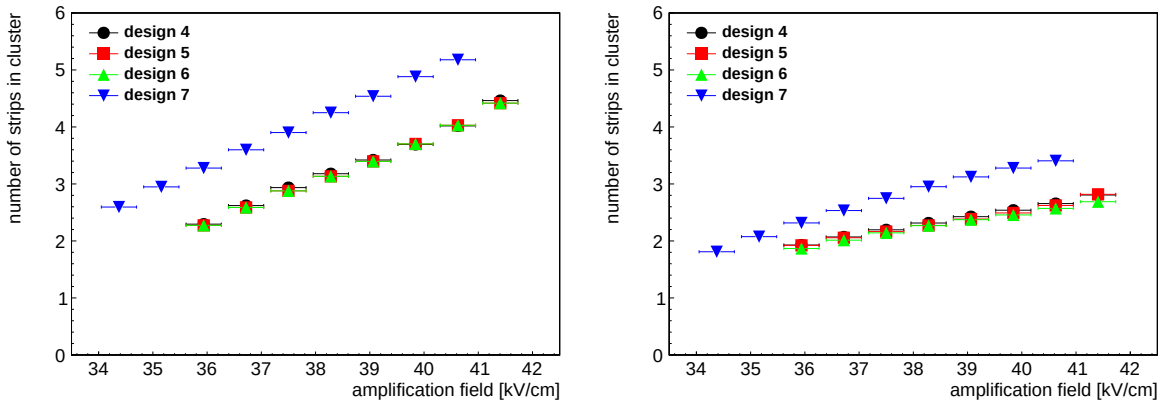

(a) x-layer (b) y-layer

Figure 6.10: Mean number of hit strips in a cluster on the x-strips (left) and y-strips (right) as a function of the amplification field strength and the anode design.

Whereas the cluster multiplicity for designs 4, 5 and 6 are almost identical over the investigated amplification field range, design 7 shows on both readout strip layers a higher multiplicity caused by the reduced pitch from 0.5 mm to 0.3 mm. The ionization cloud of the

[3] uncertainty of the measured pulse height is assumed to be smaller than 50 adc channels

traversing 20 MeV protons should be within about 0.5 - 1 mm, taking into account the electron transverse diffusion in the drift gap and the Gaussian shaped beam profile of the accelerator. Thus we expect a maximum of around 2 - 3 hit strips at a 0.5 mm pitch and 2 - 4 strips at a 0.3 mm pitch. However we see that the x-layer for all anode designs features a higher cluster multiplicity than the y-layer. It can be attributed to two different effects. First, the originally circular shaped ionization cloud entering the amplification region is slightly elongated in the direction perpendicular to the floating strips, as the electron avalanches are pulled to the anode strips, which have a small width/pitch ratio. [4] This leads to a in general higher cluster multiplicity on the x-strips compared to the y-strips. Second, the combination of the capacitive coupling between the floating strips as well as the parallel strips leads in total to a higher charge sharing between the parallel strip layers than the perpendicular strip layer. Thus strips in the x-layer may easier pass the charge level in the analysis to be counted as hit than strips in the y-layer, which causes a different slope in the cluster multiplicity graphs.

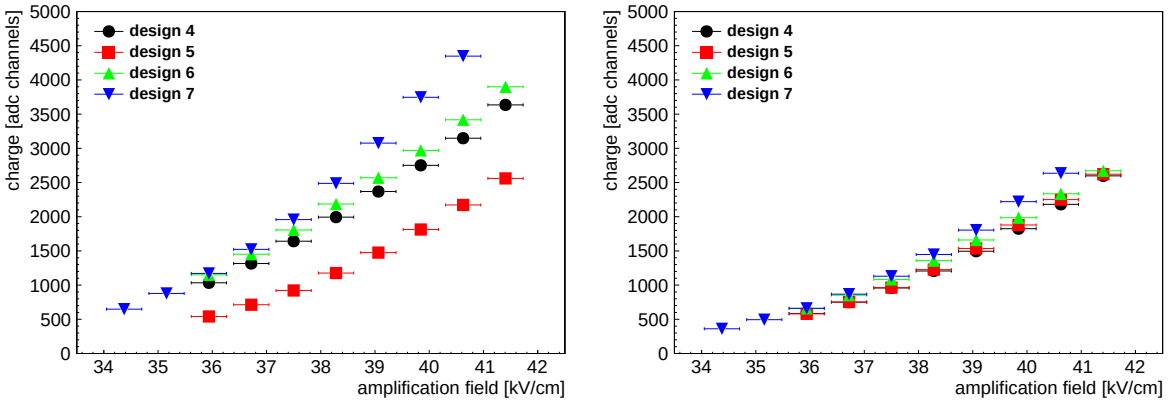

(a) x-layer (b) y-layer

Figure 6.11: Mean cluster charge on the x-strips (left) and y-strips (right) as a function of the amplification field strength and the anode design.

In terms of cluster charge we see the same effect as we have already observed in the strip charge investigation, however with design 7 performing a little better compared to the other designs. It additionally shows a steeper increase of the cluster charge as it is less affected by saturation effects due to the smaller strip pitch. However in terms of absolute pulse height it should not be interpreted too much in the results as there was a one year time difference between the test beam measurements with designs 4 - 6 and design 7, which can cause non-negligible deviations in the absolute gas gain in the detector due to different environmental parameters.

However the cluster charge ratio within one anode design is mostly independent of the environmental parameters and can thus be used to compare the four designs. It is plotted against the amplification field in Figure 6.12. As you can see anode design 4, 6 and 7 perform very similarly with a cluster charge ratio of 0.58 ± 0.03 which is constant up to around E_{amp} =37.5 kV/cm at which point saturation effects on the x-layer increase the ratio virtually. Anode design 5 actually shows that it is possible to tune the pulse height on both readout strip layers to the same value by adjusting the capacitive coupling between the floating strips and parallel readout strips with the correct perpendicular strip width.

[4] A Garfield++ simulation with a 0.3 mm floating strip pitch at a width of 0.08 mm shows that an originally 0.5 mm circular ionization cloud deforms to an ellipsoid with $a = 0.53$ mm and $b = 0.6$ mm at a amplification field of 31.25 kV/cm

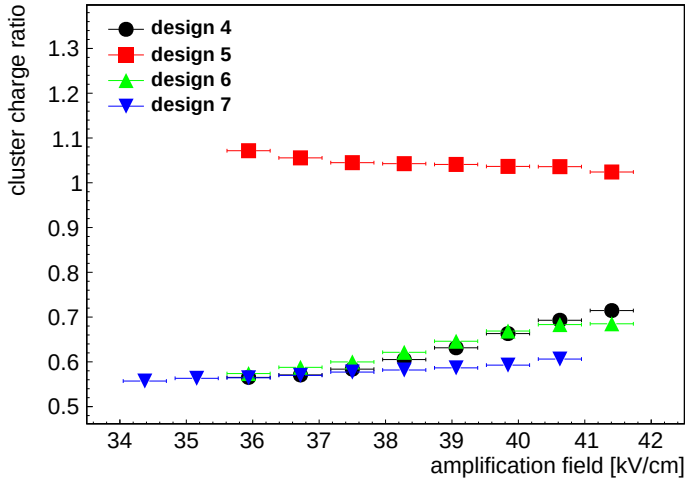

Figure 6.12: Cluster charge ratio y/x of the y-strips cluster charge divided by the x-strips cluster charge as a function of the amplification field strength and the anode design.

6.3 Signal Improvements with an Optimized Anode Design

The signals on both readout strip layers of a classical two-dimensional floating strip Micromegas anode design are compared with a novel one under identical measurement conditions. In particular anode design 3, being the only design of the classical anodes showing similar pulse height signals on both readout strip layers, is compared to the novel anode design 4, which showed the best performance in a test beam at CERN, presented in chapter 8. The measurement setup is explained in detail in the following.

6.3.1 Measurement Setup

The schematic setup of the measurements to compare the two anode designs is shown in Figure 6.13. Two detectors have been assembled carrying either anode design 3 or 4. As anode design 3 features a total of 384 strips, the active area is 9 times bigger than the detector with anode design 4. Both detectors have a 6 mm drift gap, a 25/38 µm micro-mesh and carry 128 µm high pillars on the anode floating strips, which defines the amplification gap. Only master APV25 front-end hybrid boards have been mounted on the detectors to exclude pulse height deviations between master and slave hybrids originating from the flat cable introducing a signal run-time difference, causing the analogue data from the APV25s to be digitized at different point in times. Both detectors have been put in a Memmert ICH 256 climate chamber [Memmert, 2013] to control temperature and relative humidity. During the measurement with both detectors the temperature in the climate box was within $(20 \pm 2)^\circ$ C and the relative humidity within (39 ± 4) %. The ambient pressure was monitored externally and was within (961 ± 4) mbar during both measurements. Temperature and pressure variations on this scale lead to a gas gain variation on the order of 5%, assuming a total gain of $\mathcal{O}(10^3)$, as can be seen from a Garfield++ simulation in Figure 4.6. The detectors were constantly flushed with a Ne:CF_4 80:20 vol.% gas mixture from a pre-mixed gas bottle. During detector operation an overpressure in the active volume of a few mbar was applied to prevent humidity, air or dust entering the detector. Thus the relative humidity in the detector is assumed to be much smaller than the measured value from the climate chamber. However the absolute value inside the active volume was not measured. High voltage to the cathode and anode of the detectors was provided by an ISEG SHQ series precision HV supply

[Iseg, 2017].

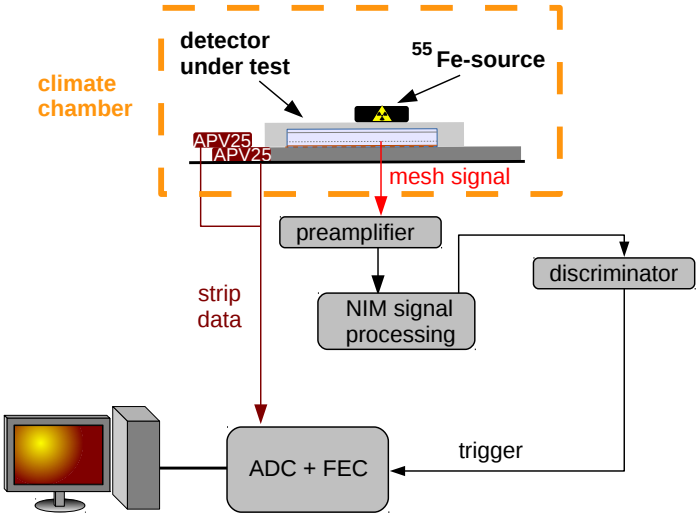

Figure 6.13: Setup for the comparison measurements of the classical and novel optimized anode designs with a ^{55}Fe source, emitting 5.9 keV photons. The trigger required for the SRS based readout system connected to the detector strips is acquired from the micro-mesh signal. The detector is placed in a climate chamber to minimize environmental effects like temperature and relative humidity influencing the signal generation in the detector.

An ^{55}Fe source was used for the comparison measurements, as it emits mono-energetic photons of 5.9 keV which transfers the full energy to a target shell electron in the detector gas volume via photo-absorption. The electron, carrying the 5.9 keV kinetic energy, gets stopped inside the drift region of the detector within less then a few hundred µm. Thus the deposited energy spectrum inside the detector is very well defined by the mono-energetic electron energy. The APV25 based strip readout was triggered by the induced signal on the micro-mesh, which has the opposite polarity compared to the floating strip signal. As typically the micro-mesh is glued to an Aluminum frame which explicitly grounds and removes the possibility to trigger on it, two PVC frames have been developed that allow to contact the micro-mesh with a copper wire and extract the signal via a lemo connection. The positive current signal from the mesh is fed into a charge sensitive Ortec Model 142PC preamplifier [Ortec, 2002], responding with a fast voltage step and an about 75 µs long exponential return to the base-line. It is followed by a 50 Ω impedance adjusted voltage divider with a ratio of about 1:10, necessary as the amplified signal was too high for the discriminator used at a later point. The pre-amplified, attenuated signal is fed into an ORTEC Model 454 Timing-Filter-Amplifier [Ortec, 1969] with the possibility to invert and amplify the signal while reducing electronic noise by additional RC-integration and differentiation stages. The well-shaped voltage pulse is fed into a CAEN Mod.N845 16 channel Low Threshold Discriminator [CAEN, 2019e], which produces a NIM standard logic pulse. To reduce double triggers caused by random electronic noise immediately after the photon trigger signal, the logic pulse is extended to a 1 µs duration by a CAEN Mod.N93B Dualtimer [CAEN, 2019d]. The 1µs long NIM pulse is fed into the NIM input of the SRS FEC, which passes the trigger signal to the APV25 front-end hybrids connected to the strips of the detector. The FEC is connected via 1 Gbit Ethernet to the DAQ computer where the strip data is saved and analyzed.

6.3.2 Strip Signals

Before comparing the signals on both anodes, a pulse height homogeneity scan over the active area was performed with both detectors to neglect pulse height variations caused by a non-uniform amplification gap. However no significant variations were found as the larger detector with the thin anode PCB was already stabilized by the Aramid honeycomb support structure glued on the bottom of the PCB and a stiff Aluminum base plate was screwed to the backside of the smaller detector. The source has then been put on a dedicated position on the entrance window of the detector, stabilized by a thin styro-foam layer. The emittance angle from the source in combination with the distance to − and including − the drift region lead to a circular shaped photon beam profile with a radius of around 1 cm on the anode.

The raw strip signal averaged over 20k photon events on the strip with maximum charge in the detector after baseline removal and common-mode noise correction are shown in Figure 6.14 for both readout strip layers of the classical and novel anode designs at the same amplification and drift field configuration of $E_{amp} = 40.6\,kV/cm$ and $E_{drift} = 0.17\,kV/cm$.

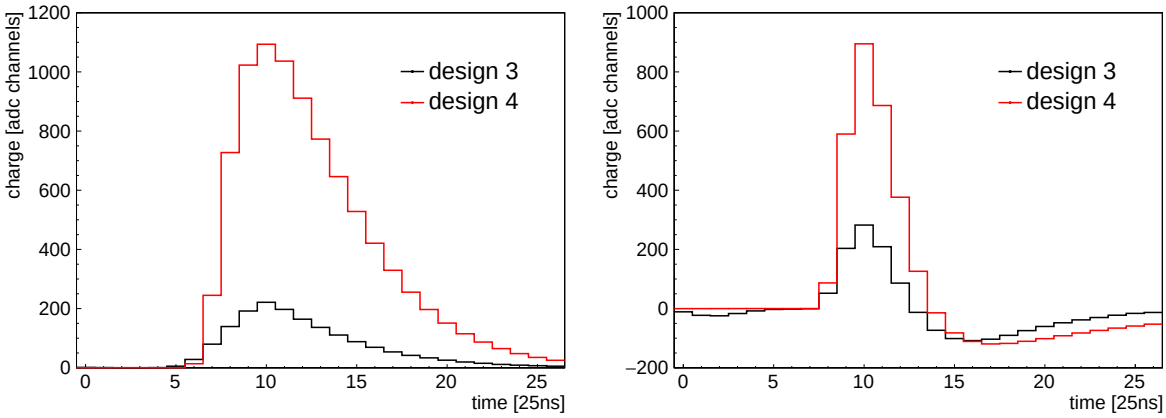

(a) x-layer (b) y-layer

Figure 6.14: Signal on the strip with highest charge on the x-layer (left) and the y-layer (right) for a classical anode (design 3) and a novel optimized anode (design4). The figures are the mean signal from around 20k 5.9 keV photo-electron events from the ^{55}Fe source, measured at 40.6 kV/cm amplification field and 0.17 kV/cm drift field.

The simultaneous improvement of the signal amplitude on both readout strip layers of the novel anode design compared to the classic design is clearly visible. The maximum value increased on the x-layer from (218 ± 50) adc channels to (1093 ± 221) adc channels, where the RMS of the maximum charge has been used as the uncertainty on the mean value. This corresponds to a gain in pulse height on the x-layer of 5 ± 1. On the y-layer the pulse height changed from (280 ± 73) adc channels to (895 ± 184) adc channels, which corresponds to an increase of 3.2 ± 0.7.

It was tried to simulate the change in pulse height on both readout strip layers with the detector model described in chapter 4, with adjusting the strip layer geometry to design 3 and 4. However, it is difficult to simulate the absolute pulse height on the strips, as it is the average over many single particle events. A simulation for 10k photon events in the detector volume would take months, due to the modeling of the avalanche process at high amplification fields. Thus to be mostly independent of statistical fluctuations of avalanche position and gain, a simplified simulation has been performed where 5k electrons have been homogeneously distributed within a radius of 0.5 mm at the beginning of the amplification

region. To speed up the avalanche simulation, the floating strips have been set at only 400 V. The same gas mixture Ne:CF_4 80:20 vol.% as used during the measurements was also used for the simulation, however note that due to the lack of the correct probabilities for the Penning transfer, it was not included in the simulations. The electron start timings have been randomized within a time window corresponding to the estimated travel duration of the electrons in the drift region. Note that thus the absolute pulse height on the y-strips is underestimated as the bipolar shaped currents lead to a lot of charge canceling if the current signal times are equally distributed. Nevertheless the relative pulse height changes of the two strip layers can be compared between the two designs. The front-end response on the strip with maximum charge for all 5k electrons is shown in Figure 6.15, taking into account the strip capacitances and the finite APV25 front-end input impedance of 300 Ω, which has been measured in chapter 4.

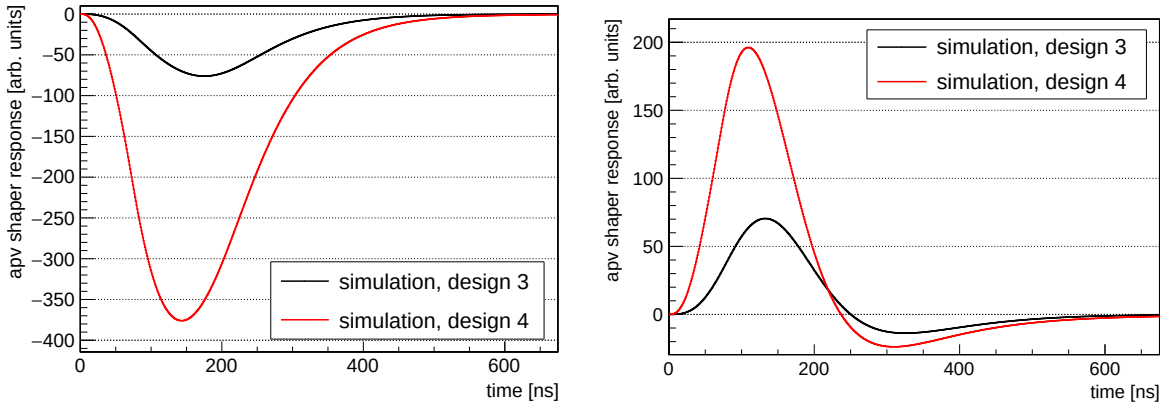

(a) x-layer (b) y-layer

Figure 6.15: Simulated APV25 response on the strip with highest charge on the x-layer (left) and the y-layer (right) for a classical anode (design 3) and a novel optimized anode (design 4). The relative pulse height changes on both layers are in good agreement with the measurements shown in Figure 6.14.

We see a similar increase of the simulated response amplitude on both readout strip layers. For the x-layer, an increase of $-376/-73 \approx 5.0$ is observed. On the y-layer an increase of $196/70 \approx 2.8$. Both simulated relative pulse height increases are close to the measurement results. The pulse height reduction caused by the strip capacitance is listed in Table 6.2. We see that in design 3 the huge strip capacitances lead to a significant reduction of the pulse height recorded by the APV25 chip, while it is negligibly small for the optimized anode design 4.

anode	strip	capacitance [pF]	pulse height reduction [%]
design 3	x-strip	79	7
design 3	y-strip	140	29
design 4	x-strip	11	0.3
design 4	y-strip	14	0.9

Table 6.2: Simulated pulse height reduction in the APV25 front-end boards caused by the strip capacitance and 300 Ω input impedance to the front-end chip.

If we correct for the pulse height reduction caused by the capacitances of the strips (see Table 6.2), we find a raw gain of the total current signal on the x-layer of $(376/0.997)/(73/0.93) \approx$

4.8 and on the y-layer of $(196/0.991)/(70/0.71) \approx 2.0$. While the increase of about a factor of 5 on the x-strips is a result of adjusting the capacitance between floating strip and congruent readout strip via the perpendicular strip width beneath the floating strip, the gain in signal yield on the y-strips of a factor of 2 is mainly caused by reducing the floating strip width-to-pitch ratio.

The charge on the strip with maximum charge as well as the fraction of saturated APV25 events is shown in Figure 6.16 as a function on the amplification field for both readout strip layers of the classical and novel anode design.

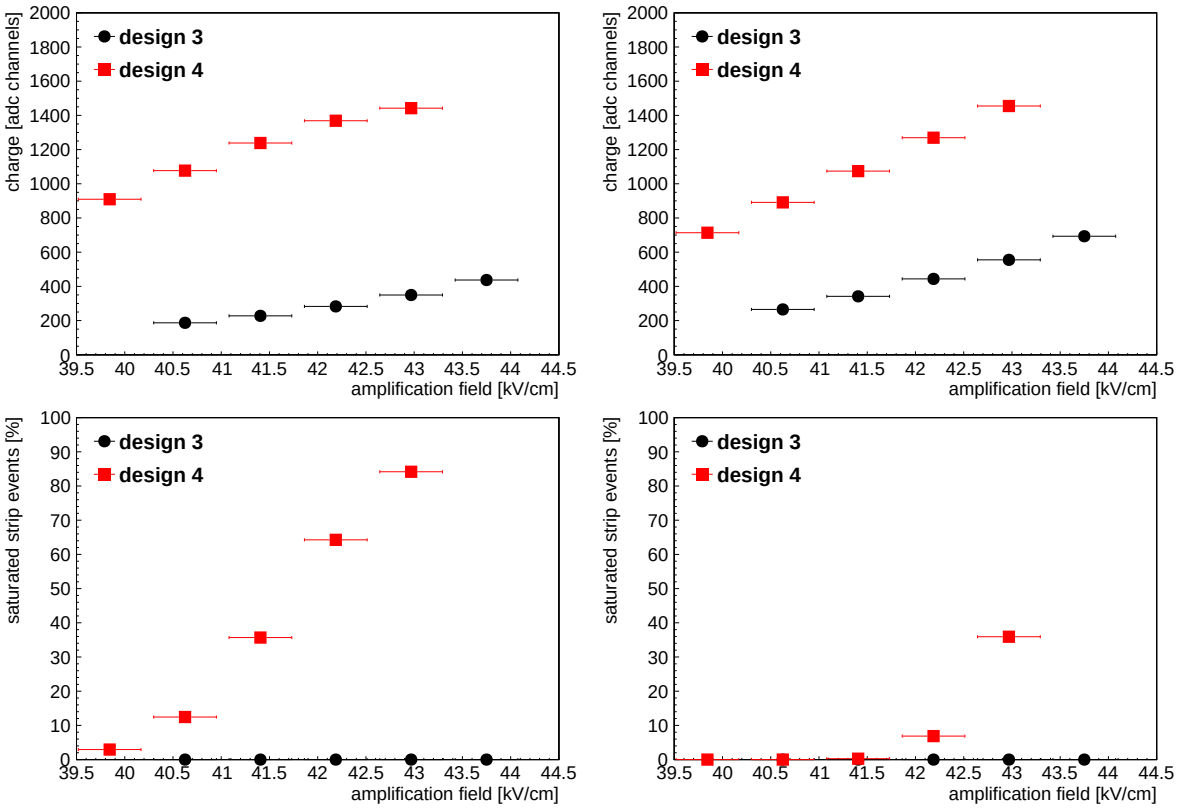

(a) x-layer (b) y-layer

Figure 6.16: Mean value of the maximum strip charge (top) and fraction of saturated strip events (bottom) on the x-layer (left) and the y-layer (right) as a function of the amplification field at $E_{drift} = 0.17\,kV/cm$ with the classical anode (design 3) and the optimized anode (design 4).

We see that the strip charge on both readout strip layers between the two designs is extremely different, as both strip layers of the novel designs show signal pulse heights that are working in a regime where the strip charge is so high that it is close to the saturation limit of the APV25, whereas for the classical designs we are on the edge of small signals barely being detectable. The comparison of the two designs performed at an amplification field of $40.6\,kV/cm$ actually shows that the x-layer of the novel design shows a fraction of around 12% saturated events, which leads to a small underestimation of the mean charge and thus of the calculated increase in pulse height. However no meaningful measurement below this amplification field was performed with the big detector due to electronic noise problems preventing a clean trigger from the mesh signal below the used discriminator threshold.

6.3.3 Cluster Charge and Cluster Multiplicity

The total cluster charge and the number of hit strips in a cluster for the classical and novel anode design are shown in Figure 6.17 as a function of the amplification field.

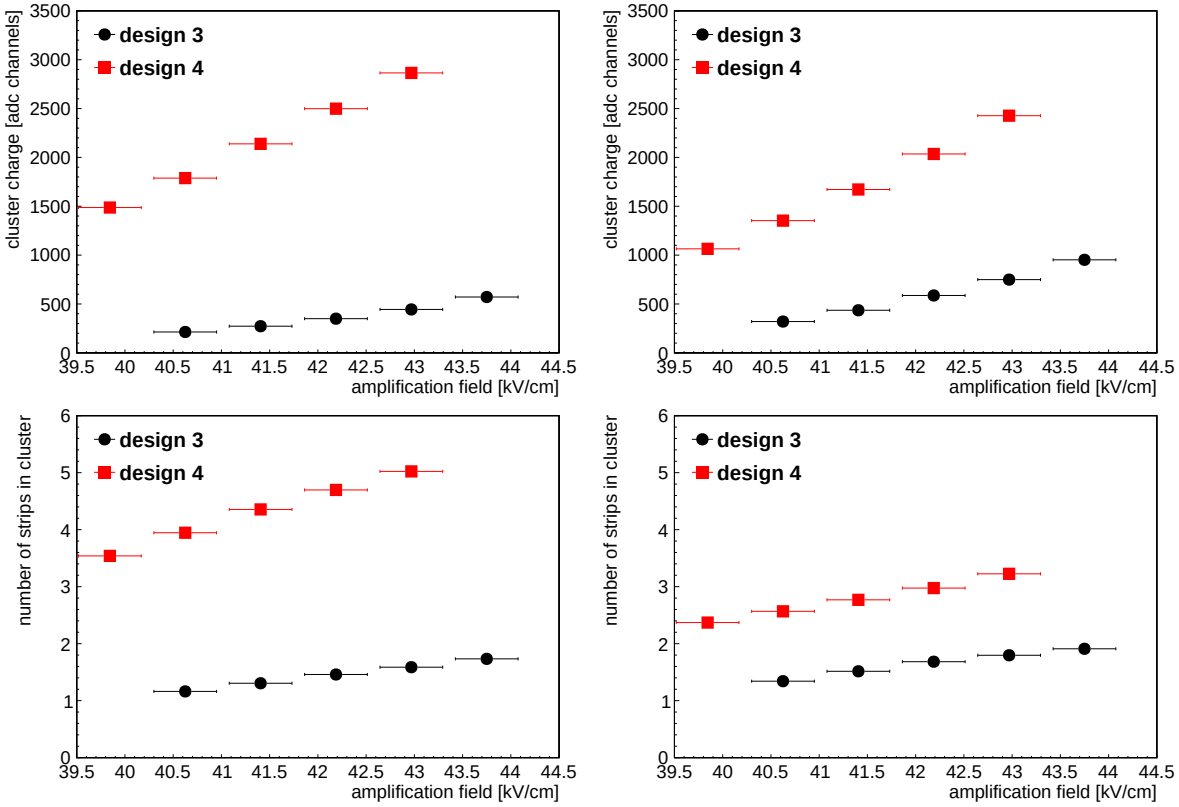

(a) x-layer (b) y-layer

Figure 6.17: Cluster charge (top) and number of strips per cluster (bottom) on the x-layer (left) and the y-layer (right) as a function of the amplification field at $E_{drift} = 0.17\,kV/cm$ with the classical anode (design 3) and the optimized anode (design 4).

A difference in cluster multiplicity between x and y-layer of the novel anode design is again visible and was already discussed in section 6.2.2. The expected exponential increase of the pulse height is suppressed by saturation of the APV25 electronics visible in Figure 6.16. However, we find for the amplification field of 40.6 kV/cm, which shows only small contribution of saturation on the x-layer of the novel anode, a measured cluster charge ratio between novel and classic anode design on the x-layer of $1788/213 \approx 8.4$ and on the y-layer of $1353/320 \approx 4.2$, which is higher than the measured and simulated strip charge ratio determined in the previous section. However, the cluster charge incorporates also charge signals from strips that only respond due to capacitive coupling from their neighboring strips, which is larger in the novel design than in the classical one. For an example lets have a look at the total capacitance of the x-strip in design 3, with $C_{x\text{-strip}} = 79.2\,pF$ which is dominantly created by the capacitance to all perpendicular readout strips with $C_{x\text{-strip}}^{y\text{-strips}} = 59.4\,pF$. Here the capacitance to the neighboring x-strips with $C_{x\text{-strip}}^{neighbors} = 13\,pF$ accounts for a charge sharing of $13/79.2 \approx 16\%$. In design 4 the x-strip capacitance is $C_{x\text{-strip}} = 11.2\,pF$ of which $C_{x\text{-strip}}^{neighbors} = 2.4\,pF$, which corresponds to a charge sharing of $2.4/11.2 \approx 21\%$. Additionally of course also the floating strip charge sharing needs to be accounted for, which was not covered in this quick calculation. Thus we understand that the cluster charge as well as the multi-

plicity is higher in the novel anode design compared to the classic one, as the capacitances are much better distributed between the strip layers.

Chapter 7

Test Beam Measurements with 20 MeV Protons at the Tandem van de Graaff Accelerator in Garching

In this chapter the four novel two-dimensional floating strip Micromegas anode structures, introduced in chapter 5, are characterized in terms of particle reconstruction efficiency with a 20 MeV DC proton beam at the Tandem accelerator in Garching, Munich. A low material budget triple GEM detector has been used as an efficiency reference point as well as for triggering the APV25 front-end hybrids connected to the strips of the detectors. Additional measurements have been carried out with the floating strip Micromegas tilted with respect to the proton beam in two dimensions to check the angle reconstruction on both readout strip layers. Furthermore the beam intensity has been varied from the low kHz regime up to almost 1 MHz, to check the high rate capability especially of the signals on the perpendicular readout strip layer i.e. the two-dimensional floating strip Micromegas in general. In the last section the signal reconstruction on both readout strip layers is compared when changing from the so far used Ne:CF_4 80:20 vol.% detector gas mixture to an Ar:CO_2 93:7 vol.% mixture.

7.1 Setup

The test beam setup for the measurements with 20 MeV protons at the Tandem accelerator presented in this chapter is sketched in Figure 7.1. In total four two-dimensional floating strip Micromegas detectors equipped with anode designs 4 - 7 were tested. The internal structure of the detectors was already described in detail in section 5.3. Upon finished measurements of a detector with one anode design, it has been replaced by the next with another anode design, without unplugging the gas distribution from the detectors. The floating strip Micromegas each have a 6 mm drift region and a 128 µm amplification region. They are flushed constantly with an Ne:CF_4 80:20 vol.% gas mixture, except for the measurements presented in the last section, where the gas has also been changed to Ar:CO_2 93:7 vol.%. The detectors equipped with anode design 4 and 6 were assembled with a 30/70 µm micro-mesh, design 5 and 7 had a 25/38 µm micro-mesh. As for efficiency studies a reference detector is needed, a low material budget triple GEM detector with two-dimensional anode readout structure was placed as close as possible in front of the Micromegas detector, to minimize beam divergence effects. A GEM detector (Sauli [1997]) is a **G**aseous **E**lectron **M**ultiplier, that collects ionization charge in a drift region and amplifies it in at least one GEM foil. The usually 50 - 200 µm thin copper clad foil allows to apply high electric fields on the order of 50 kV/cm inside holes

which are drilled homogeneously distributed over the surface of the foil. Ionization electrons are amplified in Townsend avalanches within the holes and are collected on a grounded anode, segmented into strips. The used two-dimensional GEM detector features an active area of 10 x 10 cm^2 with 250 strips at a pitch of 0.4 mm, allowing position reconstruction of the protons in x- and y-direction with a spatial resolution of below 60 µm [Flierl, 2018].

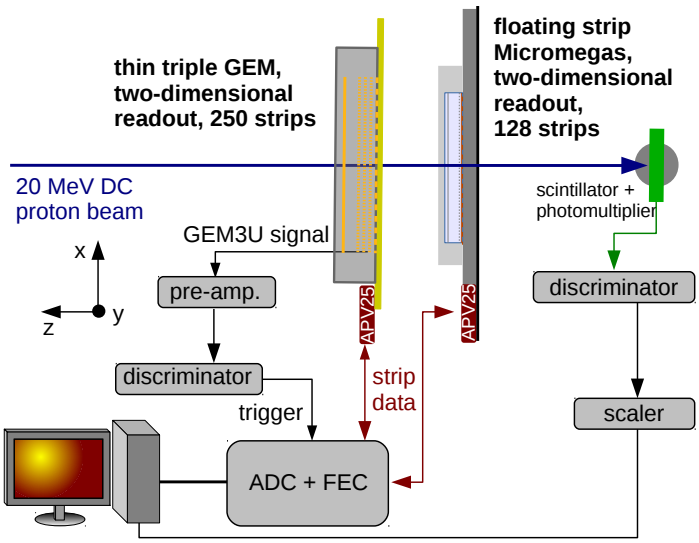

Figure 7.1: Measurement setup of the 20 MeV proton test beam described in this chapter. The trigger required for the SRS-based readout system connected to the detector strips via APV-25 front-end boards is derived from the bottom GEM foil of the triple GEM detector placed directly in front of the Micromegas. For the rate measurements presented in the later sections a scintillator connected to a photo-multiplier tube is used to monitor the beam intensity.

High voltage is provided by a CAEN SY5527 Universal Multichannel Power Supply Mainframe [CAEN, 2019f], equipped with two A1821 12 Channel boards (0.6 W) [CAEN, 2019b] with either positive or negative polarity for the strip detectors and one A1535dn 12 Channel Common Floating Return board (8W) [CAEN, 2019a] for the scintillator. The gaseous detectors have been equipped with APV25 front-end chips interfaced by the SRS. Triggers for the readout of the front-end boards are derived from the GEM detector. In particular, the fast current signal of the bottom GEM foil is fed into a charge sensitive Ortec Model 142PC preamplifier [Ortec, 2002]. The amplified, negative voltage signal, with a fast rise of around 100 ns and an about 75 µs long exponential return tail to the base-line, is directly fed into a CAEN Mod.N842 eight channel Constant Fraction Discriminator (CFD) [CAEN, 2019c], which produces the NIM standard logic pulse used to trigger the FEC. For determination of the proton intensity presented in section 7.5, the floating strip Micromegas has been replaced by a plastic scintillator equipped with a photo-multiplier tube [Hamamatsu, 2007]. The about 10 ns long scintillator signal was directly fed into the CFD. The NIM pulses were counted using FPGA based NIM scaler developed at LMU, transmitting the counted logic pulses within a 1 s time window via RS232 cable to the DAQ computer.

Note that the measurement of the floating strip Micromegas equipped with anode design 7 was performed one year later compared to the other measurements. Thus the absolute pulse height can not be compared to the others, as variations in pressure, temperature or detector gas lead to non-negligible contributions to the total gas gain in the amplification process. However as it was tried to reproduce the same environmental conditions as during the measurements with anode design 4, 5 and 6, the gas gain should be in a similar range.

7.2 Cluster Charge and Cluster Multiplicity

The cluster charge as well as the cluster multiplicity i.e. the number of strips hit within one cluster is investigated as a function of the drift field for a Ne:CF_4 80:20 vol.% gas mixture. The dependence on the amplification field has already been discussed in the previous chapter. Note that the detectors were assembled with different micro-mesh types. Thus the reconstructed pulse height is a factor of (1.42 ± 0.08) higher with the 30/70 µm micro-mesh than with the 25/38 µm micro-mesh at E_{drift}=0.33 kV/cm, which has been calculated in the previous chapter.

A typical cluster charge and multiplicity distribution is shown in Figure 7.2, measured with 30k protons traversing the detector equipped with anode design 4 at E_{amp}=37.5 kV/cm and E_{drift}=0.33 kV/cm.

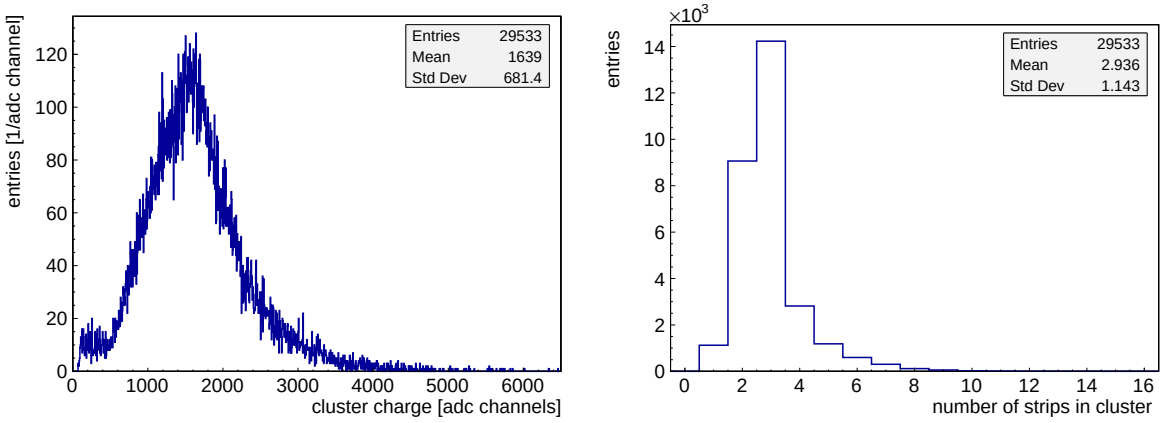

Figure 7.2: Typical distributions for the cluster charge (left) and the cluster multiplicity (right) on the x-layer of design 4 measured with 30k protons traversing the detector at E_{amp}=37.5 kV/cm and E_{drift}=0.33 kV/cm at perpendicular incidence.

The Landau shaped distribution of the proton energy loss in the 6 mm drift region is visible in the cluster charge distribution. Little asymmetries in the peak originate from events where the strip with maximum charge in a cluster exceeds the dynamic range of the APV25 front-end chip of around 1600 adc channels. The mean value of the cluster charge and multiplicity as a function of the drift field is shown in Figure 7.3 and 7.4 for the x and y-layer, respectively.

For the uncertainty on the calculated drift field an uncertainty of ±0.2 mm to the total drift gap of 6 mm is assumed. Uncertainties on cluster charge or multiplicity are the error of the mean value from the histograms. If no error bars are visible, the markers are bigger than the error.

We see for all designs and both readout layers a similar dependence of cluster charge and multiplicity on the drift field. As the cluster multiplicity is basically following the charge of the strip, the focus in the following discussion is on the charge. First, an initial rise of the charge from small drift fields up to around 0.2 - 0.3 kV/cm is observed, followed by a gentle fall for increasing fields. For high drift fields the ratio of E_{amp}/E_{drift} shrinks which reduces the micro-mesh's electron transparency, as more field lines will end on the mesh (see section 2.5). For small electron drift velocities i.e. small drift fields, ionization electron attachment to the gas atoms as well as recombination with the ionization ions reduces the total number of electrons reaching into the amplification region. Additionally the APV25 front-end chip pulse shaping time of $\tau_p = 50$ ns reduces the measured pulse height, if the arrival of individual ionization electrons at the amplification gap is deviating too much from

this time window.

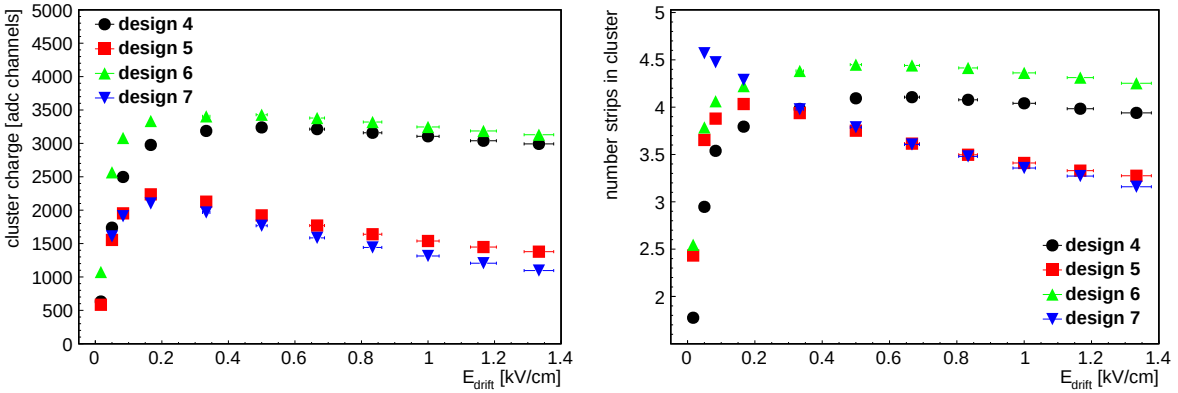

Figure 7.3: Cluster charge (left) and multiplicity (right) on the x-layer as a function of E_{drift} for all four anode designs. Note that design 4, 5 and 6 have been measured at E_{amp}=40.6 kV/cm whereas design 7 only at E_{amp}=37.5 kV/cm and that design 4 and 6 have been assembled with a 30/70 µm micro-mesh, design 5 and 7 with a 25/38 µm micro-mesh.

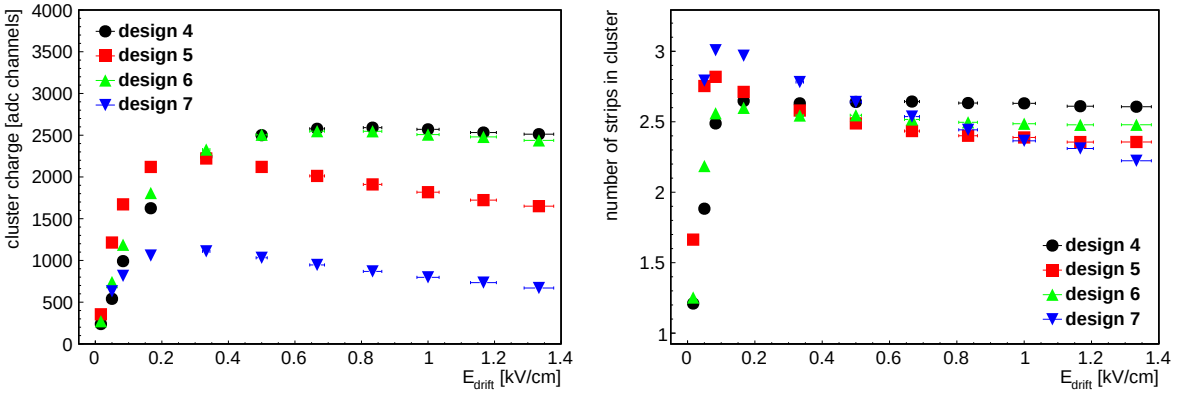

Figure 7.4: Cluster charge (left) and multiplicity (right) on the y-layer as a function of E_{drift} for all four anode designs. Note that design 4, 5 and 6 have been measured at E_{amp}=40.6 kV/cm whereas design 7 only at E_{amp}=37.5 kV/cm and that design 4 and 6 have been assembled with a 30/70 µm micro-mesh, design 5 and 7 with a 25/38 µm micro-mesh.

In the following, the pulse height dependence on the drift field is discussed using the example of the x-layer as it is mainly depending on the effects described above. The y-layer shows a similar but slightly different behavior, as also effects like electron drift velocity or diffusion can influence the pulse height. It will be discussed in more detail in section 7.6.

The differences of design 4 and 6 compared to designs 5 and 7 in Figure 7.3 are caused by the different micro-meshs used. The 30/70 µm micro-mesh shows an average pulse height drop of (8.2 ± 0.4) % from the point of maximum pulse height at around 0.33 kV/cm up to the highest investigated drift field of 1.33 kV/cm. The 25/38 µm micro-mesh leads to a pulse height reduction of (43 ± 5) %. As you can see from Figure 2.6, the simulated transparency drop for Ne:CF_4 and a 30/70 µm micro-mesh is around 10 %, which is similar to the measured pulse height drop. For the 25/38 µm micro-mesh, the simulation predicts a pulse height drop of about 47% over the drift field variation, which is in agreement with the measurement. Both measured pulse height drops are a little smaller than the simulation predicts, which can be attributed to electron attachment and recombination for smaller drift velocities, which

has not been taken into account in the simulation. A comparison of the mesh transparency for two different detector gases can be found in section 7.6.

Contrary to the expectation for a pure Ne:CF_4 80:20 vol.% gas mixture, the pulse height decreases already for drift fields smaller than 0.3 kV/cm in detectors equipped with the 30/70 µm micro-mesh. This should not occur in this drift field region due to the high electron drift velocity with this detector gas. However the µTPC angle measurements in section 7.4 show that the detector gas for this particular measurement was contaminated by about 23 % relative humidity (i.e. H_2O gas) which leads to an effective electron drift velocity smaller than 25 µm/ns for $E_{drift} \leqslant 0.2$ kV/cm that can explain the observed pulse height drop due to a higher possibility for electron attachment or recombination.

For the 25/38 µm micro-mesh in general a much stronger dependence of the mesh transparency is expected for increasing drift field, when comparing it to the 30/70 µm micro-mesh in Figure 2.6 (left). However, looking closer at designs 5 and 7, which show similar pulse height, the impact of the smaller drift velocity is again visible: The pulse height of design 7 falls more prominently than the pulse height of design 5. As design 7 was measured one year later and shows the expected transparency related decrease of pulse height for the used gas mixture (see Figure 7.18 (right)), the difference of the two curves above a drift field of 0.17 kV/cm can be attributed again to the contaminated gas in the measurements with design 5.

7.3 Efficiency

The efficiency of both readout strip layers of the two-dimensional floating strip Micromegas detectors are investigated in this section as a function of the amplification and drift field. The efficiency ϵ is defined as

$$\epsilon = \frac{n_{\text{good}}}{n_{\text{tracks}}} = \frac{n_{\text{good}}}{n_{\text{good}} + n_{\text{bad}}} \quad , \tag{7.1}$$

where n_{tracks} is the number of proton events registered by the GEM detector[1] and n_{good} the number of protons registered in the floating strip Micromegas within a window of $\pm 5\sigma$ around the Gaussian residual distribution as shown in Figure 7.5.

The residual width of $\sigma \approx 3$ mm is a combination of the proton beam divergence as well as multiple scattering of the low energy protons within the anode PCB of the GEM detector and does not represent the detector internal spatial resolution of determining the hit position of the protons. As the efficiency determination is simply a counting experiment of the two independent variables n_{good} and n_{bad}, the error of the efficiency has been calculated by Gaussian error propagation of equation 7.1.

A cut on the measured position of the protons in the GEM detector was applied to neglect protons which traverse the GEM but not the floating strip Micromegas due to the active area size difference of the two detectors. Additionally a cut on the proton signal timing in the GEM detector was applied to neglect too early or too late events registered by the GEM which may be out of the data acquisition time window of the APV25 boards attached to the floating strip Micromegas.

[1] The detection efficiency of a GEM detector is usually above 95% for MIP's, see [Flierl, 2018]. Thus for the much denser ionizing protons it is assumed to be close to 100%.

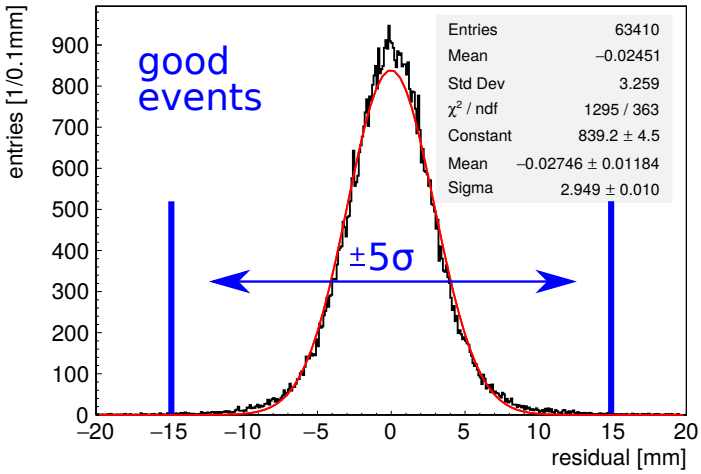

Figure 7.5: Residual between the measured hit in the x-layer of the GEM detector and the x-layer of the Micromegas, fit with a Gaussian function. To extract the efficiency of the Micromegas, the events inside a $\pm 5\sigma$ range are counted and divided by the total number of registered hits in the GEM.

The efficiency as a function of the amplification and drift field is shown in Figure 7.6. If no error bars are visible the marker size is bigger than the errors.

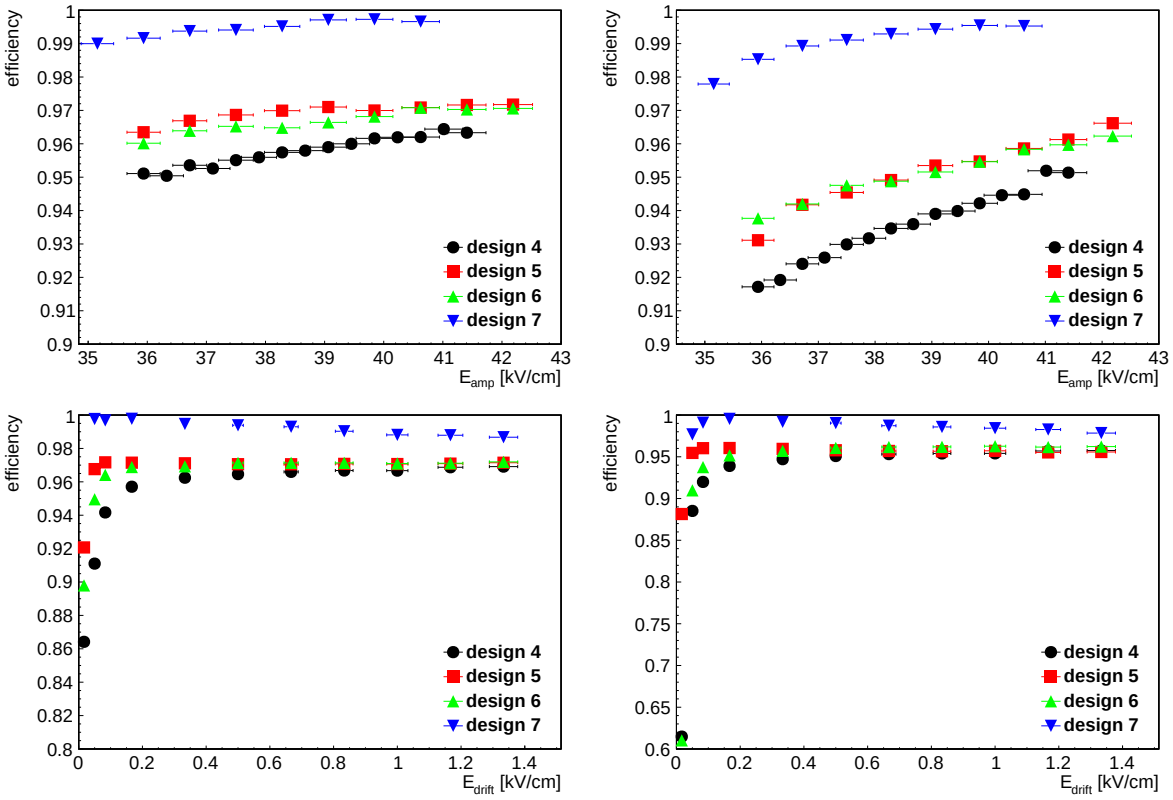

(a) x-layer (b) y-layer

Figure 7.6: Efficiency of the x-layer (left) and the y-layer (right) as a function of E_{amp} at E_{drift}=0.33 kV/cm (top) and E_{drift} (bottom) for all investigated anode designs. Note that during the drift scan design 4, 5 and 6 have been measured at E_{amp}=40.6 kV/cm whereas design 7 only at E_{amp}=37.5 kV/cm.

Over the full amplification field range an efficiency over 95% for the x-layers and over 91% efficiency for the y-layers is observed. For a dedicated choice of amplification and drift field, efficiencies above 95% are reached on both readout strip layers for anode designs 4 - 6 and over 99% efficiency for design 7. For increasing amplification field both layers reach efficiencies above 95%. However the y-layers show a stronger dependence on the amplification field as the x-layers. The events responsible for the difference in efficiency between both readout strip layers are protons traversing the detector at or close to the pillars. As the pillars are elongated in direction of the perpendicular strips with a size of 0.4 x 2 mm, one pillar can cover a perpendicular readout strip completely on the full length of 2 mm. As the induced signal on the perpendicular readout strip is a very localized coupling, the pillar shields the avalanche signal from the readout strip almost completely, while only a fraction is shielded from the floating strip. Increasing amplification field recovers the signal loss around the pillars, thus increasing the efficiency. However as the pillar size was rather big for the investigated designs, smaller pillars with dimensions 0.2 x 1.5 mm seem much more suitable for a floating strip pitch of 0.5 mm. This would reduce the single pillar surface by 62.5% and consequently reduce the impact on the perpendicular strips' efficiency considerably.

If we look at the efficiency as a function of the drift field we see the turn on of the efficiency for very small drift fields caused by also small pulse height until around 0.17 kV/cm. For drift fields up to 1.33 kV/cm almost no degradation of the efficiency is observed, staying around 95% for designs 4 - 6 and above 98% for design 7. The difference in efficiency comes from a different proton beam profile, which was much more focused for the measurements with design 7. Figure 7.7 shows the reconstructed proton beam profile measured with anode design 4 and 7. The focused beam spot with the measurements with design 7 is clearly visible. Due to the beam hitting in the middle between pillars, the inefficiency caused by the pillars is negligibly small. In contrast to that the inefficient spots of anode design 4 at the position of the pillars are clearly visible.

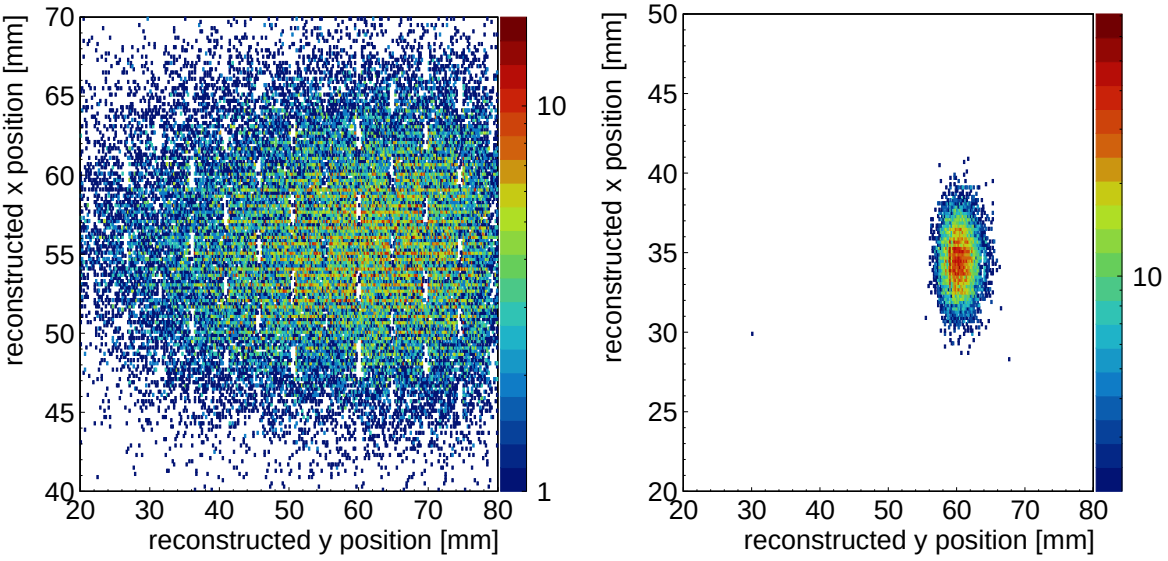

(a) anode design 4

(b) anode design 7

Figure 7.7: Reconstructed proton hit positions for a measurement with anode design 4 (left) at E_{amp}=39.8 kV/cm and E_{drift}=0.33 kV/cm and with anode design 7 (right) at E_{amp}=37.5 kV/cm and E_{drift}=0.33 kV/cm. The well focused beam spot for the measurements with anode design 7 is visible. The inefficient spots at the positions of the pillars are also visible, but much more pronounced in the measurements with anode design 4, where a more diverged beam was used.

7.4 µTPC Angle Reconstruction

To test the µTPC angle reconstruction of both readout strip layers in the novel anode structures, the detector has been tilted with respect to the proton beam axis. The underlying analysis method for inclined tracks has been explained in section 3.5.

Measurements have been performed with the detectors equipped with anode design 4, 5 and 6 at angles 15°, 30° and 40°. Usually the detectors were tilted with respect to one readout strip layer direction to explicitly test the µTPC angle reconstruction for the respective strip layer. However also a measurement with the detector being tilted simultaneously with respect to both readout strip layers has been performed with anode design 5. This is shown by the photography of the measurement setup at the test beam hall at the Tandem accelerator in Figure 7.8. The beam pipe, GEM detector for triggering and the other two floating strip Micromegas detectors equipped with anode design 4 and 6 are also visible.

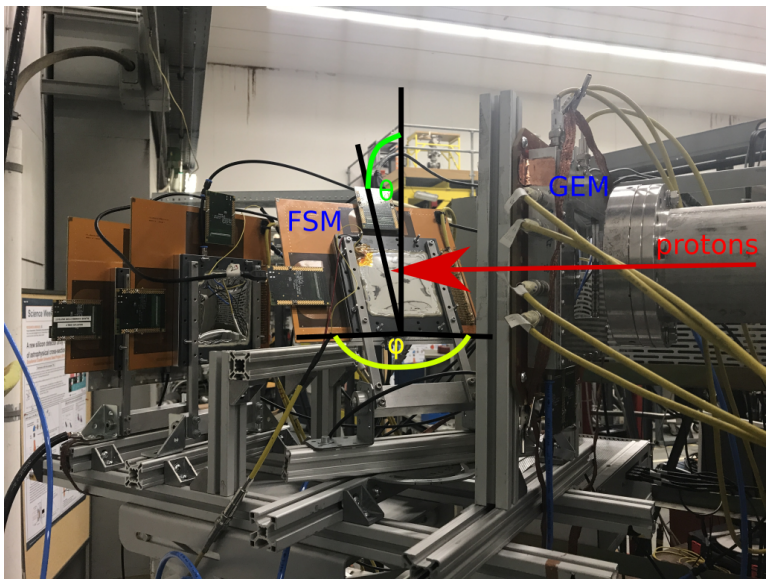

Figure 7.8: Picture of the measurement setup at the Tandem accelerator for the µTPC angle reconstruction measurements. Here, one of the floating strip Micromegas (FSM) has been tilted in both directions with respect to the proton beam, which still perpendicularly traverses the GEM detector.

The principle of a particle passage inclined with respect to both readout strip layers of the anode PCB is sketched in Figure 7.9 (left). Due to the constant drift velocity of the electrons in the drift region, the drift time can be directly translated into a position in the drift gap and thus the full track of the traversing particle can be reconstructed. The reconstructed angle is shown in Figure 7.9 (right), where the detector equipped with anode design 5 has been tilted by 40° with respect to the x-readout strips and by 30° with respect to the y-readout strips. It is clearly visible that the angle reconstruction works independently for both readout strip layers. The reconstructed angle is a little smaller on both readout strip layers. It is a consequence of a deviation between assumed and actual electron drift veloicity in the drift region. It is explained in the following.

The angle reconstruction by the µTPC method requires the precise knowledge of the electron drift velocity, as can be seen in equation 3.5. Usually it can be simulated with packages like MAGBOLTZ, if the precise volumetric gas mixture is known. However, if deviations between the µTPC reconstructed angle and the actual inclination angle – which is known in this case as the detector has been explicitly precisely tilted to that angle – are observed,

a drift time measurement can be performed to reconstruct the effective drift velocity inside the active volume of the detector. For this, the timing difference of fastest and slowest strip responding in a cluster of strips can be directly interpreted as the maximum drift time of the electrons i.e. the drift time between cathode and micro-mesh. By knowing the drift distance of (6.0 ± 0.2) mm, the drift velocity can be calculated. The simulated and measured drift velocity as a function of the drift field is shown in Figure 7.10.

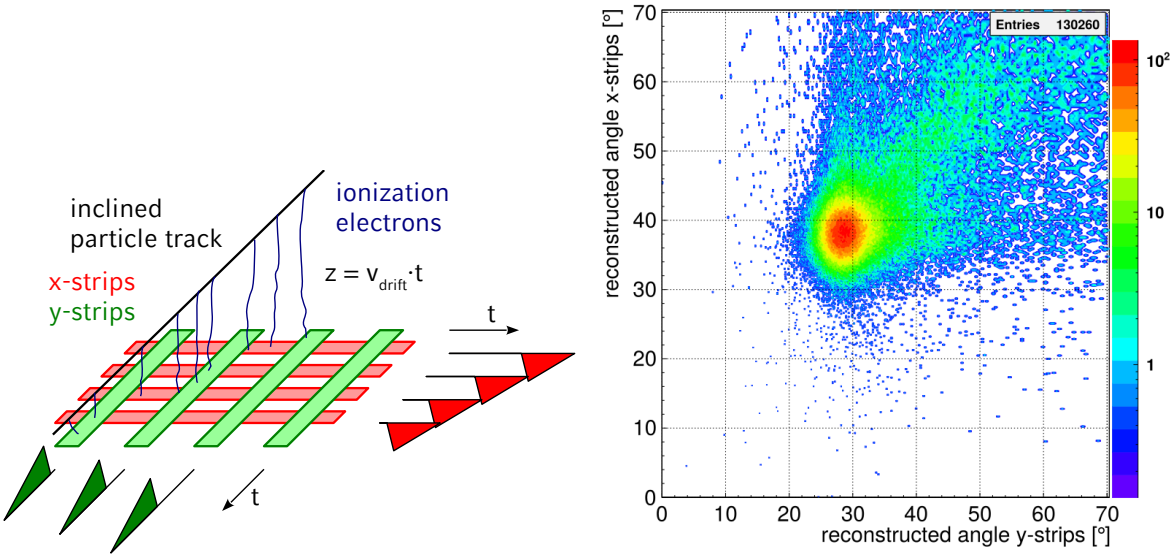

Figure 7.9: Schematic of a particle traversing the detector under an angle with respect to both readout strip orientations (left, figure courtesy of J. Bortfeldt) of the two-dimensional floating strip anode, opening the possibility to reconstruct the full track with the timing informations measured on both readout strip layers separately. Reconstructed angles of around 130 k protons (right) traversing the detector under an angle of 40° with respect to the x-readout strips and 30° with respect to the y-readout strips.

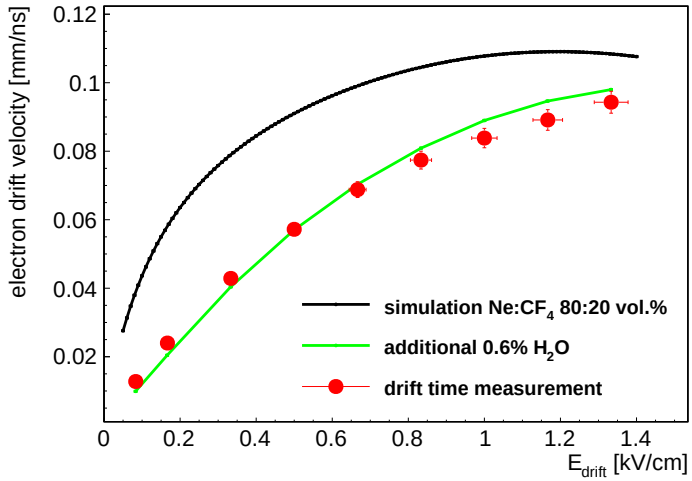

Figure 7.10: Electron drift velocity as a function of E_{drift} for a nominal Ne:CF_4 80:20 vol.% MAGBOLTZ simulation (black), an additional 0.6 vol.% humidity (green) and from a drift time measurement with the x-layer of anode design 4 at 40° inclination tilted w.r.t. the proton beam. The systematically smaller reconstructed drift velocity is clearly visible and might be due to humidity in the detector system.

As the reconstructed electron drift velocity via the drift time measurement turns out to be systematically lower than from the simulation for a Ne:CF_4 80:20 vol.% gas mixture, different MAGBOLTZ simulations have been carried out to find the reason for this. One possibility is a wrong volumetric admixture between Ne and CF_4. However, to achieve such low electron drift velocities, one would have to go to mixtures of more than 90 vol.% Neon. As a pre-mixed gas bottle has been used for all measurements presented in this chapter with an accuracy of (20.05 ± 0.40) vol.% CF_4, such a huge deviating admixture of the two components can be excluded. Another possibility is that either air or left-over humidity in the detector system cause a reduced effective drift velocity. The latter seems more plausible, as more than 10 vol.% of air are necessary to reduce the velocity to the observed, measured values. A simulation with around 0.6 vol.% H_2O left-over humidity i.e. about 23% relative humidity in the gas matches the reconstructed drift velocity, which has also been included in Figure 7.10.

The measured effective electron drift velocity, extracted from the first scan through the drift field with the y-layer of anode design 4 at 40°, has been used to calculate the angle from the µTPC line fit. In the following, the most probable reconstructed angle and the angular resolution is investigated as a function of the amplification and drift field, see Figure 7.11 and 7.12, respectively. Both are determined by a fit of a piece-wise Gaussian function to the one-dimensional angle distribution, as shown in Figure 3.10. As the µTPC reconstruction results are very similar for all anode designs, only the results for design 4 are presented.

The most probable reconstructed angle is almost constant as a function of the amplification field for 30° and 40° and matches the expected angle well. The angular resolution improves however for higher values of the amplification field, as also smaller charge signals are being recovered, increasing the number of data points usable for the µTPC line fit thus improving the quality. Only for the smallest investigated angle 15°, the reconstructed angle is systematically larger as well as the angular resolution degrades with increasing amplification field, caused by higher strip signals which are capacitively coupled also to neighboring strips of the cluster. The higher capacitive coupling of the x-layer compared to the y-layer is visible, as it is a combination of floating strip charge sharing and x-strip charge sharing. This effect is less pronounced for higher angles as the charge is distributed on more strips.

The dependence of the most probable reconstructed angle on the drift field needs some further explanation. As the effective electron drift velocity used for the angle reconstruction has been determined only once from the drift scan with the y-layer at 40°, the detector relative humidity present in the detector active volume may vary from measurement to measurement. In the chronological sequence of test beam measurements the y-layer has been investigated first from large to small inclination angles then the x-layer again from large to small angles. Thus the last measurement was with the x-layer tilted at 15°. A good agreement with the reconstructed angle at the drift scan with the y-layer at 40° and 30° is achieved. For the measurements with the x-layer we see a stronger dependence on the drift field, which tend to reconstruct too large angles for $E_{drift} \leqslant 0.5\,kV/cm$. This is equivalent to a drift velocity which has increased compared to the velocity determined from the first drift scan with the y-layer, due to flushing the detector with the dry pre-mixed gas and thus reducing the humidity present in the detector.

The angular resolution shows for all measurements a very similar dependence on the drift field. For small drift fields i.e. $E_{drift} \leqslant 0.33\,kV/cm$ the angular resolution decreases caused by smaller pulse height. For higher drift fields the combination of smaller pulse height caused by smaller micro-mesh transparency as well as faster electron drift velocities degrade the µTPC resolution. Optimum angular resolutions are observed for the highest inclination angles at high amplification fields with a drift field around (0.17 - 0.33) kV/cm, which represents the optimum between pulse height and drift velocity. For the x-layer and y-layer optimum angular

resolutions of $\binom{+2.5^\circ}{-1.9^\circ}$ and $\binom{+2.9^\circ}{-2.2^\circ}$ are found, respectively. If we compare this resolution with the optimum found angular resolution from chapter 8 measured with high energy nearly minimum ionizing particles with $\binom{+2.2^\circ}{-1.8^\circ}$ and $\binom{+2.1^\circ}{-1.7^\circ}$ for x- and y-layer respectively, we conclude that multiple Coulomb scattering of the low energy protons in the readout structure of the GEM detector as well as the beam divergence cause non-negligible degradation of the angular resolution.

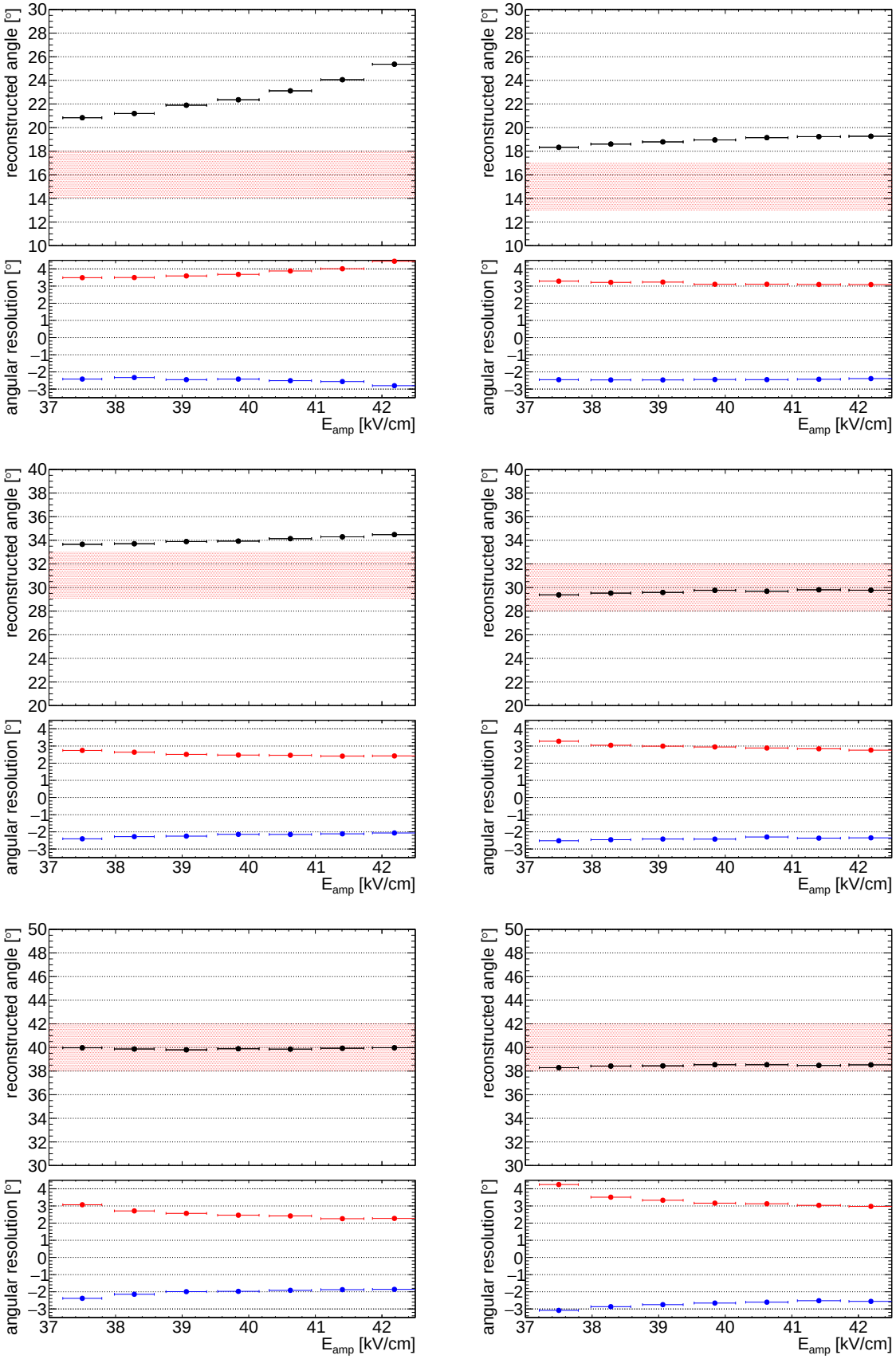

Figure 7.11: Reconstructed most probable angle and angular resolution as a function of E_{amp} at E_{drift}=0.33 kV/cm measured with the x-layer (left) and the y-layer (right) of anode design 4 at angles around $(15 \pm 2)°$ (top), $(30 \pm 2)°$ (middle) and $(40 \pm 2)°$ (bottom). The red shaded band is the inclination of the detector measured with a tilt meter.

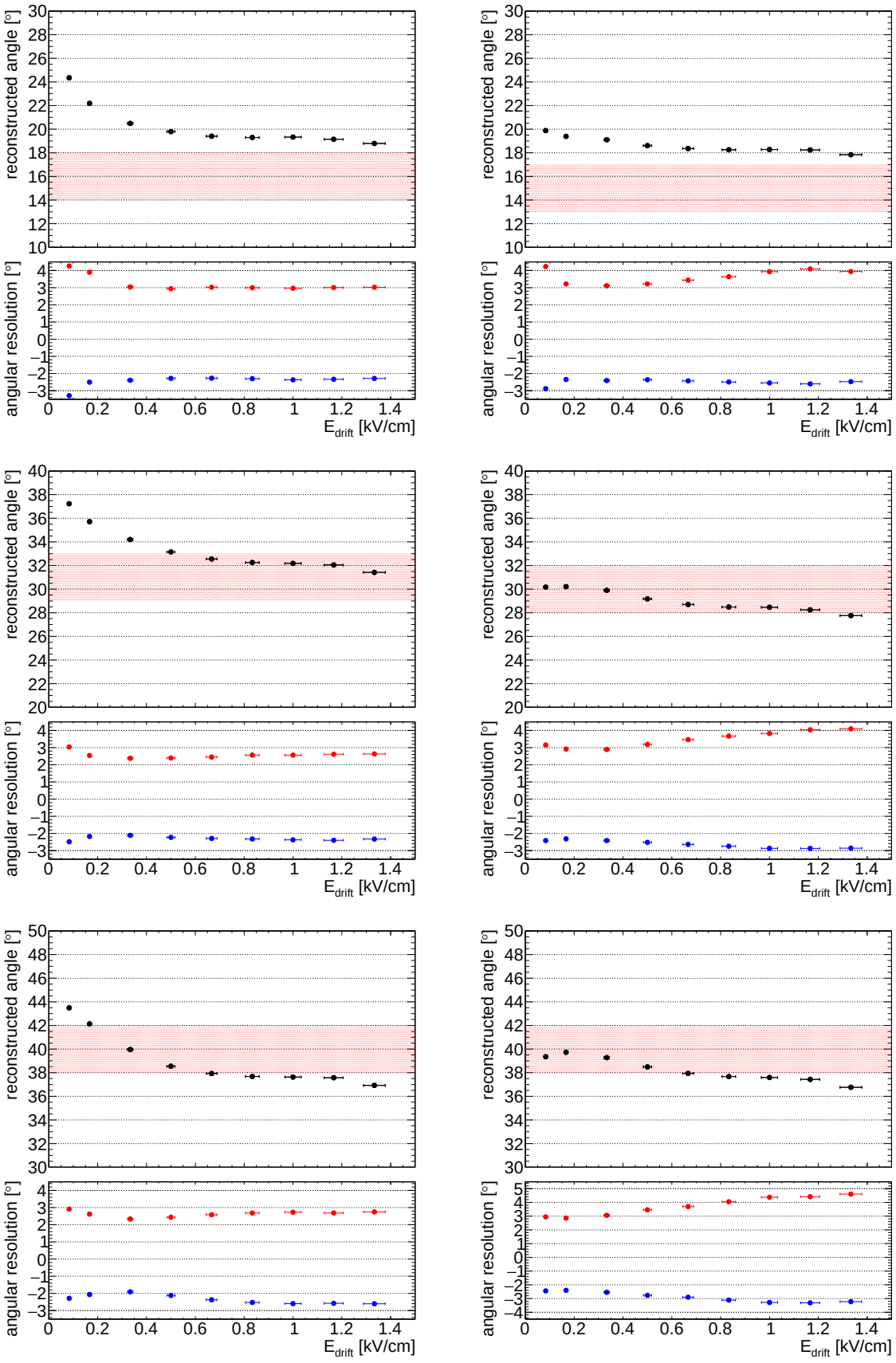

Figure 7.12: Reconstructed most probable angle and angular resolution as a function of E_{drift} at E_{amp}=40.6 kV/cm measured with the x-layer (left) and the y-layer (right) of anode design 4 at angles around $(15 \pm 2)°$ (top), $(30 \pm 2)°$ (middle) and $(40 \pm 2)°$ (bottom). The red shaded band is the inclination of the detector measured with a tilt meter.

7.5 High Rate Measurements

The signal reconstruction capabilities of both readout strip layers of the two-dimensional floating strip Micromegas is investigated as a function of the proton beam intensity in the following. For the determination of the proton rate, the Micromegas has been replaced by a scintillator, where the discriminated signals are counted in 1 s long windows with an FPGA based NIM scaler. As the lowest possible beam current of the tandem accelerator is a few nA at the beam exit window, absorbers on the high energy side of the accelerator had to be used to reduce the proton rate. Due to the internal structure of the absorbers[2], the beam profile of the protons after the absorbers is different, which makes the determination of the particle flux i.e. intensity per surface difficult. Thus in the following it is always referred to beam intensity, defined as the number of protons which are counted by the scaler. In total four different intensities have been measured from the low kHz rate up to almost 1 MHz, where the accelerator delivered the intensities with fluctuations of below 2%. The absorber permutations are listed in Table 7.1. As the passage of simultaneous protons is not always counted correctly by the discriminator, the absolute values for the two highest rate points are probably underestimated by 20%.

An event display as seen by the y-layer of anode design 5 for the highest measured intensity is shown in Figure 7.13, recorded by APV25 front-end boards. Four signals of protons traversing the detector within a time-window of around 250 ns with a spatial separation within 7 mm i.e. 14 strips are visible.

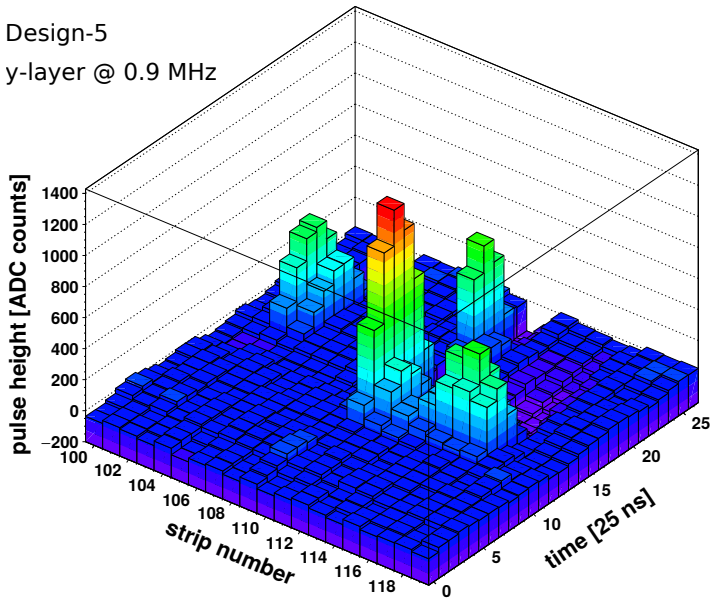

Figure 7.13: Typical event measured with the y-layer of anode design 5 at a beam intensity of 0.9 MHz with at least 4 particles traversing the detector almost simultaneously. The topology of the particle packets results from the structure of the absorbers.

The cluster charge distribution of the y-layer of anode design 5 is shown in Figure 7.14 (left), for the different beam intensities. Despite the pulse height decrease at 25 kHz, no degradation of the measured pulse height is visible. The pulse height drop is caused by a different absorber structure, which is discussed in the following.

[2]The absorbers are realized as plates with a regular pattern of tiny holes through which a specific fraction of the beam particles can pass the absorber unaffected

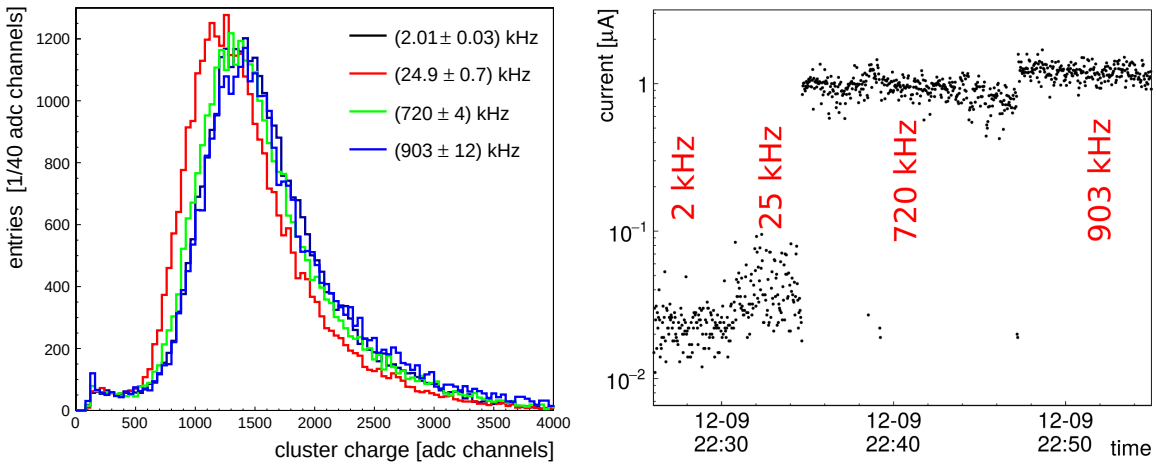

Figure 7.14: Cluster charge of the y-layer (left) and monitored current between anode and micro-mesh as a function of time (right) of anode design 5 for different beam intensities at E_{amp}=40.6 kV/cm and E_{drift}=0.33 kV/cm. The pulse height is constant over the investigated intensity range.

The beam profile during the 25 kHz rate measurement as measured by the GEM detector – which is not shown here – was split into roughly three different beam spots, where the highest hit intensity was found on a circular area with a radius of only 0.5 mm, corresponding to around 25% of the events. This results in an effective beam flux of around 3 MHz/cm^2 at this point, which leads to a visible pulse height reduction in the GEM. For the two highest intensities measured, the protons were homogeneously distributed over an area of (15×40) mm of the detector active surface, which corresponds to beam fluxes smaller than 150 kHz/cm^2. However, the current drawn by the floating strip Micromegas between mesh and anode is only around 20 nA after subtraction of the mean capacitor dark current for the measurement with the probably highest beam flux, as you can see in Figure 7.14 (right). This does not support the observed pulse height drop, as a voltage drop on the floating strips caused by the 20 nA recharge current flowing through the 22 MΩ resistors on the anode is negligibly small. Thus the only valid explanation is that during the 25 kHz rate measurement, the permutation of the used absorbers changed the energy i.e. the mean energy loss of the protons. The used absorber permutations and the resulting proton rates are listed in Table 7.1.

# measurement	absorber 33	absorber 1000_1	absorber 1000_2	scintillator rate [kHz]
1	✓	✓	✓	2.01 ± 0.03
2	–	✓	✓	24.9 ± 0.7
3	✓	–	✓	720 ± 4
4	✓	✓	–	903 ± 12

Table 7.1: Used permutations of the absorbers on the high energy side of the accelerator and resulting trigger rate as measured by the scintillator after the GEM detector. The number in the absorber name correspond approximately to the attenuation factor. Absorber 1000_1 and 1000_2 are structurally identical even though a different rate is observed.

We see, that the second measurement at (24.9 ± 0.7) kHz was the only measurement where absorber 33 was not in the beam line. As we discussed earlier, this changes the proton beam profile considerable, such that the discrete structures of absorbers 1000_1 and 1000_2 become visible as intensity peaks in the hit distribution measured by the GEM detector. As

the beam profile for the other permutations is much more spread and no discrete peaks are visible, we conclude that absorber 33 causes the proton beam to lose energy leading to a higher measured pulse height in the floating strip Micromegas. The measured pulse height difference between first and second measurement is $(15.0 \pm 0.2)\,\%$. The accelerator was operated at (9.93 ± 0.01) MV, producing protons with a kinetic energy of 20 MeV, including pre-acceleration. Neglecting the energy loss caused by the GEM detector in the beam line in front of the Micromegas, an energy difference of (3.4 ± 0.1) MeV causes a dE/dX difference of approximately 15% according to the Bethe-Bloch-formula, evaluated at an initial $\beta\gamma = 0.206$ for a singly charged particle in a Ne:CF_4 80:20 vol.% gas mixture. Thus an upper limit of (3.4 ± 0.1) MeV of energy loss can be attributed to absorber 33, if the protons have an initial kinetic energy of 20 MeV. Note that the anode PCB as well as the three foils of the GEM detector may also cause an energy loss of the protons of a few MeV, as observed by a SRIM [Ziegler et al., 2010] energy loss simulation in [Klitzner, 2016] with thin one-dimensional floating strip Micromegas. This consequently reduces the actual energy loss in the absorber, as the energy loss in the GEM detector increases accordingly. For the exact determination of the energy loss in absorber 33 a detailed simulation including the material budget of the GEM detector needs to be performed, which is not covered in this thesis.

To investigate the proton reconstruction efficiency for the floating strip Micromegas as a function of the proton rate, the residual distribution i.e. the measured proton hit position difference between GEM and Micromegas detector are calculated for the four investigated rates. Usually the residual is calculated by the two leading cluster hits i.e. hits of clusters having the highest charge in the detectors. For the lowest measured particle rate this is no problem, as on average only 1.08 ± 0.05 particle is present in the Micromegas for each triggered event. However for the highest measured rate on average 2.9 ± 0.2 protons are found within one event, making an iterative cluster matching algorithm necessary. This is shown in Figure 7.15, where the residual distributions of x- and y-layer clearly get washed out for high particle rates due to the incorrect matching of two particles, which, however, can be compensated.

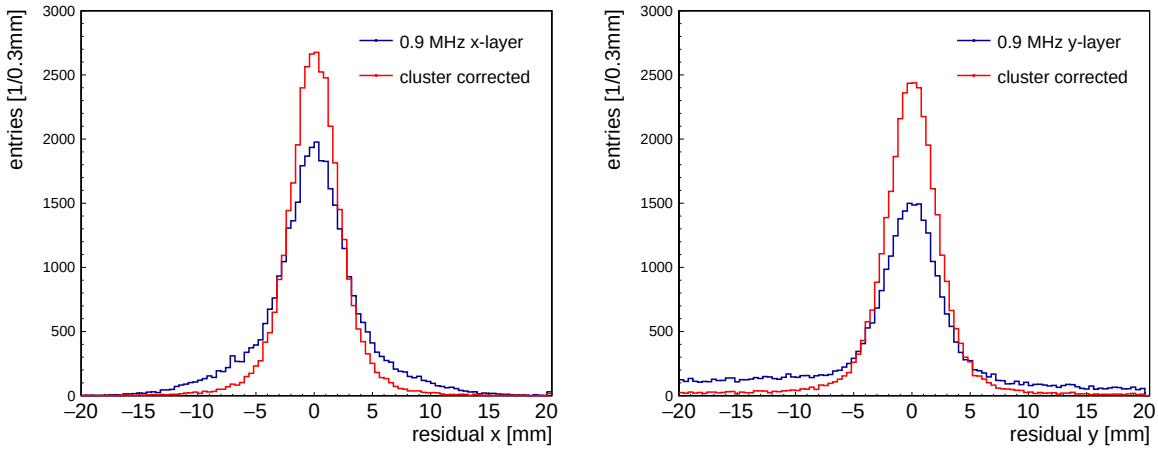

(a) x-layer (b) y-layer

Figure 7.15: Residual distribution between GEM and Micromegas hit position for the x-layer (left) and the y-layer (right) at a beam intensity of 0.9 MHz. Due to many particles in the detector in the same event, the residual distribution gets washed out (blue line) when only comparing the highest charge cluster in GEM and Micromegas. An algorithm is applied to fragment the clusters inside both detectors to find the matching particle tracks (red line). The improvement is clearly visible.

The algorithm used to identify matching clusters in the detectors is briefly explained. It is mainly using the time information as an additional ingredient. In a first step, the usual clustering is performed in both detectors as explained in section 3.3. In the second step, a Markov chain based peak finding algorithm [Morháč, 2015] is applied on each strip of each cluster, which allows to identify strips receiving signals from two particles, as it is the case in Figure 7.13 on strip 110. For simplicity reasons, always the fastest signal on a strip is used, if the found new peak amplitude exceeds $3\sigma_{\text{strip}}$. In the next crucial step, two neighboring strips in a cluster are compared and split into two separate clusters, if their peak timing differs more than 3 timebins i.e. 75 ns. The newly identified clusters in GEM and Micromegas are compared in the next step, using for the GEM detector always the leading cluster hit after the cluster fragmentation. All clusters found in the Micromegas which show a cluster timing difference smaller than 100 ns are compared with the leading cluster timing of the GEM, and sorted by position and time difference. Always the cluster with the smallest timing and position difference is furthermore used for the analysis. Note that due to the different detector technology of GEM and Micromegas, the global timing offset between the strip signals of the same particle has been corrected first.

The results of the efficiency calculated by counting the good events in a 5σ window around the Gaussian distributed residual distribution is shown in Figure 7.16.

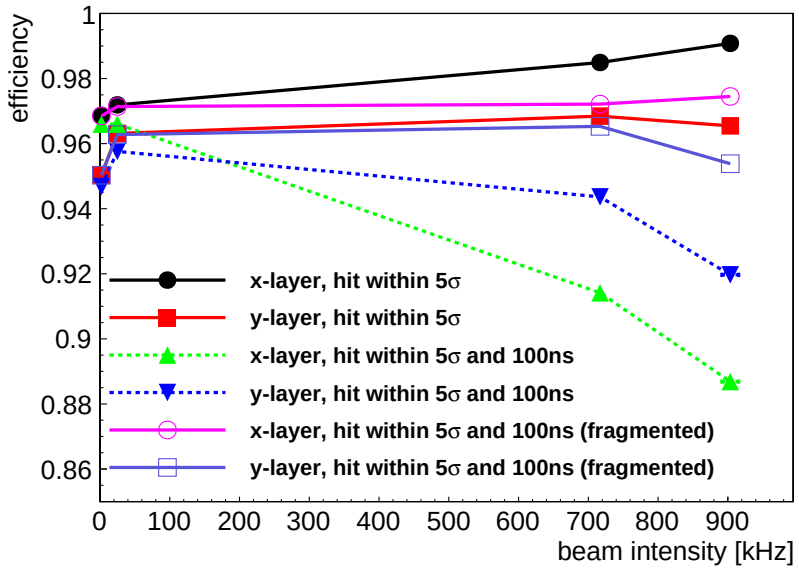

Figure 7.16: Particle reconstruction efficiency of both readout strip layers of anode design 5 as a function of the beam intensity with different cuts applied to identify the correct particles. After dedicated particle matching the efficiency stays over 95% for both readout strip layers up to almost 1 MHz beam intensity.

It is clearly visible that requiring only a timing difference cut leads to a considerable efficiency drop for the high rates, as multiple particles get merged into the same charge cluster, spoiling the cluster timing. After applying the previously described clustering algorithm, the efficiency stays above 95% for both readout strip layers up to the highest investigated intensity. The initial efficiency rise at the second rate point with (24.9 ± 0.7) kHz is partly caused by parts of the proton beam getting focused in the middle between pillars. The difference of the efficiency on x- and y-layer is caused by an asymmetric beam profile, as the proton beam profile is much broader in the y-direction than in the x-direction. This leads to an over-estimation of the efficiency due to miss-matching of the clusters in the x-layer, as the wrong cluster might still be within the 5σ window used for the efficiency determination. In general one has to say

that the efficiency at the lowest rate with $(96.8 \pm 0.2)\%$ and $(95.0 \pm 0.2)\%$ for x- and y-layer respectively represents an upper limit, which is only artificially increased for the two highest rate points due to incorrect cluster matching. For a more precise reconstruction of particle tracks at high rates, a track defined through a reference tracking system consisting of at least 3 detectors needs to be considered. This is presented in chapter 8.

7.6 Comparison between a Ne:CF_4 80:20 vol.% and Ar:CO_2 93:7 vol.% Gas Mixture

The intention of this section is to investigate the signal amplitude i.e. the cluster reconstruction on both readout strip layers of a two-dimensional floating strip Micromegas, depending on the used detector gas mixture. For this, the detector equipped with anode design 7 is tested with a Ne:CF_4 80:20 vol.% and Ar:CO_2 93:7 vol.% detector gas mixture under irradiation with 20 MeV protons. For the Neon based gas a pre-mixed gas bottle has been used. For the Argon based gas, the two constituent gases were mixed with a previously calibrated LMU self-made gas mixing system, with an estimated volumetric accuracy of 0.1%. To prevent dust or humidity from entering the detector, the gas outlet pipe was put in a bubbler filled with 3 cm of water to create a relative overpressure in the system of about 3 mbar with respect to the ambient pressure. The detector was equipped with a 25/38 µm micro-mesh, features a drift gap of 6 mm, an amplification gap of 0.128 mm and a strip pitch of 0.3 mm. The measurements have first been performed with the Neon based gas, where the detector was flushed over the night at a total flux of 3 ln/h, corresponding to roughly 50 volume exchanges per hour. After the measurements were finished, the gas was changed to Ar:CO_2 93:7 vol.%, initially flushing the detector also with 3 ln/h for one hour. However a significant fraction of relative humidity was still observed at the gas outlet of the detector. Thus the gas flux was increased to 10 ln/h, waiting until the relative humidity reduced below 6%, until the measurements were started. All measurements presented in this section have been performed within 6 hours of the same day. Environmental changes of pressure, temperature or humidity are negligibly small. No pulse height change as a function of time was observed during the measurements with the same detector gas.

The cluster charge and multiplicity on both readout strip layers is shown in Figure 7.17 as a function of the amplification voltage for both detector gas mixtures. Focusing first on the x-layer, to reach the same pulse height in the Argon based gas, an about 40 V higher amplification voltage is needed compared to the Neon based gas.

In general, the measured pulse height ph in the detector is given by

$$ph(\mathrm{E_{drift}}, \mathrm{E_{amp}}) = q_0 \cdot T(\mathrm{E_{drift}}, \mathrm{E_{amp}}) \cdot G(\mathrm{E_{amp}}) \quad , \tag{7.2}$$

where q_0 is the ionization charge created in the drift gap, T is the transport factor of the ionization electrons through the micro-mesh i.e. the electron mesh transparency and G is the gas gain in the amplification region. Considering the ionization charge q_0 created by a traversing proton, we find that actually the Argon based gas mixture shows a $q_0^{\mathrm{Ar}}/q_0^{\mathrm{Ne}} = (1.7 \pm 0.1)$ times higher ionization yield than the Neon gas, primarily due to a higher density and a lower energy required to create an electron-ion pair, see Table 2.1. Considering the electron mesh transparency T, we rely on the simulation results in Figure 2.6. We find for the Ar:CO_2 gas mixture at 0.5 kV/cm a transparency of $(33 \pm 2)\%$ with the 25/38 µm micro-mesh and for the Ne:CF_4 80:20 vol.% at 0.33 kV/cm a transparency of $(67 \pm 3)\%$. This results in a pulse height that is a factor of (0.49 ± 0.05) smaller in the Argon measurement due to the different mesh transparencies at the different drift fields.

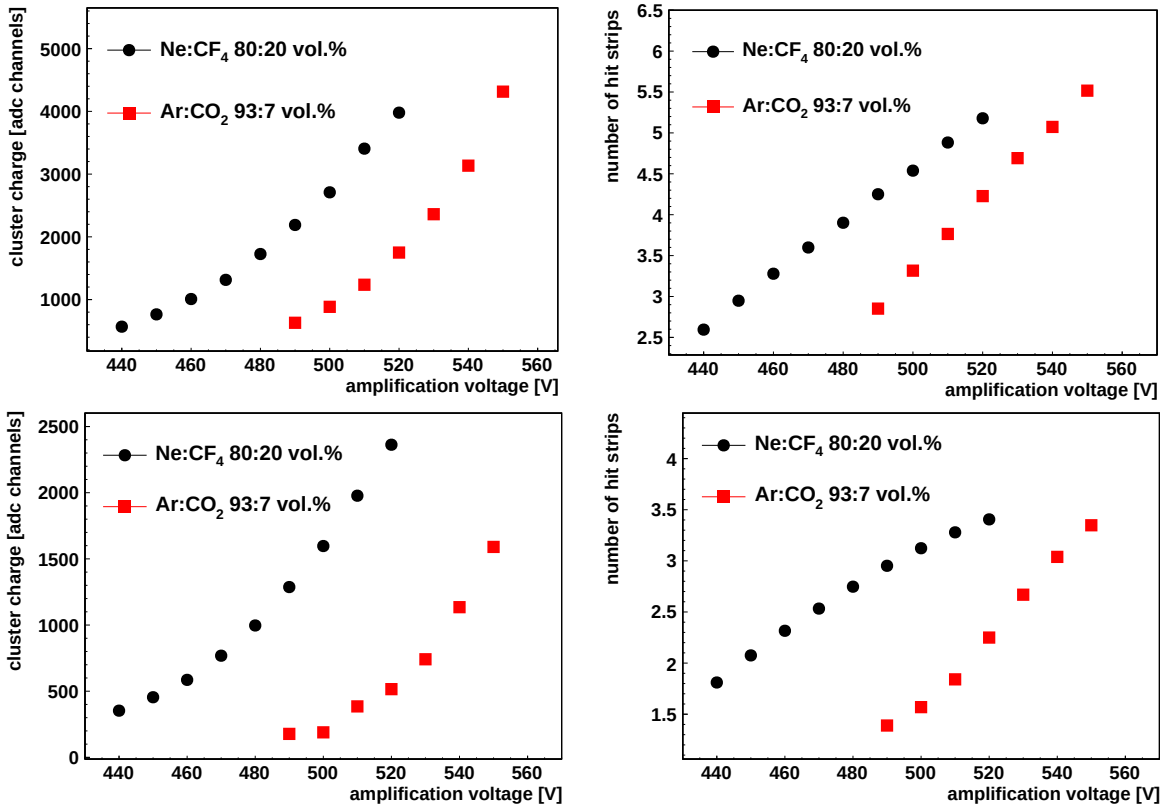

Figure 7.17: Cluster charge (left) and cluster multiplicity (right) on the x-layer (top) and the y-layer (bottom) of anode design 7 as a function of the amplification voltage U_{amp} at U_{drift}=200 V for the Ne:CF_4 80:20 vol.% measurements and U_{drift}=300 V for the Ar:CO_2 93:7 vol.% measurements.

Inserting the calculated ratio for the ionization charge $q_0^{Ar}/q_0^{Ne} = (1.7 \pm 0.1)$, the ratio of the mesh transparency found from the simulation $T_{Ar}/T_{Ne} = (0.49 \pm 0.05)$ and the measured pulse height ratio $ph(\mathrm{Ar})/ph(\mathrm{Ne}) = (0.33 \pm 0.01)$ at $U_{amp} = 500\,\mathrm{V}$, we can calculate the effective gain difference between the Argon and Neon based gas mixture G_{Ne}/G_{Ar}, starting from

$$\frac{ph(\mathrm{Ar})}{ph(\mathrm{Ne})} = \frac{q_0^{\mathrm{Ar}}}{q_0^{\mathrm{Ne}}} \cdot \frac{T_{\mathrm{Ar}}}{T_{\mathrm{Ne}}} \cdot \frac{G_{\mathrm{Ar}}}{G_{\mathrm{Ne}}} \tag{7.3}$$

and finding

$$\begin{aligned} \frac{G_{\mathrm{Ne}}}{G_{\mathrm{Ar}}} &= \frac{q_0^{\mathrm{Ar}}}{q_0^{\mathrm{Ne}}} \cdot \frac{T_{\mathrm{Ar}}}{T_{\mathrm{Ne}}} \cdot \frac{ph(\mathrm{Ne})}{ph(\mathrm{Ar})} \\ &= 1.7 \cdot 0.49 \cdot \frac{1}{0.33} \\ &= (2.5 \pm 0.1) \quad . \end{aligned} \tag{7.4}$$

From a Garfield++ simulation of the gas gain in the detector with the Argon and Neon based gas mixture, neglecting Penning transfer due to the lack of the correct transfer parameters for Neon, a ratio of (4.0 ± 0.2) is determined. Consequently, the difference is caused by the Penning transfer neglected in the simulation, being a factor of (1.6 ± 0.1) larger in the Argon based gas.

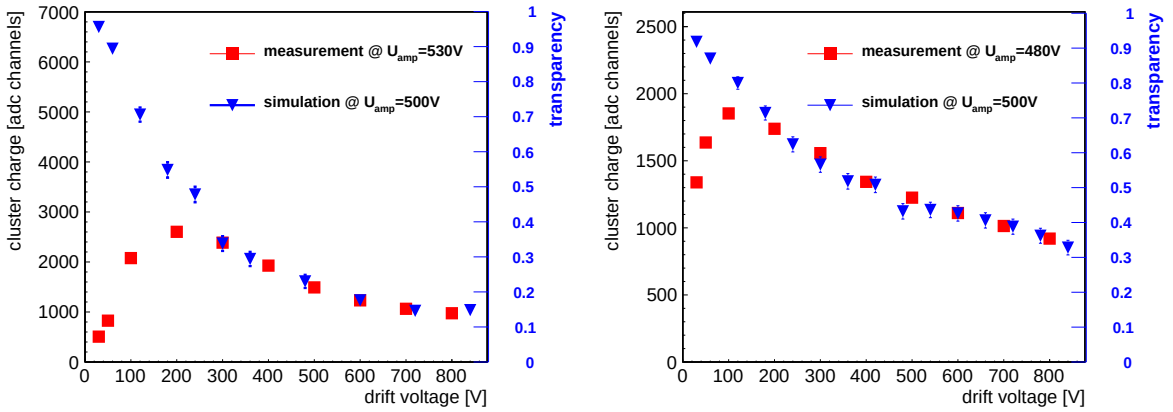

(a) $Ar:CO_2$ 93:7 vol.% (b) $Ne:CF_4$ 80:20 vol.%

Figure 7.18: Cluster charge measured on the x-layer at $U_{amp} = 530\,V$ with $Ar:CO_2$ 93:7 vol.% (left) and at $U_{amp} = 480\,V$ with $Ne:CF_4$ 80:20 vol.% (right). The simulated mesh transparency from Figure 2.6 has been superimposed and scaled to the falling shoulder of the cluster charge distribution.

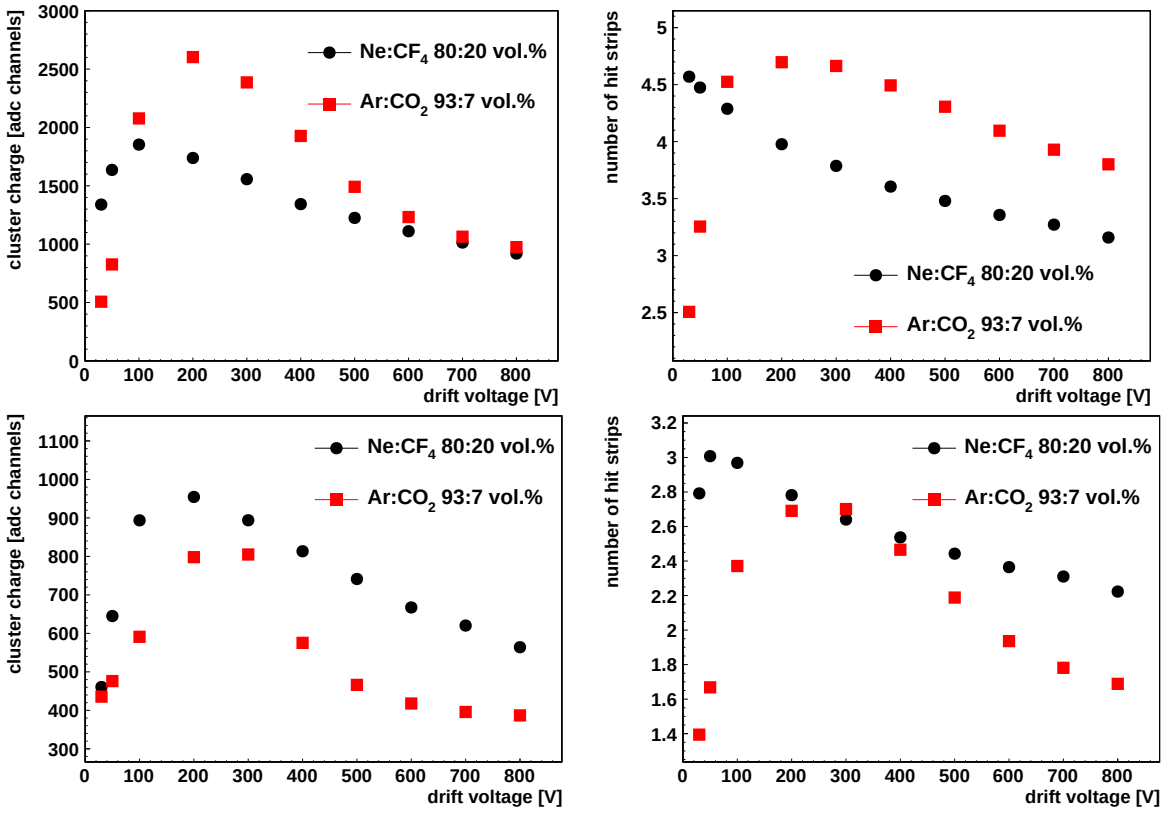

Figure 7.19: Cluster charge (left) and cluster multiplicity (right) on the x-layer (top) and the y-layer (bottom) of anode design 7 as a function of the drift voltage U_{drift} at U_{amp}=480 V for the $Ne:CF_4$ 80:20 vol.% measurements and U_{amp}=530 V for the $Ar:CO_2$ 93:7 vol.% measurements.

Figure 7.18 shows the cluster charge of the x-layer as a function of the drift voltage for Ar:CO_2 93:7 vol.% (left) and Ne:CF_4 80:20 vol.% (right). Despite the absolute pulse height difference caused by the different gain, the mesh transparency difference between the two gas mixtures is visible. The simulated transparency is superimposed and in good agreement with the measurement for higher drift fields. At lower drift fields, effects like electron attachment, recombination or readout electronics integration and shaping time lead to a significant reduction of the actual measured ionization charge. Note that the simulation has been performed at $U_{amp} = 500\,V$, while the measurements for Argon have been performed at 530 V and for Neon at 480 V. A variation of 30 V at $U_{amp} = 500\,V$ leads to a relative mesh transparency uncertainty of 30/500=6 %, assuming the transparency follows the ratio $\eta = E_{amp}/E_{drift}$ linearly.

On Figure 7.19 the cluster charge as well as the cluster multiplicity is shown for both readout strip layers as a function of the drift voltage for both gas mixtures. We see that the multiplicity follows the cluster charge, similar to the amplification scan shown in Figure 7.17. In general the higher transverse electron diffusion in the Argon based gas mixture causes a higher cluster multiplicity, best visible in the x-layer for $U_{drift} > 600\,V$, where the cluster charges are almost equal for both gas mixtures.

The y-layer signals have not been discussed so far, as the reconstructed pulse height shows an additional dependence beyond the already discussed gain and micro-mesh transparency, which is investigated in the following.

Figure 7.20 (left), shows the cluster charge ratio between y- and x-layer as a function of the amplification voltage. We see that the ratio is constant within (0.59 ± 0.03) for the Neon based gas over the investigated voltage range, which is comparable to the results of the other anode designs described in the previous chapters. However for the Argon gas mixture we see in general a lower ratio, which means that the pulse height on the y-layer drops more than the pulse height on the x-layer. For $U_{amp} \leqslant 500\,V$ the ratio is around (0.25 ± 0.01) and increases almost linearly with increasing amplification voltage. However the increase can be attributed to electronics channel saturation of the APV25 front-end hybrid connected to the x-strips, which grows due to the exponentially rising gas gain and thus limits the cluster charge on the x-layer.

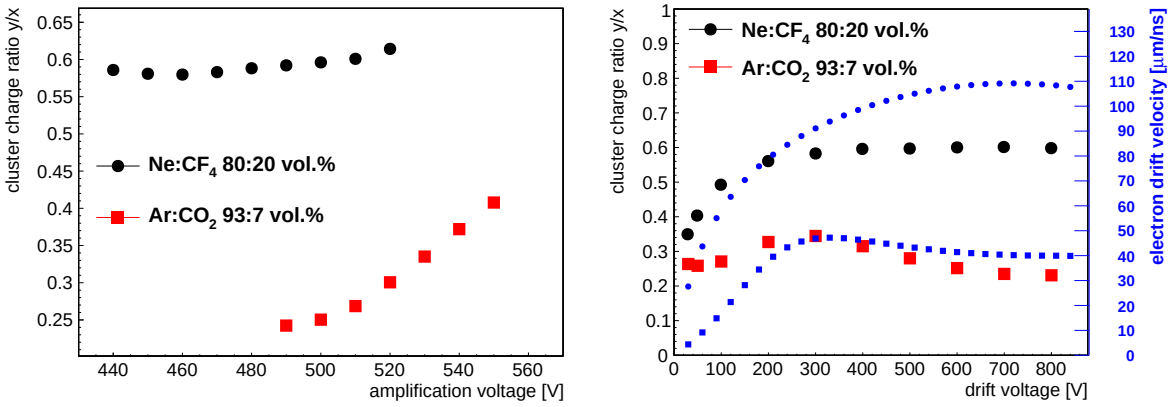

Figure 7.20: Ratio between y-layer and x-layer cluster charge of anode design 7 as a function of the amplification voltage U_{amp} (left) at U_{drift}=200 V for the Ne:CF_4 80:20 vol.% measurements and U_{drift}=300 V for the Ar:CO_2 93:7 vol.% measurements and as a function of the drift voltage U_{drift} (right) at U_{amp}=480 V for the Ne:CF_4 80:20 vol.% measurements and U_{amp}=530 V for the Ar:CO_2 93:7 vol.% measurements. The simulated electron drift velocity has been superimposed for the drift voltage scan and scaled to the Neon measurement at 200 V, at which point the pulse height on the y-layer starts to decrease.

There is not yet a fully satisfactory explanation why the signals on the y-layer are smaller with the Argon based gas. In the following, some observations are presented that may be an indication for the observed pulse height difference.

The dependence of the y/x cluster charge ratio as a function of the drift voltage is shown in Figure 7.20 (right). We see that for the Neon based gas mixture the ratio is constant for $U_{drift} \geqslant 300\,V$, while it decreases for lower drift voltages. The faster decrease in pulse height on the y-layer compared to the x-layer is also visible in the drift voltage variation in Figure 7.19 (left). Trying to understand the more distinct drop of the y-layer pulse height, compared to the drop of the x-layer pulse height, for smaller drift fields, we recall the properties of ionization electrons in the drift gap as a function of the drift field, shown in Figure 2.3. We see that for $E_{drift} \leqslant 0.5\,kV/cm$ i.e. $U_{drift} \leqslant 300\,V$ the electron transverse diffusion increases while the electron drift velocity decreases for the Ne:CF_4 80:20 vol.% gas mixture. The total signal on the y-strips is a convolution of the contributions from each drift electron entering the amplification gap. Thus, due to the bipolar signal on the y-strips, the total induced charge depends on the arrival time of individual ionization electrons. Hence, if the drift time is longer than the zero-crossing point of the signal, the positive induced signal from a late arriving electron overlaps with the negative part of the signal from an earlier ionization electron, leading to a signal cancellation. Due to the unipolar negative signal, this effect is not observed on the x-strips, leading to a drift field dependent cluster charge ratio. As we see that the ratio is almost constant for drift voltages higher than 200 V, the maximum drift time before signal cancellation effects may occur can be calculated. From the simulated drift velocity at $E_{drift} = 200\,V/6\,mm = 0.33\,kV/cm$ we find $v_d = 80\,\mu m/ns$, yielding a maximum drift time of 75 ns in the 6 mm long drift region. A similar zero-crossing time is found with a Garfield++ simulation in Figure 4.24 (right), from a signal created by a perpendicularly incident muon in a Ne:CF_4 gas mixture, which supports the hypothesis.

Another supportive argument for the above hypothesis is the fact that in the µTPC angle reconstruction, the angular resolution on the y-layer improves for decreasing drift fields similarly to the x-layer (see Figure 7.12). For not perpendicularly incident particles, the electron avalanches arriving at different times in the amplification region are being collected on different strips. Thus the bipolar signal on a single strip is not distorted by later arriving electron avalanches, as they are being collected by different strips.

For the Ar:CO_2 93:7 vol.% gas mixture we see in Figure 7.20 in general a lower y/x cluster charge ratio than with Ne:CF_4 80:20 vol.%, as was already visible in the amplification voltage scan. Furthermore, also a drift voltage dependence is visible, which shows similarities to the simulated electron drift velocity, which has been superimposed (blue markers). The effect that the ratio levels off at very low drift voltages is biased by the extremely small signals reconstructed on both layers, due to too long current signals exceeding the readout electronics integration and shaping time. As the drift velocity is in general smaller than in the Neon based gas, generally a smaller pulse height on the y-layer may be expected. However, as measurements have pointed out in the previous chapter, the cluster charge ratio of anode designs 4 and 6 measured with a Ne:CF_4 gas mixture was around 0.6 at an effective electron drift velocity of around 40 µm/ns at $U_{drift} = 200\,V$ due to a too high level of 23% relative humidity present in the gas. This is comparable to the maximum electron drift velocity in the Argon based gas mixture, however, with a ratio of only around 0.3. Consequently, the electron drift time in the gas seems not to be the only reason why such a big difference is observed between the two gas mixtures. A Garfield++ simulation shows that the factor of two smaller ion mobility in the Argon based gas leads to a single electron avalanche induced bipolar current on the y-strip with a zero-crossing much later than 50 ns, while the Ne:CF_4 based gas mixture shows a zero-crossing close to 50 ns. As the APV25 chip features a 50 ns pulse shaping time, the longer ion drift in the Argon based gas means a loss in the integration

of the positive part of the bipolar current signal.

One additional factor to consider is the diffusion of the electrons in the drift region. The transverse diffusion influences the spatial extension of the electron cloud and the longitudinal diffusion influences the arrival time of single electrons at the amplification region. Thus in general higher diffusion coefficients, as it is the case for the Argon based gas mixture, may lead to a smaller pulse height on the y-layer.

The efficiency as a function of the amplification and drift voltage are shown in Figure 7.21 and in Figure 7.22, respectively, for both gas mixtures and readout strip layers. The definition of the efficiency is the same as introduced in section 7.3.

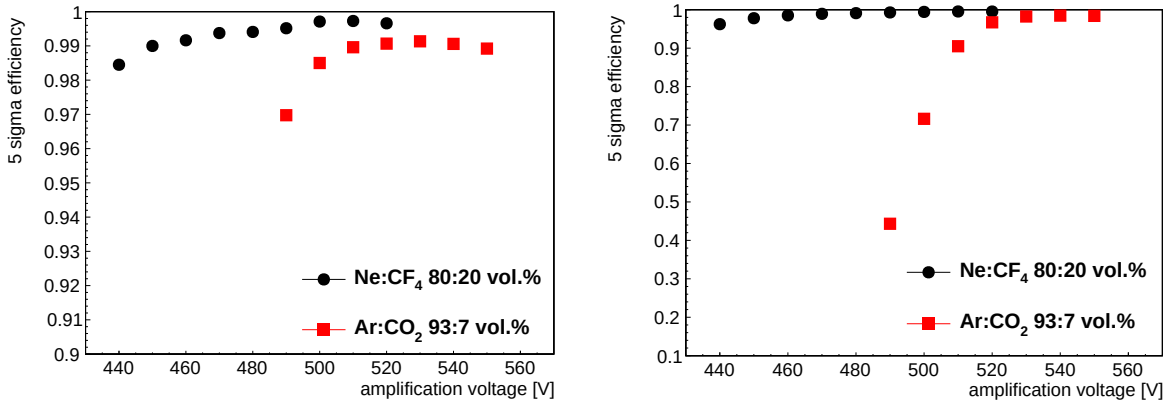

Figure 7.21: Efficiency of the x-layer (left) and the y-layer (right) of anode design 7 as a function of the amplification voltage U_{amp} at U_{drift}=200 V for the Ne:CF_4 80:20 vol.% measurements and U_{drift}=300 V for the Ar:CO_2 93:7 vol.% measurements.

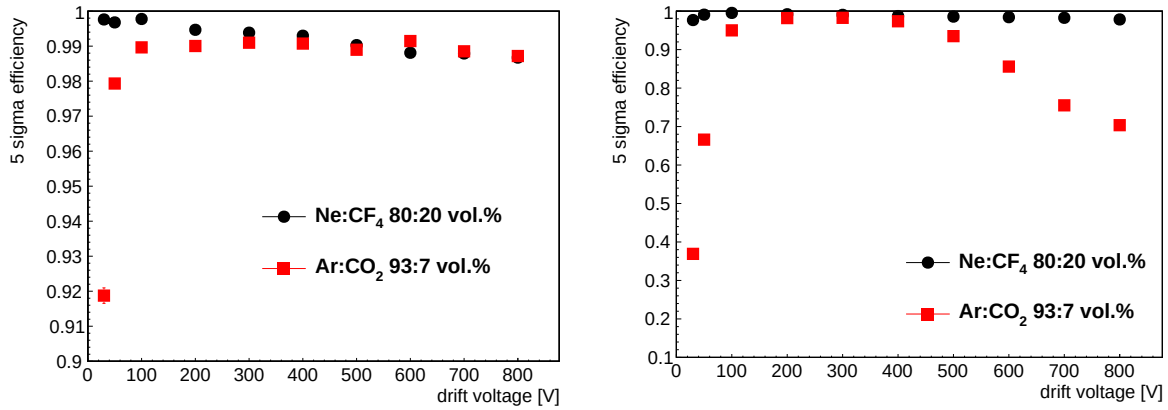

(a) x-layer (b) y-layer

Figure 7.22: Efficiency of the x-layer (left) and the y-layer (right) of anode design 7 as a function of the drift voltage U_{drift} at U_{amp}=480 V for the Ne:CF_4 80:20 vol.% measurements and U_{amp}=530 V for the Ar:CO_2 93:7 vol.% measurements.

Focusing first on the amplification voltage scan, we see that due to the higher pulse height measured with the Neon based gas on both readout strip layers, the efficiency is less depending on the amplification voltage for the investigated voltage range. The efficiency stays above 96% on both readout strip layers. For the Argon based gas we reach the plateau of (99.0 ± 0.1)% for $U_{amp} \geqslant 510$ V on the x-layer and (98.3 ± 0.2)% for $U_{amp} \geqslant 530$ V on the y-layer.

The efficiency as a function of the drift voltage is shown in Figure 7.22. For the Neon based gas the x-layer stays above 98.5% and the y-layer above 97.5% over the investigated voltage range. For the Argon based gas we see that for the x-layer the efficiency is constant within $(98.9 \pm 0.3)\%$ for $U_{drift} \geqslant 100\,V$. Smaller drift fields lead to a significant loss of ionization charge either by attachment and recombination effects or the limited integration and shaping time of the electronics, caused by the very small electron drift velocity. The efficiency of the y-layer is strongly depending on the pulse height, which is itself again depending on a combination of electron diffusion and drift velocity. However, we see an efficiency above 93% for $100\,V \leqslant U_{drift} \leqslant 500\,V$, which reaches a plateau of $(97.9 \pm 0.6)\%$ for $200\,V \leqslant U_{drift} \leqslant 400\,V$, corresponding to an electron drift velocity above 37 µm/ns, a transverse diffusion below 400 µm/cm and a longitudinal diffusion below 300 µm/cm according to MAGBOLTZ.

An optimum working point for 20 MeV protons with the Argon based gas mixture is found at $U_{amp} = 530\,V$ and $U_{drift} = 300\,V$, with a y/x cluster charge ratio of around 0.35 at an efficiency above 98% on both readout strip layers.

Chapter 8

Test Beam Measurements with 20-150 GeV Muons and Pions at the CERN SPS H8 Beam Line

This chapter presents the investigation the performance of two-dimensional floating strip Micromegas in high energy particle beams, focusing on spatial resolution, efficiency and high rate capability.

A detector telescope consisting of four two-dimensional resistive strip Micromegas (so called *TMM-chambers*) with an active area of $9 \times 9\,\mathrm{cm}^2$ allowed for precise track reconstruction of 20 GeV to 150 GeV muons and pions at a track uncertainty of below 25 µm in a test beam campaign at the SPS H8 beamline at CERN. The accelerator delivered the particle beam in a spill structure of 4.5 s duration with a cycle of 30 s or 60 s, depending on the needs of other experiments. In total four two-dimensional floating strip Micromegas equipped with anode designs 4, 5 and 6 are sandwiched by the four tracking TMM chambers. Two detectors were equipped with anode design 4, carrying either a 25/38 µm or 30/70 µm micro-mesh. As the difference between the two micro-mesh types was investigated in the previous chapter, the detector equipped with the 30/70 µm micro-mesh will not be included in the discussions in this chapter.

Due to the high energy of the particles, they almost behave like minimum ionizing particles, which leads to considerably smaller signals in the detector as compared to the signals from 20 MeV protons discussed in the previous chapter. Thus the cluster charge and multiplicity is investigated briefly in the beginning. The spatial resolution and efficiency of detectors equipped with the above mentioned anodes is determined by comparing the 25 µm accurate track prediction with the measured hit position for perpendicular and inclined particle tracks in the detector at 20°, 30° and 40°. In the last section, the reconstructed pulse height, efficiency and spatial resolution is investigated with a pion beam at fluxes up to almost $5\,\mathrm{MHz/cm}^2$.

8.1 Setup

The setup of the tracking telescope for the measurements with pions and muons presented in this chapter is schematically shown in Figure 8.1. The resistive strip Micromegas are labeled TMM1 to TMM4, the floating strip Micromegas FSM1 to FSM4, where the lowest number defines the most upstream detector.

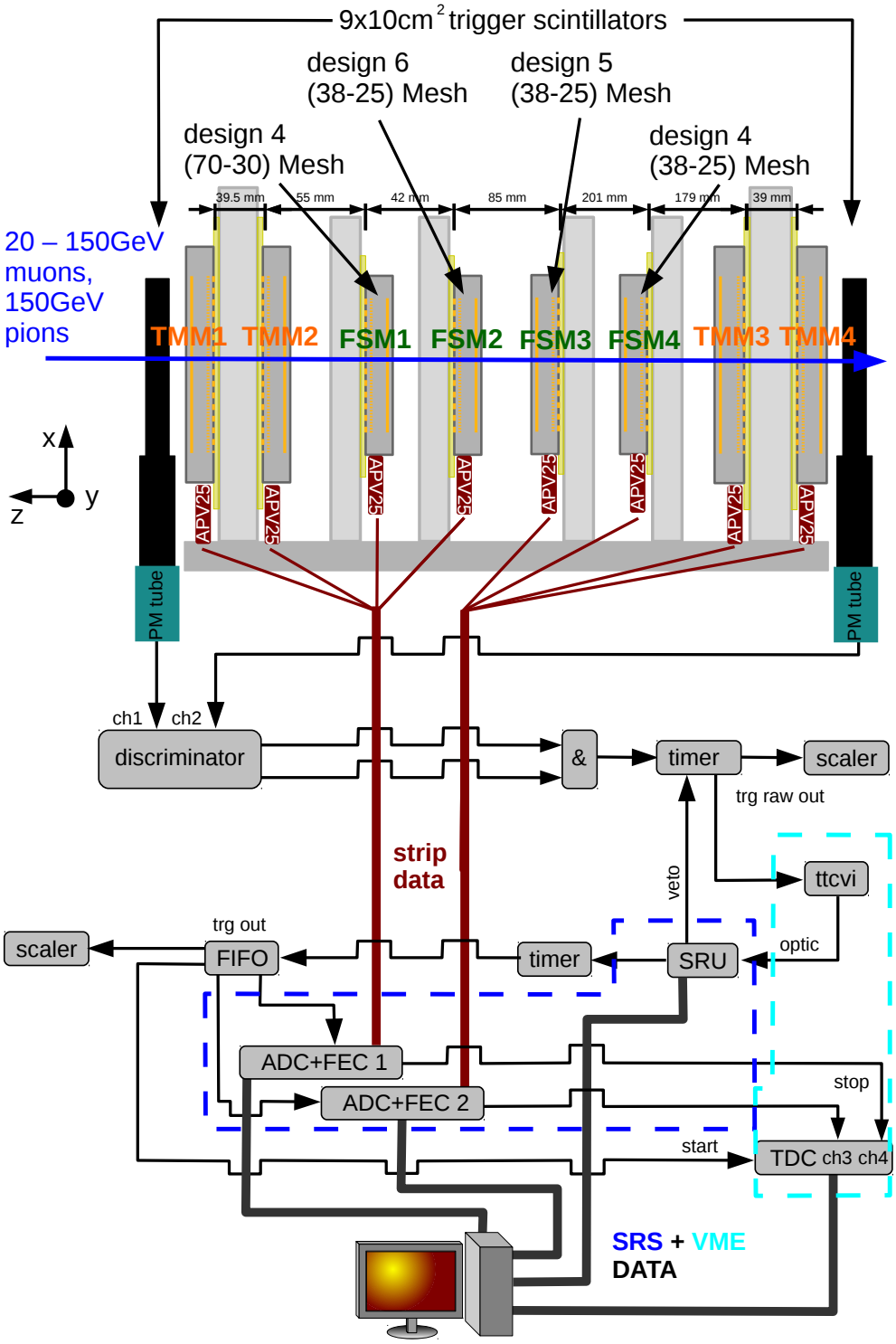

Figure 8.1: Schematic setup for the measurements at the SPS H8 beamline at CERN presented in this chapter. A muon or pion of high energy traverses the detector telescope and creates a coincident trigger signal on two scintillators. The Micromegas - four TMM type two-dimensional resistive strip Micromegas and four two-dimensional floating strip Micromegas - are fully equipped with APV25 front-end electronics which are readout after receiving the trigger signal from the scintillators. To allow for a correction of the 25 ns jitter inflicted by the SRS-based readout-system, the scintillator and the SRS trigger signal is recorded with a VME-based TDC.

Two $9 \times 10\,\mathrm{cm}^2$ active area plastic scintillators, read out with Hamamatsu R4124 photomultiplier tubes [Hamamatsu, 2007], sandwich the Micromegas telescope and are used for triggering the readout of the strip detectors. The TMM chambers, used for the determination of the reference tracks, feature 360 anode resistive strips at a pitch of 0.25 mm and a width of 0.15 mm. Two perpendicular layers of readout strips beneath the resistive strips yield a position information in x- and y-direction perpendicular to the beam direction with an active area of $9 \times 9\,\mathrm{cm}^2$. All strip detectors were fully equipped with APV25 front-end hybrid boards. Due to 128 channels per front-end hybrid, a total of 32 APV25 boards were required to readout the full detector telescope. As the ADC card in the SRS-based readout system allows a maximum of 16 APV25s, two FEC + ADC systems have been used to collect the data of all 9964 detector strips.

Upon passage of a muon or pion through the detector system, the two analogue signals from the scintillator photomultipliers are fed into a LeCroy Model 4608C Octal NIM Discriminator [LeCroy, 1997], producing two NIM standard logic pulses with a maximum length of 100 ns. The logic AND is produced by a LeCroy Model 622 Quad Coincidence Unit [LeCroy, 1996], which is extended to a duration of 500 ns by a CAEN Dual Timer [CAEN, 2019d]. The extended signal, being refered to as raw trigger signal from now on, is counted with an FPGA based NIM scaler, transmitting the NIM signal counts every 1 s via RS232 cable to the DAQ computer. As the SRS-based readout system is driven by a 40 MHz clock, the asynchronous trigger signal from the scintillators jitters within the 25 ns of a clock cycle. To eliminate the jitter in the APV raw data software-wise in the analysis later on, the trigger signal has been recorded with a VME V775(N) Time-To-Digital-Converter [CAEN, 2019g]. The trigger signals i.e. the event numbers are counted in the VME-world by a CERN custom made TTCvi module [Farthouat and Gällnö, 2000] and in the SRS-world by an SRU. To assure that the SRS-world doesn't miss triggers caused by the large data accumulation of the non-zero-suppressed AVP25 analogue data, the SRU vetos the raw trigger dual timer until the two FEC cards have transmitted the complete APV data set, controlled by a custom made software on the DAQ computer[1].

High voltage is provided by a CAEN SY5527 Universal Multichannel Power Supply Mainframe [CAEN, 2019f], equipped with two A1821 12 Channel boards (0.6 W) [CAEN, 2019b] with either positive or negative polarity for the strip detectors and one A1535dn 12 Channel Common Floating Return board (8W) [CAEN, 2019a] for the scintillator. Voltage and current were monitored during all measurements.

The gas detectors have been continuously flushed at a flux of 2 ln/h with a Ne:CF_4 80:20 vol.% gas mixture from a pre-mixed gas bottle. To prevent humidity or dust entering the detector system, a relative over-pressure of a few mbar with respect to the ambient pressure of around (1005 ± 8) mbar at CERN was assured by the water level in a bubbler. The temperature changes in the measurement hall during the measurement period were within $(20 \pm 3)\,^\circ$C.

8.2 Cluster Charge and Cluster Multiplicity

The energy loss of muons and pions in the investigated range of 20 GeV to 150 GeV is similar to the energy loss of minimum ionizing particles. As the signals in the detectors are thus considerably smaller than the signals we have seen so far in this thesis, the cluster charge and multiplicity is briefly discussed in the following.

The cluster charge distribution for x- and y-layer is shown in Figure 8.2 for a perpendicular incident muon beam. Discrete peaks in the distribution of the x-layer are originating from

[1] code mainly developed by B. Flierl

events where the charge on the strip with maximum charge exceeded the dynamic range of the APV electronics. The peak at charge values below 200 adc channels is due to uncorrelated electronic noise.

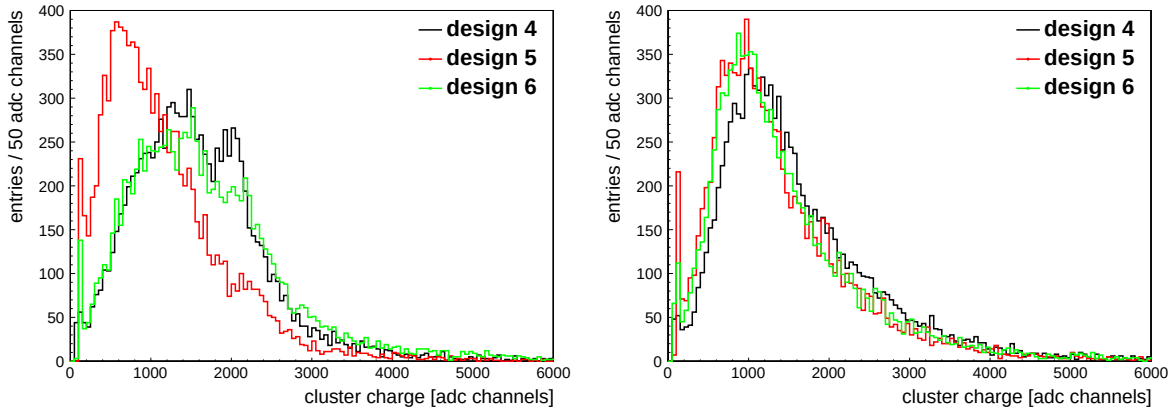

(a) x-layer (b) y-layer

Figure 8.2: Cluster charge distributions for all three anode designs, measured at E_{amp} = 46.9 kV/cm and E_{drift} = 0.17 kV/cm with perpendicularly incident muons.

The mean value of the cluster charge and multiplicity distributions as a function of the amplification and drift field is shown in Figure 8.3 and 8.4, respectively. If no error bars are visible in the graphs, the markers are bigger than the errors. Note that a different algorithm has been used for the determination of the APV25 channel specific offset, which uses the minimum ADC value found on a strip rather than the mean. This increases the pulse height on the y-strip compared to the measurements in the previous chapters due to the negative undershoot of the signal, which, however, is a part of the signal.

To reach similar pulse height as with 20 MeV protons discussed in the last chapters (assume ∼1200 adc channels cluster charge on the x-layer of design 5), the amplification field needs to be increased from 38.3 kV/cm (for protons) to 46.9 kV/cm (for muons). This corresponds to a gain increase from 1550 to 15740 according to a MAGBOLTZ simulation of the first Townsend coefficient (see Figure 2.4, when linearly extrapolating the Ne:CF_4 coefficient to E_{amp} = 46.9 kV/cm), which is in agreement with roughly a factor of 10 reduced energy loss of muons in that energy range ($\beta\gamma \approx 100 \ldots 1000$) compared to 20 MeV protons ($\beta\gamma \approx 0.2$) according to the Bethe-Bloch-formula (see Figure 2.1).

The cluster charge follows the expected exponential increase for increasing amplification field and the shape typical for Micromegas in the drift field scan, which is dominated by signal loss caused by electron attachment for small drift fields and by the decreasing mesh transparency for increasing drift field. While the pulse height on the y-layer is very similar for all anode designs, the x-layer pulse height changes according to the capacitance between floating strip and parallel readout strip, as has been discussed in chapter 6.

The cluster multiplicity follows generally the pulse height for the amplification and drift field scan except for drift fields smaller than 0.2 kV/cm, where the significant increase of electron diffusion in the drift gap leads to a higher cluster multiplicity even though the cluster charge is decreasing simultaneously. Furthermore we see that the average number of strips per cluster is fairly low on both readout strip layers, caused by the small diffusion of the gas mixture and the very straight tracks of the perpendicular incidence muons with an average track inclination of below 1 mrad, as determined by the TMM chamber reference tracking system.

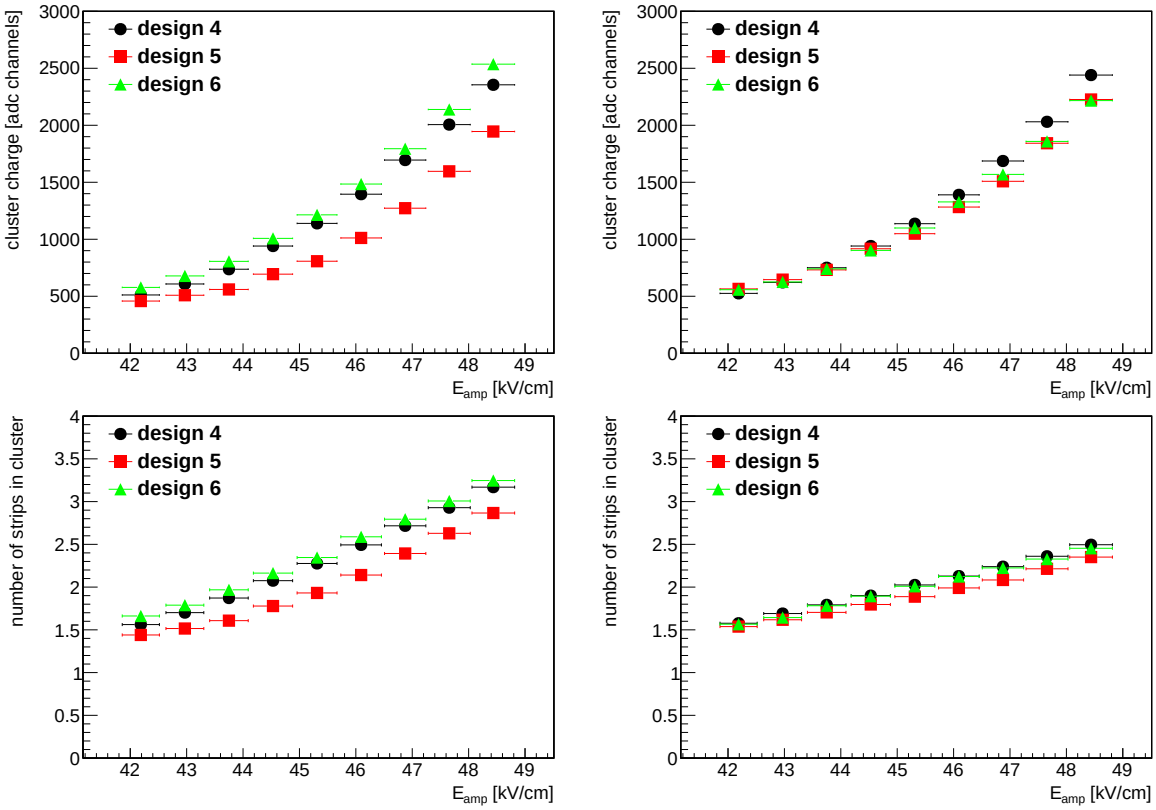

Figure 8.3: Mean cluster charge (top) and cluster multiplicity (bottom) on the x-layer (left) and the y-layer (right) as a function of E_{amp} at E_{drift}=0.17 kV/cm for all three anode designs.

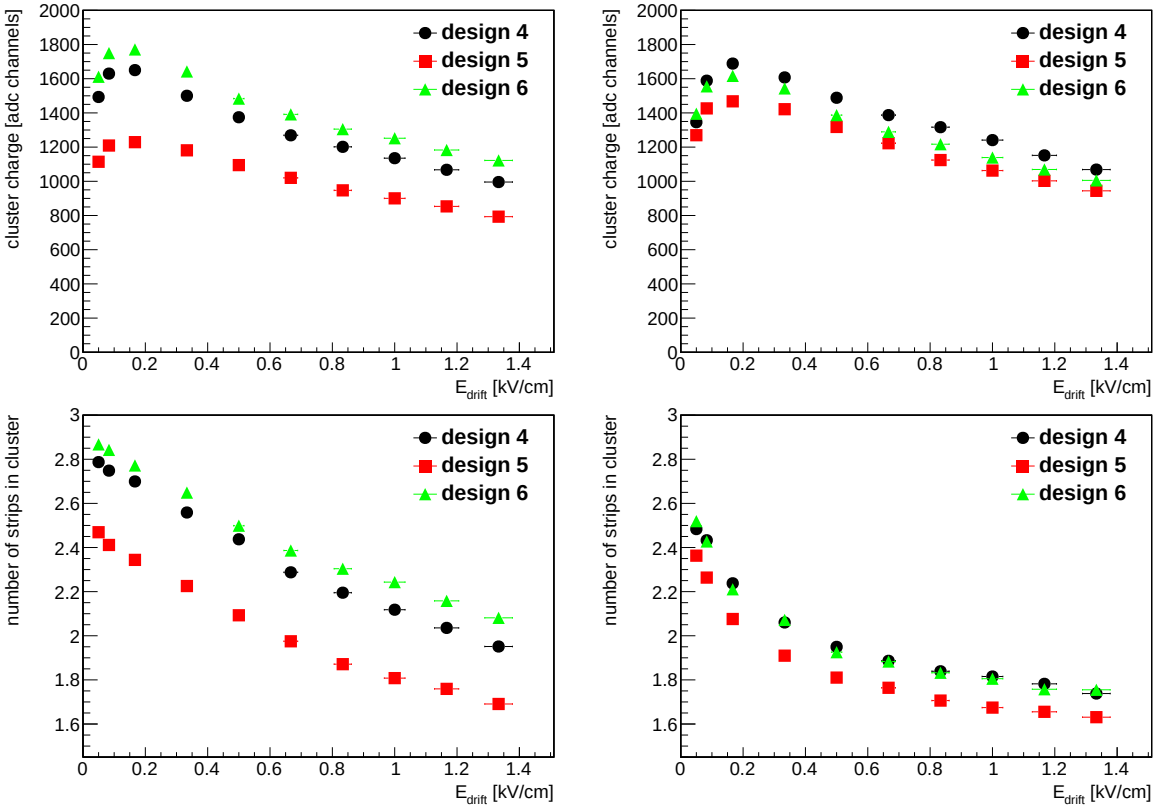

Figure 8.4: Mean cluster charge (top) and cluster multiplicity (bottom) on the x-layer (left) and the y-layer (right) as a function of E_{drift} at E_{amp}=46.9 kV/cm for all three anode designs.

The fraction of saturated strip events where the charge on an APV25 channel exceeded the internal dynamic range is shown in Figure 8.5.

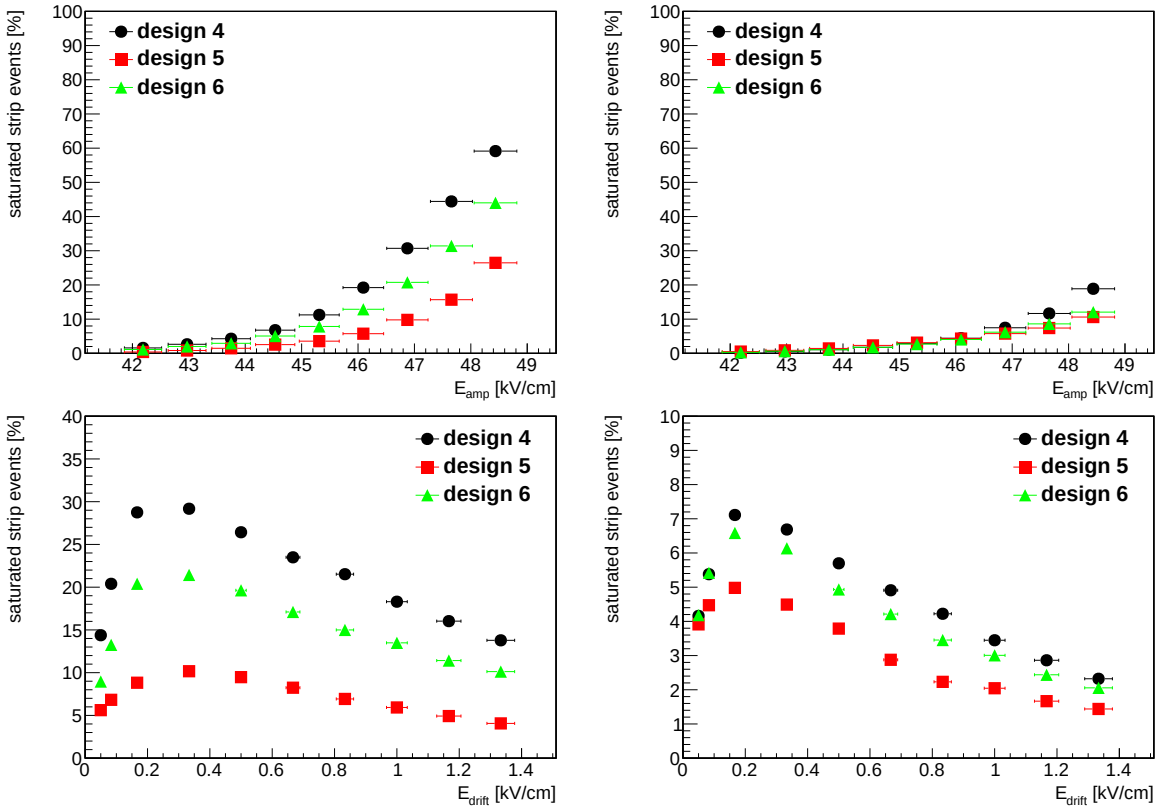

(a) x-layer (b) y-layer

Figure 8.5: Electronics channel saturation on the x-layer (left) and y-layer (right) as a function of E_{amp} at E_{drift}=0.17 kV/cm (top) and as a function of E_{drift} at E_{amp}=46.8 kV/cm (bottom) for all three anode designs.

We see that the x-layer of anode design 4 shows a higher saturation than design 6, even though the cluster charge is lower. However this is only related to a problem with the APV25 front-end chip connected to the x-layer of anode design 4, which reduced the dynamic range of the chip by around 200 adc channels compared to design 6.

In general a significant fraction of up to 40% saturated events −neglecting design 4− are observed on the x-layer, which is a result of the small electron transverse diffusion leading to a charge cloud entering the amplification region of the same size as the strip pitch. This is also visible in the x-layer cluster charge distribution in Figure 8.2 at around 2000 adc channels. We see that the coupling of the signals to the readout strip layers is sufficiently high to yield saturated strip signals simultaneously on both readout strip layers also for minimum ionizing particles within a feasible amplification field range.

To reduce the saturation effects, the pitch of the anode strips can be reduced from 0.5 mm to 0.3 mm, which does not negatively influence the coupling strength to both readout strip layers, as we have seen in the characterization measurements with anode design 7 in chapter 6 and chapter 7.

8.3 Spatial Resolution

The spatial resolution of both readout strip layers of the two-dimensional floating strip Micromegas anode designs is investigated in this section for perpendicular and also inclined particle tracks. The analysis routine that has been applied to extract the spatial resolution is explained briefly.

Typically around 30k to 40k events have been recorded for each data point in a drift or amplification field scan, either with a pion or muon beam.

As the muons are from the boosted two-body decay of pions in the channel $\pi^- \rightarrow \mu^- + \bar{\nu}_\mu$ using a few meters long collimator, the beam spot size of the muons is larger than the trigger scintillators. Due to an active area of the trigger scintillators of $9 \times 10\,\mathrm{cm}^2$, the TMM tracking chambers with $9 \times 9\,\mathrm{cm}^2$ and the floating strip Micromegas of $6.4 \times 6.4\,\mathrm{cm}^2$, around 50% of the triggered particle events are outside of the floating strip Micromegas active area if measurements were taken with a muon beam. For the pion beam a very collimated beam spot of $\sigma_x = (2.39 \pm 0.02)\,\mathrm{mm}$ and σ_y=$(3.25 \pm 0.03)\,\mathrm{mm}$ was visible during all measurements, leading to less events lost due to the active area difference of the detectors. However due to hadronic interaction of the pions with the detector material or other materials in the beam line, it was possible that during the pion measurements more than one particle is present in the detector telescope. To be sure that the correct particles are matched in the tracking algorithm, these events were discarded. Thus, depending on the pion beam rate − which is around 2 to 3 orders of magnitude higher than the muon beam − a maximum of 25% of the triggered events are discarded for the highest particle rates.

A *good* particle event which is used to determine the spatial resolution of the floating strip Micromegas is defined in the following way: For each of the four TMM tracking chambers a hit is required which lies in the active area of the floating strip Micromegas. The hits per detector layer are determined by the charge weighted mean hit position according to the recipe in section 3.3. For the inclined particle track measurements with the floating strip Micromegas, either the charge weighted mean or the µTPC hit position has been used. In the next step, a track is defined through the four hits in the TMM chambers, two in front and two behind the floating strip Micromegas, with requiring a $\chi^2/\mathrm{ndf} < 10$ for the track fit quality. Both requirements discard additionally around 20% of the events. In the end between 6000 and 15000 events were usually left in which the track was interpolated into the three floating strip Micromegas and the residual was calculated between the track predicted and the hits measured by the FSM detectors. The residual distribution is usually fit with a double Gaussian function $f(x)$, defined as follows :

$$f(x) = A_{\mathrm{core}} \cdot e^{\left(-\left(\frac{x-x_{\mathrm{core}}}{\sqrt{2}\sigma_{\mathrm{core}}}\right)^2\right)} + A_{\mathrm{tail}} \cdot e^{\left(-\left(\frac{x-x_{\mathrm{tail}}}{\sqrt{2}\sigma_{\mathrm{tail}}}\right)^2\right)} \quad , \tag{8.1}$$

where 'core' describes a narrow distribution reflecting the detector intrinsic spatial resolution and 'tail' a broad distribution which is caused by delta electrons, created inside the active volume of the detector, that can leave itself a track in the detector and thus bias the reconstructed hit position.

In the next step, the spatial resolution is determined by deconvolution of the track accuracy (following the recipe given in section. 3.6.3 in equation 3.15) from either the core or the combined sigma of the Gaussian fit, where the combined sigma $\sigma_{\mathrm{combined}}$ is defined by

$$\sigma_{\mathrm{combined}} = \frac{I_{\mathrm{core}} \cdot \sigma_{\mathrm{core}} + I_{\mathrm{tail}} \cdot \sigma_{\mathrm{tail}}}{I_{\mathrm{core}} + I_{\mathrm{tail}}} \quad , \tag{8.2}$$

where I_{core} and I_{tail} are the events covered by each of the two Gaussian functions i.e. the integral below the core and tail residual distribution, respectively.

The spatial resolution of the tracking chambers, which needs to be known for the determination of the track accuracy, has been previously determined with the Geometric Mean Method. Both methods are described in section 3.6.3. The spatial resolution of the four TMM chambers was found to be very similar and within (43 ± 4)µm for all measurements, leading to a track prediction accuracy of better than 25 µm at the position of the floating strip Micromegas.

All detectors have been aligned in a global 3d-coordinate system with the help of the very straight particle tracks according to the methods described in section 3.6.2. Actually the track resolution as well as the spatial resolution of the floating strip Micromegas was good enough to reconstruct an intrinsic relative rotation of around 4 mrad between parallel and perpendicular readout strip layer of anode design 4 and 6.

8.3.1 Perpendicular Particle Tracks

The measurements discussed in this section have been taken at perpendicularly incident muon or pion beams with respect to the anode plane of the strip detectors. The particle flux densities are around 15 Hz/cm^2 for the muon beams and 420 kHz/cm^2 for the pion beams.

To quickly summarize the spatial resolution results of the two-dimensional floating strip Micromegas for perpendicular incidence: Charge discretization effects on the periodic anode strip structure degrade the spatial resolution on the x-layer of the detector, as the lateral size of the ionization charge cloud of the traversing particle is of the same size as the anode strip pitch of $p = 0.5$ mm, due to the low diffusion of the used gas mixture and the very straight particle tracks. The spatial resolution on the y-layer is almost not degraded by this effect due to the different signal coupling process (see section 4.3.2). Nevertheless, optimum spatial resolution of (79 ± 4) µm for the x-layer and (54 ± 2) µm for the y-layer of anode design 4 are reached, measured with a pion beam at 420 kHz/cm^2. The charge discretization visible on the anode strips and the used method to correct for it is described in detail in the following. After applying the correction, the spatial resolution of the three floating strip Micromegas is investigated as a function of drift and amplification field.

The residual distributions of x and y-layer of anode design 4, fit with the double Gaussian defined in equation 8.1, are shown in Figure 8.6. They are split into two-strips and three-strips cluster, which cover the vast majority of events. The much broader residual distribution on the x-layer compared to the y-layer is clearly visible.

As was already pointed out in the cluster charge and multiplicity discussion in the last section, the lateral charge spread in the amplification region is of the same size as the anode strip pitch. This ultimately leads to charge discretization effects caused by the periodic strip structure, which results in a systematic mis-reconstruction of the particle hit position, as has already been discussed by Bortfeldt [2014].

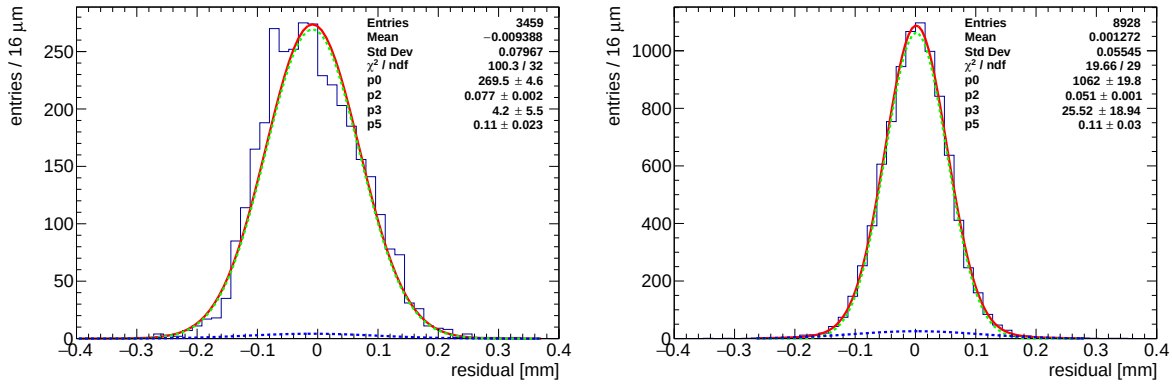

(a) x-layer, 2 strips cluster

(b) y-layer, 2 strips cluster

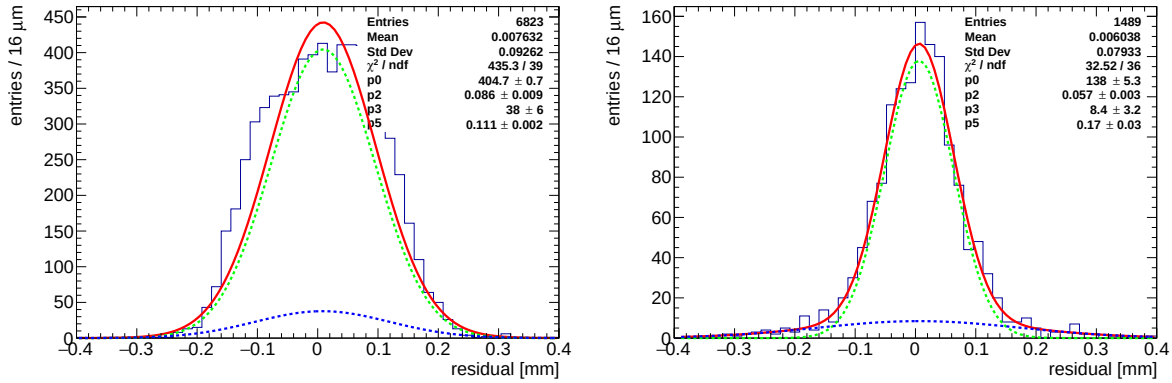

(c) x-layer, 3 strips cluster

(d) y-layer, 3 strips cluster

Figure 8.6: Residual calculated for two-strip clusters (top) and three-strip clusters (bottom) measured on the x-layer (left) and the y-layer (right) with pions on anode design 4 with E_{drift}=0.33 kV/cm and E_{amp}=47.6 kV/cm. The difference of the residual width between x and y-layer is clearly visible.

Hence, the residual between track predicted and measured hit in the floating strip Micromegas is investigated in the following as a function of η, which is defined as the *difference between the reconstructed hit position*[2] *and the center of the nearest strip*. Figure 8.7 shows the results of a high statistics overnight muon run for both readout strip layers measured with anode design 4, differentiating between two and three-strip clusters.

First of all, a difference is observed in the pure η-distributions in two- and three-strip clusters (if one imagines the projection of the points onto the x-axis), which can be understood in the following way:

For two-strip clusters, the particle traverses the detector anywhere between two strips. Thus, $\eta = 0$ is not possible, as it would reflect a situation where the particle traverses centrally through one of the two strips, which corresponds to either a one-strip or a three-strip cluster.

For three-strip clusters, the particle traverses the anode plane centrally through one strip. Depending on the charge spread in the drift and amplification region, either only one or three strips receive charge and are merged into a cluster. However, in both cases, the central strip receives most of the charge. Consequently, the η-distribution is centered around 0, as the charge weighted hit position is centered around the middle strip.

[2] in units of strips

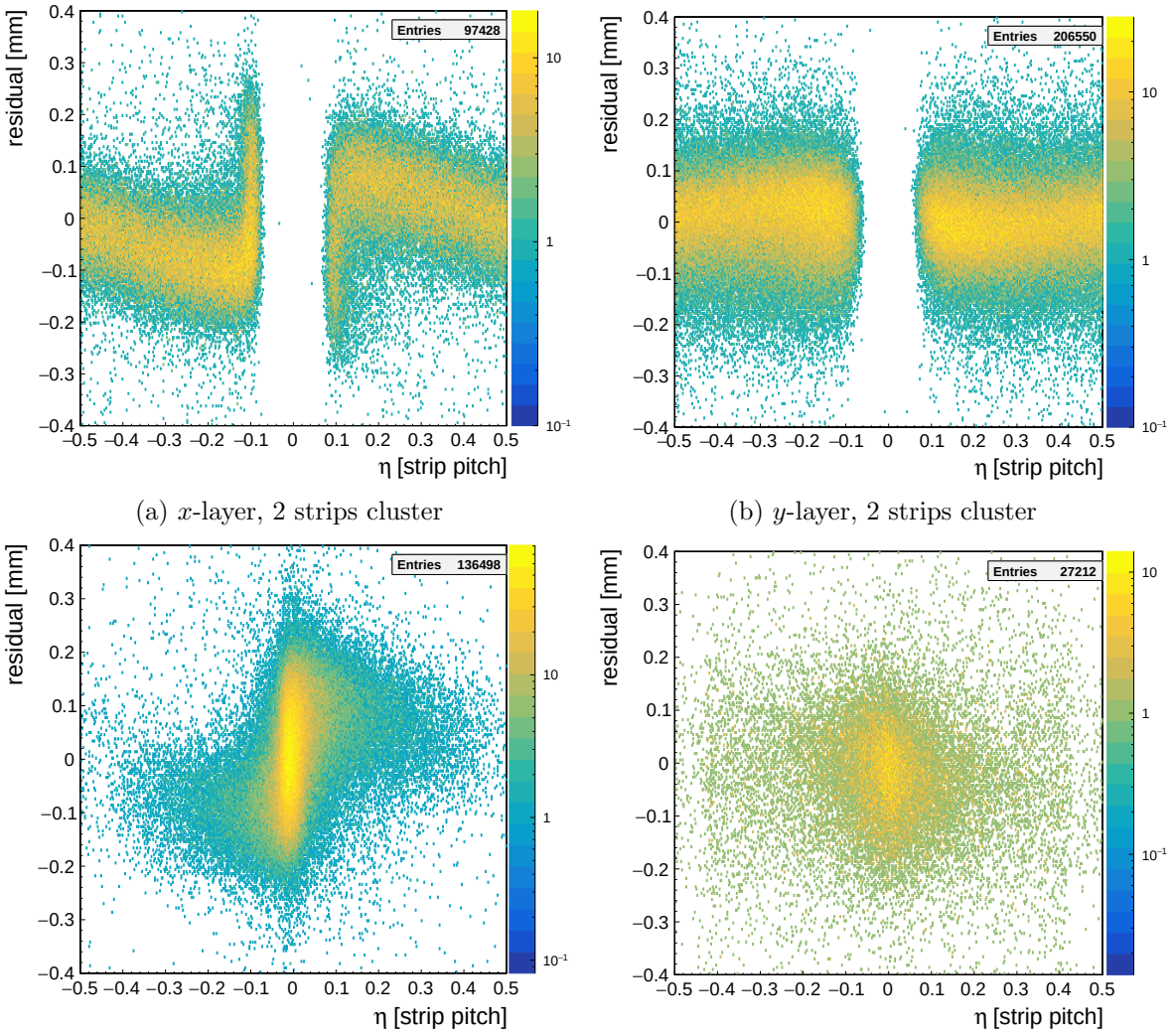

(a) x-layer, 2 strips cluster

(b) y-layer, 2 strips cluster

(c) x-layer, 3 strips cluster

(d) y-layer, 3 strips cluster

Figure 8.7: Residual calculated for two-strip clusters (top) and three-strip clusters (bottom) as a function of η, measured on the x-layer (left) and the y-layer (right) of anode design 4 with an over-night muon beam at E_{amp}=46.8 kV/cm and E_{drift}=0.33 kV/cm, resulting in a total of 290k muon events in the active area of the floating strip Micromegas.

If we now compare the two distributions for the two-strip clusters, we see a clear dependence of the residual i.e. the reconstructed hit position on η with the x-layer, while the dependence is negligibly small on the y-layer. As the x-strips receive their charge through capacitive coupling from the floating strip signal, the reconstructed charge weighted mean position on the x-layer is given by the charge distribution on the floating anode strips. We see that the residual is centered around 0 i.e. the correct particle position is reconstructed if $|\eta| \approx 0.5$ or $|\eta| \approx 0.1$, corresponding to either a particle traversing the two strips right in the middle between the two strips or very close to one of the two strips. However the latter scenario at $|\eta| \approx 0.1$ shows a very broad residual distribution in general. It is caused by the strongly asymmetric charge distribution on the two strips, spoiling the hit position reconstruction through electronics channel saturation. For all other scenarios, the reconstructed position is shifted more towards one of the two strips, as it actually should. Consequently, one of the two strips received more charge than it actually should according to the dimensions of the ionization cloud at the end of the drift region. However this is just the result of the segmented anode strip structure, as the electron avalanches are pulled towards the floating

strips. This effect is more enhanced due to the small floating strip width of $w = 0.15\,\mathrm{mm}$ compared to the pitch of $p = 0.5\,\mathrm{mm}$, as the electron avalanches are earlier separated by the amplification field lines bending earlier in the amplification gap towards the strips. In the limit of $w \to p$, no discretization i.e. dependence on η is expected as the charges arrive on the anode according to the spread of charges at the end of the drift region. In the case of the perpendicular readout strip layer, almost no dependence is visible, as no discretization of the electric field lines i.e. the electron avalanches is present along the floating strips. The small dependence can be attributed to the discretization of ions created at the edges of the floating strips following the field lines which are bending towards the grounded perpendicular readout strips (see Figure 4.2). However, this effect is rather small, as the strip width of the y-strips with $w = 0.4\,\mathrm{mm}$ is close to the pitch of $p = 0.5\,\mathrm{mm}$.

For the three-strip cluster events we see a very narrow distribution for the x-layer and a much more spread 'blob'-like structure on the y-layer. Note the logarithmic scale on the contours. While a small dependence is visible on the parallel readout strips, no dependence is visible on the perpendicular readout strips. The dependence of the x-strips follows from a similar argument as for the two-strip clusters: For $|\eta| > 0.1$, even though the particle did not centrally hit the floating strip, still the avalanches are preferably pulled to it, which causes a systematic mis-reconstruction. All other events with $|\eta| < 0.1$ can be attributed to particles very centrally hitting a floating strip, resulting in a very narrow eta distribution. Thus we conclude that the central floating strip receives almost the complete charge, while the other two strips receive either only very few ionization charge or both neighboring strips just get the same fraction of charge capacitively coupled from the central strip, as it has a very high signal. Additionally the charge on the central strip exceeds for almost all three-strip cluster events the dynamic range of the APV25 chip. This leads to a degradation of the reconstructed position of the traversing particle and thus to a broadening of the residual distribution, as the charge values on the three strips do not reflect the actual charge collected by the floating strips.

As we see a clear correlation of the residual on η in the two-strip clusters and also in the three-strip clusters on the x-layer for $|\eta| \gtrsim 0.1$, an iterative η-based hit correction was performed. For the two-strip clusters i.e. the even number strip clusters, the correlation is parametrized with a 3rd order polynomial. For three-strip clusters i.e. odd number strip clusters, the correlation is parametrized with a 5th order polynomial, defined by

$$\Delta x(\eta) = p_0\eta + p_1\eta^3 + p_2\eta^4 + p_3\eta^5 \quad . \tag{8.3}$$

In general one must say that the residual as a function of η can be parametrized with every arbitrary function, as long as it reflects the correlation. However attention is required for small values of $|\eta| \approx 0.1$ in the x-layer, as there a very strong dependence on η is observed, which is distorted by electronics channel saturation. Little imperfections of the parametrization to the residual data may cause a biased hit correction. Thus the η-based hit correction was only applied where a clear correlation was visible e.g. for $|\eta| > 0.12$ on the x-layer and for two-strip cluster on the y-layer. In particular, in a second iteration, the reconstructed hit position (yielding η) was corrected by the parametrization − for even or odd cluster multiplicity − evaluated at η. The fit parameters for two and three-strip cluster are listed in Table 8.1.

readout layer	strips in cluster	p_0	p_1	p_2	p_3
x	2	0.13 ± 0.02	2.2 ± 0.3	6.8 ± 0.8	6.2 ± 0.9
y	2	-0.041 ± 0.009	-0.5 ± 0.2	-1.6 ± 0.5	-1.4 ± 0.6
x	3	0.84 ± 0.02	-10.0 ± 0.1	-1.2 ± 0.2	30 ± 2

Table 8.1: Parameters of the two and three-strip-cluster fit to the correlation between residual and η. Note that only the parameters for $\eta < 0$ are stated in the two-strip cluster case. No correction was applied to the three-strip cluster on the y-layer, thus the parameters are not listed.

The η-corrected residual distributions for two- and three-strip clusters fit with the double Gaussian function described in equation 8.1 are shown in Figure 8.8, measured with pions.

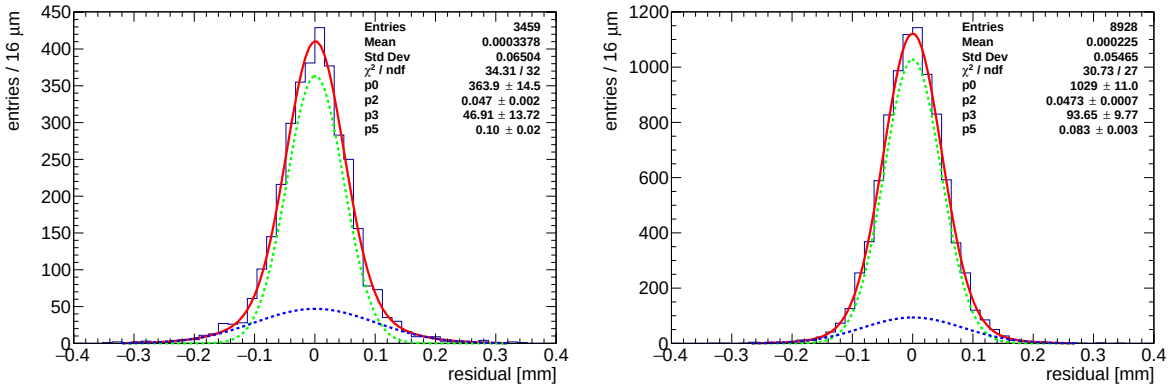

(a) x-layer, 2 strips cluster

(b) y-layer, 2 strips cluster

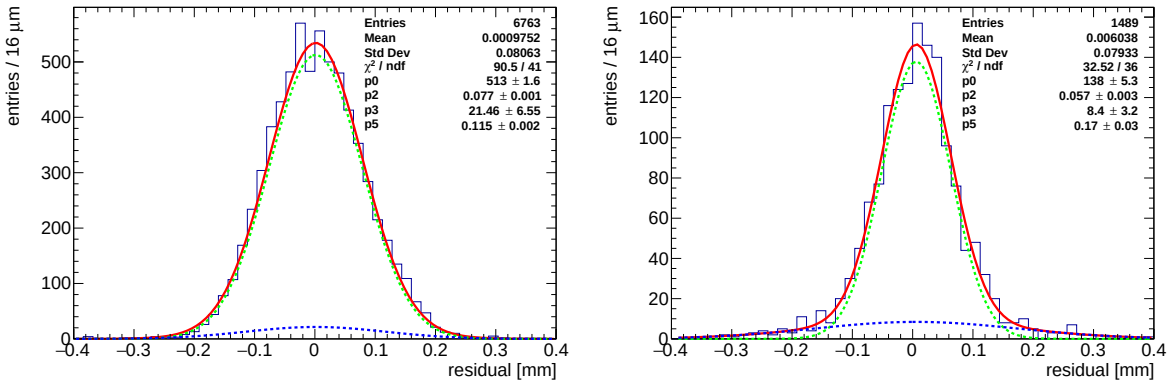

(c) x-layer, 3 strips cluster

(d) y-layer, 3 strips cluster

Figure 8.8: η-corrected residual calculated for two-strip clusters (top) and three-strip clusters (bottom) measured on the x-layer (left) and the y-layer (right) with pions on anode design 4 with E_{drift}=0.33 kV/cm and E_{amp}=47.6 kV/cm. The difference of the residual core width σ^{core} ($p2$ in the legend) of 30 µm on the x-layer between 2 and 3 strip clusters is clearly visible. It is caused by events where the central cluster strip receives almost the complete charge, which additionally drives the electronics channel into saturation. The reconstructed hit position of the particle is thus distorted. Note that the three-strip cluster on the y-layer were not η-corrected, as no correlation was visible.

Focusing first on the two-strip clusters, we see a core residual width of $\sigma_x^{core} = (47 \pm 2)$ µm and $\sigma_y^{core} = (47.3 \pm 0.7)$ µm on the x and y-layer, respectively (parameter $p2$ in the legend box). While the hit-correction yielded a considerable improvement of the spatial resolution on the

x-layer due to the distinct correlation between the residual and η, the y-layer improvement is negligibly small. We can conclude, that the charge discretization effects caused by the segmented anode structure can be corrected for the two-strip cluster, leading to a similar spatial resolution on both readout strip layers.

For the three-strip clusters one would assume that the spatial resolution is better, as the charge gets spread over more anode strips and thus the charge weighted hit position is defined better. However, for the x-layer, three-strip clusters are mainly created by capacitive coupling of the high, saturated signal on the central cluster strip to its neighbors ($\eta < 0.12$), as the charge cloud arriving in the amplification region is of the same size as the strip pitch and in this case, centered above a floating strip. Nevertheless, after applied correction for $\eta > 0.12$, an optimum residual width of $\sigma_x^{\text{core}} = (77 \pm 1)\,\mu\text{m}$ is observed on the x-layer. On the y-layer we find a residual width of $\sigma_y^{\text{core}} = (57 \pm 2)\,\mu\text{m}$, which is around 10 µm worse than the two-strip cluster resolution. The degradation in the three-strip cluster is caused by high signals that also drive the central y-strip into saturation. In addition to that, the discretization effect is in general much smaller on the perpendicular readout strip layer due to the fact that only the ion movement from the floating strip towards the y-strips contributes to the discretization, having itself a strip width of 0.4 mm close to the pitch of 0.5 mm.

The total residual distribution, which is the sum of all strip residual distributions, is shown in Figure 8.9 for the x and y-layer, fit with the double Gaussian function from equation 8.1. With a track uncertainty of 23 µm, the combined spatial resolution is $(79 \pm 4)\,\mu\text{m}$ for the x-layer and $(54 \pm 2)\,\mu\text{m}$ for the y-layer. If we count the good events as defined in section 7.3 in a 5σ window around the Gaussian residual distribution, an efficiency of $(98.0 \pm 0.2)\,\%$ is observed for both layers. The core spatial resolutions are $(66 \pm 4)\,\mu\text{m}$ and $(45 \pm 2)\,\mu\text{m}$, respectively, and cover 78.5% of the events on the x-layer and 87.4% of the events on the y-layer.

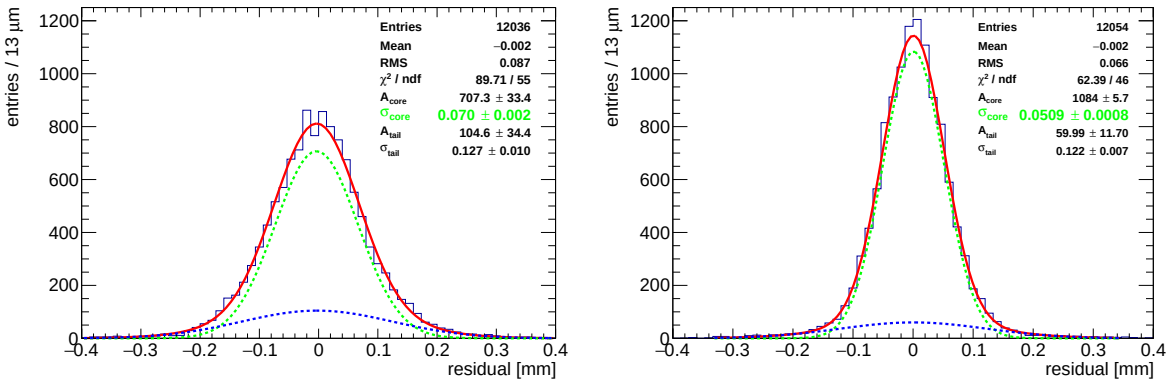

(a) x-layer (b) y-layer

Figure 8.9: Exclusive corrected residual distribution measured with anode design 4 at a perpendicular incident pion beam at a rate of 420 kHz/cm^2 with E_{drift}=0.33 kV/cm and E_{amp}=47.6 kV/cm. The core Gaussian width σ_{core} is marked in green.

Usually the broader Gaussian distribution, denoted by σ_{tail}, is caused by delta-electrons created in the ionization process of the particle traversing the drift region, biasing the Gaussian charge distribution. However, the more pronounced broad tail in the x-layer can be attributed to the worse spatial resolution of three-strip clusters (as discussed above) in combination with one-strip clusters.

As for one-strip cluster events no η-value can be calculated, no hit-correction can be performed. This should yield a spatial resolution similar to $0.150\,\text{mm}/\sqrt{12} \approx 43\,\mu\text{m}$, which is

not observed [3]. However, a distinct difference is visible when looking at the residual distribution of one-strip cluster in x and y-layer separately: For the x-strips a very broad distribution with two peaks are observed centering around $\pm 150\,\mu m$ (see Figure 8.26). The expected distribution centered around 0 is observed for the y-strips. Consequently, many of the one-strip cluster events of the x-layer are wrongly identified two-strip cluster events, caused by the strong anode strip charge discretization, leading to a very small signal on one of the two strips, thus vanishing in noise. As we almost see no discretization effects on the y-layer, this effect is not observed on the y-layer.

The core spatial resolution as well as the combined i.e. the core and tail integral weighted spatial resolution are shown in Figure 8.10 as a function of amplification and drift field for both readout strip layers of the three anode designs, measured with a perpendicular incident muon beam.

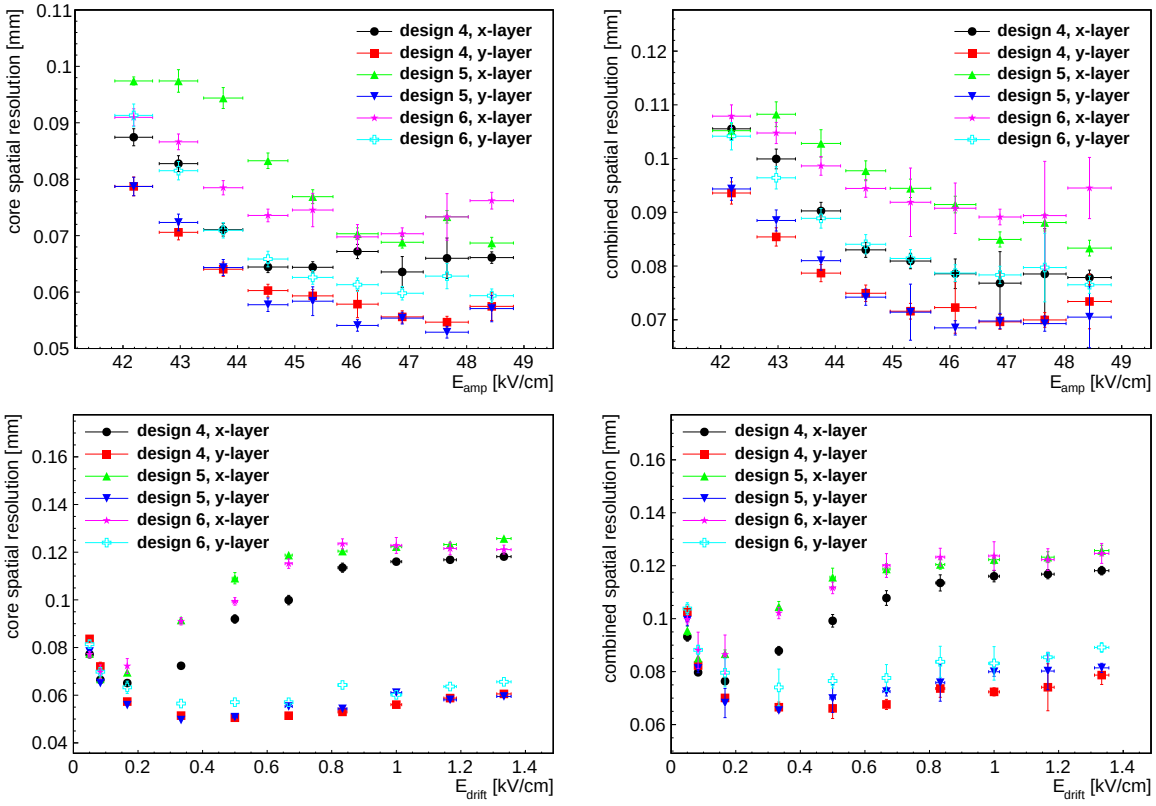

(a) core Gaussian (b) combined double Gaussian

Figure 8.10: Spatial resolution derived from the core Gaussian (left) and the combined double Gaussian (right) as a function of E_{amp} at E_{drift}=0.17 kV/cm (top) and as a function of E_{drift} at E_{amp}=46.9 kV/cm (bottom), measured at a perpendicularly incident muon beam for all three anode designs.

We see that for $E_{amp} \approx 46\,kV/cm$ the spatial resolution reaches a minimum. Above it stays almost constant for all anode designs, which is due to the gain necessary to also measure small signals in a cluster. In the plateau the core spatial resolution reaches for both readout strip layers of all designs values below 80 µm and for the combined resolution below 90 µm. In general a worse resolution is observed on the x-layer compared to the y-layer, due to the charge discretization effects caused by the ionization cloud lateral size being in the same order as the strip pitch in combination with saturated front-end electronics, as previously

[3] Definition of the standard deviation σ of a uniform distribution on a length x: $\sigma = x/\sqrt{12}$

discussed. The best simultaneous signal reconstruction is observed on anode design 4, with a combined spatial resolution below 80 µm for both readout strip layers.

The spatial resolution as a function of the drift field shows a distinct difference between x- and y-layers. While for very small drift fields the spatial resolution degrades for both readout strip layers similarly, the resolution reaches a minimum around 0.17 kV/cm on the x-layer. When increasing the drift field it steadily degrades and reaches a plateau at $E_{drift} > 0.8$ kV/cm, while the y-layer resolution stays almost constant for increasing drift field. At very high drift fields the resolution marginally degrades on the y-layer. The different behavior of the two readout strip layers can be explained by the electron diffusion dependence on the drift field of the used Ne:CF_4 80:20 vol.% gas mixture, as shown in Figure 2.3 (right). We see that for increasing drift field the electron transverse diffusion steadily decreases up to $E_{drift} > 0.6$ kV/cm at which point a minimum is reached that stays constant up to the investigated range of 1.4 kV/cm.

The minimum of the spatial resolution for the x-layer is reached at 0.17 kV/cm is a result of a combination of maximum pulse height at the drift field of maximum mesh transparency and a relatively high electron diffusion. The higher electron diffusion for lower drift fields is beneficial for the x-layer, as the charge is thus more spread over the anode strips leading to a smaller charge discretization and electronics saturation effect. For higher drift fields the diffusion is so small that for almost 50% of the events only a one-strip cluster is found, dominantly degrading the spatial resolution. This manifests also in the similar values of core and combined spatial resolution for very high drift fields.

The y-layer follows pretty much the electron diffusion dependence on the drift field, however, degrading for very high drift fields due to the steadily decreasing mesh transparency causing a lower pulse height, as visible in Figure 8.4. As we have already previously discussed, we know that the signal formation on the y-strips is only weakly influenced by charge discretization effects. This leads to an improved spatial resolution for a small diffusion, as the electron avalanche positions as well as the ion movement in the amplification region are reflecting the particle trajectory accurately, allowing the very localized induced signal coupling to the perpendicular readout strip to reconstruct the true particle position with high precision.

As we have seen in the previous chapters, it is possible to build a two-dimensional floating strip anode at a pitch of 0.3 mm, which should reduce the charge discretization visible on the x-layer and thus improve the spatial resolution. However, the design was not yet available during the measurements presented in this chapter.

8.3.2 Inclined Particle Tracks

In this section the spatial resolution of anode design 4 is investigated as a function of the inclination angle. The detector was mounted such that particle angles of 20°, 30° and 40° could be adjusted with a precision of about 1° with respect to both readout strip layers. The µTPC angle reconstruction results can be found in appendix C. A photography of the measurement setup at the H8 beam line is shown in Figure 8.11, where the detector equipped with anode design 4 was tilted by 20° with respect to the y-coordinate of the tracking detectors.

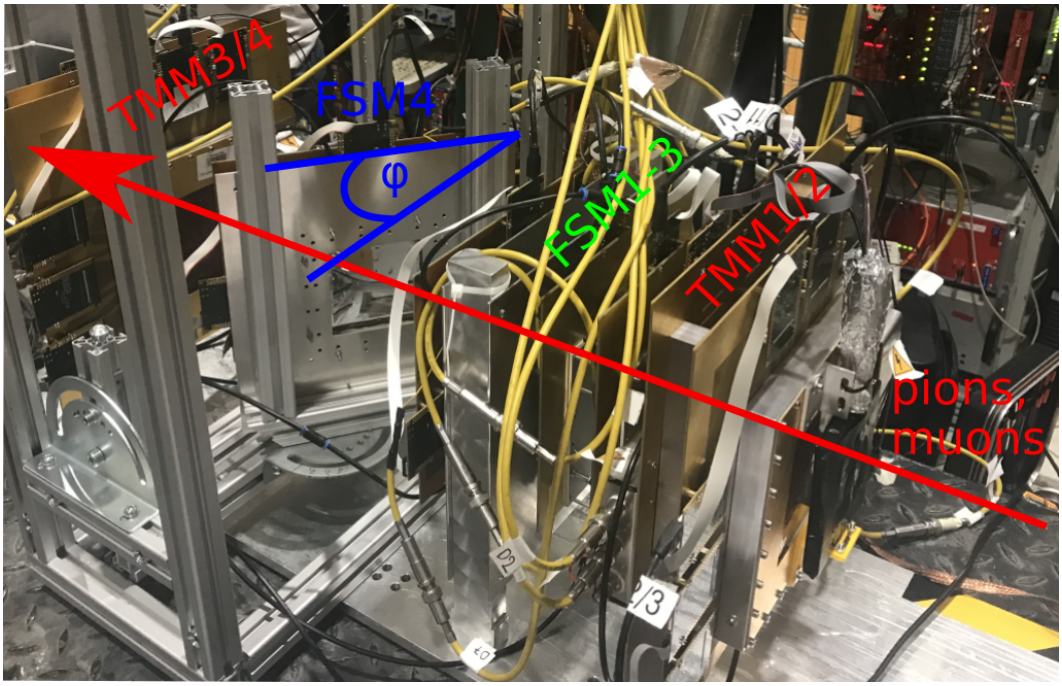

Figure 8.11: Picture of the measurement setup at the H8 beamline at CERN. Here, the detector equipped with anode design 4 is tilted by 30° with respect to the other detector layers measuring the particles in y-direction.

The spatial resolution is determined by both the centroid method, i.e. the charge weighted mean position, as well as the µTPC position reconstruction method. Both methods have been described in section 3.4 and 3.5, respectively.

As the µTPC method relies on the precise knowledge of the drift time, the drift velocity of the electrons has been previously determined. The results showed that the drift velocity was about 10-15% lower than a MAGBOLTZ simulation predicts for a pure Ne:CF_4 80:20 vol.% gas mixture at NTP, probably caused by 0.05 vol.% of humidity in the gas, corresponding to a relative humidity of about 2%. The measured electron drift velocity at the two lowest drift field points of 0.083 kV/cm and 0.17 kV/cm is (30 ± 2) µm/ns and (48 ± 3) µm/ns, respectively.

As the trigger signal from the scintillators is not synchronized to the 40 MHz clock of the SRS-based readout system including the APV25 front-end hybrid boards, the trigger signal and consequently the digitized strip signals jitter within one 25 ns clock cycle. As the jitter corresponds to a translation of the µTPC line fit in the time-domain, the reconstructed µTPC position is shifted in the position-domain. To be able to correct for the jitter, the trigger signal has been additionally recorded with a VME-based TDC, as described in section 8.1. The µTPC residual is defined as the difference between reconstructed µTPC position and track predicted position in the middle of the drift gap. It is plotted against the trigger timing in Figure 8.12. The clear correlation between position reconstruction and trigger timing is visible, which degrades the spatial resolution considerably, if not corrected.

Thus for all following analysis results, the jitter recorded by the TDC has been explicitly subtracted on the event-basis and consequently eliminated in the APV25 raw data.

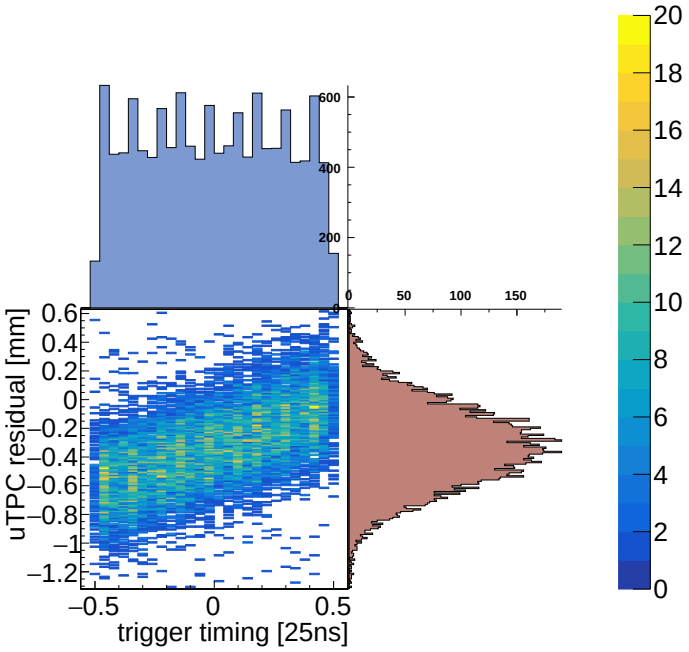

Figure 8.12: µTPC residual for 30° incident muons plotted against the timing of the trigger signal, recorded with a VME based TDC. The correlation is clearly visible and needs to be corrected.

The analysis procedure to determine the µTPC spatial resolution is briefly described. After jitter elimination and determination of the timing in the middle of the drift gap, described in section 3.5, the µTPC position in the middle of the drift gap can be determined. Figure 8.13 (a) shows the µTPC residual as a function of the cluster timing at 20° incident muons with E_{drift}=0.083 kV/cm and E_{amp}=50 kV/cm. The cluster timing has been defined as the average time of the maximum of all signals in a cluster. A correlation between residual and cluster timing is still visible, even though the jitter has already been eliminated. Assuming that the jitter correction worked reliably, the dependence may be explained by capacitive coupling between neighboring strips. As e.g. the first responding strip in a cluster couples the signal capacitively to its neighboring strips, signals that would arrive at later time are shifted to earlier time values and vise versa. This results in a disturbed strip and consequently cluster timing, which is shifted either to earlier or later time values, depending on the charge deposition on the strips i.e. the in-homogeneous charge deposition along the track in the drift region.

A method to correct neighboring strips for capacitive coupling has been presented in [Lösel, 2017], which performes the correction on the raw strip signals. A similar algorithm was implemented also for this analysis, which showed indeed a reduction of the correlation between residual and timing, however, not completely removing it. Additionally it was observed, that the correction led to more failed µTPC line fits. Thus this approach of charge correction i.e. capacitive coupling correction on the raw data was not further pursued in the following analysis.

In fact, the correlation visible in the residual distribution as a function of the cluster timing is investigated in more detail. The strength of the correlation i.e. the slope of the line fit to the correlation is shown in Figure 8.13 (b) as a function of the drift field for 20°, 30° and 40° inclination angle, measured on the parallel readout strip layer. A very similar result is also observed for the perpendicular readout strip layer, which, however, is not shown here. We see

a dependence of the slope on the drift field for all investigated angles: For increasing drift field, the correlation becomes stronger i.e. the effect of capacitive coupling seems to be stronger. As for higher drift fields, the strip signals arrive closer in time which leads to an increased interference of the strip signals by capacitive coupling, this is understandable. Furthermore, the correlation is found to be independent of the inclination angle for $E_{drift} \leqslant 0.17\,kV/cm$, corresponding to electron drift velocities $v_{drift} \leqslant (48 \pm 3)\,\mu m/ns$. For higher drift fields, the correlation seems to show a trend of increasing correlation with increasing inclination angle. However, note that for high drift fields the high electron drift velocity in combination with a lower strip pulse height (caused by reduced mesh transparency as well as a higher inclination angle), degrades the µTPC reconstruction considerably. In general the capacitive coupling is expected to be independent of the inclination angle.

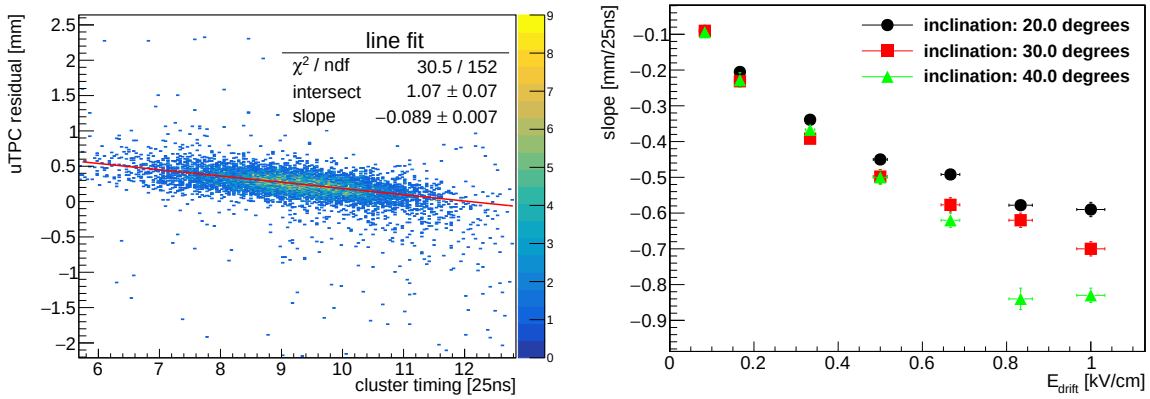

(a) line fit to the correlation

(b) slope dependence

(c) corrected residual, 20°

Figure 8.13: µTPC residual of the x-layer plotted against the cluster timing (a) for a 20° incident muon beam at E_{drift}=0.083 kV/cm and E_{amp}=50 kV/cm, fit with a straight line. (b) Slope from the line fit as a function on E_{drift} at E_{amp}=50 kV/cm for three different angles. (c) Corrected µTPC residual for a 20° incident muon beam at E_{drift}=0.083 kV/cm and E_{amp}=50 kV/cm. To extract the spatial resolution the distribution is fit with a Gaussian function. The fit parameters are stated in the legend.

The fit parameters i.e. the slope p_1 and intersect p_0 can be used to iteratively correct the µTPC hit position $x_{\mu TPC}$ for the dependence on the cluster timing $t_{cluster}$, following

$$x_{\mu TPC,corr} = x_{\mu TPC} - p_1 \cdot t_{cluster} - p_0 \quad . \tag{8.4}$$

The corrected µTPC residual distribution of the x-layer for 20° inclination angle is shown in Figure 8.13 (c). To extract the spatial resolution, the residual distribution is fit with a

single Gaussian function and the σ from the fit is corrected by the track uncertainty at the detector position. The residual width from the Gaussian fit improved from $(150 \pm 2)\,\mu m$ to $(117 \pm 2)\,\mu m$, when applying the cluster timing correction.

The following figures (Figure 8.14 to 8.17) compare the achieved centroid and µTPC spatial resolution as a function of amplification and drift field at inclination angles 20°, 30° and 40°, measured with both readout strip layers. The cluster timing correction was applied for the determination of the µTPC resolution.

We see that very similar results in terms of dependence of spatial resolution on drift and amplification field are observed on x- and y-layer. However, big differences between centroid and µTPC resolution are found, which are discussed in the following.

Looking at the dependence on the amplification field in Figure 8.14 and 8.15 measured at $E_{drift} = 0.083\,kV/cm$, we see that the µTPC method yields a considerably better position information than the centroid method.

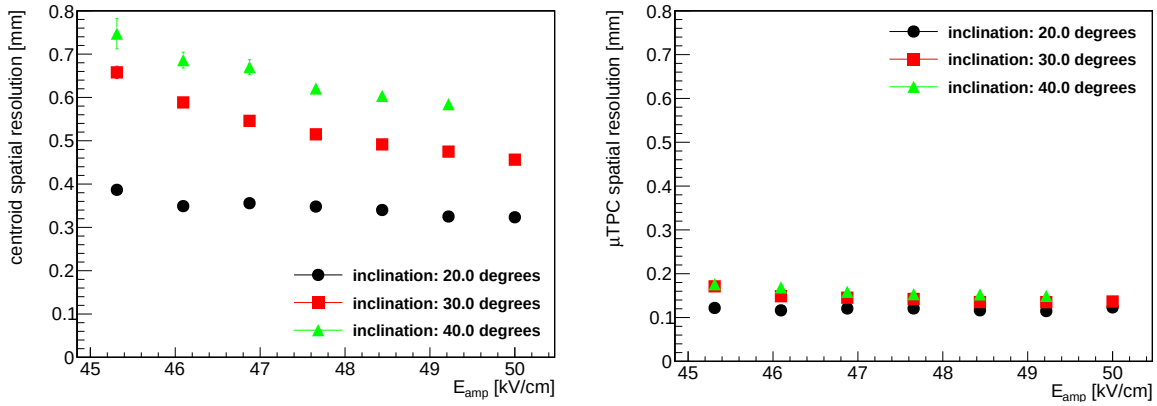

Figure 8.14: Spatial resolution of the x-layer determined with the centroid method (left) and the µTPC method (right) as a function of E_{amp} at E_{drift}=0.083 kV/cm for three different inclination angles.

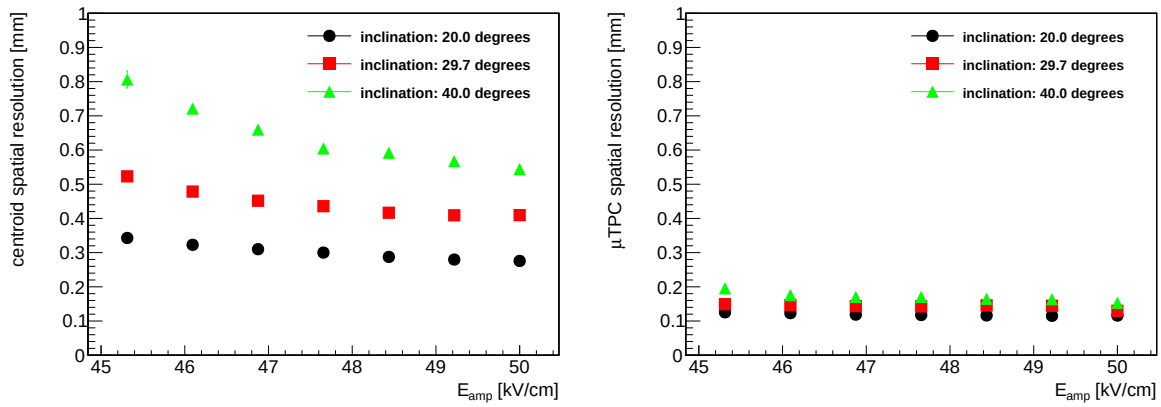

Figure 8.15: Spatial resolution of the y-layer determined with the centroid method (left) and the µTPC method (right) as a function of E_{amp} at E_{drift}=0.083 kV/cm for three different inclination angles.

The difference can be attributed to the non-homogeneous ionization of the muons and pions, when traversing the 6 mm long drift region. This leads to non-Gaussian shaped cluster charge distributions arriving in the amplification region, which degrades the position information by the centroid method (see Figure 3.12). While the centroid resolution degrades for increasing

inclination angles up to almost 0.8 mm for the smallest investigated amplification field, the µTPC method yields a spatial resolution below 0.2 mm over the full amplification field range. Due to the centroid method relying only on the strip charge information to reconstruct the position, in general a stronger dependence on the amplification field is observed than for the µTPC method.

The dependence of the spatial resolution on the drift field is shown in Figure 8.16 and 8.17 measured at $E_{amp} = 50\,kV/cm$ for x- and y-layer, respectively. We see that the centroid resolution is generally independent of the chosen drift field. Only for very high drift fields the pulse height reduction caused by decreasing mesh transparency degrades the resolution. However for the µTPC spatial resolution we see a distinct dependence on the drift field: The smaller the drift field, the better the resolution. This is understandable, as the line-fit quality to the strip-time data points improves, if the signal timings are well separated, which is the case for small drift fields. The optimum spatial resolution is achieved at the lowest measured drift field of $E_{drift} = 0.083\,kV/cm$, corresponding to a measured electron drift velocity of $v_{drift} = (30 \pm 2)\,\mu m/ns$. We find a µTPC resolution for both readout strip layers of $(115 \pm 4)\,\mu m$ for 20°, of $(132 \pm 6)\,\mu m$ for 30° and of $(152 \pm 8)\,\mu m$ for 40°. The µTPC method out-performes the centroid method for all investigated inclination angles by almost a factor of 3.

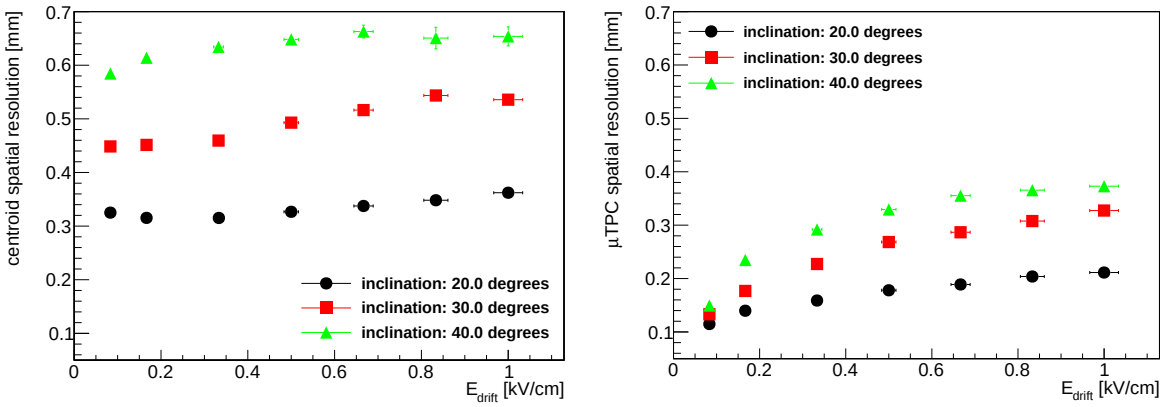

Figure 8.16: Spatial resolution of the x-layer determined with the centroid method (left) and the µTPC method (right) as a function of E_{drift} at E_{amp}=50 kV/cm for three different inclination angles.

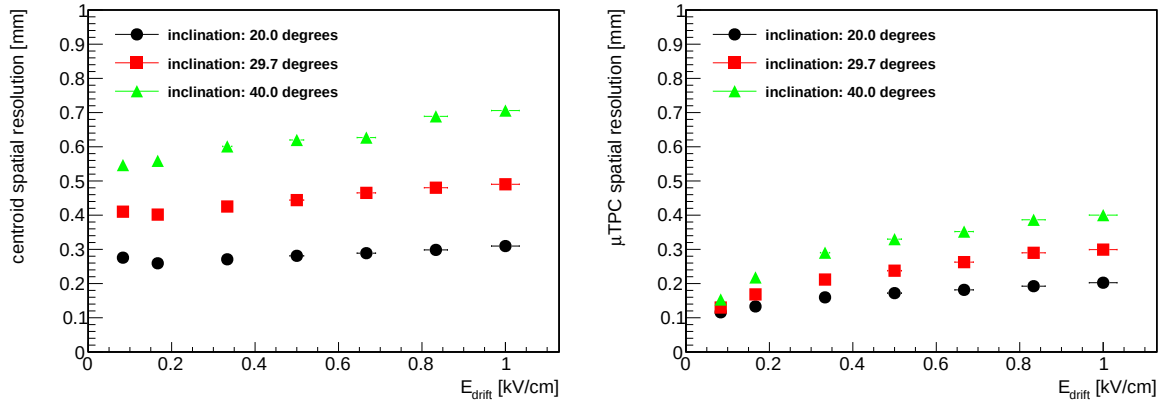

Figure 8.17: Spatial resolution of the y-layer determined with the centroid method (left) and the µTPC method (right) as a function of E_{drift} at E_{amp}=50 kV/cm for three different inclination angles.

Figure 8.18 summarizes the optimum found spatial resolution of centroid and µTPC method, as a function of the particle inclination angle. A GARFIELD simulation as well as the centroid spatial resolution at perpendicular incidence have been superimposed. We see that the two-dimensional floating strip Micromegas detector is able to resolve particles on both readout strip layers with a precision of around (100 ± 50) µm over the investigated inclination angle range, if drift and amplification voltages are chosen accordingly.

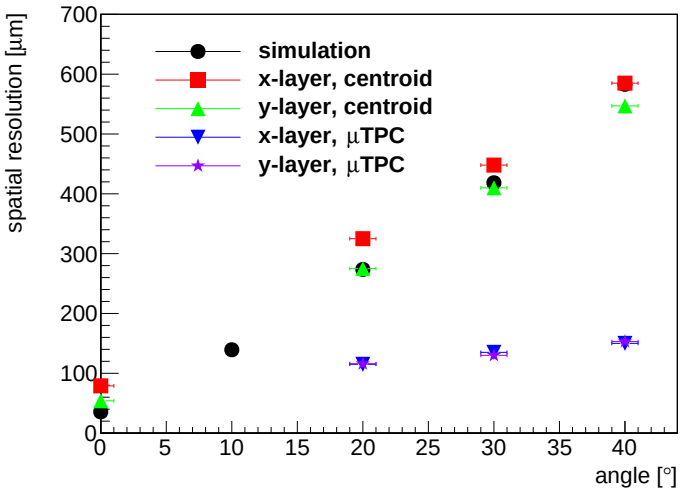

Figure 8.18: Spatial resolution for both readout strip layers as a function of the incidence angle of the particle. The simulated centroid resolution of a MIP traversing a 6 mm long gas gap filled with Ne:CF_4 has been superimposed. The optimum centroid resolution for perpendicular incidence is also shown, measured at E_{amp}=47.6 kV/cm and E_{drift}=0.33 kV/cm. For the µTPC resolution the measurements at E_{amp}=50 kV/cm and E_{drift}=0.083 kV/cm are shown. The values almost coincide.

8.4 Efficiency

To characterize the detection efficiency of both readout strip layers, the residual between track predicted and measured hit is determined. From a Gaussian fit to the residual distribution, the 'good' events are counted in a $5{\cdot}\sigma_{res}$ wide window around the expected position and compared to the number of tracks found by the reference tracking system, similar as shown in Figure 7.5. σ_{res} represents the width of the residual used for the determination of the spatial resolution as described in the previous section. For the residual distribution of the perpendicular tracks, usually a double Gaussian function is fit to also account for delta electrons, degrading the spatial resolution. Consequently, σ_{res} is determined by weighting σ_{core} and σ_{tail} with the events covered by the two different Gaussian distributions. For the determination of the efficiency with anode design 4 tilted at 20°, 30° and 40°, always a single Gaussian fit was performed, as no distinct tail was observed like for the perpendicular incidence measurements. This is because the µTPC algorithm identifies strip-time data points that do not agree with a straight line and excludes them from the line fit. The algorithm as explained in section 3.5.

The efficiency of anode designs 4, 5 and 6 is shown in Figure 8.19 as a function of the amplification field for both readout strip layers, measured with a perpendicular incident muon beam. The efficiency turn on is visible on both readout strip layers. The plateau of around 95% is reached for all designs for $E_{amp} > 46$ kV/cm, where we also see a plateau for the spatial resolution in Figure 8.10. The spread of the turn on curves on the x-layer is caused by the spread of pulse height visible in Figure 8.3, which is a result of the different

perpendicular strip width configurations. Due to a dead APV25 channel connected to the x-layer of anode design 6, the detection efficiency is lower compared to design 4, even though a higher pulse height is observed. Additionally, the detector equipped with anode design 6 became slightly unstable for $E_{amp} > 46\,kV/cm$. This is due to either cleanliness related issues or an anode PCB defect, which affected the efficiency a little for $E_{amp} > 46\,kV/cm$.

We see that the best performance is observed for anode design 4, which shows an efficiency above 90% over the full range of the amplification field scan. The plateau is reached for $E_{amp} > 45\,kV/cm$ with $(96.9 \pm 0.5)\%$ on the x-layer and $(97.0 \pm 0.6)\%$ on the y-layer.

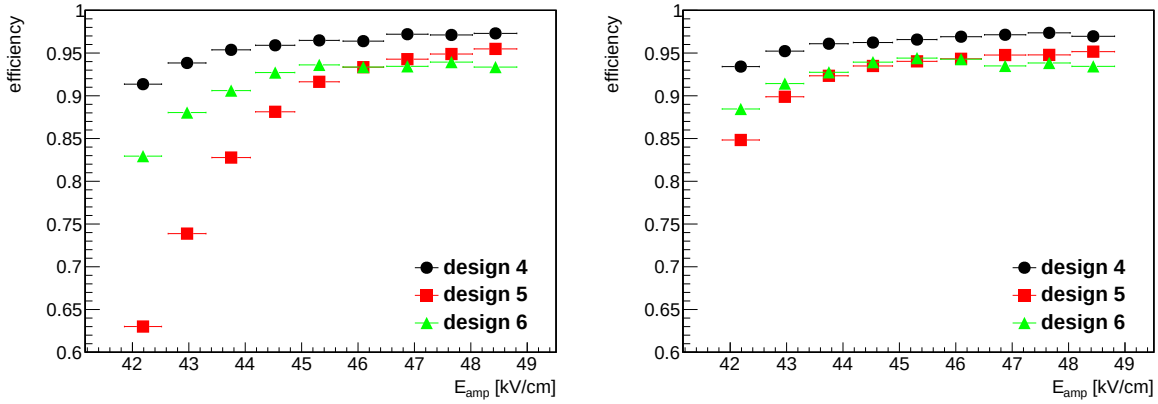

(a) x-layer (b) y-layer

Figure 8.19: Efficiency of the x-layer (left) and the y-layer (right) as a function of E_{amp} at E_{drift}=0.17 kV/cm for all three anode designs at a perpendicular incident muon beam.

Figure 8.20 shows the efficiency as a function of the drift field at E_{amp}=46.9 kV/cm for a perpendicular incident muon beam. While we see that the efficiency is decreasing with increasing drift field on the x-layer, the y-layer stays quite constant.

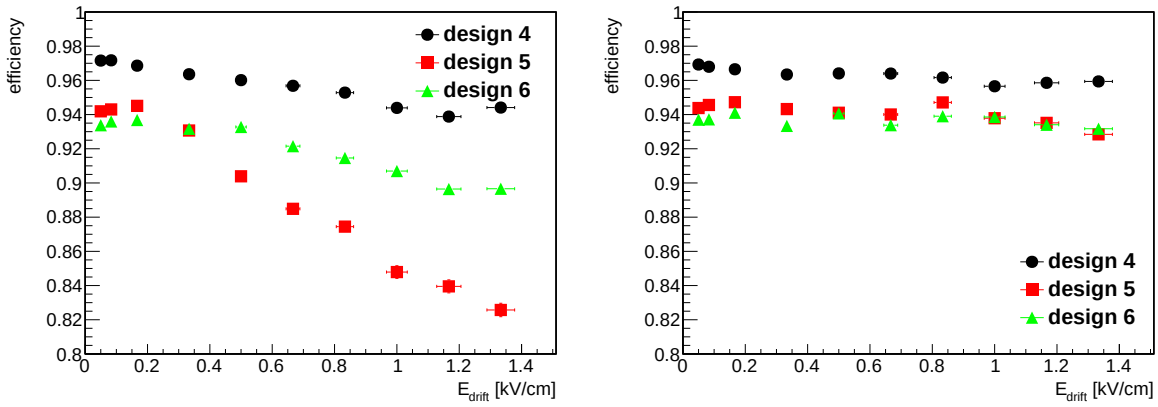

(a) x-layer (b) y-layer

Figure 8.20: Efficiency of the x-layer (left) and the y-layer (right) as a function of E_{drift} at E_{amp}=46.9 kV/cm for all three anode designs at a perpendicular incident muon beam.

This can be attributed to the similar shape of the x-layer spatial resolution as a function of the drift field, as visible in Figure 8.10. As for higher drift fields the electron diffusion in the drift region decreases, the spatial resolution on the x-layer is degraded due to increasing number of one-strip clusters, as discussed in the previous section. This consequently leads to a reduced efficiency. As the y-layer spatial resolution is almost constant for increasing drift

field, so is the efficiency. The little trend of degrading resolution for very high fields is caused by the decreasing mesh transparency, resulting in a lower pulse height. The fact that the efficiency is not reaching values above 97% can be attributed mostly to the non-negligible contribution of the pillars present in the active area, as clearly visible in Figure 8.23.

In the following, the efficiency on the example of the y-layer of anode design 4 is discussed for inclination angles 20°, 30° and 40° with respect to the beam direction. The x-layer results are very similar and can be found in appendix C.

Figure 8.21 to 8.22 show the efficiency for an amplification and drift field scan, respectively, comparing the centroid (left) with the µTPC method (right).

First focusing on the amplification field scan shows an excellent mean centroid efficiency of $(99.2 \pm 0.6)\%$, independent of E_{amp} and the particle inclination angle[4]. The efficiency is in general able to reach almost 100% as for inclined particle tracks the ionization charge cloud entering the amplification region is much bigger than the pillar size. The µTPC efficiency shows a turn-on curve, similar to the perpendicular incidence efficiency turn-on, which reaches values above 96% for $E_{amp} > 48\,kV/cm$.

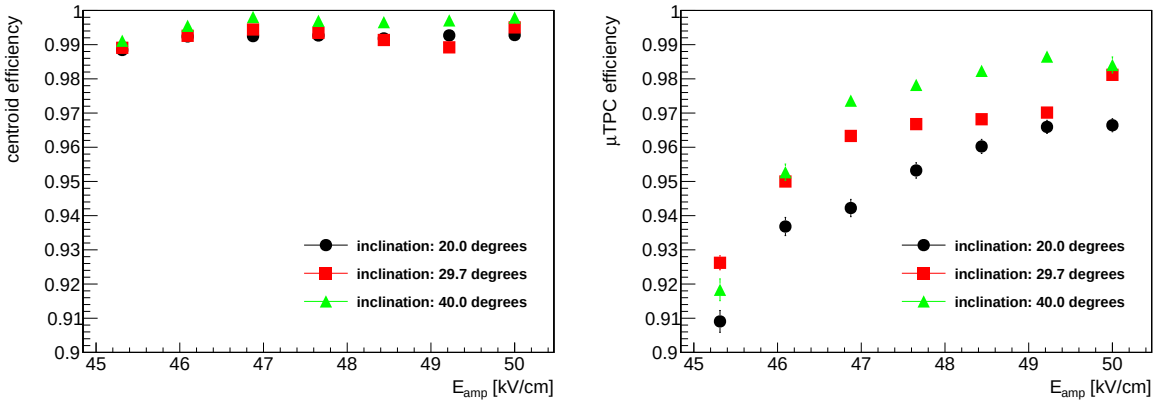

Figure 8.21: Efficiency of the y-layer determined with the centroid method (left) and the µTPC method (right) as a function of E_{amp} at E_{drift}=0.083 kV/cm for three different inclination angles, measured with muons.

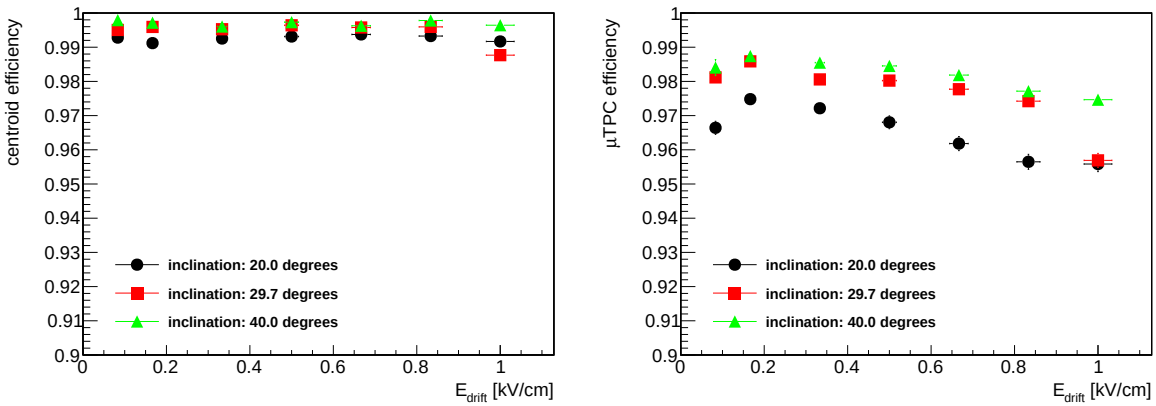

Figure 8.22: Efficiency of the y-layer determined with the centroid method (left) and the µTPC method (right) as a function of E_{drift} at E_{amp}=50 kV/cm for three different inclination angles measured with muons.

[4]Note that the efficiency definition with $5 \times \sigma_{res}$ refers to the width of the residual distribution for each point in the figures. Thus the acceptance range for good hits is generally larger for the centroid method, as the spatial resolution is worse than the µTPC method

We see that the µTPC reconstruction efficiency is vulnerable to failed line fits, if the amplification field is not chosen sufficiently high. For increasing inclination angle, the µTPC efficiency increases as expected.

Only a week dependence on the drift field is observed for centroid as well as µTPC method (see Figure 8.22). Again, we find that the centroid efficiency is very close to 100% for almost the full investigated drift field range. As the µTPC method is not as robust as the centroid method, pulse height changes caused by decreasing mesh transparency are visible in the efficiency as well.

The 'inefficiency' of the floating strip Micromegas equipped with anode design 4 is plotted as a function of the particle position, for an overnight measurement with a perpendicular incident muon beam. It is clearly visible, that the inefficiency inside the active area accumulates almost only on the position of the pillars, which demonstrates the excellent performance of the detector.

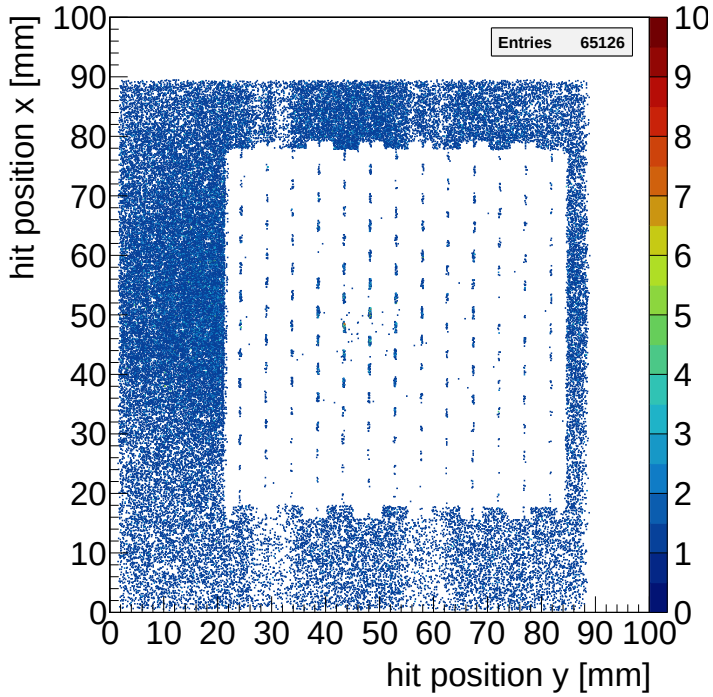

Figure 8.23: Map of inefficient regions on anode design 4 measured with an overnight muon run at perpendicular incidence with E_{amp}=46.8 kV/cm and E_{drift}=0.33 kV/cm. The beam is illuminating the full area of the tracking system, thus the inefficiency outside the active area of the floating strip Micromegas is clearly visible. Inefficient spots inside the active area are located mostly at the pillars.

8.5 High Rate Measurements

To investigate the high rate capability of both readout strip layers of a two-dimensional floating strip Micromegas, all anode designs are tested on particle reconstruction performance such as cluster charge, efficiency and spatial resolution for pion beam fluxes up to almost 5 MHz/cm^2.

Measurements with four different pion beam intensities have been carried out. The intensity has been increased by adjusting the collimators at the beginning of the experiment. For the highest measured rate, the Gaussian beam profile covered an area with $\sigma_x = (2.39 \pm 0.02)$ mm

and σ_y=(3.25 ± 0.03) mm. It changed only marginally when the intensity was varied. The beam flux J has been calculated by

$$J = \frac{n_s}{t_s \cdot \pi \cdot \sigma_x \sigma_y} \quad , \tag{8.5}$$

where n_s are the particles per spill and t_s is the spill duration. The values are listed in Table 8.2.

measurement	# 1	# 2	# 3	# 4
particles per spill	4.54×10^5	5.78×10^5	1.23×10^6	5.18×10^6
spill duration [s]	4.5	4.5	4.5	4.5
mean particle rate [kHz]	100	128	273	1151
mean particle flux J [MHz/cm^2]	0.42	0.53	1.1	4.7

Table 8.2: List of the four measurement points with different beam intensities discussed in this section. The particles per spill are determined by beam diagnostic chambers located in front of each experiment and are provided to the user. The spill duration is defined by the accelerator steering cycle.

Upon increasing the pion beam intensity, the probability rises to record also secondary fragments created by pion-nucleus interactions in materials along the beam line. Thus, the number of charge clusters per event rises in the detector, as it is visible in the first tracking TMM chamber, see Figure 8.24 (left). A mean value of 1.8 is observed for the highest measured intensity, with a clearly visible tail to higher values. An event display, also for the highest rate of 4.7 MHz/cm^2, measured on the y-layer of anode design 4 is shown in Figure 8.24 (right). Around 6 particles are traversing the detector nearly simultaneously.

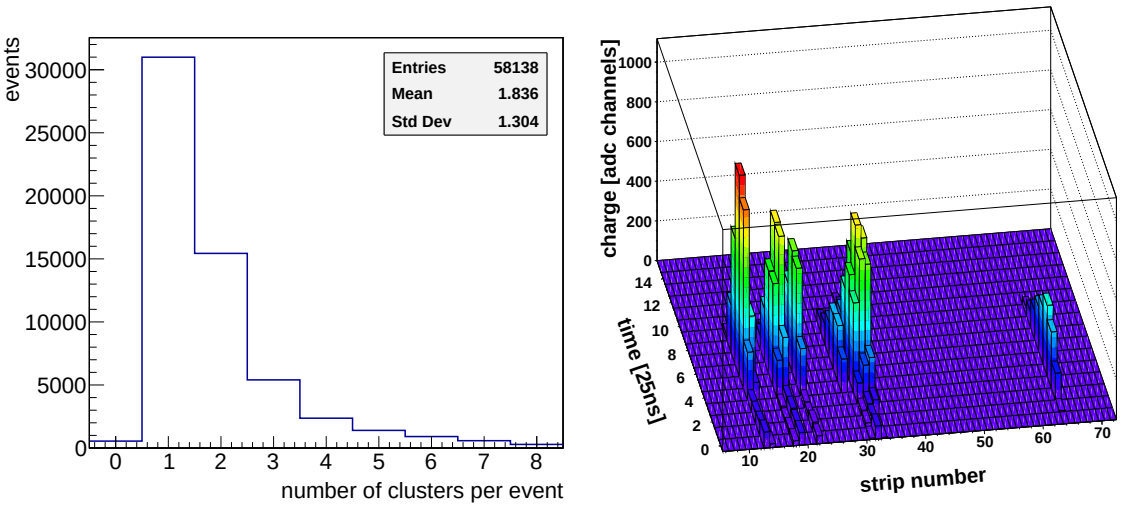

(a) TMM1, y-layer (b) FSM4, y-layer

Figure 8.24: Left: Number of charge cluster per event reconstructed with the first TMM chamber for the highest measured beam intensity of 4.7MHz/cm^2. Right: Display of an event where six particles are traversing the floating Micromegas with anode design 4 at the same time, measured at a beam flux of 4.7 MHz/cm^2. These events are originating from nucleus fragments created by pion-nucleus interactions along the beam line.

For simplicity reasons, the measurements presented in this section will cover only events with strictly one charge cluster present in the full telescope[5]. This reduces the number of events to around 25% at the highest rate, as in all four TMM chambers i.e. all 8 readout strip layers a simultaneous one-cluster event is required. Additionally, a $\chi^2/\text{ndf} < 10$ requirement on the track quality was applied, leaving around 17% of the initial events for the highest rate point, where the track is interpolated into the floating strip Micromegas. This corresponds to around 10k particle events, which is a sufficiently high statistics to check the particle reconstruction performance of the detectors.

The cluster charge as a function of the beam flux is shown in Figure 8.25 (left), for both readout strip layers of all anode designs. Due to slightly unstable operation of anode design 5 and 6, amplification voltages were adjusted for individual rate points. This was already observed during measurements presented in the previous sections, probably caused by a cleanliness related issue. The amplification voltages applied to the three detectors during the rate measurements are listed in Table 8.3.

rate measurement	# 1	# 2	# 3	# 4
U_{amp}, anode design 4	600	600	600	600
U_{amp}, anode design 5	590	580	580	570
U_{amp}, anode design 6	600	600	600	595

Table 8.3

Anode design 4 showed a very stable operation during all measurement points, which allowed to stay at a constant amplification field of E_{amp}=46.8 kV/cm and a drift field of E_{drift}=0.33 kV/cm.

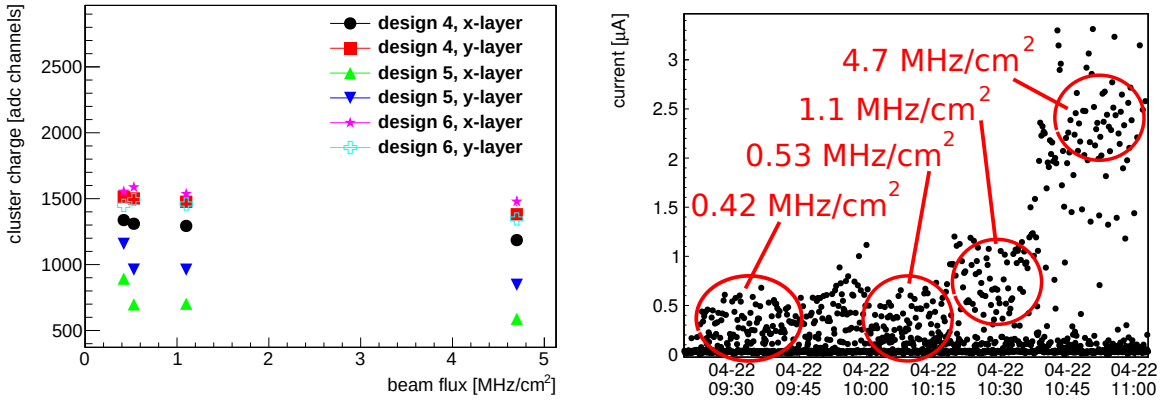

Figure 8.25: Left: Mean cluster charge for all anode designs as a function of the pion beam flux. Note that only the detector with anode design 4 was operated at E_{amp}=46.8 kV/cm and E_{drift}=0.33 kV/cm over the full rate range. Right: Current between micro-mesh and anode measured on anode design 4 as a function of time. The steps in the current correspond to the different beam intensities.

Only a small decrease of the measured pulse height is observed on both readout strip layers, when increasing the beam flux by around one order of magnitude from 0.42 MHz/cm^2 to 4.7 MHz/cm^2. Quantitatively, the x-layer pulse height drops from (1338 ± 14) adc channels at 0.42 MHz/cm^2 to (1186 ± 26) adc channels at 4.7 MHz/cm^2. On the y-layer, a drop from (1515 ± 15) adc channels at 0.42 MHz/cm^2 to (1382 ± 30) adc channels at 4.7 MHz/cm^2 is

[5]Due to the small beam spot this assumption does not reduce the effective particle rate

observed. This corresponds to a pulse height reduction of $(11.4 \pm 0.4)\%$ on the x-layer and of $(8.8 \pm 0.3)\%$ on the y-layer.

The current drawn by the anode is shown in Figure 8.25 (right). A current step from $(0.25 \pm 0.05)\,\mu A$ at $0.42\,MHz/cm^2$ to $(2.5 \pm 0.1)\,\mu A$ at $4.7\,MHz/cm^2$ is observed. The current is distributed on average on 11 floating strips which are dominantly hit, representing the full-width-half-maximum (FWHM) of the Gaussian beam profile in x-direction. As the floating strips are recharged through a $22\,M\Omega$ resistor, a current of about $0.25\,\mu A/11$ strips $= 23\,nA$ per strip at $0.42\,MHz/cm^2$ leads to a voltage drop of 0.5 V. The same calculation at a rate of $4.7\,MHz/cm^2$ leads to a voltage drop of 5 V. Extrapolating the simulated Townsend coefficient shown in Figure 2.4 to the amplification field of 46.8 kV/cm, a voltage reduction of 5 V at 600 V corresponds to a gain reduction of 10.8 %. A voltage reduction of only 0.5 V leads to a gain reduction of 1.8%. Thus we expect a pulse height difference between the two rate points of 9%, which is in good agreement with the observed pulse height drop on the y-layer of $(8.8 \pm 0.3)\%$. The higher pulse height reduction measured on the x-layer of $(11.4 \pm 0.4)\%$ may be attributed to the much more pronounced charge discretization effects, leading more often to one-strip clusters for decreasing pulse height and consequently reducing the measured average cluster charge, as the second strip falls below the minimum strip charge requirement in the analysis.

In the following, the spatial resolution of both readout strip layers is investigated as a function of the particle rate. The η-corrected residual distribution of design 4 is shown in Figure 8.26 at the highest measured rate of $4.7\,MHz/cm^2$. The η-correction method is described in section 8.3.1.

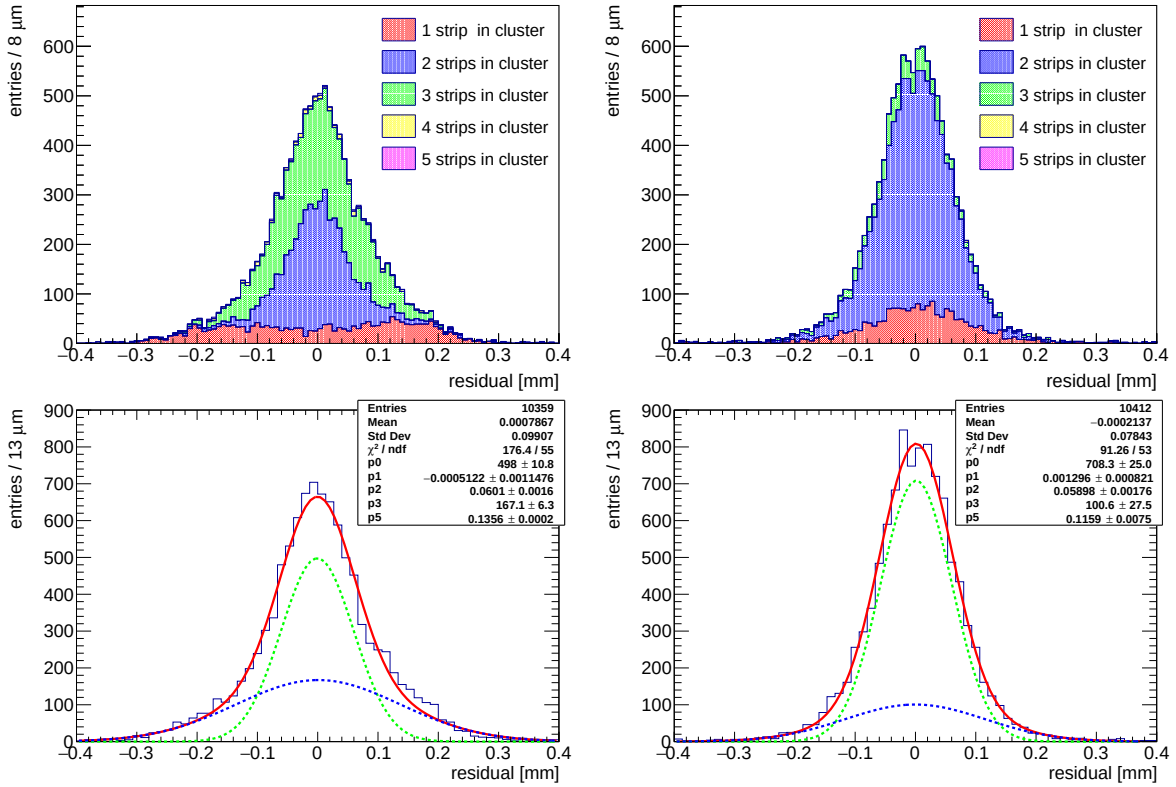

(a) x-layer (b) y-layer

Figure 8.26: Exclusive η corrected residual distribution as a function of the cluster multiplicity (top) and fit with a double Gaussian function (bottom), measured with anode design 4 at the highest rate of $4.7\,MHz/cm^2$ with E_{drift}=0.33 kV/cm and E_{amp}=46.8 kV/cm.

The residual distributions split up into the different cluster multiplicity contributions shows that the broad tail of the x-layer is mainly created by one-strip cluster events. A fit with a double Gaussian function leads to a combined spatial resolution on the x-layer of (90 ± 2) µm and on the y-layer of (68 ± 3) µm at the highest measured beam flux of 4.7 MHz/cm^2. At the first rate measurement point of 420 kHz/cm^2, a resolution of (83 ± 2) µm and (63 ± 3) µm is extracted for x- and y-layer, respectively. We see that the spatial resolution is only marginally degraded when increasing the beam flux by one order of magnitude, mainly caused by the 9% gas gain drop at the highest rate. This leads on the x-layer to an increased number of one-strip clusters, which additionally degrade the spatial resolution, as discussed in section 8.3.1. It should be noted again that the APV25 chip connected to the x-layer of anode design 4 had a reduced dynamic range by 200 adc channels compared to the other APV25s, as can be seen in Figure 8.5, which additionally increases saturation effects and thus degrades the spatial resolution.

A spatial resolution improvement was observed on the y-layer, which is shown in Figure 8.27, when the results from the rate scan at the lowest rate point (measurement run #51) were compared to a measurement (run #198) that was taken after lowering the scintillator trigger thresholds in the discriminator. As a result, also smaller signals were accepted which diminishes resolution degrading saturation effects. Additionally, the gas quality may have improved for the latter measurement, as the two measurements were taking 3 days apart and thus the detector was flushed longer at the second measurement. Indeed a small increase in pulse height was observed in run #198, which may be a hint for this.

The resolution improved by 10% from (63 ± 3) µm to (56 ± 2) µm, which is comparable to the optimum spatial resolution found in section 8.3.1, Figure 8.9, as the two measurements were performed consecutively.

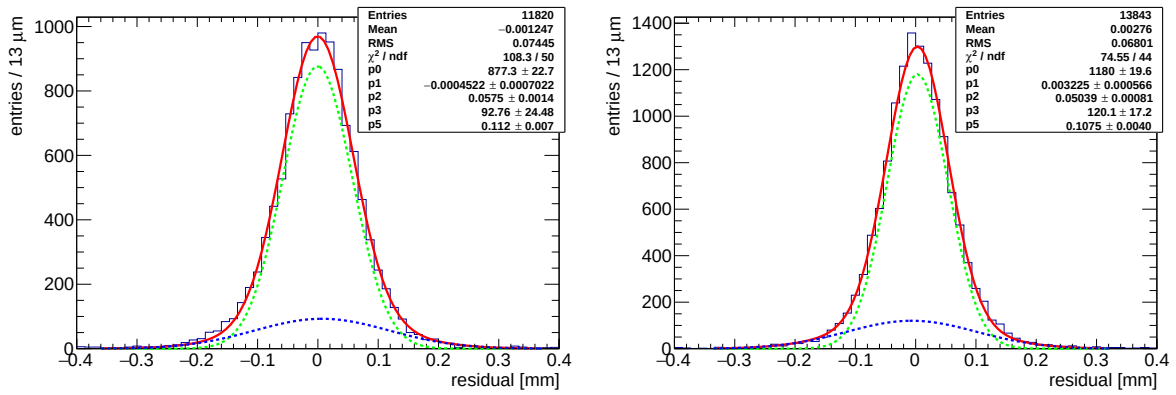

(a) run #51 (b) run #198

Figure 8.27: Exclusive η corrected residual of the y-layer of anode design 4 at a pion beam flux of 420 kHz/cm^2 at two different points in time, both measured with E_{drift}=0.33 kV/cm and E_{amp}=46.8 kV/cm. The resolution improved by 10% from (63 ± 3) µm at run #51 to (56 ± 2) µm at run #198, probably due to a combination of scintillator trigger threshold adjustment as well as an improved gas quality due to a longer flushing period for the second measurement.

The core and combined spatial resolution of the three anode designs as a function of the beam flux are shown in Figure 8.28. We see that the spatial resolution is almost constant over the investigated rate range, independent of the anode design and the readout strip layer.

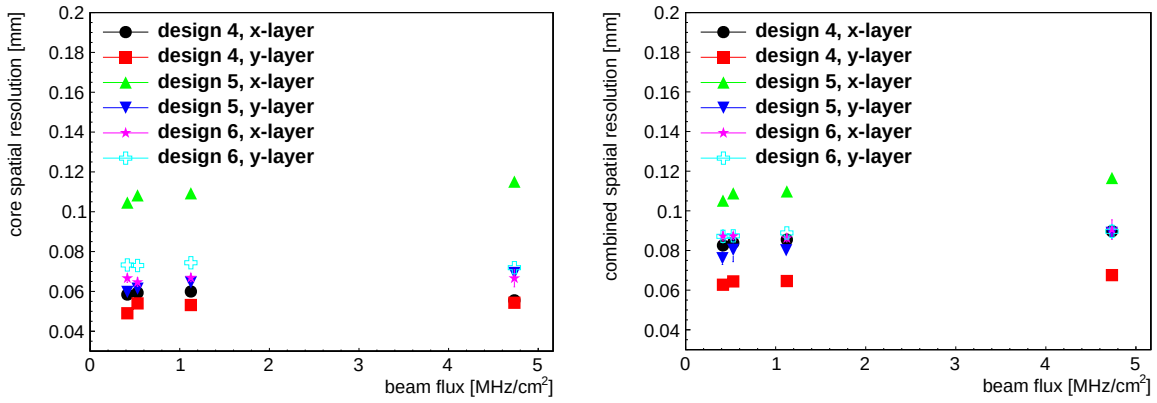

(a) core Gaussian (b) combined double Gaussian

Figure 8.28: Spatial resolution derived from the core Gaussian (left) and the combined double Gaussian (right) for all anode designs as a function of the pion beam flux at E_{drift}=0.33 kV/cm.

Due to the smaller pulse height on the x-layer of anode design 5 compared to the x-layers of the other two anode designs (see Figure 8.3), in combination with the adjusted amplification voltage U_{amp} as listed in Table 8.3, the spatial resolution is dominated by one-strip cluster events. Thus the residual was almost single Gaussian-like distributed, however still leading to a constant good spatial resolution of $\sigma_{SR} = (110 \pm 5)$ µm up to 4.7 MHz/cm^2.

All other readout strip layers show a combined spatial resolution of $\sigma_{SR} \leqslant 90$ µm, only weakly influenced by the gain drop induced by the high particle rate.

The particle detection efficiency as a function of the beam flux is shown in Figure 8.29, calculated as explained in section 8.4. Except for the variations caused by the adjusted amplification voltages as listed in Table 8.3, the efficiency stays almost constant over the investigated intensity range. Optimum values are reached for anode design 4, which shows an efficiency above 95% for both readout strip layers with a spatial resolution of (90 ± 2) µm on the x-layer and of (68 ± 3) µm on the y-layer for the highest measured beam flux.

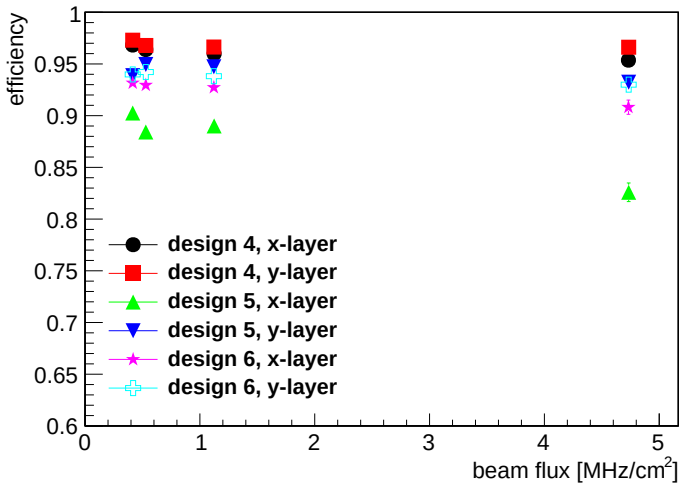

Figure 8.29: Efficiency for all anode designs as a function of the pion beam flux. Note that the detectors have been operated at a different gain i.e. amplification voltage, which explains the difference in efficiency. The values are listed in Table 8.3. A drift voltage of 200 V was applied for all measurements, yielding a field strength of E_{drift}=0.33 kV/cm.

It should be mentioned again that the spatial resolution of the x-layer is dominated by charge discretization effects due to the ionization charge cloud having a size similar to the strip pitch. A reduction of the drift field from $E_{drift} = 0.33\,kV/cm$, which has been used for the rate measurements presented in this section, to a value of $E_{drift} = 0.17\,kV/cm$ yields already a significant improvement of the spatial resolution on the x-layer, as visible in Figure 8.10, due to the significant increased electron transverse diffusion for smaller drift fields.

Furthermore, a reduction of the pitch from 0.5 mm to 0.3 mm will further reduce the charge discretization effects considerably and thus improve the spatial resolution.

As it has been shown at the example of anode design 7 in the previous chapters, it is possible to build a two-dimensional floating strip anode with a 0.3 mm pitch, while maintaining the signal yields on both readout strip layers.

Chapter 9

Application of Two-Dimensional Floating Strip Micromegas: Track Reference for Ion Radiography at the Heidelberg Ion Therapy Center

Ion transmission based radiography or tomography has undergone extensive research over the past years in medical imaging applications, also with heavier particles like carbon, as they show a reduced amount of multiple scattering [Rinaldi, 2011].

This chapter aims at showing the feasibility of including two-dimensional floating strip Micromegas detectors as a single particle tracking device in such medical imaging applications. The measurement results presented in this thesis so far show that these detectors provide excellent particle reconstruction efficiency and spatial resolution on both readout strip layers, up to the several MHz/cm^2 particle flux regime. Additionally, they can be constructed with very low material budget, in order to minimize scattering inside the Micromegas. With the knowledge of each particle track direction in front and behind the object of interest, the most likely path can be calculated [Schulte et al., 2003]. In combination with a Residual Range Detector (RRD) also capable of measuring single particles, this can help to increase the image spatial resolution [Li et al., 2006].

Within the same measurement campaign described in this chapter, a single particle scintillator based telescope was successfully tested in combination with a floating strip Micromegas tracking system. Radiographies of phantoms with $\mathcal{O}(1\,\mathrm{mm})$ spatial resolution were acquired with only around 40k single ion tracks. The results can be found in [Bortfeldt et al., 2017].

For an integration mode RRD, the beam spot shape reconstructed by the Micromegas in combination with the integrated signal from the range telescope may help to disentangle multiple Bragg-peaks visible in the same integration time-window (i.e. in the same raster point) [Magallanes, 2017].

The measurements described in this chapter were performed in collaboration with colleagues from the LMU medical physics chair at the Heidelberg Ion Therapy Center (HIT), which houses a synchrotron. More information about the accelerator can be found in [Kleffner et al., 2009]. In the following the effects of multiple coulomb scattering of protons and Carbon ions on the pencil-like beam shape is discussed, after traversing a homogeneous PMMA stepped-wedge phantom and a tissue equivalent slab phantom. Parts of the results have already been discussed in [Magallanes, 2017]. This chapter is focused on the analysis strategy that was applied to the Micromegas experimental data. As data loss was observed during data-taking

due to the readout system working on the extreme edge of the bandwidth limit, an outlook to a faster readout system with on-chip zero-suppression featuring VMM front-end chips was given in section 3.2.2.

The floating strip Micromegas tracking telescope consists of six active planes: Four Micromegas with a one-dimensional strip anode and two Micromegas equipped with the two-dimensional anode design 1, described in chapter 5. The six tracking detectors were assembled in a back-to-back doublet configuration with a material budget on the order of $\mathcal{O}(0.01\,X_0)$ per plane. The two one-dimensional doublets were placed in front, the two-dimensional doublet behind the phantom.

Measurements have been taken with proton and Carbon ion beams, following a discrete raster scanning pattern with a $5 \times 5\,\mathrm{cm}^2$ field of view. A sliding-window based algorithm (see section 9.2.1) was necessary to identify the beam movement in the coordinate system of the Micromegas, as the beam control system was not synchronized to the Micromegas readout. The Gaussian profile of the raster points is investigated before and after the particles traverse different phantoms. It should be noted at this point that the analysis of the Micromegas data was a collaborative work. The experimental data from the proton beam measurements have been analyzed by the author of this thesis, the data from the Carbon ions were analyzed by J. Bortfeldt.

9.1 Setup

The setup is shown in Figure 9.1, including the three low-material budget floating strip Micromegas doublets. Each detector features 128 floating anode strips at a pitch of 0.5 mm and a width of 0.3 mm, thus yielding an active area of $6.4 \times 6.4\,\mathrm{cm}^2$.

The first two doublets with one-dimensional strip anode structure are positioned in front of the beam isocenter, where later a phantom is placed. The two used phantoms are shown in Figure 9.2. To achieve two-dimensional position resolution of the particles also in front of the phantom, the two doublets are rotated 90° with respect to each other. The anode strips of the first doublet are oriented in y-direction, thus precisely measuring the particle position in x-direction. The second doublet consequently measures particle hits in y-direction. The third Micromegas doublet is placed behind the isocenter and is equipped with a two-dimensional anode design (see chapter 5, Figure 5.1, anode 'design 1'), thus enabling the possibility to reconstruct the particle x and y-coordinates simultaneously in two planes. The detectors are equipped with APV25 front-end boards interfaced by the SRS. Triggers are derived from coincident signals of two off-axis placed scintillators.

The gas detectors were continuously flushed with a Ne:CF_4 84:16 vol.% gas mixture with an overall flux of about 2 ln/h.

High voltage is provided by a CAEN SY5527 Universal Multichannel Power Supply Mainframe [CAEN, 2019f], equipped with A1821 12 channel boards [CAEN, 2019b] with either positive or negative polarity for the strip detectors and one A1535dn 12 channel common floating return board [CAEN, 2019a] for the scintillator.

Due to a mistake in the HV cabling during the measurement setup, no drift voltage was applied to the Micromegas detectors. This significantly reduced the total charge detected in the detector, as only a small fraction of the ionization charge created in close proximity around the mesh was transferred to the amplification region. This made the signal reconstruction for the protons challenging, as will be explained in the coming sections.

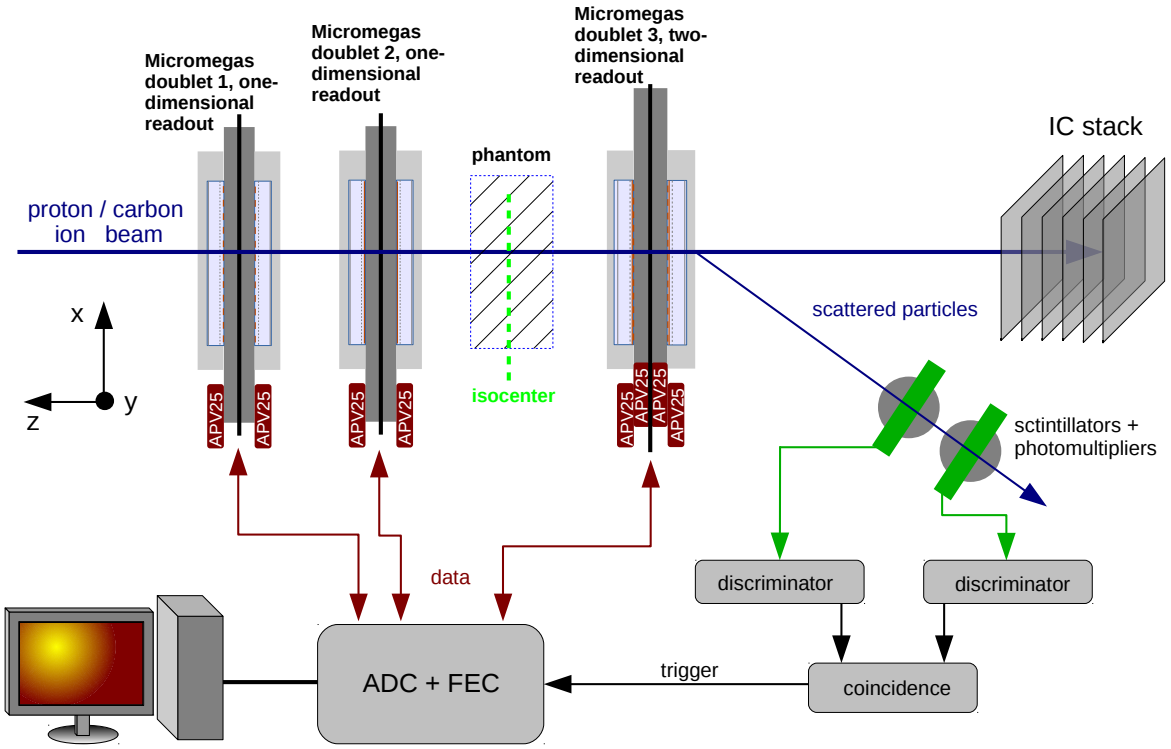

Figure 9.1: Test beam setup at HIT for the measurements with three floating strip Micromegas doublets serving as a single particle tracking telescope. Phantoms are placed in the isocenter of the beam between the second and third doublet. Triggers for the APV25 based SRS electronics are derived from scintillators placed o ff-axis. The beam is stopped in an ionization chamber stack with a completely decoupled readout system.

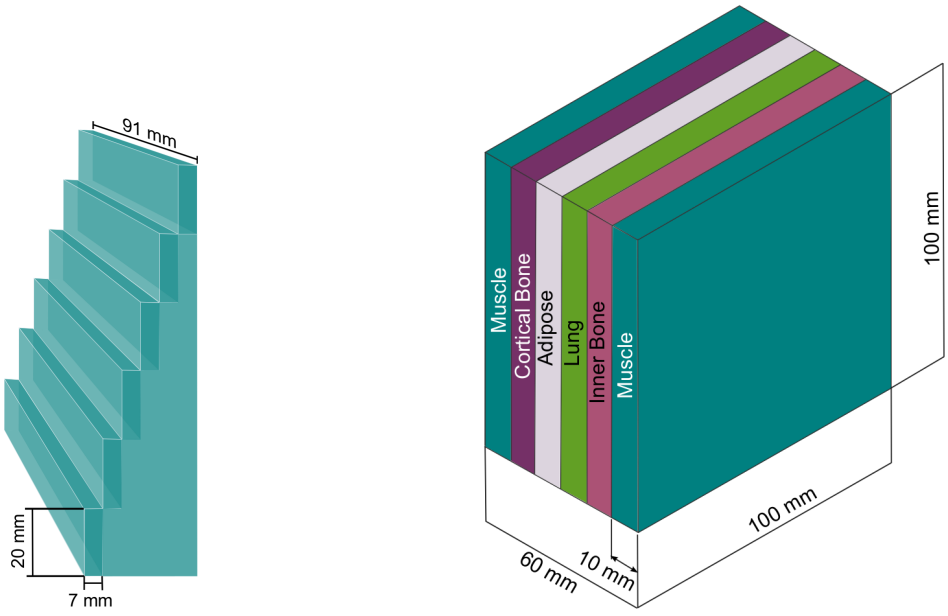

Figure 9.2: The two phantoms used for the proton and Carbon ion measurements described in this chapter. Left: A homogeneous PMMA stepped-wedge phantom. Right: A heterogeneous slab phantom composed of five different tissue equivalent materials: muscle, cortical bone, adipose, lung and inner bone. Pictures taken from [Magallanes, 2017].

9.2 Raster Point Reconstruction from Single Particle Events

In the following section, the algorithm used to identify the beam movement in the coordinate system of the Micromegas is described. Afterwards, the results of the reconstructed raster point width for proton and Carbon ion beams are presented before and after traversing the PMMA stepped-wedge phantom and the tissue equivalent slab phantom.

9.2.1 Method

During all measurements, the proton and Carbon ion beam covered a $5 \times 5\,\mathrm{cm}^2$ field of view (FOV), which fits into the $6.4 \times 6.4\,\mathrm{cm}^2$ active area of the Micromegas. To cover most of the FOV with the pencil beam, it is scanned in a horizontally oriented zig-zagged pattern. This pattern translates into long steps in the Micromegas x-coordinate and short steps in the Micromegas y-coordinate. It can be seen in Figure 9.3, where the Micromegas hit position in x and y is plotted as a function of the readout event number, measured with a proton beam.

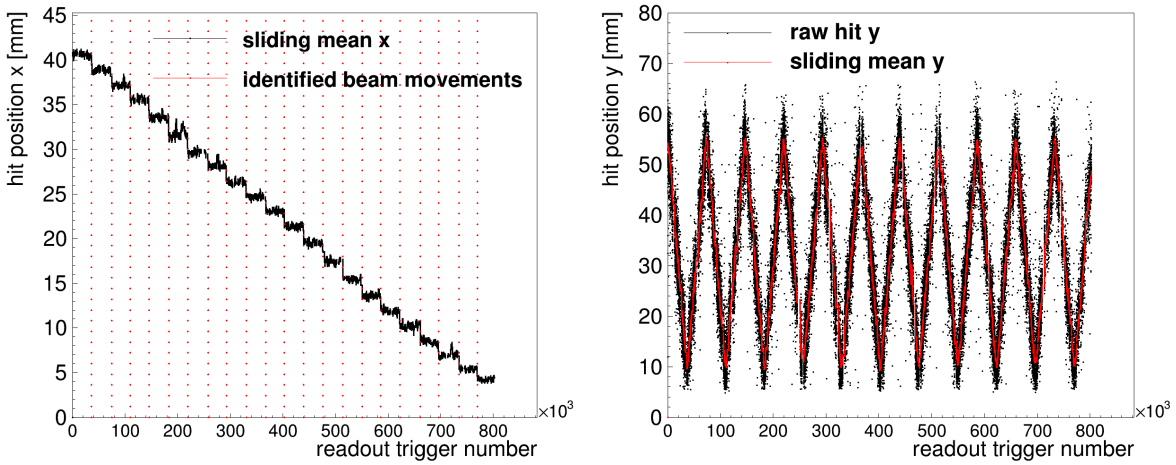

(a) x-direction (b) y-direction

Figure 9.3: Beam route for a measurement with 157.43 MeV protons from the Micromegas point of view, tracking the particles in x (left) and in y-direction (right) at a beam of 10.7 mm FWHM, 2 mm raster point spacing and a particle rate of 0.8 MHz.

As the beam movement was not synchronized with the readout of the Micromegas, the individual raster points need to be reconstructed from the Micromegas hit position data. For this reason, a sliding-window based mechanism was used to identify the beam movements between two raster points.

The principle of the method is to use two time-wise i.e. event-wise separated but adjacent windows, containing a fixed number of events, and calculate the average position inside each window. The content of the windows is updated with each new measurement point and both average values are continuously compared. At a transition to a new raster point, the difference between the two average hit positions is maximum and thus can be used to identify the beam movements. Due to different beam characteristics for the proton and Carbon ion measurements, the algorithm was adjusted to the specific measurement settings. The main differences of the two beams are listed in the following:

- For the measurements with the Carbon ions, the width of the pencil beam was 3.9 mm FWHM with scanning steps of 5 mm. The lowest beam intensity of 2 MHz was used,

allocating either 8×10^6 or 2×10^6 particles per raster point in a 4 s or 1 s irradiation, respectively.

- For the proton beams, the accelerator was operated in research mode, which allowed to reduce the intensity to about 1% of the lowest nominal intensity of 80 MHz. 8×10^5 particles were allocated per raster point in a 1 s irradiation. The pencil beam featured a width of either 10.7 mm or 8.1 mm FWHM with 2 mm scanning steps.

Due to the analogue, not zero-suppressed data format of the APV25 chips used to readout the strip data of the Micromegas, only a fraction of the particle hits per raster point were accepted as a valid trigger in the readout system. This is explained in the following:

In total 11 APV25 front-end hybrid boards were connected to detectors (eight APVs on the floating strip Micromegas, three on a different detector system). Thus, the maximum accepted trigger rate $f_{\max}$ of the readout system is given by

$$f_{\max} = \frac{1\,\text{Gbit/s}}{(140\,\text{c.c.}) \cdot 16\,\text{bit/(c.c.)} \cdot 24 \cdot 11} = 1.69\,\text{kHz} \quad , \tag{9.1}$$

taking into account the 1 GBit network bandwidth bottleneck, 24 timebins read out as well as the 140 clock cycle (c.c.) long data structure of the AVP25 chips. Including also the overhead produced by the FEC, the maximum achievable readout rate is even lower. A description of the front-end chip interfaced by the SRS is given in section 3.2.1. This yields a maximum of 1.69 kHz $\cdot$ 4 s = 6760 accepted triggers per raster point during the Carbon ion measurements and 1.69 kHz $\cdot$ 1 s = 1690 triggers during the proton measurements. For the carbon measurements an effective trigger rate of 1.43 kHz was registered, thus yielding around 5700 accepted trigger per raster point during a 4 s irradiation. An effective trigger rate of 1.6 kHz was observed during the proton measurements, leading to around 1600 accepted triggers per raster point, which is very close to the calculated maximum possible trigger rate.

A zoom into the distribution of hits in y-direction for the first 17k accepted triggers in a proton measurement is shown in Figure 9.4. The calculated sliding mean hit position as well as the identified beam movements have been superimposed. For this particular figure, a window size of 70 hits with a distance between the two windows of 15 events were chosen. A beam movement was identified, whenever a difference of the two average window values of 1.2 mm was observed. Due to the readout system producing data on the extreme edge of the bandwidth limit, data loss is observed from time to time in the hit distribution as a function of the trigger number. This caused a loss of information during the proton measurements, leading to an unavoidable loss of reconstructed raster points.

To avoid that two hit distributions of different raster points are merged into the same identified raster point, data points are ignored until a next beam movement is identified by the sliding window algorithm. Due to the fact that erroneously no drift voltage was applied to the Micromegas, from the 1600 accepted events per raster point, only on average 220 useful hits were found in the detectors, additionally showing large fluctuations. Thus, the sliding window algorithm needed some modifications to reliably reconstruct the raster point transitions for the proton beams, which is explained in the next section.

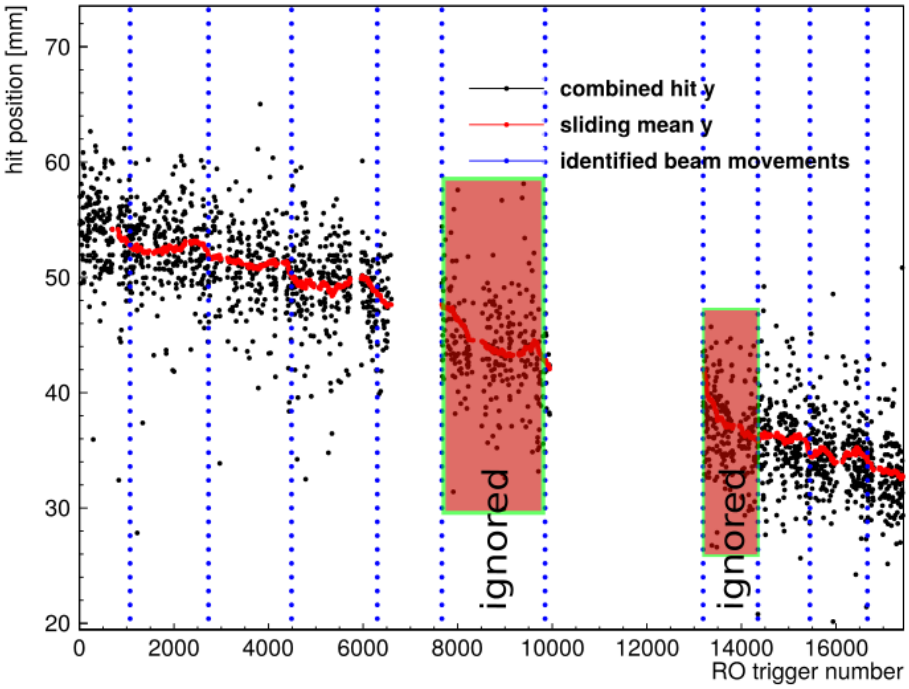

Figure 9.4: Reconstructed y hit position (black) in the center of the second doublet as a function of the trigger number, zoomed into the first 17k accepted events. The sliding window mean position (red) and the identified beam movements (blue) are superimposed. Due to the overloaded readout system at a trigger rate of 0.8 MHz massive data loss (white spaces) occurred during the measurements. To avoid that two raster points are merged into one, data points after a data gap are ignored until the next beam movement is identified. The phrase 'combined hit' will be explained in the next section.

For the measurements with the Carbon ions, the much denser ionization lead to higher signals in the Micromegas, which greatly enhanced the particle reconstruction efficiency. Actually, a hit efficiency well above 90% was observed for some detectors, even though no drift voltage was applied. The results are shown in section 9.2.3.

9.2.2 Results from Proton Beams

Due to usually more than one particle being present in each detector layer per triggered event, the use of an iterative track finding algorithm is necessary. The working principle of the Kalman-filter based algorithm is explained in appendix A.2. However as a consequence of no drift voltage, a bad track reconstruction efficiency was found, as on average only three to four simultaneous hits were detected. Additionally, the perpendicular readout strip layer of the two-dimensional floating strip Micromegas yielded only small signals, as the perpendicular strip width was not yet optimized for this design. Thus a second position information in x-direction behind the isocenter was only available with very reduced reconstruction efficiency.

As consequently an efficient track reconstruction simultaneously in x- and y-direction was not possible, a different approach was chosen. By only requiring simultaneous hits of two detectors in the same doublet, the number of usable events was sufficient to apply the sliding window algorithm, separately for x- and y-direction. The individual hits have been matched iteratively, comparing all clusters in both detectors and taking the two cluster with minimal distance. From the three doublets, thus in total three combined hits have been reconstructed, as shown in Figure 9.5.

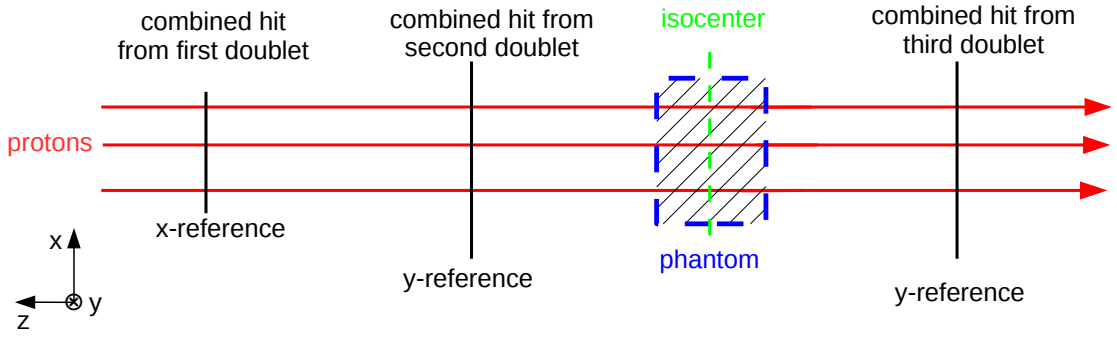

Figure 9.5: Combined position reconstruction layers of the doublets used for the analysis of the proton data. The two different phantoms are placed in the isocenter of the beam, between the second and third doublet. As the pulse height on the perpendicular strip layer of the third doublet was very low due to not optimized strip layer configurations, the hits in x-direction behind the phantom were not usable.

The combined hit is the extrapolated hit position in the middle of the two detectors, with the advantage, that no simultaneous hit in x- and y-direction within the same raster point needs to be present. The raster point movements are identified by the sliding window technique under following additional requirements:

- only combined hits are used that show individual hits within 5 mm in the x-direction or 20 mm (due to lower statistics) in the y-direction
- a new raster point is identified, if the two window average values differ by 1.2 mm in the x-direction or by $1.2\,\text{mm} \times \frac{n_{\text{mean}}}{n_{\text{curr}}}$ in the y-direction, where n_{mean} and n_{curr} define the mean and the current number of found hits per raster point
- a raster point is ignored if it contains less than 50 events

Within the same raster point, the combined hits are filled into separate histograms for x- and y-layer, as can be seen in Figure 9.6.

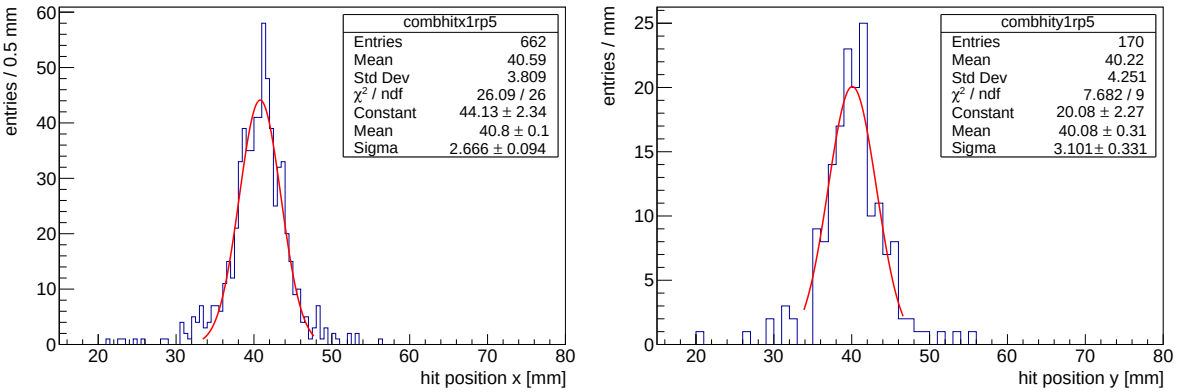

(a) x-direction (b) y-direction

Figure 9.6: Reconstructed hit position for a single raster point from the combined hit of the first doublet i.e. in x-direction (left) and from the combined hit of the second doublet i.e. in y-direction (right), measured with 157.43 MeV protons at a rate of 0.8 MHz. The higher statistics in the x-direction is a consequence of a higher gain in the first doublet compared to the second one and thus a higher efficiency.

The distributions are then fit with a single Gaussian function in a $\pm 1.8 \times \sigma$-window; mean as well as σ are extracted for each raster point. On average around 220 useful hits are found per raster point in the y-layer, which however varies due to data loss in the Micromegas raw data caused by the readout system running on the edge of the bandwidth limit.

In the following, the raster point width is investigated as a function of the position, in front and behind the isocenter. The x-position is defined by the measurement from the first doublet, the y-position by the second and third doublet located in front and behind the isocenter, respectively. As only in y-direction a reliable hit information of the raster point width behind the isocenter was available, the beam spot width will for this analysis always be deduced from the raster point width reconstructed by the hits of the y-layer in the second and third doublet.

The reconstructed raster point width i.e. the beam width without a phantom in the beamline is in agreement with the expectations from the accelerator list of ion beam characteristics. It has already been discussed in detail by Magallanes [2017] and is thus only briefly summarized in the next paragraph.

The raster point width i.e. σ_y as a function of the position without a phantom in the beam is shown in Figure 9.7. No position dependence of the width is expected, neither in front, nor behind the isocenter. Irregularities in the reconstruction by the third doublet behind the isocenter are caused by a combination of dead strips in the active area of both detectors. As the combined hit is greatly influenced by a mis-reconstruction in one of the two detectors, dead strips can lead to a mis-matching of hits, stemming from two different particles. This effect is greatly enhanced by the fact that no drift voltage was applied, as this results in a cluster size of often only one strip. This consequently leads to a broadening of the raster point width.

The results for measurement with the heterogeneous slab phantom are shown in Figure 9.8. A position dependence of the raster point width is visible after the beam traversed the phantom, if it is compared to the measurement without the phantom in the beam in Figure 9.7 (right). The histograms are displayed using the same color scale. The main scattering centers can be attributed to the inner bone and cortical bone, located at around $(15 < y < 25)$ mm and $(45 < y < 55)$ mm, respectively. The largest beam spread is observed in the cortical bone, which also features the highest density.

The results for the measurement with the homogeneous PMMA stepped-wedge phantom are shown in Figure 9.9. The phantom has been placed such that the highest traversed thickness is expected at low values of x. The beam energy during the measurement was increased to the highest proton energy of 221.06 MeV, that the accelerator can deliver. This should additionally decrease the beam spot width according to the accelerator ion beam characteristics. This is visible in the color coding, if the measurement in front of the phantom is compared with the measurement shown in Figure 9.7. After the phantom, no position dependence of the raster point width is visible. Thus, such small thickness variations (of the same material) seem not to influence the beam profile with protons of this energy.

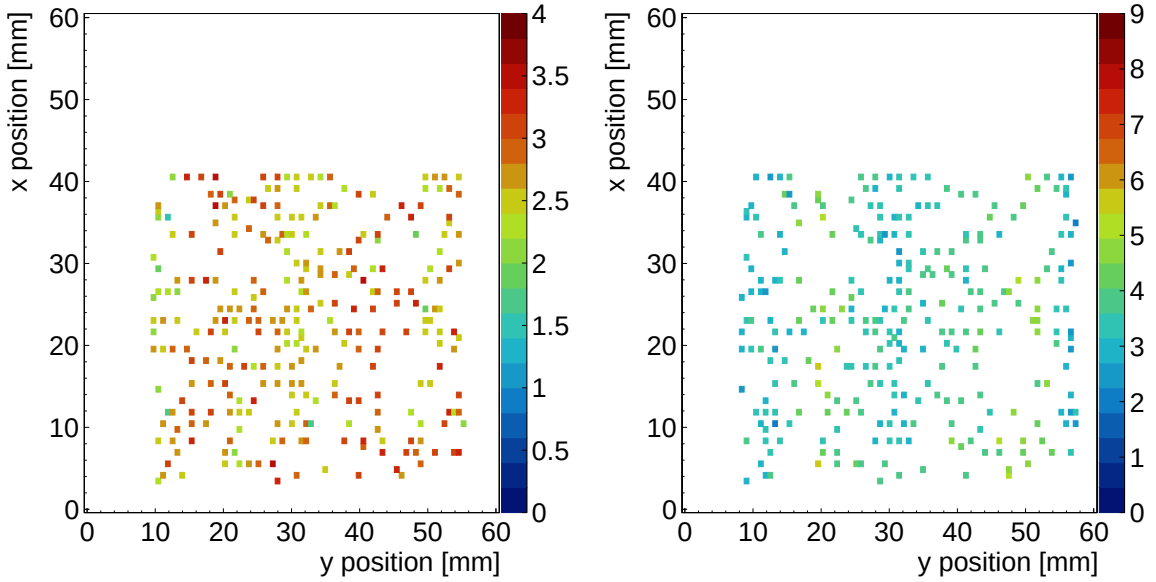

(a) combined hit 2nd doublet

(b) combined hit 3rd doublet

Figure 9.7: Reconstructed raster point width in mm as a function of the position in front (left) and behind (right) the isocenter without a phantom in the proton beam with an energy of 157.43 MeV. The beam is expected to have a FWHM of 10.7 mm in the isocenter at 2 mm scanning steps. As no phantom is in the beam, a homogeneous width distribution is expected. Inhomogenities in the right figure are due to a combination of dead strips in the third doublet.

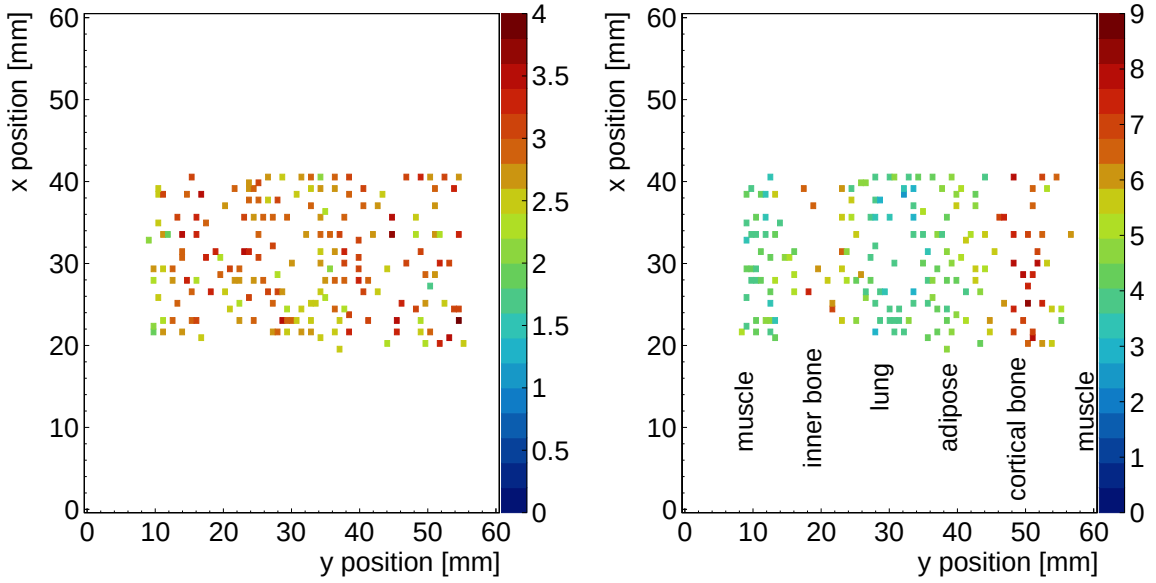

(a) in front of slab phantom

(b) behind slab phantom

Figure 9.8: Reconstructed raster point width in mm as a function of the position in front (left) and behind (right) the heterogeneous slab phantom for 157.43 MeV protons. The histograms are displayed using the same color scale as the measurement without phantom in the beam, see Figure 9.7. A width dependence on the position is visible. The different tissue equivalent layer positions have been superimposed. The highest beam spread is observed at the inner bone and cortical bone.

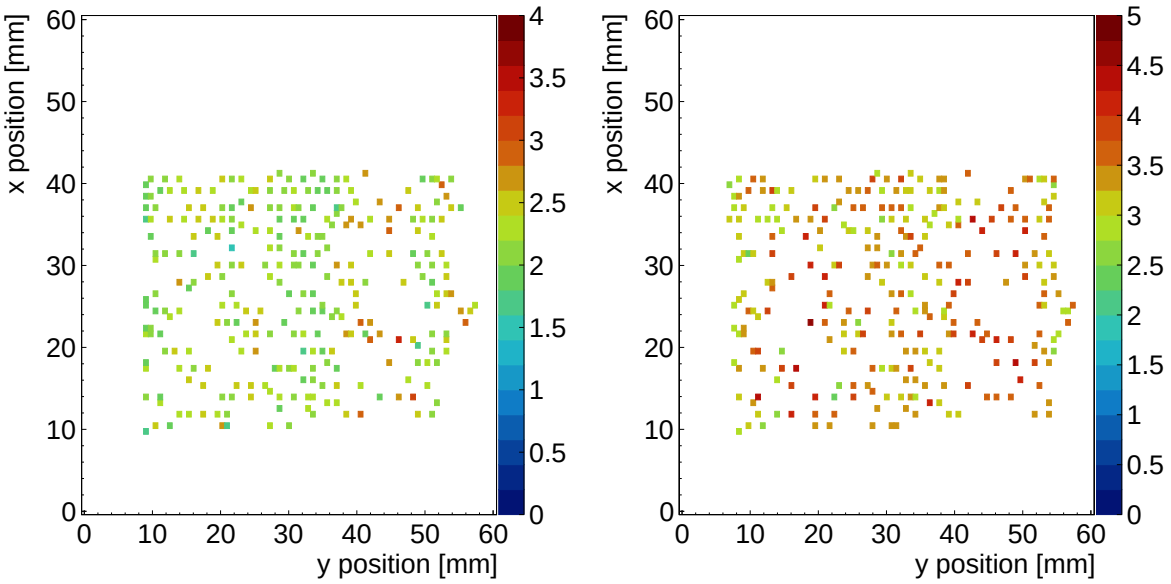

(a) in front of step phantom

(b) behind step phantom

Figure 9.9: Reconstructed raster point width in mm as a function of the position in front (left) and behind (right) the homogeneous PMMA stepped-wedge phantom for a 221.06 MeV proton beam with an expected 8.1 mm FWHM in the isocenter. The observed raster point width after the phantom is not depending on the position.

9.2.3 Results from Carbon Ion Beams

The higher energy loss of the Carbon ions compared to the protons allowed to perform single ion tracking throughout the full detector system, even though no drift voltage was applied to the Micromegas. The underlying iterative Kalman filter based track reconstruction is explained in appendix A.2. The ion tracks are measured by all six Micromegas layers and extrapolated into two virtual planes in front and behind the isocenter, as shown in Figure 9.10.

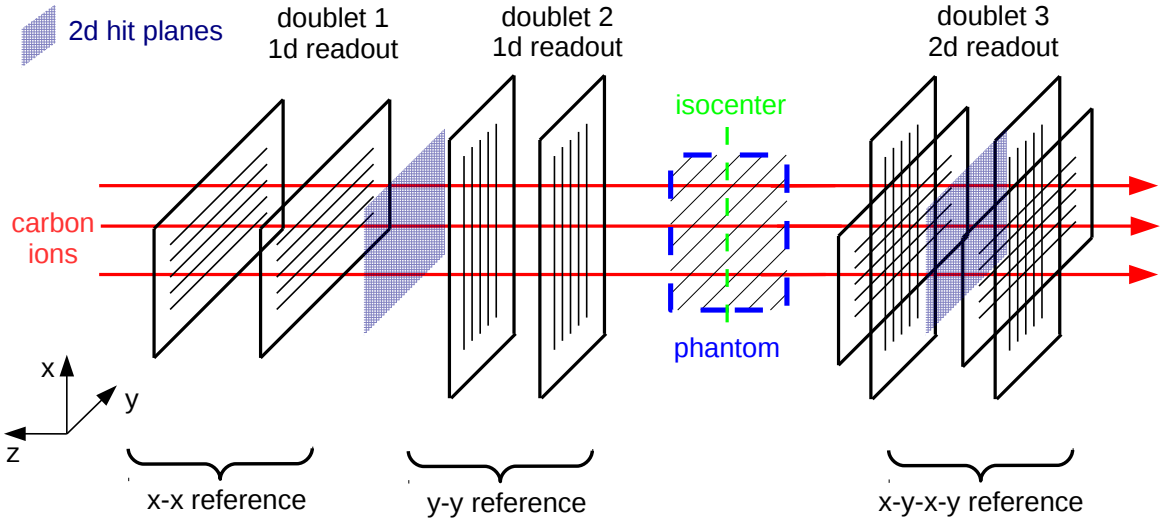

Figure 9.10: For the measurements with the Carbon ions, the deposited charge in the Micromegas was sufficiently high to allow 2d-tracking with the full detector telescope. For the raster point analysis, the track has been extrapolated into two virtual planes, one between the first and the second doublet and one in between the two detectors of the third doublet.

To identify well reconstructed tracks, a $\chi^2/\text{ndf} < 10$ - cut has been applied. The cut removes events where multiple scattering within the readout structure of the Micromegas lead to a degradation of the track straightness, or where the reconstructed position in one of the Micromegas was biased by e.g. dead anode strips or readout channels. The used cut eliminates around 25% of the particle tracks.

The extrapolated x- and y-track position at the two virtual planes in front and behind the isocenter are used for the raster point identification via the sliding window algorithm. Due to denser ionization of the Carbon ions leading to the full ion track information, a requirement of 3 mm difference between the average values of the two windows was sufficient to identify the 5 mm wide steps of the beam.

The distribution of hits for a single raster point in the virtual plane in front of the isocenter is shown in Figure 9.11, measured with 299.9 MeV/u Carbon ions at 2 MHz particle rate with an expected width of 3.9 mm FWHM at the position of the isocenter, for 8×10^6 particles/point (left) and 2×10^6 particles/point (right). Due to the low readout rate of the used electronics, only a fraction of the particles per raster point are registered. As the hit information is available in both dimensions simultaneously, a two-dimensional Gaussian function is fit in a $\pm 2\sigma$ - range around the distribution. The raster point position and width for x- and y-direction can be directly extracted from the fit parameters.

Good agreement of the reconstructed beam width with the accelerator predictions at the two virtual planes along the beam-line was found, see [Magallanes, 2017].

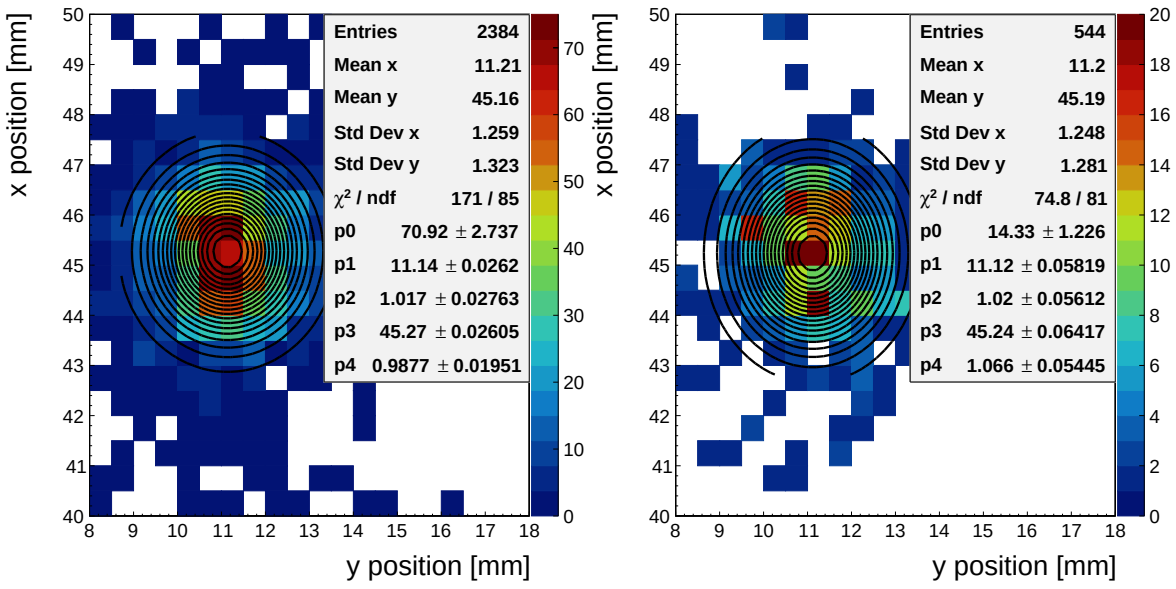

(a) 8×10^6 particles/point (b) 2×10^6 particles/point

Figure 9.11: Reconstructed two-dimensional hit distribution for a typical raster point in the hit plane in front of the isocenter for a 299.9 MeV/u Carbon ion beam at 2 MHz particle rate, measured with two beam configurations allocating a different number of particles per raster point. The two measurements yield very similar results as expected, despite the factor four reduced number of particles. A two-dimensional Gaussian function is fit to the distribution to extract the raster point width and position. The raster point width in x and y-direction are the σ of the Gaussian fit i.e. parameters $p4$ and $p2$, respectively. Figure adapted from [Bortfeldt and Klitzner, 2017].

As no significant difference was observed between the raster point width in x- and y-direction (parameters $p2$ and $p4$ in Figure 9.11), the width in y-direction is in the following used for

the analysis of the beam shape after traversing the two different phantoms. Due to the better quality of the Carbon ion data, each raster point in the $5 \times 5\,\mathrm{cm}^2$ FOV could be reconstructed from the Micromegas hit information. Note that in the following two figures the raster point data was filled into histograms with a bin width of 1.4 mm for visibility reasons. Thus the position of the raster points may jitter from one bin to a neighbor, resulting in a deviation more pronounced than it actually is.

The raster point width of the beam as a function of the position before and after traversing the homogeneous PMMA stepped-wedge phantom (Figure 9.2, left) is shown in Figure 9.12. The phantom has been placed such that the highest amount of material is expected for low values of x. As already observed for the measurements with the protons, no position dependence of the raster point width is visible after the Carbon ions traverse the step phantom. A homogeneous widening of the beam across the phantom is observed, about a factor of 1.5 higher than for the beam after traversing the same path in air.

The results for the measurement with the tissue equivalent slab phantom in the beam are shown in Figure 9.13. The phantom was positioned the same way as for the proton measurements shown in Figure 9.8. Also similar to the results of the proton measurement, a position dependence of the raster point width behind the slab phantom is visible, even for the much heavier Carbon ions. The highest amount of scattering is observed for the material with the highest density, i.e. the cortical bone.

This motivates including low material budget single ion trackers also in medical imaging applications with heavier particles like carbons, as multiple Coulomb scattering effects in dense materials like bone-structures lead to non-negligible spreads of the ion beam.

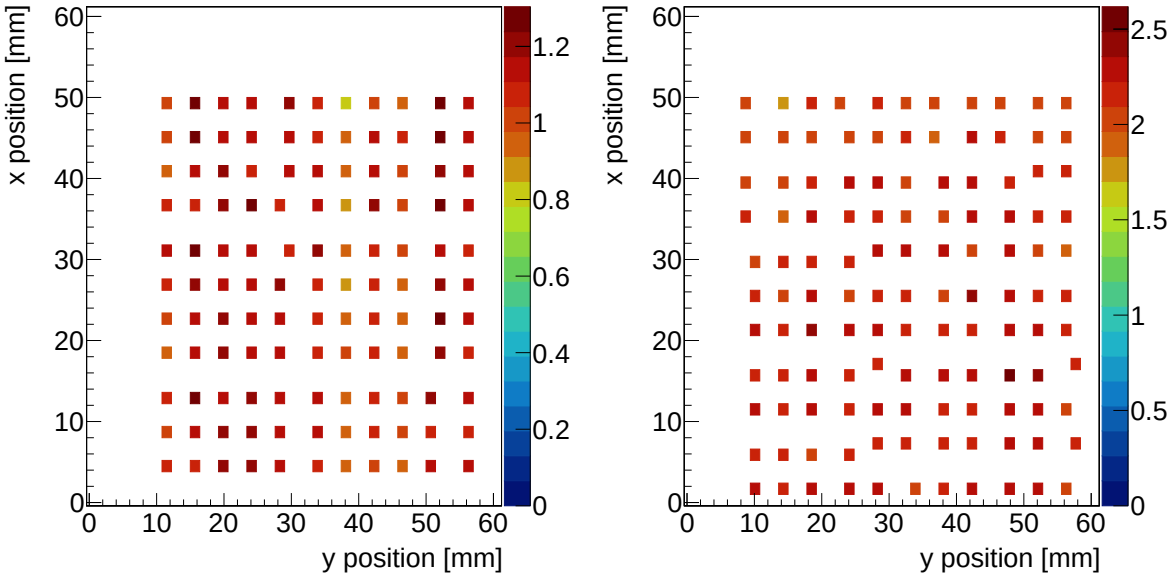

(a) in front of step phantom

(b) behind step phantom

Figure 9.12: Reconstructed raster point width (in y-direction) as a function of the position in front (left) and behind (right) the homogeneous PMMA stepped-wedge phantom measured with a 299.9 MeV/u Carbon ion beam, allocating 8×10^6 particles per point. The highest amount of material is expected at low values of x. No position dependence of the beam width is observed after the phantom. Figure adapted from [Bortfeldt and Klitzner, 2017].

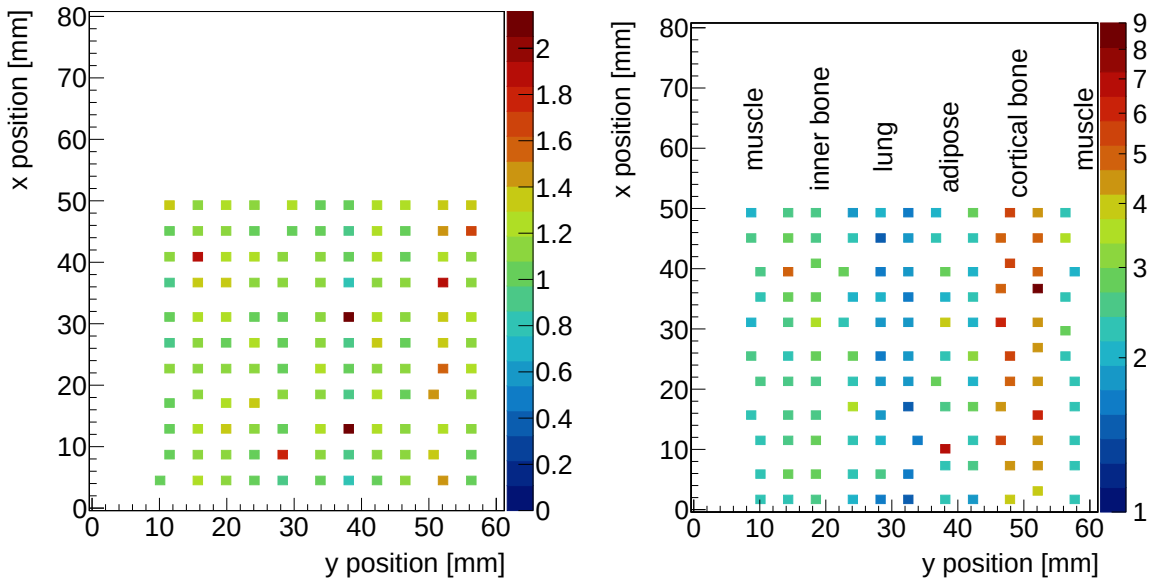

(a) in front of slab phantom

(b) behind slab phantom

Figure 9.13: Reconstructed raster point width (in y-direction) as a function of the position in front of (left) and behind (right) the heterogeneous slab phantom measured with a 299.9 MeV/u Carbon ion beam, allocating 2×10^6 particles per point. Note the logarithmic scale of the raster point width in the right figure. The six tissue equivalent layers of the phantom are oriented in y-direction. A position dependence of the raster point width according to the different layers is visible. Figure adapted from [Bortfeldt and Klitzner, 2017].

9.3 Summary and Conclusion

A floating strip Micromegas tracking telescope, consisting of six active layers has been used to investigate multiple Coulomb scattering of protons and Carbon ions in a therapeutic energy range at the Heidelberg Ion Therapy Center (HIT).

A homogeneous PMMA stepped-wedge phantom and a tissue equivalent slab phantom have been placed in the middle of the tracking system. As the beam followed a discrete raster scanning pattern and the beam movement was not synchronized with the Micromegas DAQ system, the raster points were reconstructed from the hit data of the strip detectors via a sliding window algorithm.

Despite that the Micromegas were operated without drift voltage due to a cabling mistake, which lead to a considerable pulse height decrease, the detectors showed sufficient sensitivity to investigate their applicability for medical imaging. While it did only marginally affect the Carbon ion measurements thanks to their much denser ionization, a full track reconstruction of single protons was not possible. However by combining always a set of two detectors, also a sufficient fraction of the raster points could be reconstructed for the proton measurements.

Due to the limited readout rate of the used readout electronics, only a fraction of the particles allocated per raster point were written to disk. Additionally, data loss was observed as the electronics were producing data at the edge of the 1 GBit/s bandwidth limit of the network. This lead to a significant loss of reconstructable raster points during the proton measurements. However, a new ASIC with on-board zero-suppression will allow for a significantly higher trigger rate in future measurements. More information about the new front-end chip can be found in section 3.2.2.

A positive finding from proton measurements with often below 100 particles per raster point[1] is that the reconstruction of the beam shape was not impaired by the small statistics. In combination with a new readout chip and system that is synchronized with the beam movement, also very low dose images in combination with an integration based RRD could be acquired.

The beam profiles at each raster point reconstructed by the tracking detectors showed that even for heavier ions like carbon, multiple Coulomb scattering processes in dense tissue layers like bones lead to a non-negligible spread of the beam. Thus also carbon based images in a clinical environment may benefit from the individual ion scattering information provided by the gaseous low material budget tracking detectors, as it was already motivated by [Magallanes, 2017].

[1] caused by the lack of drift voltage and the overloaded readout system

Chapter 10

Summary and Outlook

In this thesis novel two-dimensional floating strip Micromegas detectors were developed and studied extensively. Micromegas detectors are planar, gaseous detectors with a highly segmented readout structure. Due to short ion drift paths they are highly efficient single particle tracking devices up to very high particle rates. Floating strip Micromegas in particular differ from standard Micromegas by individually powering the anode strips with high-voltage via high ohmic resistors. In combination with small coupling capacitances to retrieve the strip signals, this enables a powerful discharge protection. The detector is split into two main regions: A typical few mm wide drift gap and an approximately 0.1 mm wide amplification gap, separated by a thin conductive micro-mesh. If a particle traverses the detector, it produces electron-ion-pairs in the drift region, which are separated by a moderate electric field. Electrons drift towards the micro-mesh and into the amplification region, where the high electric field leads to a signal amplification via avalanches.

In a previous work with a floating strip Micromegas anode design with two layers of readout strips, parallel and perpendicular to the floating strips, it was shown, that it is possible to retrieve also the position information along the floating strips with the perpendicular readout strip layer (y-strips). However, in a straight forward design, the signal turned out to be significantly smaller than the signal on the parallel readout strips (x-strips). Furthermore, contrary to the unipolar negative signal visible on the x-strips, an initially positive, bipolar signal is observed on the y-strips.

The goal of this thesis was to understand the signal formation in the two-dimensional floating strip Micromegas detector, to optimize the design of the anode printed circuit board (PCB) and to increase the signal yield accordingly. For this purpose, a detector simulation was set up, where a two-dimensional floating strip Micromegas anode PCB geometry was modeled with the finite-element-method simulation program ANSYS. Charge carrier drift and amplification in the gas volumes of the detector was simulated with the Garfield++ package, importing the three-dimensional electric field configuration calculated by ANSYS. A model has been developed from which the capacitive coupling between the individual electrodes in the anode PCB can be deduced. The induced signals on all electrodes by the movement of charges in the amplification region were simulated via weighting fields within the same Garfield++ framework. From the combination of direct induced signals on the electrodes as well as capacitive coupling between the electrodes, the signals measured with APV25 based readout electronics connected to both readout strip layers could be reconstructed with the detector simulation.

Based on the simulation results, novel two-dimensional floating strip anode PCBs have been developed. The new anode PCBs have been designed taking into account the following main simulation findings:

- The initially positive, bipolar signal visible on the perpendicular readout strip, is directly induced by the movement of charges in the amplification region, as the capacitive coupling to the floating strip is negligibly small. To increase the signal yield on the y-strip layer, its distance to the amplification region should be minimized.
- To maximize the induced current on the perpendicular readout strip, the strip width should be as large as possible, while at the same time, the floating strip width should as small as possible.
- To not completely shield the capacitive coupling between floating strip and parallel readout strip and additionally not to create huge capacitances in the detector, the perpendicular readout strip width needs to be small under the floating strip.

Thus, to increase the signal yield on the perpendicular readout strip, while at the same time maintaining a signal on the parallel readout strip with similar amplitude, a non-uniform y-strip width is necessary. For optimization, seven different two-dimensional floating strip Micromegas anode structures have been investigated in this thesis, six of them were developed by the author. While chronologically the first three featured classical straight readout strips with uniform width, four novel anode designs were developed with different alternating y-strip patterns underneath the floating strips, to compare it to the detector simulation model and adapt it accordingly.

For characterization measurements with the novel anode designs, three $6.4 \times 6.4\,\mathrm{cm}^2$ and one $3.84 \times 3.84\,\mathrm{cm}^2$ active area detector was constructed. While all detectors featured 128 floating strips, three of them were designed with a strip pitch of 0.5 mm and one with a pitch of 0.3 mm, thus having a smaller active area than the others.

Motivated by the inclusion of two-dimensional floating strip Micromegas detectors as single particle trackers in medical imaging applications, a $19.2 \times 19.2\,\mathrm{cm}^2$ active area detector with low material budget was constructed. It features 384 floating strips at a pitch of 0.5 mm. Due to the thin Kapton flex anode of only 0.15 mm thickness, a Nomex honeycomb support structure was glued on the back-side of the PCB to prevent deformations introduced by temperature and humidity changes. A homogeneous pulse height distribution is observed over the active area, measured with a radioactive ^{55}Fe source.

Comparing the classical and novel anode PCB designs, at least a factor of 2 gain in raw signal amplitude is observed on the perpendicular readout strip and a factor of 4.8 on the parallel readout strip. No resonance or signal reflection effects are observed which could be caused by impedance differences of the non-uniform width pattern on the perpendicular stripline.

A proof of principle with all four novel two-dimensional anode designs in a 20 MeV proton beam at a particle rate of up to almost 1 MHz demonstrates the high rate capability of the detector, and in particular that of the perpendicular readout strip layer. Hit efficiencies above 95% are observed on both readout strip layers, independent of the rate. Measurements with rotated detectors with respect to the beam allowed for investigation of the µTPC angle reconstruction on both readout strip layers. For the x-layer and y-layer optimum angular resolutions of $\binom{+2.5^\circ}{-1.9^\circ}$ and $\binom{+2.9^\circ}{-2.2^\circ}$ are found, respectively.

The performance of the detectors is investigated in a high energy muon and pion beam with energies between 20 and 150 GeV. A four layer resistive strip Micromegas tracking system provided a track reference with a track accuracy better than 25 µm in both dimensions. Optimum spatial resolution for perpendicularly incident particles of (79 ± 4) µm for the x-layer and (54 ± 2) µm for the y-layer are observed. The spatial resolution on the x-layer is impaired by charge discretization effects on the anode strips, caused by the ionization charge cloud being of the same size as the 0.5 mm strip pitch. Note that the two-dimensional floating

strip anode with 0.3 mm pitch was finalized after this measurements and operated without loss of signal amplitude on either of the two readout strip layers. This should reduce the charge discretization effects considerably. Nevertheless, optimum hit efficiencies of (98.0 ± 0.2) % are observed for both readout strip layers at a perpendicular incident particle beam. Measurements with an inclined detector allowed testing the µTPC position reconstruction for angles up to 40°. Optimum spatial resolution for both readout strip layers of (115 ± 4) µm for 20°, of (132 ± 6) µm for 30° and of (152 ± 8) µm for 40° is achieved. Optimum µTPC angular resolutions of $\binom{+2.2^\circ}{-1.8^\circ}$ and $\binom{+2.1^\circ}{-1.7^\circ}$ for x- and y-layer, respectively, are observed. Efficiencies above 96% are reached on both readout strip layers for all investigated angles. The spatial resolution as well as efficiency is only minimally impaired at an observed 10% pulse height drop at particle flux densities of up to 4.7 MHz/cm^2.

The highly efficient single particle tracking capability of the detectors at high particle flux densities as well as the possibility to construct the gaseous detectors with very low material budget make them attractive for medical imaging applications. The multiple scattering of carbon and proton beams in a therapeutic energy range was investigated at the Heidelberg Ion Therapy center. The single particle tracking detectors were placed in front of and behind phantoms. The beam width after the slab phantom with tissue equivalent layers allowed to distinguish tissues according to their density, even for heavier particles like carbon ions. To considerable increase the data collection efficiency, an outlook to new high-rate capable front-end electronics is given.

New detector concepts with new anode structures are foreseen, for which additionally an increase of the perpendicular strip pulse height of 50% is expected. To reduce the material budget of the detector even further, the copper strip line thickness will be reduced from 35 µm to 17 µm and the parallel readout strip layer removed, decoupling the signals from the floating strips with SMD capacitors. This allows to reduce the already thin PCB thickness from 0.155 mm to 0.059 mm, which reduces multiple Coulomb scattering of low energy particles in the high Z materials of the PCB considerably.

Bibliography

[Abgrall et al.(2011)] N. Abgrall et al. *Time projection chambers for the T2K near detectors.* Nuclear Instruments and Methods in Physics Research Section A: Accelerators, Spectrometers, Detectors and Associated Equipment, 637(1):25 – 46, 2011. ISSN 0168-9002. doi:https://doi.org/10.1016/j.nima.2011.02.036. URL `http://www.sciencedirect.com/science/article/pii/S0168900211003421`.

[Alexopoulos et al.(2011)] T. Alexopoulos, J. Burnens, R. de Oliveira, G. Glonti, O. Pizzirusso, V. Polychronakos, G. Sekhniaidze, G. Tsipolitis, and J. Wotschack. *A spark-resistant bulk-micromegas chamber for high-rate applications.* Nuclear Instruments and Methods in Physics Research Section A, Accelerators, Spectrometers, Detectors and Associated Equipment, 640(1):110–118, June 2011. doi:101016/jnima201103025.

[ANSYS, Inc.(2013)] ANSYS, Inc. ANSYS - Mechanical APDL Release 15.0 UP20131014. ANSYS Acadamic Teaching Advanced, October 2013.

[Arik et al.(2011)] M. Arik et al. *Search for Sub-eV Mass Solar Axions by the CERN Axion Solar Telescope with* ^{3}He *Buffer Gas.* Phys. Rev. Lett., 107:261302, Dec 2011. doi:10.1103/PhysRevLett.107.261302. URL `https://link.aps.org/doi/10.1103/PhysRevLett.107.261302`.

[Autodesk(2018)] Autodesk. Autodesk Inventor 2018, 2018. URL `https://www.autodesk.de`.

[Barfüsser(2018)] A. Barfüsser. *Studies on the Reconstructed Pulse Height in Two Dimensional Floating Strip Micromegas Detectors with Different Readout PCB Structures.* Bachelor's thesis (unpublished), Ludwig-Maximilians-Universität München, 2018.

[Bencivenni et al.(2015)] G. Bencivenni, R. De Oliveira, G. Morello, and M. Poli Lener. *The micro-Resistive WELL detector: a compact spark-protected single amplification-stage MPGD.* Journal of Instrumentation, 10(02):P02008–P02008, February 2015. doi:10.1088/1748-0221/10/02/p02008. URL `https://doi.org/10.1088%2F1748-0221%2F10%2F02%2Fp02008`.

[Biagi(2018)] S. Biagi. *Magboltz - transport of electrons in gas mixtures*, April 2018. URL `http://magboltz.web.cern.ch/magboltz/`.

[Bichsel(1988)] H. Bichsel. *Straggling in thin silicon detectors.* Rev. Mod. Phys., 60:663–699, July 1988.

[Bidault et al.(2007)] J. M. Bidault, I. Crotty, A. Di Mauro, P. Martinengo, P. J. R. Fonte, F. Galy, V. Peskov, I. Rodionov, and O. Zanette. *The first applications of newly developed gaseous detectors with resistive electrodes for UV imaging in daylight conditions.* Nucl. Instrum. Methods Phys. Res., A, 580(2):1036–1041, 2007. URL `http://cds.cern.ch/record/1066011`.

[Bidault et al.(2006)] J.M. Bidault, P. Fonte, T. Francke, P. Galy, V. Peskov, and I. Rodionov. *A Novel UV Photon Detector with Resistive Electrodes.* Nuclear Physics B - Proceedings Supplements, 158:199 – 203, 2006. ISSN 0920-5632. doi:https://doi.org/10.1016/j.nuclphysbps.2006.07.009. URL http://www.sciencedirect.com/science/article/pii/S0920563206004518.

[Blum et al.(2008)] Walter Blum, Werner Riegler, and Luigi Rolandi. *Particle detection with drift chambers; 2nd ed.* Springer, Berlin, 2008. URL https://cds.cern.ch/record/1105920.

[Bortfeldt and Klitzner(2017)] J. Bortfeldt and F. Klitzner. *Analysis of Experimental Micromegas Data Collected During the HIT Test Beam.* The carbon data have been analyzed by J. Bortfeldt, the proton data by the author of this thesis., 2017.

[Bortfeldt et al.(2017)] J. Bortfeldt, O. Biebel, B. Flierl, R. Hertenberger, F. Klitzner, Ph. Lösel, L. Magallanes, R. Müller, K. Parodi, T. Schlüter, B. Voss, and A. Zibell. *Low material budget floating strip Micromegas for ion transmission radiography.* Nuclear Instruments and Methods in Physics Research Section A: Accelerators, Spectrometers, Detectors and Associated Equipment, 845:210 – 214, 2017. ISSN 0168-9002. doi:https://doi.org/10.1016/j.nima.2016.05.003. URL http://www.sciencedirect.com/science/article/pii/S0168900216303606.

[Bortfeldt(2014)] Jonathan Bortfeldt. *Development of Floating Strip Micromegas Detectors.* PhD thesis, Ludwig-Maximilians-Universität München, March 2014.

[Bravar(1999)] A Bravar. *The COMPASS experiment at CERN; 1999 ed.* AIP Conf. Proc., 459: 390–398, 1999. URL https://cds.cern.ch/record/366494.

[Bungard(2010)] Bungard. Bungard RLM 419 Trockenresist Laminator, 2010. URL https://www.bungard.de.

[Byszewski and Wotschack(2012)] M. Byszewski and J. Wotschack. *Resistive-strips micromegas detectors with two-dimensional readout.* Journal of Instrumentation, 7(02):C02060, 2012. URL http://stacks.iop.org/1748-0221/7/i=02/a=C02060.

[CAEN(2019a)] CAEN. CAEN - Tools for Discovery - A1535dn 12/24 Channel 3.5 kV/3 mA (8 W) Common Floating Return Boards, 2019a. Obsolete.

[CAEN(2019b)] CAEN. CAEN - Tools for Discovery - A1821 12 Channel 3 kV, 200/20 µA Common Ground Dual Range Board, 2019b. Obsolete.

[CAEN(2019c)] CAEN. CAEN - Tools for Discovery - Mod.N842 8 Channel Constant Fraction Discriminator, 2019c. URL https://www.caen.it/products/n842/.

[CAEN(2019d)] CAEN. CAEN - Tools for Discovery - Mod.N93B Dualtimer, 2019d. URL https://www.caen.it/products/n93b/.

[CAEN(2019e)] CAEN. CAEN - Tools for Discovery - Mod.N845 16 Channel Low Threshold Discriminator, 2019e. URL https://www.caen.it/products/n845/.

[CAEN(2019f)] CAEN. CAEN - Tools for Discovery - SY5527 Universal Multichannel Power Supply System , 2019f. URL https://www.caen.it/products/sy5527/.

[CAEN(2019g)] CAEN. CAEN - Tools for Discovery - Mod.V775N 16 Channel Multievent TDC, 2019g. URL https://www.caen.it/products/v775n/.

[Combs et al.(2010)] S. E. Combs, O. Jäkel, T. Haberer, and J. Debus. *Particle therapy at the Heidelberg Ion Therapy Center (HIT) – Integrated research-driven university-hospital-based radiation oncology service in Heidelberg, Germany.* Radiotherapy and Oncology, 95(1): 41 – 44, 2010. ISSN 0167-8140. doi:https://doi.org/10.1016/j.radonc.2010.02.016. URL http://www.sciencedirect.com/science/article/pii/S016781401000109X.

[Core Composites(2017)] Core Composites. Nomex Honeycomb - Lightweight Non-metallic Composite Honeycomb, 2017. URL http://www.corecomposites.com.

[Cortez et al.(2019)] A. Cortez et al. *Measurement of the ion mobility in a Neon Tetra-fluor methan based gas mixture.* submitted to JINST for publication in February 2019, April 2019.

[Şahin et al.(2010)] Ö. Şahin, I. Tapan, E.N. Özmutlu, and R. Veenhof. *Penning transfer in Argon-based gas mixtures.* Journal of Instrumentation, 5(05):P05002, 2010. URL http://stacks.iop.org/1748-0221/5/i=05/a=P05002.

[De Geronimo et al.(2012)] G. De Geronimo, J. Fried, S. Li, J. Metcalfe, N. Nambiar, E. Vernon, and V. Polychronakos. *VMM1 - An ASIC for micropattern detectors.* Proceedings, 2012 IEEE Nuclear Science Symposium and Medical Imaging Conference (NSS/MIC 2012): Anaheim, California, USA, October 29-November 3, 2012, pages 633–639, 2012. doi:10.1109/NSSMIC.2012.6551184.

[Diener(2012)] R. Diener. *Development of a TPC for an ILC Detector.* Physics Procedia, 37: 456 – 463, 2012. ISSN 1875-3892. doi:https://doi.org/10.1016/j.phpro.2012.02.393. URL http://www.sciencedirect.com/science/article/pii/S1875389212017245.

[DuPont(2011)] DuPont. DuPont Pyralux PC 1000 Series, 2011. URL https://www.dupont.com.

[Ellis et al.(1976)] H.W. Ellis, R.Y. Pai, and E.W. McDaniel. *Transport properties of gaseous ions over a wide energy range.* Atomic Data and Nuclear Data Tables, 17:177–210, 1976.

[ESL ElectroScience(2017)] ESL ElectroScience. ESL ElectroScience - Thick Film Materials and Ceramic Tapes, 2017. URL http://www.electroscience.com/.

[Farthouat and Gällnö(2000)] Ph. Farthouat and P. Gällnö. *TTC-VMEbus INTERFACE TTCvi - MKII*, 2000. URL http://ttc.web.cern.ch/TTC/TTCviSpec.pdf.

[Flierl(2018)] Bernhard Matthias Flierl. *Particle Tracking with Micro-Pattern Gaseous Detectors.* PhD thesis, Ludwig-Maximilians-Universität München, March 2018.

[Francke and Peskov(2014)] Tom Francke and Vladimir Peskov. *Innovative applications and developments of micro-pattern gaseous detectors.* Advances in chemical and materials engineering (ACME) book series. Engin. Sci. Ref., Hershey, 2014. ISBN 9781466660144, 9781466660151. doi:10.4018/978-1-4666-6014-4. URL http://www.igi-global.com/book/innovative-applications-developments-micro-pattern/97377.

[Frank(2017)] I. Frank. *Printing High Ohmic Resistors and Improvement of a Thin Anode for Two-dimensional Floating Strip Micromegas Detectors.* Master's thesis, Ludwig-Maximilians-Universität München, September 2017. URL https://www.etp.physik.uni-muenchen.de/publications/theses/download/master_ifrank.pdf.

[French et al.(2001)] M. J. French, L. L. Jones, Q. R. Morrissey, A. Neviani, R. Turchetta, J. R. Fulcher, G. Hall, E. Noah, M. Raymond, G. Cervelli, P. Moreira, and G. Marseguerra. *Design and results from the APV25, a deep sub-micron CMOS front-end chip for the CMS tracker.* Nucl. Instrum. Methods Phys. Res., A, 466(2):359–65, 2001. URL http://cds.cern.ch/record/516812.

[Gatti(2018)] C. Gatti, 2018. private communication.

[Giomataris et al.(1996)] Y. Giomataris, Ph. Rebourgeard, J. P. Robert, and G. Charpak. *Micromegas: a high-granularity position-sensitive gaseous detector for high particle-flux environments.* Nucl. Instrum. Methods Phys. Res., A, 376(1046):29–35, 6 1996.

[Goitein(2007)] M Goitein. *Radiation Oncology: A Physicist's- Eye View.* Springer, 2007.

[Groom et al.(2001)] D. Groom et al. *Muon Stopping Power and Range Tables 10MeV - 100 TeV.* Atomic Data and Nuclear Data Tables, 76(2), July 2001. doi:LBNL-44742. URL `http://pdg.lbl.gov/2017/AtomicNuclearProperties/adndt.pdf`.

[Grupen and Shwartz(2008)] C. Grupen and B. Shwartz. *Particle Detectors.* Cambridge University Press, 2008.

[GW INSTEK(2018)] GW INSTEK. GW INSTEK - Precision LCR Meter 8000G Series, 2018. URL `https://www.gwinstek.com/en-global/products/detail/LCR-8000G`.

[Hamamatsu(2007)] Hamamatsu. Photomultiplier Tube R4124, 2007. URL `https://www.hamamatsu.com/eu/en/product/type/R4124/index.html`.

[Horvat(2005)] S. Horvat. *Study of the Higgs Discovery Potential in the Process* $pp \longrightarrow H \longrightarrow 4\mu$. PhD thesis, University of Zagreb, April 2005.

[Hough(1959)] P. V. C. Hough. *Machine Analysis of Bubble Chamber Pictures.* Conf. Proc., C590914:554–558, 1959.

[Iakovidis(2014)] G. Iakovidis. *Research and Development in Micromegas Detector for the ATLAS Upgrade.* PhD thesis, National University of Athens, October 2014.

[Iakovidis(2018)] G. Iakovidis. *VMM3, an ASIC for Micropattern Detectors.* Technical Report ATL-MUON-PROC-2018-003, CERN, Geneva, March 2018. URL `http://cds.cern.ch/record/2309951`.

[Iseg(2017)] Iseg. SHQ Series - Digital Controlable High Precision Desktop HV Supply, 2017. URL `https://iseg-hv.com/en/products/detail/SHQ`. Discontinued.

[Jones(2001)] L. Jones. *APV25-S1 User Guide*, September 2001. URL `https://cds.cern.ch/record/1069892/files/cer-002725643.pdf`.

[Kawamoto et al.(2013)] T. Kawamoto, S. Vlachos, L. Pontecorvo, J. Dubbert, G. Mikenberg, P. Iengo, C. Dallapiccola, C. Amelung, L. Levinson, R. Richter, and D. Lellouch. *New Small Wheel Technical Design Report.* Technical Report CERN-LHCC-2013-006. ATLAS-TDR-020, CERN, Geneva, June 2013. ATLAS New Small Wheel Technical Design Report.

[Kleffner et al.(2009)] C. Kleffner, D. Ondreka, and U. Weinrich. *The Heidelberg Ion Therapy (HIT) Accelerator Coming into Operation.* AIP Conference Proceedings, 1099(1):426–428, 2009. doi:10.1063/1.3120065. URL `https://aip.scitation.org/doi/abs/10.1063/1.3120065`.

[Kleinknecht(2005)] K. Kleinknecht. *Detektoren für Teilchenstrahlung, 4. Auflage.* Teubner Stuttgart, 2005.

[Klitzner(2016)] F. Klitzner. *Studies on floating strip micromegas detectors in proton and carbon ion beams with a fast gas mixture.* Master's thesis, Ludwig-Maximilians-Universität München, April 2016. URL `https://www.etp.physik.uni-muenchen.de/publications/theses/download/master_fklitzner.pdf`.

[Klitzner et al.(2017)] F. Klitzner, O. Biebel, B. Flierl, B. Gillich, R. Hertenberger, P. Lösel, J. Scherzer, and J. Bortfeldt. *Novel Two-Dimensional Floating Strip Micromegas Detectors.* PoS, ICHEP2016:1190, 2017. doi:10.22323/1.282.1190.

[König(2015)] V. König. *Zusammenbau und Inbetriebnahme von dünnen Floating Strip Micromegas mit zweidimensionaler Auslesestruktur.* Bachelor's thesis (unpublished), Ludwig-Maximilians-Universität München, 2015.

[Kuger(2017)] F. Kuger. *Signal Formation Processes in Micromegas Detectors and Quality Control for large size Detector Construction for the ATLAS New Small Wheel.* PhD thesis, Julius-Maximilians-Universität Würzburg, July 2017.

[LeCroy(1996)] LeCroy. *Model 662 Quad 2-Input Logic Unit*, 1996. URL `https://teledynelecroy.com/lrs/dsheets/365al.htm`.

[LeCroy(1997)] LeCroy. *8 Channel NIM Discriminator Model 4608C*, 1997. URL `http://cdn.teledynelecroy.com/files/manuals/4608cman.pdf`.

[Levinson(2011)] Harry Levinson. *Principles of lithography: Third edition.* SPIE. Digital Library, 01 2011. doi:10.1117/3.865363.

[Li(2017)] H. Li. *Optimization Studies of Floating Strip Micromegas Detectors with a 2-Dimensional Readout Structure.* Bachelor's thesis (unpublished), Ludwig-Maximilians-Universität München, 2017.

[Li et al.(2006)] T. Li, Z. Liang, J. V. Singanallur, T. Satogata, D. C. Williams, and R. W. Schulte. *Reconstruction for proton computed tomography by tracing proton trajectories: a Monte Carlo study.* Medical physics, 33 3:699–706, 2006.

[Lin et al.(2014)] T. Lin, A. Düdder, M. Schott, C. Valderanis, L. Wehner, and R. Westenberger. *Signal characteristics of a resistive-strip micromegas detector with an integrated two-dimensional readout.* Nuclear Instruments and Methods in Physics Research Section A: Accelerators, Spectrometers, Detectors and Associated Equipment, 767:281–288, 2014. ISSN 0168-9002. doi:10.1016/j.nima.2014.09.002. URL `http://www.sciencedirect.com/science/article/pii/S0168900214009942`.

[Linstrom and Mallard(2019)] P. J. Linstrom and W. G. Mallard, editors. *NIST Chemistry WebBook, NIST Standard Reference Database Number 69.* National Institute of Standards and Technology, Gaithersburg MD, 20899, March 2019. URL `http://webbook.nist.gov`.

[Lippert(2012)] B. Lippert. *Studien zur Signalentstehung und Parametrisierung der Gasverstärkung in einem Micromegas Detektor.* Bachelor's thesis (unpublished), Ludwig-Maximilians-Universität München, 2012.

[Lösel(2017)] Philipp Lösel. *Precision Calibration of Large Area Micro Pattern Gaseous Detectors.* PhD thesis, Ludwig-Maximilians-Universität München, June 2017.

[Lupberger et al.(2018)] M. Lupberger, L. Bartels, F. M. Brunbauer, M. Guth, S. Martoiu, H. Müller, E. Oliveri, D. Pfeiffer, L. Ropelewski, A. Rusu, and P. Thuiner. *Implementation of the VMM ASIC in the Scalable Readout System.* Nucl. Instrum. Methods Phys. Res., A, 903:91–98. 8 p, 2018. URL `https://cds.cern.ch/record/2630908`.

[Magallanes(2017)] L. Magallanes. *Low-dose ion-based transmission radiography and tomography for optimization of carbon ion-beam Therapy.* PhD thesis, Ludwig-Maximilians-Universität München, January 2017.

[Martoiu et al.(2013)] S. Martoiu, H. Müller, A. Tarazona, and J. Toledo. *Development of the scalable readout system for micro-pattern gas detectors and other applications.* Journal of Instrumentation, 8(03):C03015–C03015, March 2013. doi:10.1088/1748-0221/8/03/c03015. URL https://doi.org/10.1088%2F1748-0221%2F8%2F03%2Fc03015.

[Memmert(2013)] Memmert. Memmert - Experts in Thermodynamics, ICH 260 Klimabox, 2013. URL https://www.memmert.com/products/climate-chambers/climate-chamber/ICH260/.

[Meyer(2019)] S. Meyer. *On the clinical potential of ion computed tomography with different detector system and ion species – in preperation.* PhD thesis, Ludwig-Maximilians-Universität München, April 2019.

[Mitin and Zietman(2014)] T. Mitin and A. L. Zietman. *Promise and Pitfalls of Heavy-Particle Therapy.* Journal of Clinical Oncology, 32(26):2855–2863, 2014. doi:10.1200/JCO.2014.55.1945. URL https://doi.org/10.1200/JCO.2014.55.1945.

[Moll(2013)] Samuel Moll. *Entladungsstudien an Micromegas - Teilchendetektoren.* Diploma thesis, Ludwig-Maximilians-Universität München, 2013.

[Morháč(2015)] M. Morháč. *TSpectrum Manual: 6 Release Cycle*, 2015. URL https://root.cern.ch/guides/tspectrum-manual.

[Müller(2017)] Ralph Müller. *Quality Control of Micromegas Detectors for the ATLAS New Small Wheel Upgrade Project and Optimization of the Spatial Resolution of PoSSuMuS Detectors in two Dimensions.* PhD thesis, Ludwig-Maximilians-Universität München, March 2017.

[Ntekas(2016)] Konstantinos Ntekas. *Performance characterization of the Micromegas detector for the New Small Wheel upgrade and Development and improvement of the Muon Spectrometer Detector Control System in the ATLAS experiment.* PhD thesis, National Technical University of Athens, 2016. URL http://cds.cern.ch/record/2143887. Presented 2016.

[Nührmann(2002)] Dieter Nührmann. *Das komplette Werkbuch Elektronik Band 3 und 4.* Franzis, 2002.

[Nygren(1974)] D. R. Nygren. *The Time-Projection Chamber - A new 4π detector for charged particles.* PEP-144, 1974.

[Ortec(1969)] Ortec. Ortec Model 454 Timing Filter Amplifier, 1969. URL https://groups.nscl.msu.edu/nscl_library/manuals/eggortec/454.pdf. [online, accessed: April 2019].

[Ortec(2002)] Ortec. Ortec Model 142PC Preamplifier, 2002. URL https://www.ortec-online.com/products/electronics/preamplifiers/142pc.

[Pancin et al.(2004)] J. Pancin et al. *Measurement of the nTOF beam profile with a micromegas detector.* Nucl. Instrum. Methods Phys. Res., A, 524:102–114, 2004. URL http://cds.cern.ch/record/816780.

[Paul(2007)] Clayton R. Paul. *Analysis of Multiconductor Transmission Lines.* Wiley-IEEE Press, 2nd edition, 2007. ISBN 0470131543.

[Penning(1927)] F. M. Penning. *Über Ionisation durch metastabile Atome.* Naturwissenschaften, 15:818–818, October 1927. doi:10.1007/BF01505431.

[R. K. Carnegie(2005)] M. S. Dixit J. Dubeau D. Karlen J.-P. Martin H. Mes K. Sachs R. K. Carnegie. *Resolution studies of cosmic-ray tracks in a TPC with GEM readout.* Nucl. Instrum. Methods Phys. Res., A, 2005.

[Raether(1964)] H. Raether. *Electron Avalanches and Breakdown in Gases*. Butterworths advanced physics series. Butterworths, 1964.

[Ramo(1939)] S. Ramo. *Currents Induced by Electron Motion*. Proceedings of the IRE, 27(9): 584–585, September 1939. ISSN 0096-8390. doi:10.1109/JRPROC.1939.228757.

[Rinaldi(2011)] I. Rinaldi. *Investigation of novel imaging methods using therapeutic ion beams*. PhD thesis, Ruperto-Carola University of Heidelberg, October 2011.

[Santos et al.(2018)] M.A.G. Santos, M.A. Kaja, A.F.V. Cortez, R. Veenhof, P.N.B. Neves, F.P. Santos, F.I.G.M. Borges, and C.A.N. Conde. *Experimental ion mobility measurements for the LCTPC collaboration—Ar-CF_4 mixtures*. Journal of Instrumentation, 13(04):P04012, 2018. URL http://stacks.iop.org/1748-0221/13/i=04/a=P04012.

[Sauli(1997)] F. Sauli. *GEM: A new concept for electron amplification in gas detectors*. Nuclear Instruments and Methods in Physics Research Section A: Accelerators, Spectrometers, Detectors and Associated Equipment, 386(2):531 – 534, 1997. ISSN 0168-9002. doi:https://doi.org/10.1016/S0168-9002(96)01172-2. URL http://www.sciencedirect.com/science/article/pii/S0168900296011722.

[Schneider et al.(2004)] U. Schneider, J. Besserer, P. Pemler, M. Dellert, M. Moosburger, E. Pedroni, and B. Kaser-Hotz. *First proton radiography of an animal patient*. Medical Physics, 31(1046), 2004.

[Schulte et al.(2003)] Reinhard Schulte, Vladimir Bashkirov, Tianfang li, J.Z. Liang, Klaus Mueller, J Heimann, Leah Johnson, B Keeney, H.F.-W Sadrozinski, A Seiden, D.C. Williams, Lan Zhang, Zheng Li, S Peggs, T Satogata, and C Woody. *Design of a proton computed tomography system for applications in proton radiation therapy*. In *IEEE Nuclear Science Symposium Conference Record*, volume 3, pages 1579 – 1583 Vol.3, 11 2003. ISBN 0-7803-8257-9. doi:10.1109/NSSMIC.2003.1352179.

[Segrè et al.(1953)] E. Segrè, H. Staub, H. A. Bethe, J. Ashkin, et al. *Experimental nuclear physics*, volume I p.253. New York : John Wiley & Sons, 1953.

[Shockley(1938)] W. Shockley. *Currents to Conductors Induced by a Moving Point Charge*. Journal of Applied Physics, 9(10):635–636, 1938. doi:10.1063/1.1710367. URL https://doi.org/10.1063/1.1710367.

[Sidiropoulou et al.(2017)] O. Sidiropoulou, B. Alvarez Gonzalez, D. Andreou, L. Barak, J. Bortfeldt, M.T. Camerlingo, F. Dubinin, E.M. Farina, P. Iengo, E. Oliveri, J. Samarati, G. Sekhniaidze, and J. Wotschack. *Characterization of Micromegas with elongated pillars*. Journal of Instrumentation, 12(02):C02076–C02076, February 2017. doi:10.1088/1748-0221/12/02/c02076. URL https://doi.org/10.1088%2F1748-0221%2F12%2F02%2Fc02076.

[Smirnov(2005)] I. Smirnov. *HEED - Modeling of ionization produced by fast charged particles in gases*, 2005. URL http://ismirnov.web.cern.ch/ismirnov/heed.

[Tanabashi et al.(2018)] M. Tanabashi et al. *Review of Particle Physics*. Phys. Rev. D, 98:030001, August 2018. doi:10.1103/PhysRevD.98.030001. URL https://link.aps.org/doi/10.1103/PhysRevD.98.030001.

[Townsend(1910)] J. S. Townsend. *The Theory of Ionization of Gases By Collision*. Constable & Company Ltd, 1910.

[Veenhof(2010)] R. Veenhof. *Garfield - simulation of gaseous detectors*, Sep 2010. URL https://garfieldpp.web.cern.ch/garfieldpp/.

[Wang and Nelson(2002)] Erke Wang and Thomas Nelson. *Structural Dynamic Capabilities of ANSYS*. ANSYS, Inc., 2002. URL `https://www.ansys.com/-/media/Ansys/corporate/resourcelibrary/conference-paper/2002-Int-ANSYS-Conf-200.PDF`.

[Wieland(2017)] A. Wieland. *Studies on Thin Two-Dimensional Floating Strip Micromegas Detectors with a Paper Honeycomb Supported Anode Structure*. Bachelor's thesis (unpublished), Ludwig-Maximilians-Universität München, 2017.

[William(1993)] R. L. William. *Techniques for Nuclear and Particle Physics Experiments*. Springer, 1993.

[Zibell(2014)] A. Zibell. *High-Rate Irradiation of 15 mm Muon Drift Tubes and Development of an ATLAS Compatible Readout Driver for Micromegas Detectors*. PhD thesis, Ludwig-Maximilians-Universität München, April 2014.

[Ziegler et al.(2010)] J. F. Ziegler, M. D. Ziegler, and J. P. Biersack. *SRIM - The stopping and range of ions in matter (2010)*. Nucl. Instrum. Methods Phys., B, 268:1818–1823, June 2010. doi:10.1016/j.nimb.2010.02.091.

Appendix A

Tracking Methods

The tracking methods described in the following have been taken from [Klitzner, 2016] and are included for the sake of completeness.

A.1 Analytic χ^2-Minimization

The fit of a two parameter function, such as a straight line $x(z) = az + b$, to a set of data points (z_i, x_i), $i = 1, ..., n$ can be performed analytically [Horvat, 2005].
The parameters a and b can be determined by minimizing the χ^2 function

$$\chi^2 = \sum_{\mathrm{i}\,=\,1}^{\mathrm{n}} w_i (x_i - az_i - b)^2 \ , \tag{A.1}$$

where w_i is the weight of a given data point. The weights for the track fit in a Micromegas reference system are given by an estimate of the spatial resolution $\tilde{\sigma}_i$, with $w_i = 1/\tilde{\sigma}_i^2$. Thus,

$$\chi^2 = \sum_{\mathrm{i}\,=\,1}^{\mathrm{n}} \frac{1}{\tilde{\sigma}_i^2} (x_i - az_i - b)^2 \ . \tag{A.2}$$

From the minimization requirements $\frac{\delta\chi^2}{a} = 0$ and $\frac{\delta\chi^2}{b} = 0$ follows

$$\begin{aligned} \chi^2 &= \sum_{\mathrm{i}\,=\,1}^{\mathrm{n}} \frac{z_i}{\tilde{\sigma}_i^2} (x_i - az_i - b) \ , \\ \chi^2 &= \sum_{\mathrm{i}\,=\,1}^{\mathrm{n}} \frac{1}{\tilde{\sigma}_i^2} (x_i - az_i - b) \ . \end{aligned} \tag{A.3}$$

We can now define parameters g_1, g_2 and Λ_{11}, Λ_{12} and Λ_{22} with

$$\begin{aligned} (g_1, g_2) &= \sum_{\mathrm{i}\,=\,1}^{\mathrm{n}} \frac{x_i (1, z_i)}{\tilde{\sigma}_i^2} \ , \\ (\Lambda_{11}, \Lambda_{12}, \Lambda_{22}) &= \sum_{\mathrm{i}\,=\,1}^{\mathrm{n}} \frac{x_i (1, z_i, z_i^2)}{\tilde{\sigma}_i^2} \ . \end{aligned} \tag{A.4}$$

Inserting Eq. A.4 into Eq. A.3 gives

$$\begin{aligned} \Lambda_{11} b + \Lambda_{12} a &= g_1 \ , \\ \Lambda_{12} b + \Lambda_{22} a &= g_2 \ . \end{aligned} \tag{A.5}$$

Slope a and intersect b of the track can now be determined by applying Cramers's rule, yielding

$$a = \frac{\Lambda_{11} g_2 - \Lambda_{12} g_1}{D}$$
$$\text{and}$$
$$b = \frac{\Lambda_{22} g_1 - \Lambda_{12} g_2}{D} \tag{A.6}$$
$$\text{with}$$
$$D = \Lambda_{11}\Lambda_{22} - \Lambda_{12}^2 \ .$$

The uncertainty of the track fit σ_{track} can be determined at each detector position (z_i, x_i), e.g. if needing it for the determination of the spatial resolution as described in section **??**, given by

$$\sigma^2_{\text{track}}(z_i, x_i) = \text{Var}(b) + 2 z_i \text{Covar}(b, a) + z_i^2 \text{Var}(a) \ . \tag{A.7}$$

For an approximation of the true spatial resolution σ_i with the estimate $\tilde{\sigma}_i$ this leads to

$$\sigma^2_{\text{track}}(z_i, x_i) = \frac{1}{D}[\Lambda_{22} - 2 z_i \Lambda_{12} + z_i^2 \Lambda_{11}] \ . \tag{A.8}$$

A detailed derivation of the variance and covariance can be found in [Horvat, 2005].

A.2 Kalman Filter Based Track Reconstruction

Consider a detector system consisting of n detector layers with registered hit positions $\vec{x}_i(x_i, y_i, z_i)$, for layer $i = 0, ..., n$. The hits are reconstructed in the $x-y$ detector plane, with z defining the detector position in the perpendicular direction. Consider the hit x_i measured by detector layer i in x-direction. The estimation of the local track at layer i can thus be described by the so called state estimation vector $\vec{x}_i$ and the estimate covariance error matrix $\mathbf{C_i}$, with

$$\vec{x}_i = \begin{bmatrix} x_i \\ y_i \\ m_{x,i} \\ m_{y,i} \end{bmatrix} \quad \text{and} \quad \mathbf{C_i} = \begin{bmatrix} \text{var}(x) & \text{covar}(x,y) & \text{covar}(x,m_x) & \text{covar}(x,m_y) \\ \text{covar}(y,x) & \text{var}(y) & \text{covar}(y,m_x) & \text{covar}(y,m_y) \\ \text{covar}(m_x,x) & \text{covar}(m_x,y) & \text{var}(m_x) & \text{covar}(m_x,m_y) \\ \text{covar}(m_y,x) & \text{covar}(m_y,y) & \text{covar}(m_y,m_x) & \text{var}(m_y) \end{bmatrix} , \tag{A.9}$$

where $m_{x,i}$, $m_{y,i}$ describes the slope of the track in the x-z- and y-z plane at detector position z_i of layer i, respectively. The 4×4 error covariance matrix $\mathbf{C_i}$ of the two independent variables x_i and y_i and their respective slopes describes the variances on the diagonal part of the matrix, whereas the off-diagonal encode correlations between the variables.
In the next step, the track information of layer i, encoded in the state estimation vector $\vec{x}_i$, is extrapolated to the next layer $i+1$ via multiplication with the transport matrix $\mathbf{J_{i+1}}$, thus yielding the state estimation vector $\vec{x}_{i+1}$ with

$$\begin{aligned} \vec{x}_{i+1} &= \mathbf{J_{i+1}} \cdot \vec{x}_i \\ &= \begin{bmatrix} 1 & 0 & \Delta z_{i,i+1} & 0 \\ 0 & 1 & 0 & \Delta z_{i,i+1} \\ 0 & 0 & 1 & 0 \\ 0 & 0 & 0 & 1 \end{bmatrix} \cdot \begin{bmatrix} x_i \\ y_i \\ m_{x,i} \\ m_{y,i} \end{bmatrix} \\ &= \begin{bmatrix} x_i + m_{x,i} \cdot \Delta z_{i,i+1} \\ y_i + m_{y,i} \cdot \Delta z_{i,i+1} \\ m_{x,i} \\ m_{y,i} \end{bmatrix} = \begin{bmatrix} x_{i+1} \\ y_{i+1} \\ m_{x,i} \\ m_{y,i} \end{bmatrix} \end{aligned} \tag{A.10}$$

where $\Delta z_{i,i+1} = z_{i+1} - z_i$ describes the distance between detector layers i and $i+1$. The covariance matrix $\mathbf{C_{i+1}}$ after transport to layer $i+1$ is then given by

$$\mathbf{C_{i+1}} = \mathbf{J_{i+1}} \cdot \mathbf{C_i} \cdot \mathbf{J_{i+1}^\top} \ , \tag{A.11}$$

defining the errors e.g. uncertainties at state $i+1$. The residual $\Delta_{\text{res}}^{i+1}$ between the measured hit $x_{i+1,\text{meas}}$ in layer $i+1$ and the predicted hit x_{i+1} of Eq. (A.10) can thus be calculated:

$$\Delta_{\text{res x,y}}^{i+1} = (x_{i+1,\text{meas}}, y_{i+1,\text{meas}}) - \mathbf{H}^\top \cdot \vec{x}_{i+1} \tag{A.12}$$

with

$$\mathbf{H} = \begin{bmatrix} \cos(\alpha) \\ \sin(\alpha) \\ 0 \\ 0 \end{bmatrix} \tag{A.13}$$

describing the orientation of the measured hit, either in x- or y-direction, via the angle α between the y-axis and the orientation of the measured strip. For a measured hit i.e. in the x direction, $x_{i+1,\text{meas}}$, the resulting angle α=0, as the x-strips are always oriented in y-direction, thus

$$\begin{aligned} \Delta_{\text{res x}}^{i+1} &= x_{i+1,\text{meas}} - \mathbf{H}^\top \cdot \vec{x}_{i+1} \\ &= x_{i+1,\text{meas}} - \begin{bmatrix} 1 & 0 & 0 & 0 \end{bmatrix} \cdot \begin{bmatrix} x_{i+1} \\ y_{i+1} \\ m_{x,i} \\ m_{y,i} \end{bmatrix} \\ &= x_{i+1,\text{meas}} - x_{i+1} \ . \end{aligned} \tag{A.14}$$

The weight of the measured hit, used for fitting the track, is defined as the inverse sum of an estimate of the spatial resolution σ_{i+1} at layer $i+1$ and the covariance matrix $\mathbf{C_{i+1}}$, translated on the respective direction via multiplication with the 1×4 rotation matrix $\mathbf{H}$, as defined in Eq. (A.13), yielding the weight w_{i+1}

$$w_{i+1} = (\sigma_{i+1}^2 + \mathbf{H}^\top \mathbf{C_{i+1}} \mathbf{H})^{-1} \tag{A.15}$$

The update $\vec{u}_{i+1}$ of the state estimate vector $\vec{x}_{i+1}$, after the measurement in layer $i+1$, is then given by

$$\vec{u}_{i+1} = w_{i+1} \cdot \Delta_{\text{res x,y}}^{i+1} \cdot \mathbf{C_{i+1}} \cdot \mathbf{H} \ , \tag{A.16}$$

thus defining the updated state for layer $i+1$

$$\vec{x}_{i+1} = \vec{x}_{i+1} + \vec{u}_{i+1} \tag{A.17}$$

and the updated estimate covariance matrix $\mathbf{C_{i+1}}$

$$\mathbf{C_{i+1}} = \mathbf{C_{i+1}} - \mathbf{C_{i+1}} \cdot \mathbf{H} \cdot w_{i+1} \cdot \mathbf{H}^\top \cdot \mathbf{C_{i+1}} \ . \tag{A.18}$$

χ_{i+1}^2 can now be calculated after the measurement update in layer $i+1$, following

$$\chi_{i+1}^2 = \frac{\left(\Delta_{\text{res,new}}^{i+1}\right)^2}{v_{i+1}} \ , \tag{A.19}$$

where

$$\Delta_{\text{res,new}}^{i+1} = \Delta_{\text{res x,y}}^{i+1} - \mathbf{H}^\top \cdot \vec{u}_{i+1} \tag{A.20}$$

describes the new residual after the measurement update and

$$v_{i+1} = \sigma_{i+1}^2 - \mathbf{H}^\top \mathbf{C_{i+1}} \mathbf{H} \tag{A.21}$$

includes the updated error information of the estimate covariance matrix $\mathbf{C_{i+1}}$.
For a calculated value of $\chi^2_{i+1} > 50$, the measured hit of layer $i+1$ is not accepted for track fitting, marking the used as bad. The algorithm now searches for a matching cluster in layer $i+1$, until $\chi^2_{i+1} < 50$. If no matching cluster is found, the algorithm jumps back to layer i and searches for a matching cluster in this layer.
Assuming the algorithm converges after a finite number of steps reaching the last layer $i = n$, then the information of the resulting found track is saved in the state estimation vector $\vec{x_n}^{\text{for}}$ and the corresponding estimate covariance matrix $\mathbf{C_n}^{\text{for}}$, respectively. for denotes that the algorithm performed the track finding procedure in the $forward$ direction, searching from layer 0 to layer n, thus increasing the number of layer with each step.
In a next step, the algorithm repeats the track finding process, now starting in the last layer n, extrapolating the hit in the reverse direction into layer $n-1$. The track parameters are saved in the state $\vec{x_0}^{\text{rev}}$ and $\mathbf{C_0}^{\text{rev}}$, after completed search in the $reverse$ direction, arriving at layer 0.
In a last step, the final track parameters are determined from the average of the reverse and forward search, yielding $\mathbf{C_i}^{mean}$ and $\vec{x_i}^{mean}$ at layer i with

$$\mathbf{C_i}^{mean} = \left(\left(\mathbf{C_i}^{for}\right)^{-1} + \left(\mathbf{C_i}^{rev}\right)^{-1} \right)^{-1} \tag{A.22}$$

and

$$\vec{x_i}^{mean} = \mathbf{C_i}^{mean} \cdot \left(\left(\mathbf{C_i}^{for}\right)^{-1} \cdot \vec{x_i}^{for} + \left(\mathbf{C_i}^{rev}\right)^{-1} \cdot \vec{x_i}^{rev} \right)^{-1} . \tag{A.23}$$

As the algorithm performes the track search consecutively at each detector position z_i, it is possible to include uncertainties of the track caused by multiple scattering of particles within layer i. After the measurement update of the estimate covariance matrix $\mathbf{C_i}$ in layer i, the scattering angle $d\Theta$ is then quadratically added to the variances of both track slopes m_x and m_y, encoded on the diagonal elements of $\mathbf{C_i}$ in the 2nd and 3rd column, see Eq. (A.10). As a consequence, the track determined by the algorithm needs not necessarily to be straight. This allows for example comparing tracklets before and after a certain z position.

Appendix B

Signal Characteristics

B.1 Classical Anode Designs

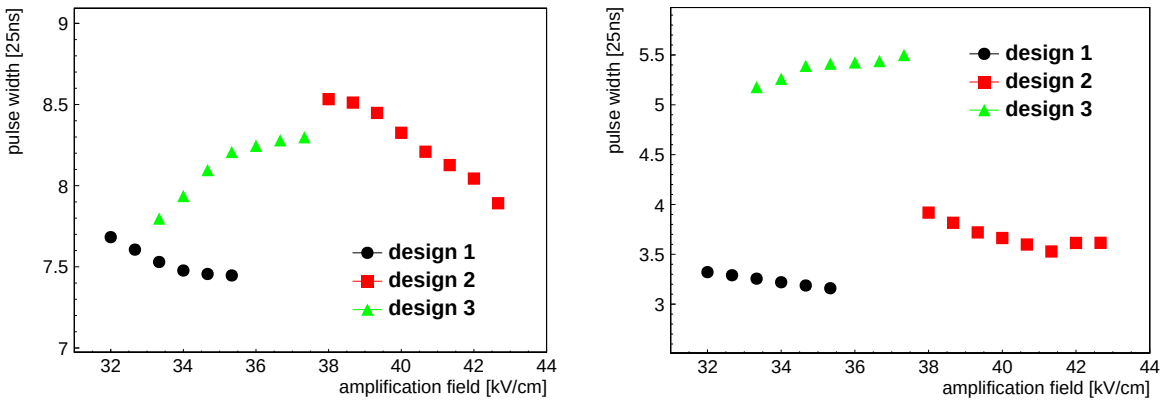

(a) x-layer (b) y-layer

Figure B.1: Pulse width in the time dimension on the x-strips (left) and y-strips (right) as a function of the amplification field strength and the anode design.

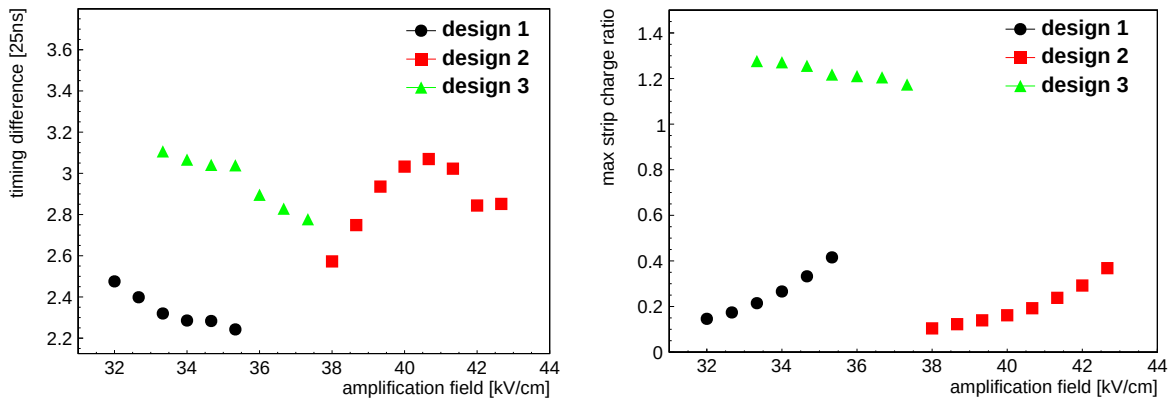

Figure B.2: Timing difference between x-strips and y-strips (left) and maximum strip charge ratio y/x (right) as a function of the amplification field strength.

B.2 Novel Anode Designs

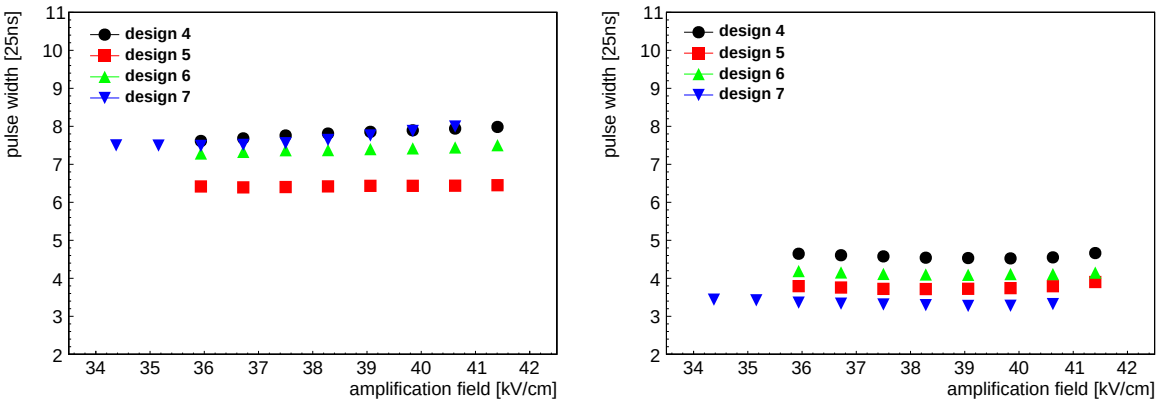

(a) x-layer (b) y-layer

Figure B.3: Pulse width in the time dimension on the x-strips (left) and y-strips (right) as a function of the amplification field strength and the anode design.

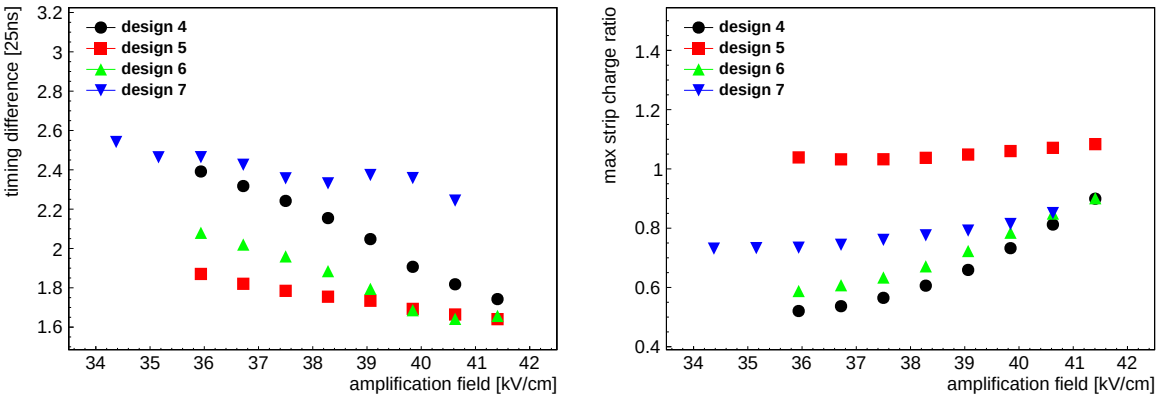

Figure B.4: Timing difference between x-strips and y-strips (left) and maximum strip charge ratio y/x (right) as a function of the amplification field strength.

Appendix C

µTPC Reconstruction with MIP-like Particles

C.1 Variation of the Amplification Field

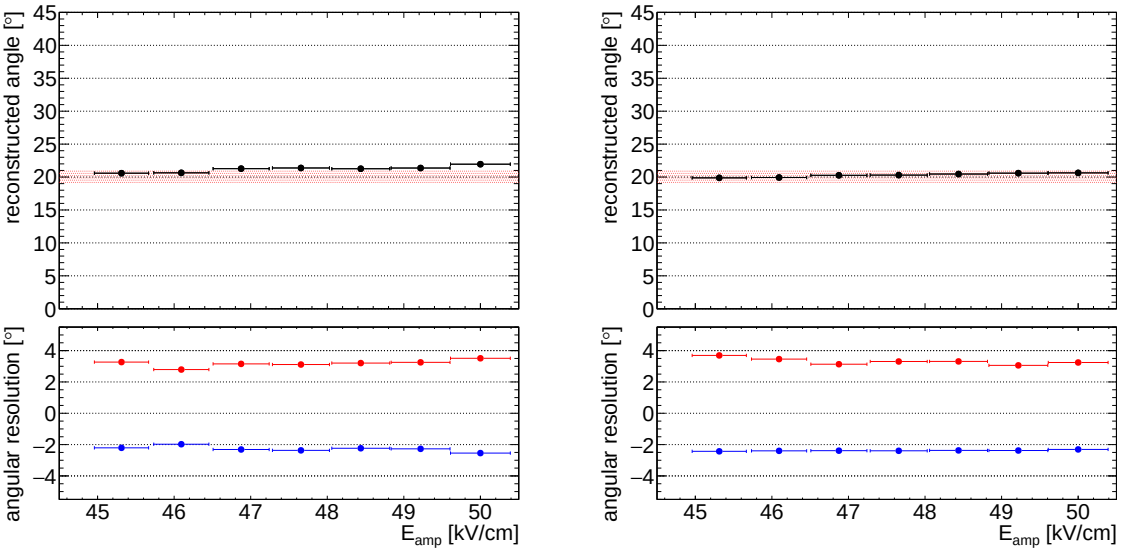

(a) x-layer

(b) y-layer

Figure C.1: Reconstructed most probable angle and angular resolution as a function of E_{amp} at E_{drift}=0.08 kV/cm measured with the x-layer (left) and the y-layer (right) of anode design 4 at an angle of $(20 \pm 1)°$. The measured inclination of the detector with a ruler is marked in red.

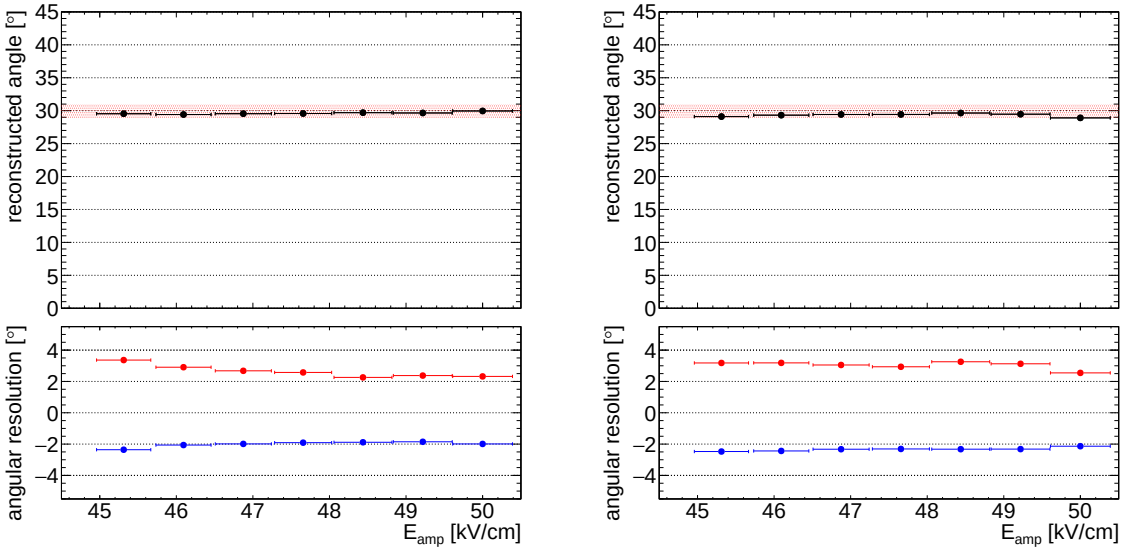

(a) x-layer (b) y-layer

Figure C.2: Reconstructed most probable angle and angular resolution as a function of E_{amp} at E_{drift}=0.08 kV/cm measured with the x-layer (left) and the y-layer (right) of anode design 4 at an angle of $(30 \pm 1)°$. The measured inclination of the detector with a ruler is marked in red.

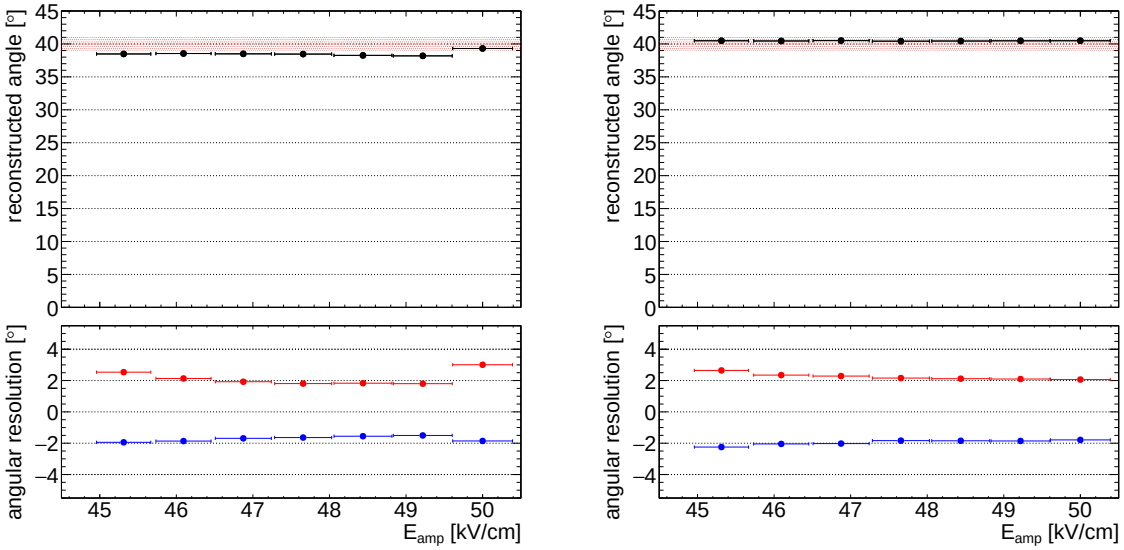

(a) x-layer (b) y-layer

Figure C.3: Reconstructed most probable angle and angular resolution as a function of E_{amp} at E_{drift}=0.08 kV/cm measured with the x-layer (left) and the y-layer (right) of anode design 4 at an angle of $(40 \pm 1)°$. The measured inclination of the detector with a ruler is marked in red.

On the x-layer, an APV25 chip with 4 dead channels degrade the centroid efficiency at 20° and 30°, leading to a 'turn-on' curve beginning at around 95% at the lowest measured amplification field, visible in Figure C.4. However, after replacing the APV25, the efficiency stays also around 99% for the x-layer at 40° over the full amplification field range. An efficiency above 96% is also expected for the x-layer, assuming a fully functional APV25 chip

for the measurements at 20° and 30°.

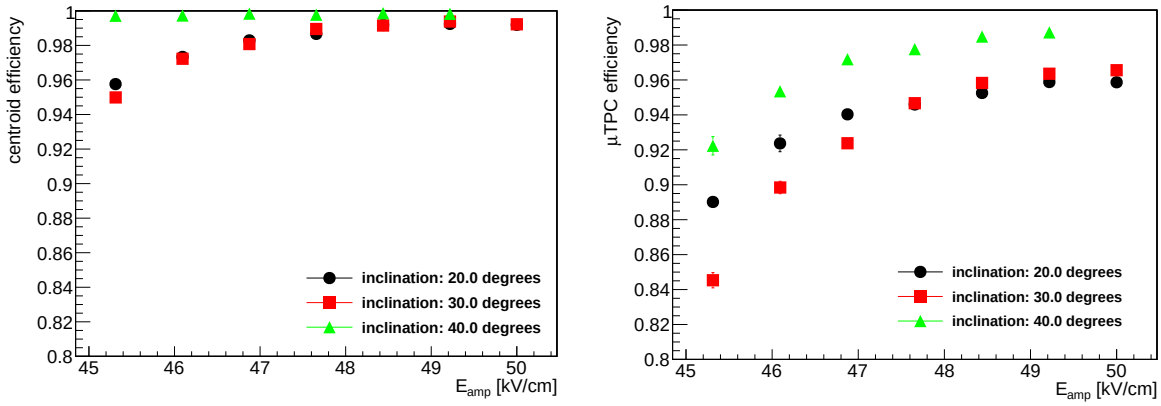

Figure C.4: Efficiency of the x-layer determined with the centroid method (left) and the µTPC method (right) as a function of E_{amp} at E_{drift}=0.083 kV/cm for three different inclination angles with muons. The difference in efficiency in the left figure between 20, 30 and 40° is due to an APV25 chip with 4 dead channels, which was replaced for the 40° measurement.

C.2 Variation of the Drift Field

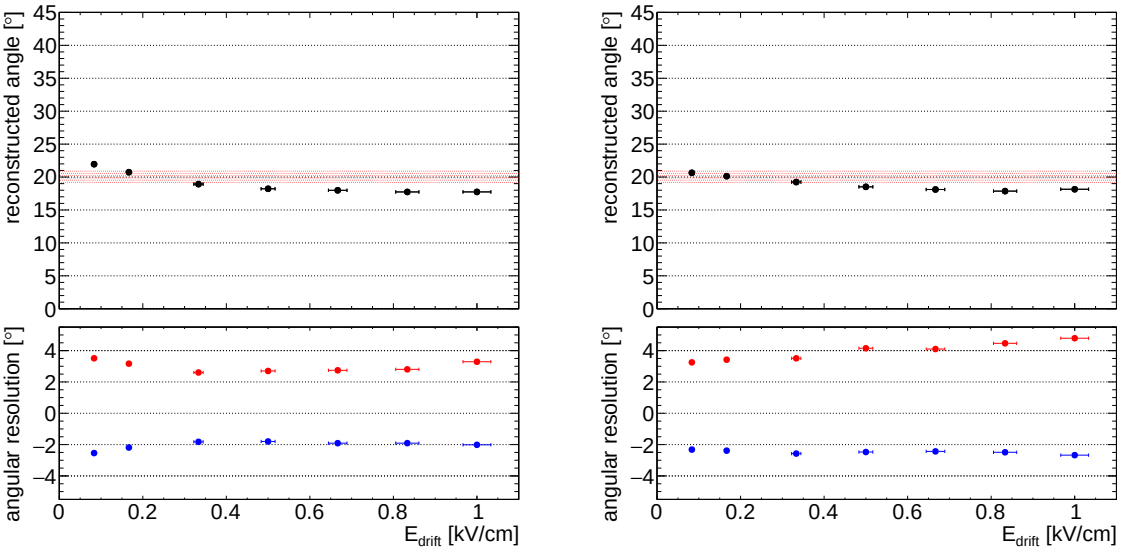

(a) x-layer (b) y-layer

Figure C.5: Reconstructed most probable angle and angular resolution as a function of E_{drift} at E_{amp}=50 kV/cm measured with the x-layer (left) and the y-layer (right) of anode design 4 at an angle of $(20 \pm 1)°$. The measured inclination of the detector with a ruler is marked in red.

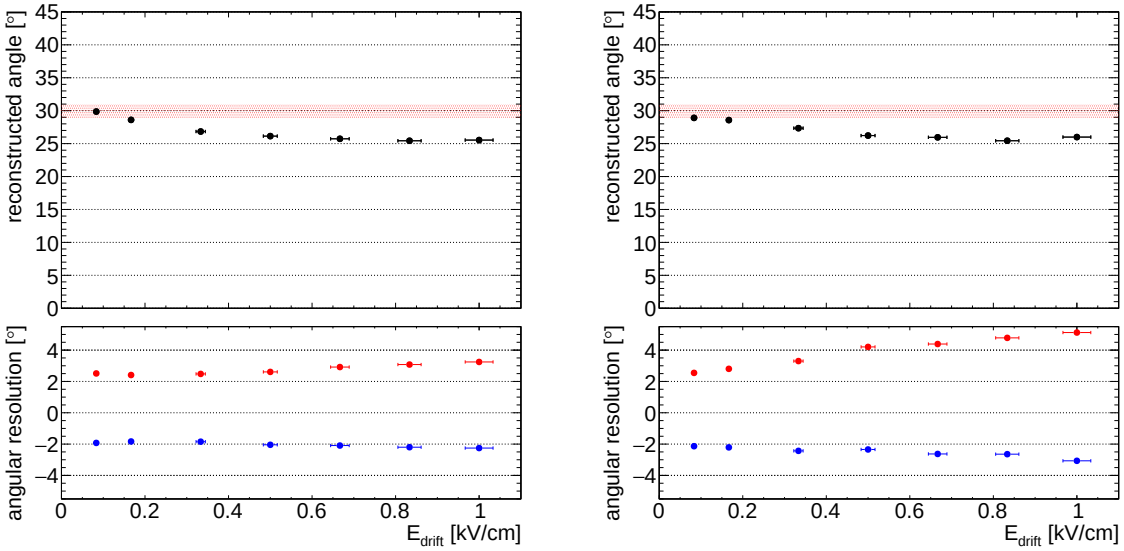

(a) x-layer (b) y-layer

Figure C.6: Reconstructed most probable angle and angular resolution as a function of E_{drift} at E_{amp}=50 kV/cm measured with the x-layer (left) and the y-layer (right) of anode design 4 at an angle of $(30 \pm 1)°$. The measured inclination of the detector with a ruler is marked in red.

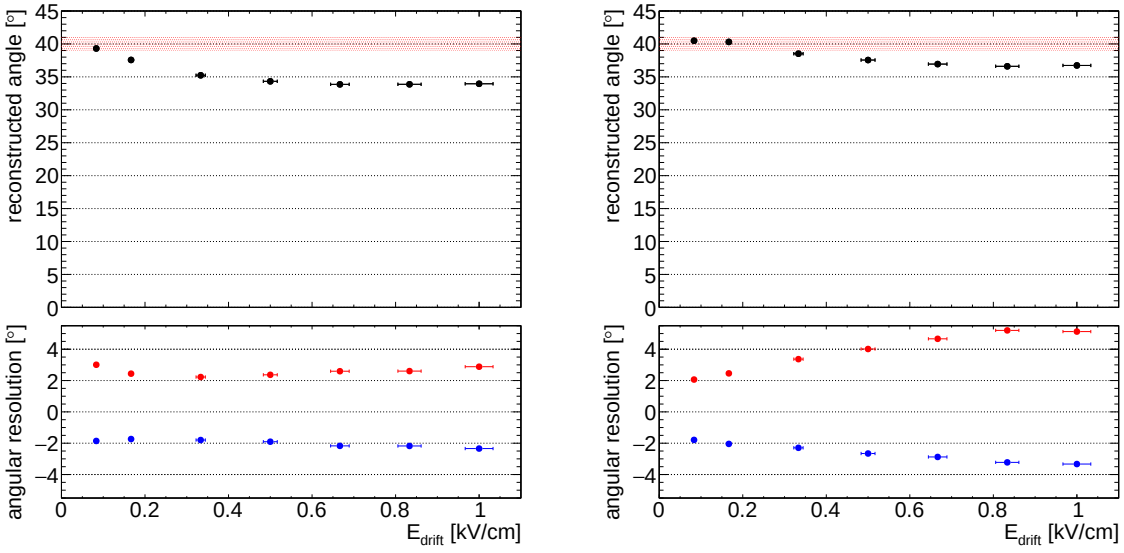

(a) x-layer (b) y-layer

Figure C.7: Reconstructed most probable angle and angular resolution as a function of E_{drift} at E_{amp}=50 kV/cm measured with the x-layer (left) and the y-layer (right) of anode design 4 at an angle of $(40 \pm 1)°$. The measured inclination of the detector with a ruler is marked in red.

In the drift field scan on the x-layer visible in Figure C.8, the muon beam was changed by the main test beam user to a pion beam for drift field points between 0.17 kV/cm and 0.83 kV/cm. This leads to generally reduced efficiency of the detector for two reasons: First, the pion beam is very localized with a beam spot size of $\sigma_x = (2.39 \pm 0.02)$ mm and σ_y=(3.25 ± 0.03) mm. Due to the much smaller size compared to the muon beam halo, which is bigger than the

active area of all detectors, the inefficiency caused by the pillars has a bigger impact with the pion beam. Second, the pion beam flux is with 420 kHz/cm^2 four orders of magnitude higher than the beam flux of the muons with 15 Hz/cm^2. This leads to a voltage drop of 0.5 V on the floating strip i.e. a reduction of the pulse height of about 2%.

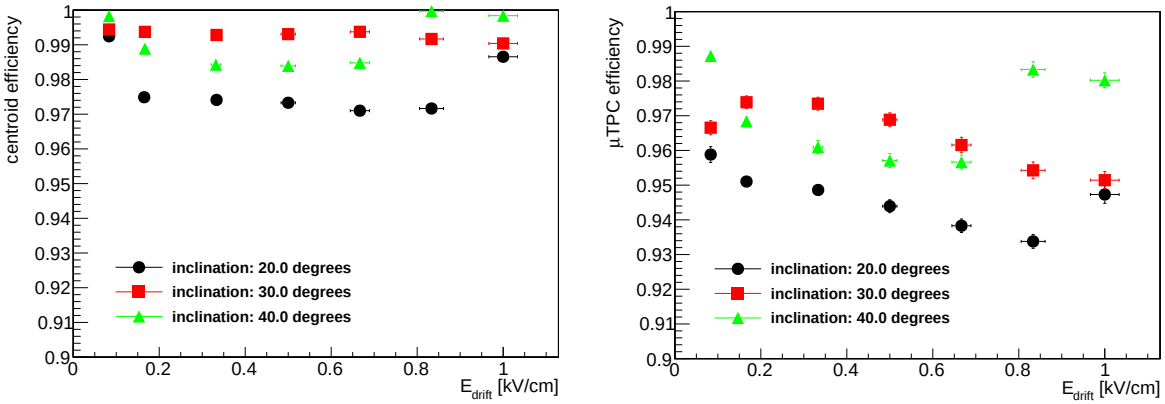

Figure C.8: Efficiency of the x-layer determined with the centroid method (left) and the μTPC method (right) as a function of E_{drift} at E_{amp}=50 kV/cm for three different inclination angles. The step in efficiency visible on both figures is due to a change from muon beam to pion beam, as the pion beam halo is much smaller and thus the pillars have a bigger effect on the inefficiency.

Acknowledgments

At this point, I would like to thank all the people that supported me during the last three years. I am truly sorry, if I missed anyone.

First of all, I would like to thank my Doktorvater Prof. Dr. Otmar Biebel for giving me the freedom to pursue the different aspects of my research, his always opend door, fruitful discussions and late evening coffee breaks in the kitchen.

I would like to thank Dr. Ralf Hertenberger especially for the support during test beam measurements at the Tandem accelerator in Garching and also for discussions regarding my work even though being busy with some other big detector construction project.

I want to thank Prof. Dr. Dorothee Schaile for giving me the opportunity to work on this project and Dr. Otto Schaile for his continuous support with ROOT problems.

I also want to thank Dr. Jonathan Bortfeldt for proof reading big parts of the thesis, the support during various test beams and the very fruitful discussions before and after his time at the chair.

I want to thank Dr. Werner Riegler for the helpful discussion about signal generation in Micromegas detectors.

I want to thank the medical physics chair around Prof. Dr. Katia Parodi and especially Dr. Lorena Magallanes, Dr. Chiara Gianoli and Sebastian Meyer for the interesting discussions and the possibility of the test beam measurement at HIT.

Of course I want to thank all the members of the chair, but especially: Dr. Bernhard Flierl, Maximilian Herrmann, Dr. Philipp Lösel, Dr. Ralph Müller, Dr. Chrysostomos Valderanis, Dr. Andre Zibell, Dr. Thomas Maier, Helge Danger, Maximilian Rinnagel and Christoph Jagfeld.

I would like to thank the mechanical workshop around Rolf Oehm, Felix Grundner and Attila Varga for the support during the PCB finalization processes.

I want to also thank Dr. Friedrich Hönig, Martin Loder and Maximilian Dornieden for proof reading parts of my thesis.

Zu guter Letzt möchte ich mich natürlich bei meiner Familie und Freunden bedanken, die mich während den letzten drei Jahren sehr unterstützt haben, under anderem: Bei meinen Eltern Heidi Teichmann-Klitzner und Jürgen Klitzner, meinen Geschwistern Karina Teichmann mit Enrico Dehler und Stefan Teichmann mit Sonja Teichmann. Vor allem aber bei meiner Freundin Cathrin Grolig, da sie mich in den letzten Monaten noch mehr als sonst unterstützt hat.